TECHNICKÁ UNIVERZITA V LIBERCI
Fakulta strojní

Vysokoteplotní oxidační a korozní odolnost slitin na bázi aluminidů železa

HABILITAČNÍ PRÁCE

Ing. Adam Hotař, Ph.D.

Obor habilitačního řízení: Technologie a materiály

katedra materiálu, Fakulta strojní, Technická univerzita v Liberci
Liberec, 2020

Poděkování

Rád bych poděkoval všem kolegům a spolupracovníků, bez jejichž přispění by tato práce nevznikla. Vřelé poděkování patří především prof. RNDr. Petru Kratochvílovi, DrSc. z katedry fyziky materiálů MFF UK v Praze, který mě a mé kolegy k výzkumu intermetalických slitin přivedl, dále za dlouholeté vedení a podněty, za cenné rady a konzultace nejen při přípravě této habilitační práce, dále Dr. Martinu Palmovi z Max-Planck-Institut für Eisenforschung v Düsseldorfu za cenné rady a připomínky v oblasti oxidace aluminidů železa a bratrovi doc. Ing. Vlastimilu Hotařovi, Ph.D. za spolupráci při vývoji metodiky pro kvantifikaci korozního nebo oxidačního napadení slitin. Také bych rád poděkoval všem spoluautorům komentovaných publikací a kolegům, na jejichž projektech jsem mohl spolupracovat. Za pomoc a podporu rovněž děkuji svým blízkým spolupracovníkům z katedry materiálu Technické univerzity v Liberci. Poděkování patří také mé rodině a mým blízkým za trpělivost a podporu.

Abstrakt

Habilitační práce je zaměřena na studium oxidačního a korozního chování aluminidů železa za vysokých teplot. Výzkum je založen na rozsáhlých vysokoteplotních oxidačních a korozních testech, které umožňují pomocí termogravimetrické analýzy definovat kinetiku oxidace či koroze slitin. Vysokoteplotní chování slitin na bázi Fe_3Al na vzduchu a ve sklovině je popsáno na základě analýz okují či korozních produktů. Je použita především rentgenová difrakce, elektronová mikroskopie, energiově dispersní analýza, EBSD a také optická mikroskopie.

Je popsán vliv legujících prvků především zirkonia, dále tantalu, céru a titanboridu na oxidační chování Fe_3Al slitin. Podrobná analýza oxidů a struktury pod povrchem aluminidů železa určuje fázové složení okují a charakter oxidace slitin v závislosti na chemickém složení slitiny a podmínek oxidace. Je popsáno také korozní chování Fe_3Al slitin v sodnovápenaté sklovině a v olovnatém křišťálu. K popisu a kvantifikaci korozního nebo oxidačního napadení aluminidů železa a srovnávacích ocelí je nově použita metodika využívající fraktální geometrii a statistické nástroje.

Abstract

The habilitation thesis is focused on the oxidation and corrosion behaviour of iron aluminides at high temperatures. The research is based on extensive high-temperature oxidation and corrosion tests, which make possible to define the kinetics of oxidation or corrosion of alloys using thermogravimetric analysis. The high-temperature behaviour of Fe_3Al-based alloys in air and in molten glass is described based on analyzes of scales or corrosion products. X-ray diffraction, electron microscopy, energy dispersion analysis, EBSD and also optical microscopy are used.

The influence of alloying elements mainly zirconium, as well as tantalum, cerium and titanboride on the oxidation behaviour of Fe_3Al alloys is described. Detailed analyzes of oxides and structures below the surface of iron aluminides determine the phase composition of scale and the character of oxidation of alloys depending on the chemical composition of the alloy and oxidation conditions. The corrosion behaviour of Fe_3Al alloys in soda-lime glass and lead crystal is also described. The methodology that uses fractal geometry and statistical tools is newly used to describe and quantify corrosion or oxidation attack of iron aluminides and comparative steels.

Obsah

1. Úvod

Aluminidy železa na bázi Fe_3Al a FeAl jsou uvažovány jako konstrukční materiály, které mají nahradit žáruvzdorné oceli s vysokým obsahem chromu a niklu. Přednosti aluminidů železa spočívají v nižší materiálové ceně, v nižší měrné hmotnosti (5,8 – 6,3 $g.cm^{-3}$) a ve velmi dobré korozní odolnosti v různých agresivních prostředích, především v oxidačních a sulfidačních atmosférách [1-4], dále v silně nauhličujících plynných směsích [4], v taveninách solích [3, 4, 6], v parách obsahujících chlór [3, 7] a v neposlední řadě v roztavených sklovinách [8]*.

Se slitinami na bázi aluminidů železa jsme se setkali již v padesátých letech dvacátého století, kdy se vyvíjely nové žáruvzdorné materiály bez obsahu deficitních prvků chromu a niklu. Jedná se o slévárenskou slitinu s obchodním názvem Pyroferal, vyvinutou v Československu [9, 10], v zahraničí pak Tchugal vyráběný v Sovětském svazu a Thermagal vyráběný ve Francii. Pyroferal vyniká dobrými slévárenskými vlastnostmi, nízkou opotřebitelností a vynikající korozní odolností v prostředí obsahujícím kyslík a také ve spalinách až do teplot 1100 °C [9, 10]. Své uplatnění Pyroferal našel také ve sklářství, kde nahrazoval výrobky z litiny, např. části hořáků [11]. Testované výrobky z Pyroferalu se vyznačovaly tenkou a přilnavou vrstvou okují, čímž nedocházelo k znečišťování skloviny a prodloužila se výrazně životnost součástí.

Návrat k intenzivnímu výzkumu slitin na bázi aluminidů železa nastal až na konci 20. století, a to nejen v USA, ale i v Evropě (Německo, Španělsko, Francie či Polsko). V této době výzkum slitin FeAl a Fe_3Al v České republice navázal nejen na poznatky získané v padesátých letech dvacátého století (Pyroferal), ale také na výsledky publikované ve světě (např. řada konferencí k této tématice, publikace v periodiku Intermetallics).

Studium vlastností aluminidů železa na katedře materiálu Technické univerzity v Liberci je věnováno, vedle zvýšení houževnatosti při pokojových teplotách, především zvýšení pevnosti a creepové odolnosti za vysokých teplot. Zvýšení pevnosti při teplotách nad 600 °C se nejčastěji dosahuje legováním prvky s malou rozpustností v matrici, které po překročení rozpustnosti způsobují vznik eutektik nebo precipitátů jako jsou karbidy, boridy nebo intermetlické fáze (např. Lavesovy fáze). Výsledky byly publikovány například v [12, 13, 14, 15]. Tyto fáze či částice bohaté na legující prvek zlepšují mechanické vlastnosti za vysokých teplot, ale mohou snížit korozní odolnost aluminidů. Proto souběžně s výzkumem

* viz také [P3-1]

mechanických vlastností (zejména za vysokých teplot) na katedře materiálu probíhá studium oxidačního a korozního chování vyvíjených aluminidů železa.

2. Vysokoteplotní oxidace slitin na bázi Fe_3Al na vzduchu

Kovy a jejich slitiny, které mají velmi dobře odolávat oxidačnímu nebo koroznímu prostředí za vysokých teplot, se musí pokrývat ochrannou oxidickou vrstvou [16]. Ochranná oxidická vrstva má rychle vytvořit účinnou bariéru mezi vnějším prostředím a kovovým materiálem, aby nedocházelo k další oxidaci povrchu. To znamená, že vrstva oxidů se má v ideálním případě rychle vytvořit a posléze růst velmi pomalu. Dále se vrstva oxidů musí vyznačovat vysokou stabilitou a přilnavostí, musí být rovnoměrná, souvislá, prostá prasklin a pórů. Slitiny na bázi aluminidů železa se vyznačují tvorbou oxidu α-Al_2O_3, který se ideálním vlastnostem oxidické vrstvy, viz výše, blíží. Pro vznik této modifikace oxidu hlinitého je třeba splnit dva důležité faktory. Za prvé, slitina musí obsahovat dostatečné množství hliníku a za druhé, oxidace musí probíhat při dostatečně vysokých teplotách. Za jiných podmínek se oxid hlinitý vyskytuje v různých krystalických formách, které jsou stabilní v odlišných teplotních intervalech:

$$\gamma\text{-}Al_2O_3 \xrightarrow{750\ °C} \delta\text{-}Al_2O_3 \xrightarrow{900\ °C} \theta\text{-}Al_2O_3 \xrightarrow{1000\ °C} \alpha\text{-}Al_2O_3 \quad (1)$$ [17].

Dostatečné množství hliníku v aluminidech železa zaručuje tvorbu souvislé vrstvy oxidu hlinitého po celém povrchu. Pro binární slitinu Fe-Al se minimální obsah pohybuje kolem 19 at. % Al [18], značí se C_b. Na tuto hranici má vliv obsah legur, např. obsah chromu kritickou hranici hliníku snižuje, naopak obsah niklu hranici zvyšuje [19]. Dále na minimální obsah hliníku mají vliv metalurgické postupy, například u oxidicky zpevněných Fe-Al slitin (ODS alloys) se minimální obsah Al snížil při teplotě oxidace 900 °C přibližně o 4 at. % [20].

Dostatečné množství hliníku je také nutné z hlediska oxidační životnosti slitiny (oxidation lifetime). Oxidační životnost je definována jako čas, kdy okuje Al_2O_3 (vznikající přednostní oxidací hliníku) vytváří ochrannou vrstvu na povrchu aluminidů železa a tím oxidace postupuje velmi pomalu [19]. Nicméně, vlivem tvorby, růstu a případného odlupování okují dochází k odčerpávání atomů Al pod vrstvou oxidů Al_2O_3 a po určité době může klesnout obsah hliníku pod hranici C_b, která je nutná pro tvorbu souvislé a ochranné vrstvy oxidů Al_2O_3. Jestliže k takovému poklesu dojde, začnou se tvořit oxidy (nebo jiné produkty koroze v případě sulfidace, nauhličení atd.), které slitinu nechrání a rychlost oxidace se prudce zvýší. Někdy je rychlost oxidace tak vysoká, že může dojít i ke ztrátě strukturní integrity slitiny. Náhlé urychlení

oxidace v důsledku poklesu hliníku pod C_b je nazýváno katastrofickou oxidací („catastrophic breakaway oxidation“). Oxidační životnost se tedy může formálně definovat jako čas do katastrofické oxidace („time-to-breakaway“), nebo jako čas, při kterém dojde k poklesu koncentrace hliníku pod hranici nutnou k tvorbě souvislé vrstvy oxidu hlinitého. Pro stanovení času do katastrofické oxidace se používá tento model:

$t_b = \{A \cdot (C_0 - C_b) \cdot \rho \cdot h / K\}^{1/n}$ (2) [19]

kde je

C_0 … úvodní koncentrace hliníku

C_b … koncentrace hliníku, která je nutná pro tvorbu souvislé a ochranné vrstvy oxidů Al_2O_3

A … konstanta (zohledňuje hmotnostní poměr Al/O [21])

ρ … hustota slitiny

h … tloušťka vzorku

K …oxidační rychlost (úbytek kovu), je typicky charakterizována parabolickou rychlostní konstantou k_p

Model (rovnice 2) ukazuje, že oxidační životnost závisí na množství hliníku dostupného pro reakce (hliníkový reservoár) přes C_0 a h, dále je přímo úměrná k oxidační rychlosti. Z tohoto pohledu obsahují aluminidy železa na bázi Fe_3Al a FeAl dostatečné množství hliníku a tím je zajištěna dlouhá oxidační životnost.

Z hlediska oxidační a korozní odolnosti slitin na bázi aluminidů železa je nejvhodnější modifikace α-Al_2O_3, která vytváří nejúčinnější bariéru vůči okolnímu prostředí. Kinetiku oxidace lze v mnoha případech popsat pomocí parabolického zákona (parabolického rychlostního zákona kontrolované difusní oxidací) [22]

$$(\Delta m/S)^2 = k_p \cdot t \quad (3)$$

kde Δm/S je hmotnostní přírůstek (případně úbytek) na jednotku plochy (mg/cm^2), k_p je parabolická rychlostní konstanta a t je čas (h).

Pro snadné porovnání oxidačního chování testovaných slitin (např. sledování vlivu legujících prvků nebo vlivu teploty na oxidační chování) se často používá parabolická rychlostní konstanta, kterou lze stanovit z rovnice (3). Konstanta k_p představuje sklon křivky růstu oxidické vrstvy, tj. čím menší sklon křivky (nízké k_p), tím pomaleji roste oxidická vrstva a naopak, viz Obr. 1. Odchylky od parabolického zákona lze pozorovat jednak v průběhu celé oxidace při teplotách nižších než 900 °C (případně 1000 °C), nebo i při teplotě nad 900 °C, ale pouze v úvodní fázi oxidace (cca do 200 h). Odchylky lze vysvětlit vznikem odlišných modifikací

oxidu hlinitého, jako jsou γ-, δ-, θ-Al_2O_3, viz rovnice (1), které jsou objemnější a méně ochranné.

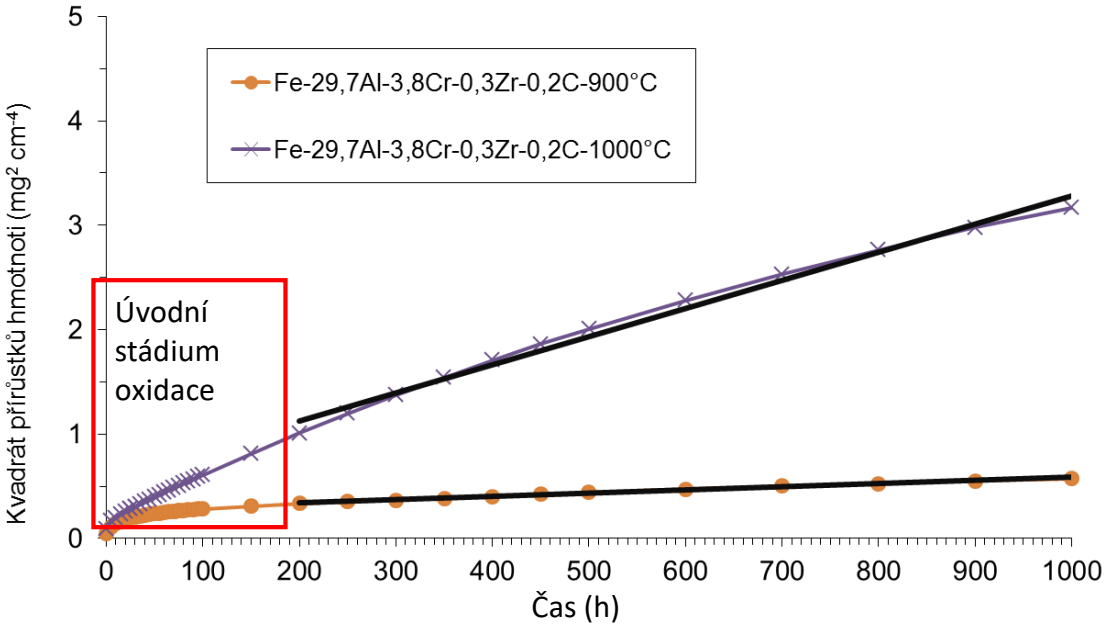

Obr. 1. Závislost kvadrátu přírůstku hmotnosti v závislosti na čase [23]*

Vznik modifikací oxidu hlinitého na slitinách na bázi Fe-Al se však neřídí striktně dle teplot uvedených ve schématu (rovnice 1). Například γ-Al_2O_3 byla pozorována na Fe-Al slitinách v teplotním rozsahu 700-900 °C [16]. Při teplotách oxidace 800 až 850 °C binární slitiny Fe-Al (s cca 40 at.% Al) byla také zjištěna ve vrstvě oxidů modifikace θ-Al_2O_3 [24]. Na téže slitině byla při teplotách oxidace 950 °C a 1000 °C v prvních hodinách identifikovány metastabilní modifikace Al_2O_3, charakteristické vysokou hodnotou parabolické rychlostní konstanty. Po delší době se výrazně parabolická rychlostní konstanta snížila vlivem tvorby α-Al_2O_3 [24]. Na binární slitině Fe_3Al θ-modifikace oxidu hlinitého byla pozorována i při teplotách 952 °C a 1057 °C [25]. Při teplotách 1152 °C a 1257 °C již dominuje stabilní forma α-Al_2O_3 [25]. Chevalier a kol. [26] zjistili, že po oxidaci na teplotě 900 °C se na povrchu binární slitiny Fe_3Al a slitiny Fe_3Al legované Zr vytváří α-Al_2O_3 a také θ-Al_2O_3. Při teplotě přibližně 950 °C se θ-Al_2O_3 transformuje na α-Al_2O_3 a při vyšších teplotách oxidace (1000 °C a výše) se v okujích vyskytuje pouze α-Al_2O_3. Vedle různých modifikací Al_2O_3 se na povrchu mohou také vyskytovat oxidy železa. Lee a Lin po oxidaci slitiny Fe_3Al-5Cr (at.%) na vzduchu při teplotě 605 °C pozorovali na povrchu malé množství útvarů Fe_2O_3 [27].

* viz také [P2-1]

Jedním z hlavních motivů předkládané habilitační práce je objasnění vlivu zirkonia a dalších legujících prvků jakou jsou tantal, cer atd. na kinetiku oxidace a oxidačního chování binárních slitin na bázi Fe-Al.

2.1 Vliv zirkonia na oxidační chování aluminidů železa na bázi Fe_3Al

Pro vynikající oxidační odolnost je zásadní přilnavost na rozhraní mezi vrstvou oxidů a Fe-Al slitin. Zlepšení adheze oxidů k substrátu lze dosáhnout přídavkem malého množství tzv. reaktivních prvků (reactive elements) jako jsou Hf, Y, Zr atd. [26, 16] Tyto prvky navíc podporují vznik termodynamicky stabilnějších oxidů, které pomaleji rostou. Prescott a Graham se velmi podrobně zabývají ve své práci [16] mechanismy (difusními pochody v oxidické vrstvě, segregací částic bohatých na reaktivní prvky, vlivem reaktivních prvků na velikost a tvar zrn oxidů atd.) zvyšujícími oxidační odolnost slitin vlivem reaktivních prvků, především ytria.

Mezi významné reaktivní prvky, které ovlivňují oxidační vlastnosti Fe-Al slitin, patří také zirkonium. Je známo, že oxidační chování slitin na bázi Fe-Al zlepšuje malý přídavek Zr do 0,1 at.% [28, 29]. Malé množství Zr urychluje vznik stabilní modifikace α-Al_2O_3 [29] a také dochází k zlepšení přilnavosti α-Al_2O_3 okují [26, 30, 31]. Dalším důvodem legování slitin Fe-Al zirkoniem je zvyšování pevnosti za vysokých teplot. V tomto případě se do slitin přidává větší množství Zr, než je maximální rozpustnost v tuhém roztoku, tak aby vznikaly zpevňující částice (např. Lavesovy fáze, ZrC) [32]. Zvýšení množství Zr (nad 0,1 at. %) a tím vznik zpevňujících precipitátů se prospěšně projevilo ve zlepšení mechanických vlastností za vysokých teplot [33]. Vliv částic obsahujících Zr na oxidační chování aluminidů železa však zkoumali pouze Pint a kol. [34] a později Janda a kol. [35]. V obou případech pozorovali přednostní oxidaci částic bohatých na Zr (vstupní oxidaci) a také zhoršení adheze okují k substrátu. Proto bylo nutné provést systematický (detailní) výzkum vlivu zirkonia (vliv precipitátů – množství i druh) na oxidační chování aluminidů železa. Výsledky výzkumu jsou shrnuty v [P2-1 a P2-2].

[P2-1]	HOTAŘ, A., M. PALM, P. KRATOCHVÍL, V. VODIČKOVÁ a S. DANIŠ. High-temperature oxidation behaviour of Zr alloyed Fe_3Al-type iron aluminide. *Corrosion Science*. 2012, 63, 71-81.
[P2-2]	HOTAŘ, A., P. KEJZLAR, M. PALM a J. MLNAŘÍK. The effect of Zr on high-temperature oxidation behaviour of Fe_3Al-based alloys. *Corrosion Science*. 2015, 100, 147-157.

V práci [P2-1] byly studovány dvě komplexní slitiny Fe-Al-Cr-Zr-C, které vykazovaly slibné mechanické vlastnosti pro vysokoteplotní aplikace [36]. Slitiny byly podrobeny izotermickým oxidačním testům při teplotách 900, 1000, 1100 a 1200 °C na zařízení Setaram SYSTÉM 16/18 (termováhy s kontinuálním záznamem hmotnostního přírůstku) v syntetickém vzduchu po dobu až 1000 h. Vzniklé oxidy byly poté analyzovány pomocí elektronového mikroskopu vybaveného EDS analýzou, pro zjištění fázového složení oxidických okují byla také použita RTG difrakční analýza, následovalo rovněž pozorování strukturních změn v řezu kolmém na povrch vzorků pomocí optického a elektronového mikroskopu.

Dále v [P2-2] byl podrobně zkoumán vliv obsahu Zr na oxidační chování slitin Fe-30Al-xZr a Fe-25Al-xZr (x=0,3-5,2 at.% Zr) při teplotách 900 a 1100 °C. Tentokrát byla provedena cyklická oxidace v laboratorním vzduchu, abychom se přiblížili k pracovním podmínkám. Oxidace vzorků probíhala v korundových kelímcích tak, aby byly zachyceny odpadávající okuje. Po ukončení oxidačního testu chladly vzorky v peci a studené vzorky v kelímcích byly následně zváženy. Pro analýzu oxidického napadení byly použity stejné analytické metody jako v práci [P2-1].

2.1.1 Složení okují na povrchu slitin Fe-Al-Zr s obsahem zirkonia větším než 0,1 at.% Zr po vysokoteplotní oxidaci

Rentgenová difrakce a EDS analýza prokázaly, že na povrchu slitin na bázi Fe_3Al se vytváří okuje složené z Al_2O_3, ZrO_2 a v některých případech z Fe_2O_3 (Tab. 1). Na přítomnost jednotlivých oxidů má vliv teplota oxidace a chemické složení slitin. Vliv teploty oxidace se především projevil na obsahu oxidu železitého, viz Tab. 1 a Obr. 2. Při nižších teplotách oxidace, tj. při teplotě 900 °C, se u těchto slitin vždy vyskytuje Fe_2O_3, viz Obr. 2. Naopak při vyšších

teplotách (nad 1000°C) obsah Fe_2O_3 klesá, okuje jsou složené převážně z Al_2O_3 a ZrO_2, přičemž dominuje podíl Al_2O_3.

Tab. 1. Vliv teploty na fázové složení okují, detekované pomocí RTG difrakce a EDS analýzy [P2-1, P2-2]

slitiny	900 °C	1100 °C	Druh oxidace
Fe-29,7Al-3,8Cr-0,3Zr-0,2C	Al_2O_3, málo ZrO_2, minoritní množství Fe_2O_3	Al_2O_3, ZrO_2	isotermická
Fe-26,4Al-2,8Cr-0,2Zr-0,6C	Al_2O_3, málo Fe_2O_3, minoritní množství ZrO_2	Al_2O_3, ZrO_2	isotermická
Fe-25,7Al-0,3Zr	Al_2O_3, Fe_2O_3, málo ZrO_2	Al_2O_3, málo Fe_2O_3, málo ZrO_2	cyklická
Fe-25,7Al-1,0Zr	Al_2O_3, Fe_2O_3, málo ZrO_2	Al_2O_3, málo Fe_2O_3, málo ZrO_2	cyklická
Fe-29,3Al-0,4Zr	Al_2O_3, Fe_2O_3, málo ZrO_2	Al_2O_3, málo ZrO_2	cyklická
Fe-29,2Al-0,9Zr	Al_2O_3, Fe_2O_3, ZrO_2	Al_2O_3, málo Fe_2O_3, málo ZrO_2	cyklická
Fe-30,1Al-5,2Zr	Al_2O_3, Fe_2O_3, ZrO_2	Vzorek se rozpadl – nebylo měřeno	cyklická

Výzkum aluminidů železa s odlišným obsahem zirkonia prokázal, že Zr ovlivňuje fázové složení oxidické vrstvy (Tab. 2, Obr. 3). V případě legování aluminidů železa malým množstvím Zr (několik desetin atomových procent) obsahuje oxidický film převážně Al_2O_3, Fe_2O_3 a malé množství ZrO_2 [P2-2]. Naopak s rostoucím obsahem Zr (k 1 at. % a více) ve slitině klesá v oxidech zastoupení Al_2O_3, zatímco frakce Fe_2O_3 a ZrO_2 stoupá, jak dokládá chemické složení oxidů (Tab. 2). Tento trend byl pozorován nejen při oxidaci na teplotě 1100 °C, ale i na teplotě 900 °C.

Tab. 2. Složení povrchových okují po oxidaci při teplotě 1100 °C (po 500 h) stanovené EDS analýzou (při urychlovacím napětí 10kV)

slitina	at.% Fe	at.% Al	at.% Zr	at.% O
Fe-29,3Al-0,4Zr	1,32	38,7	0,88	59,1
Fe-29,2Al-0,9Zr	3,8	37,2	1,43	57,6
Fe-30,1Al-5,2Zr	9,4	29,5	2,46	58,6

Pozornost byla také věnována mechanismu růstu oxidické vrstvy. Přednostní oxidací částic bohatých na Zr způsobuje vznik ZrO_2, které je „obaleno“ Al_2O_3 [P2-2]. Zdá se, že ZrO_2 má katalytický efekt pro nukleaci Al_2O_3, stejný efekt byl pozorován i v [37]. Dokonce byly kolem Zr-částic pozorovány místo rovnoosých zrn Al_2O_3 zrna kolumnární [P2-2], podobně jako v [26].

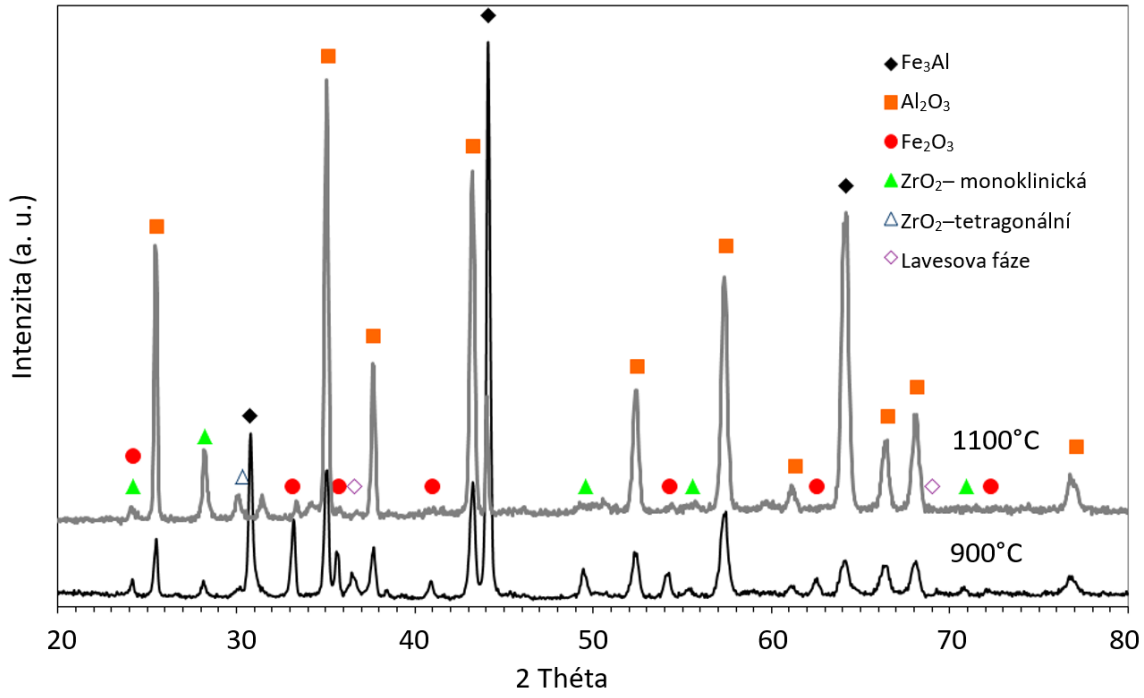

Obr. 2. RTG difrakční analýza Fe-25,7Al-0,3Zr při teplotě 900 °C a 1100 °C

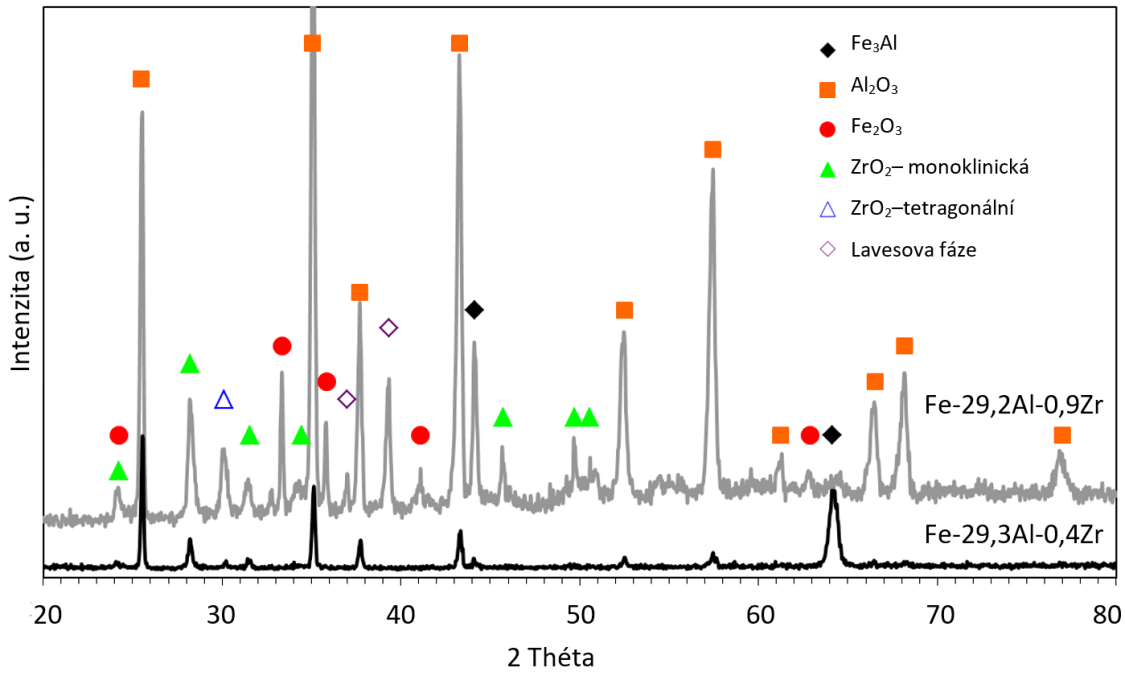

Obr. 3. RTG difrakční analýza slitin Fe-29,3Al-0,4Zr a Fe-29,2Al-0,9Zr při teplotě 1100 °C

Z obrázků 2 a 3 je také patrné, že po oxidaci 900 °C a 1100 °C se oxid zirkoničitý vyskytuje v okujích nejen v monoklinické formě, ale i v tetragonální. Přitom teplota fázové transformace mezi čistým ZrO_2 s monoklinickou a tetragonální mřížkou je 1170 °C [38, 39]. Lze však předpokládat, že v tomto případě stabilitu tetragonální formy ZrO_2 při nižších teplotách (než 1170 °C) podporuje přítomnost nečistot, velikost zrn nebo tlakové napětí [38, 39].

2.1.2 Vysokoteplotní oxidace slitin Fe-Al-Zr s obsahem zirkonia v rozmezí 0,1 až 1 at.% Zr při teplotě 900 °C

U slitin Fe-Al-Cr-Zr-C během isotermické oxidace vznikala na povrchu přilnavá a tenká vrstva okují. Během střídání teplot při cyklické oxidaci slitin Fe-Al-Zr se však objevilo praskání okují. V případě slitin obsahujících 0,3 až 0,4 at. % Zr docházelo vlivem teplotních napětí (způsobených odlišným koeficientem teplotní roztažnosti oxidického filmu a matrice) ke vzniku trhlin na rozhraní matrice/oxid a tím k snadnému odlupování oxidického filmu. U slitin s obsahem Zr kolem 1 at. % bylo pozorováno také praskání okují, ale nedocházelo k jejich odlupování. K odlupování nedochází pravděpodobně proto, že okuje obsahují četné póry, které eliminují vzniklá teplotní napětí.

Po cyklické oxidaci byla také zjištěna vstupní oxidace, především podél hranic zrn, způsobená přednostní oxidací Lavesovy fáze nebo eutektika složeného z Lavesovy fáze a Fe-Al. Oxidace vstupuje do menších hloubek u slitin s vyšším obsahem Al a nižším obsahem Zr. Přesto si i po cyklické oxidaci slitiny Fe-Al legované zirkoniem ponechávají velmi dobrou oxidační odolnost při teplotě 900°C, což je patrné z nízkých hodnot „zdánlivé parabolické rychlostní konstanty“ k_p (Apparent parabolic rate constant), viz Tab. 3. V tomto případě byla použita zdánlivá parabolická rychlostní konstanta [P2-1, P2-2], protože pro výpočet skutečné k_p (rovnice 3) je nutné, aby růst oxidů byl nejen parabolický, ale také aby vzniklá vrstva oxidů na povrchu byla hladká. Jinými slovy, zdánlivou parabolickou rychlostní konstantu lze vypočítat u slitin, které jsou charakteristické růstem oxidů dle parabolické křivky a vyznačují se vstupní oxidací. Zdánlivá k_p byla počítána také podle rovnice 3.

Tab. 3. Zdánlivá parabolická rychlostní konstanta k_p (Apparent parabolic rate constants) aluminidů železa po oxidaci při teplotě 900 °C v laboratorním vzduchu

Slitiny (at. %)	k_p (g^2 cm^{-4} s^{-1})	Druh oxidace	Práce
Fe-29,7Al-3,8Cr-0,3Zr-0,2C	$8,3 \times 10^{-14}$	isotermická	[P2-1]
Fe-26,4Al-2,8Cr-0,2Zr-0,6C	$1,1 \times 10^{-13}$	isotermická	[P2-1]
Fe-25,7Al-0,3Zr	$2,8 \times 10^{-14}$	cyklická	[P2-2]
Fe-25,7Al-1,0Zr	$3,1 \times 10^{-12}$	cyklická	[P2-2]
Fe-29,3Al-0,4Zr	$6,4 \times 10^{-13}$	cyklická	[P2-2]
Fe-29,2Al-0,9Zr	$5,8 \times 10^{-13}$	cyklická	[P2-2]
Fe-28Al-3Cr-0,02Ce	$4,2 \times 10^{-13}$	cyklická	[P2-4]
Fe-30Al-4Cr-2,7TiB_2	$6,9 \times 10^{-13}$	cyklická	[P2-4]
Fe-25Al	$1,0 \times 10^{-13}$		[40]

2.1.3 Vysokoteplotní oxidace slitin Fe-Al-Zr s obsahem zirkonia v rozmezí 0,1 až 1 at.% Zr při teplotě nad 1000 °C

Zvýšená teplota oxidace urychluje difusní pochody (hliníku, zirkonia i kyslíku) a tím dochází k rychlejšímu růstu oxidického filmu. Při isotermické oxidaci růst oxidů probíhal většinou dle parabolického zákona [P2-1]. Během cyklické oxidace při teplotě 1100 °C slitin Fe-Al-Zr docházelo k růstu oxidů podle lineárního nebo dokonce podle hyperbolického zákona [P2-2]. Tato zvýšená progrese nárůstu oxidů souvisí především s pronikáním oxidace podél fází bohatých na Zr pod povrch vzorků, které bylo pozorováno jak při cyklické, tak i při isotermické oxidaci. Rozsah pronikání oxidace roste s teplotou a s rostoucí přítomností fází bohatých na zirkonium [P2-1, P2-2]. Například hmotnostní přírůstky slitiny na bázi Fe-Al legované 5,2 at.% Zr již po několika hodinách nabývají výrazně vyšších hodnot než slitina legovaná 0,4 at.% Zr (Obr. 4). Po 100 hodinách cyklické oxidace při teplotě 1100 °C u slitiny Fe-30,1Al-5,2Zr nastává již katastrofická oxidace. To znamená, že oxidický film nevytváří účinnou bariéru, oxidace velmi rychle postupuje, protože se neomezuje pouze na precipitáty bohaté na Zr, ale napadá i matrici. Po 300 hodinách oxidace prostoupila téměř celým objemem vzorku, proto hmotnost vzorku dál již výrazně neroste (Obr. 4).

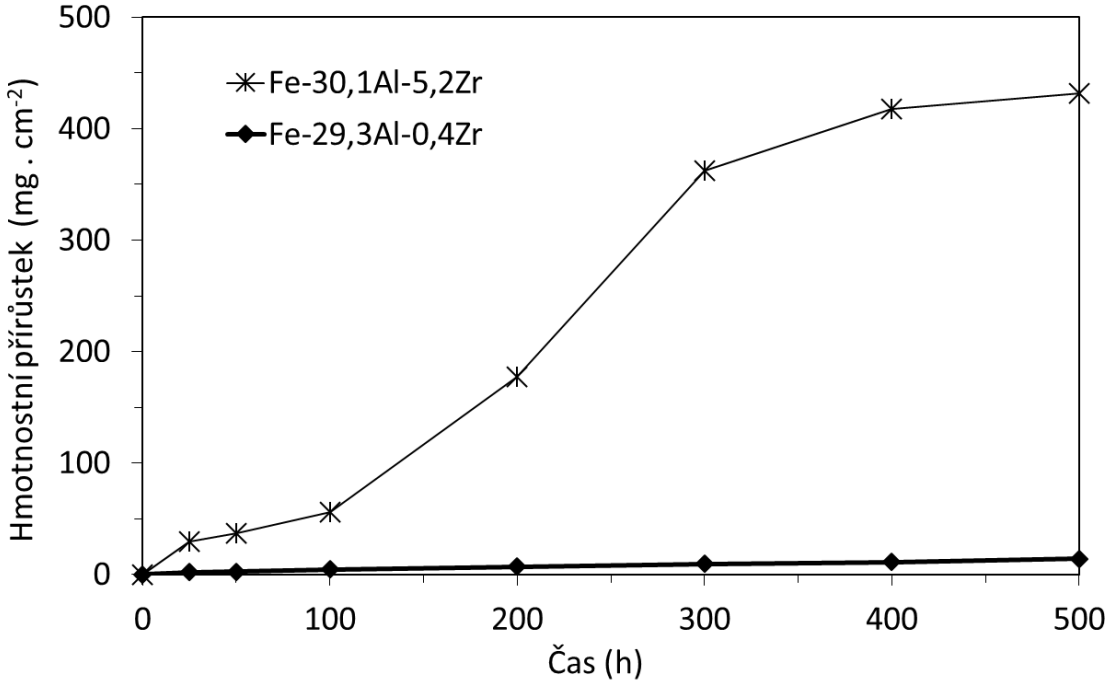

Obr. 4. Závislost hmotnostních přírůstků na čase slitin s nízkým a vysokým obsahem Zr během oxidace na teplotě 1100 °C

Výzkum slitin v řezu kolmém na povrch vzorku opět prokázal, že přednostně oxiduje Lavesova fáze $(Fe, Al)_2Zr$ nebo eutektikum (Lavesova fáze+Fe-Al), a v případě slitin obsahující zvýšený obsah uhlíku přednostně oxiduje ZrC [P2-1]. Dokonce bylo pozorováno, že právě karbidy zirkonia oxidují snadněji než Lavesova fáze. V některých případech byla pozorována nejen oxidace fází bohatých na Zr, ale i masivní vstup oxidace do Fe-Al matrice. Jedná se například o slitinu Fe-25Al-1Zr [P2-2], která byla vystavena cyklické oxidaci při teplotě 1100 °C, nebo o slitinu Fe-26,4Al-2,8Cr-0,2Zr-0,6C, vystavenou stálé teplotě oxidace nad 1000 °C [P2-1].

2.2 Vliv dalších legur na oxidační chování aluminidů železa na bázi Fe_3Al (Ta, Ce, TiB_2)

Ve spolupráci s Max Planck institutem v Düsseldorfu byla věnována pozornost legování aluminidů železa tantalem jak z hlediska zlepšení mechanických vlastností za vysokých teplot [41], tak i z hlediska vysokoteplotní oxidace [P2-3]. Tantal má omezenou rozpustnost v Fe-Al slitinách (přibližně do 1 at. %) a při vyšších obsazích vytváří ve slitinách ternární Lavesovy fáze [42].

Dalším způsobem jak zvýšit tažnost a zároveň zvýšit vysokoteplotní pevnost je kombinované legování aluminidů železa chromem s přídavkem TiB_2 (nebo titanu a bóru za vzniku titanboridu) nebo céru [43, 44]. Kombinací legování chromu a dalších legur (TiB_2 nebo Ce) lze dosáhnout výrazně vyšší tažnosti a pevnosti než přídavkem samotného chromu [44].

Titanborid se ve slitinách vyskytuje nejčastěji ve formě precipitátů tyčinkovitého tvaru. Titanborid také způsobuje zpomalení růstu zrna v průběhu tepelného nebo tepelně-mechanického zpracování [43, 45]. Oxidační testy při teplotě 800 °C prokázaly, že přítomnost TiB_2 nemá nepříznivý vliv na oxidační odolnost [43].

Cér způsobuje vznik precipitátů zejména na hranicích zrn a také, jako titanborid, zjemňuje zrno [46]. Byl také zjištěn příznivý vliv céru (0,25 at. %) na oxidační odolnost slitiny Fe-28Al-4Cr při teplotách nad 1000 °C [47]. Přídavek céru výrazně snížil hmotnostní přírůstky. Okuje jsou oproti slitině bez Ce hladké, prosté prasklin a velmi dobře přilnavé k substrátu (nebylo pozorováno odlupování okují).

Studium oxidačního chování aluminidů železa je stále aktuální. V poslední době je věnována nejen na našem pracovišti pozornost především vlivu křemíku [48] a také niobu na vysokoteplotní oxidační odolnost (při teplotách 900 °C a 1100 °C) slitin na bázi Fe-Al.

[P2-3]	HOTAŘ, A. a M. PALM. Oxidation resistance of Fe–25Al–2Ta (at.%) in air. *Intermetallics*. 2010, 18(7), 1390-1395.
[P2-4]	HOTAŘ, A., P. KRATOCHVÍL a J. CÍZNER. Oxidation resistance of Fe28Al3Cr0.02Ce and Fe30Al4Cr2.7TiB2 (at. %) in air. In: *METAL 2010 - 19th International Conference on Metallurgy and Materials*. Ostrava: TANGER, 2010, s. 915-919. ISBN 978-808729417-8.

2.2.1 Vysokoteplotní oxidační chování aluminidu železa legovaného tantalem (Fe-25Al-2Ta) v teplotním intervalu 600 – 1000 °C

Slitina Fe-25Al-2Ta má vynikající oxidační odolnost do 800 °C. Oxidace probíhá dle parabolického zákona (Obr. 5). Počáteční oxidace (cca do 100 h) je doprovázena vznikem rychleji rostoucích metastabilních fází Al_2O_3 a také Fe_2O_3, poté se na povrchu vytváří tenká a přilnavá vrstva oxidů [P2-3].

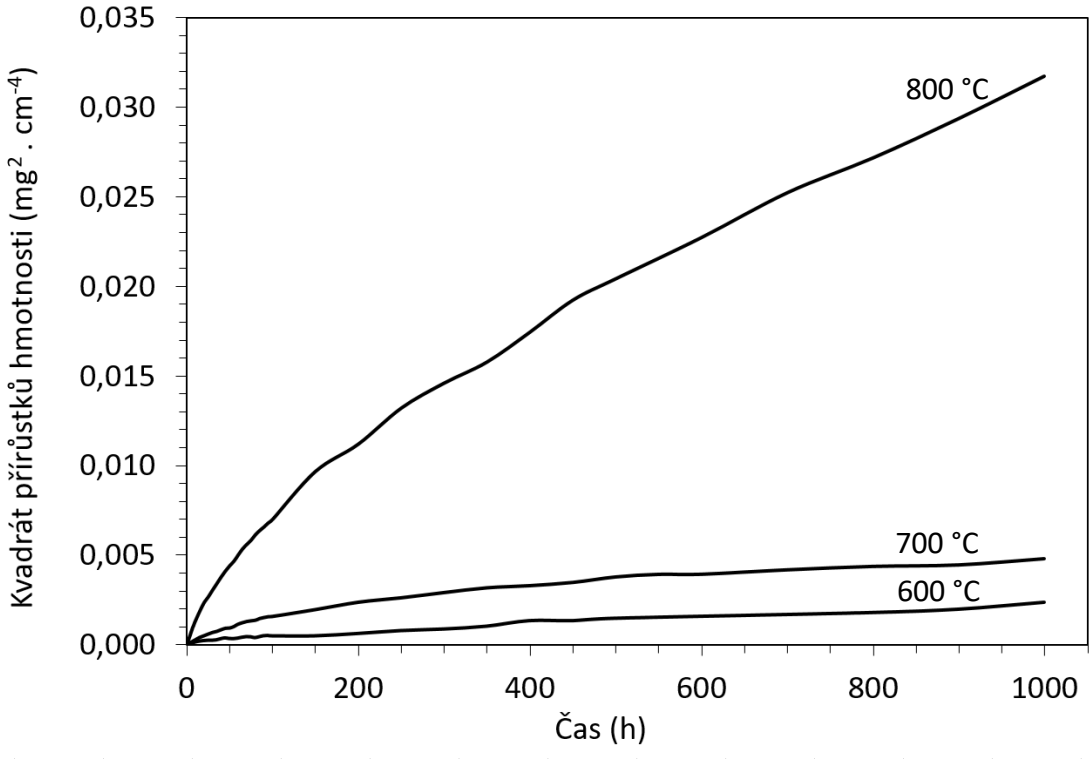

Obr. 5. Kvadrát přírůstků hmotnosti v závislosti na čase slitiny Fe–25Al–2Ta při teplotách 600, 700, 800 °C v syntetickém vzduchu

Během oxidace při teplotě 900 °C došlo po několika stovkách hodin k náhlému nárůstu přírůstků hmotnosti, což pravděpodobně souvisí s popraskáním oxidické vrstvy, která se vzápětí obnovila (Obr. 6). Tento jev byl pozorován opakovaně [P2-3]. Kinetika oxidace při teplotě 1000 °C je výrazně odlišná než při nižších teplotách. Vzniklé oxidy nevytváří na slitině Fe-25Al-2Ta ochrannou bariéru, proto oxidy rostou velmi rychle, dle lineárního až hyperbolického zákona (Obr. 6).

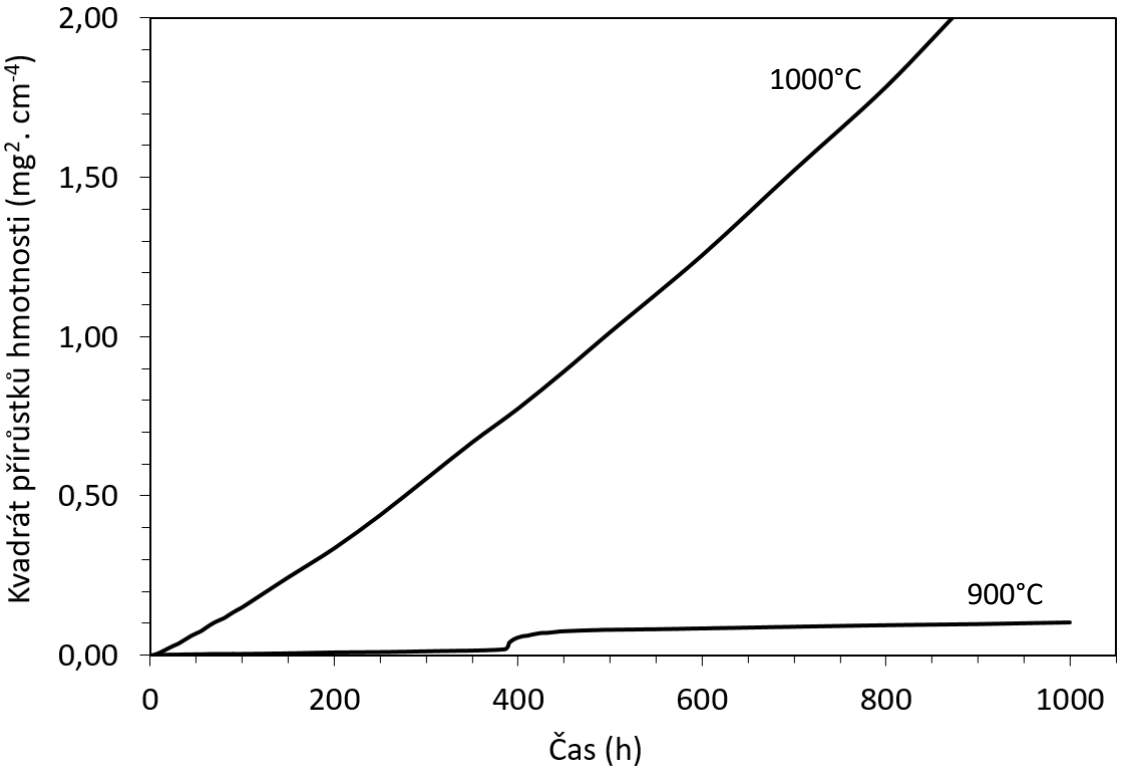

Obr. 6. Kvadrát přírůstků hmotnosti v závislosti na čase slitiny Fe–25Al–2Ta při teplotách 900 a 1000 °C v syntetickém vzduchu po dobu 1000 hodin

Rentgenová difrakce odhalila, že slitina Fe-25Al-2Ta se pokrývá vrstvou složenou z Al_2O_3, Fe_2O_3 a Ta_2O_5 [P2-3]. S rostoucí teplotou oxidace množství Fe_2O_3 klesá a naopak množství Al_2O_3 a Ta_2O_5 roste. Překvapivě bylo zjištěno, že již během oxidace při nižších teplotách (700 °C) ve slitině výrazně precipituje Lavesova fáze Fe_2Ta. Na základě dřívějších testů [42] byl pozorován výrazný objemový nárůst této fáze až při teplotě 1000 °C.

Analýza pomocí optického a především elektronového mikroskopu prokázala, že při oxidaci v intervalu teplot 600-800 °C vzniká na povrchu tenká rovnoměrná vrstva okují. Například po oxidaci při teplotě 700 °C byl povrch pokryt vrstvou oxidů do 2 µm, jen na několika málo místech byla tloušťka oxidů větší, případně došlo k odpadávání oxidů. V místech oxidů o větší tloušťce byly analyzovány Al_2O_3, Fe_2O_3, směs oxidů a také Lavesova fáze Fe_2Ta [P2-3]. Občasné opadávání oxidů bylo pozorováno zejména v místech, kde se vyskytovaly velké částice Fe_2Ta.

Naopak, na povrchu slitiny Fe–25Al–2Ta během oxidace při teplotě 900 °C vznikl oxidický film o výrazně větší tloušťce, ten se však snadno odlupoval především během a po ochlazení

z testovací teploty. Tam, kde vrstva okují odpadla [P2-3], byly na obnaženém povrchu nalezeny drobné částice Fe_2Ta o velikosti několika mikrometrů, které byly pravděpodobně pokryty Ta_2O_5. Jestli jsou částice Lavesovy fáze Fe_2Ta příčinou praskání okují na povrchu během oxidačního testu, není zřejmé. Zdá se však, že růstem těchto částic se také zvyšuje mechanické napětí mezi matricí a okujemi, což má pravděpodobně za následek odlupování okují během ochlazování vzorku.

Při teplotě 1000 °C se netvoří ochranné okuje, ale rychle rostoucí směs oxidů Al_2O_3, Fe_2O_3 a Ta_2O_5. Rychlý nárůst oxidické vrstvy je pravděpodobně způsoben přítomností většího množství Ta_2O_5 (většího než při nižších teplotách oxidace) uvnitř okují Al_2O_3. Bylo zjištěno, že takový vznik sekundárních částic může vést k teplotním roztažným napětím a/nebo k místům s koncentrovaným napětím stejně jako k rychlému transportu kyslíku skrz okuje, viz např. [49, 50]. Odlupování okují během nebo po ochlazení z teplot vyšších než 1000 °C lze vysvětlit stejným způsobem jako v případě oxidace při teplotě 900 °C, viz výše.

Předpokladem vzniku precipitátů Lavesovy fáze Fe_2Ta na povrchu slitiny Fe–25Al–2Ta je fakt, že slitina je přesycena Ta, navíc precipitaci u povrchu může podporovat vyčerpání Al a Fe v důsledku vzniku Al_2O_3 a Fe_2O_3. Precipitace pravděpodobně probíhá podobně jako v superslitinách na bázi niklu [49, 51, 52]. U těchto slitin byla pozorována difuse Ta směrem z matrice do okují na rozhraní kov/oxid (outward diffusion of Ta) za vzniku fází bohatých na Ta. Přítomnost těchto precipitátů vedla k odlupování oxidů [49, 51]. Oxidy se odlupovaly společně s precipitáty bohatými na Ta a následně během ochlazování praskaly na rozhraní kov/oxid [51]. V případě slitiny Fe-25Al-2Ta nebylo společné odlupování oxidů a precipitátů prokázáno, protože precipitáty Fe_2Ta i po odloupnutí oxidického filmu na povrchu zůstávají. Proto se jako nejpravděpodobnější způsob odlupování během ochlazování jeví rozdílný koeficient teplotní roztažnosti nejen mezi Fe-Al matricí a okujemi, ale především odlišný koeficient teplotní roztažnosti mezi Lavesovou fází a okujemi.

2.2.2 Vysokoteplotní oxidační chování aluminidů železa legovaných cérem nebo titanboridem

Obě slitiny Fe-28Al-3Cr-0,02Ce a Fe-30Al-4Cr-2,7TiB_2 se po cyklické oxidaci pokrývají tenkou vrstvou oxidů a jejich růst probíhá dle parabolického zákona. Velmi dobrou oxidační odolnost dokládá nízká hodnota zdánlivé parabolické rychlostní konstanty, viz Tab. 3 v kapitole 2.1.2.

Při teplotě 1100 °C vyniká svou oxidační odolností slitina Fe-30Al-4Cr-2,7TiB_2, která se i při této teplotě vyznačuje růstem okují dle parabolického zákona (Obr. 7). Vysoká odolnost proti oxidaci je pravděpodobně způsobena velmi jemnozrnnou strukturou slitiny Fe-30Al-4Cr-2,7TiB_2. Naopak u Fe-28Al-3Cr-0,02Ce proniká oxidace především podél hranic hrubých zrn hluboko pod povrch, a proto růst oxidů má lineární až hyperbolický průběh [P2-4].

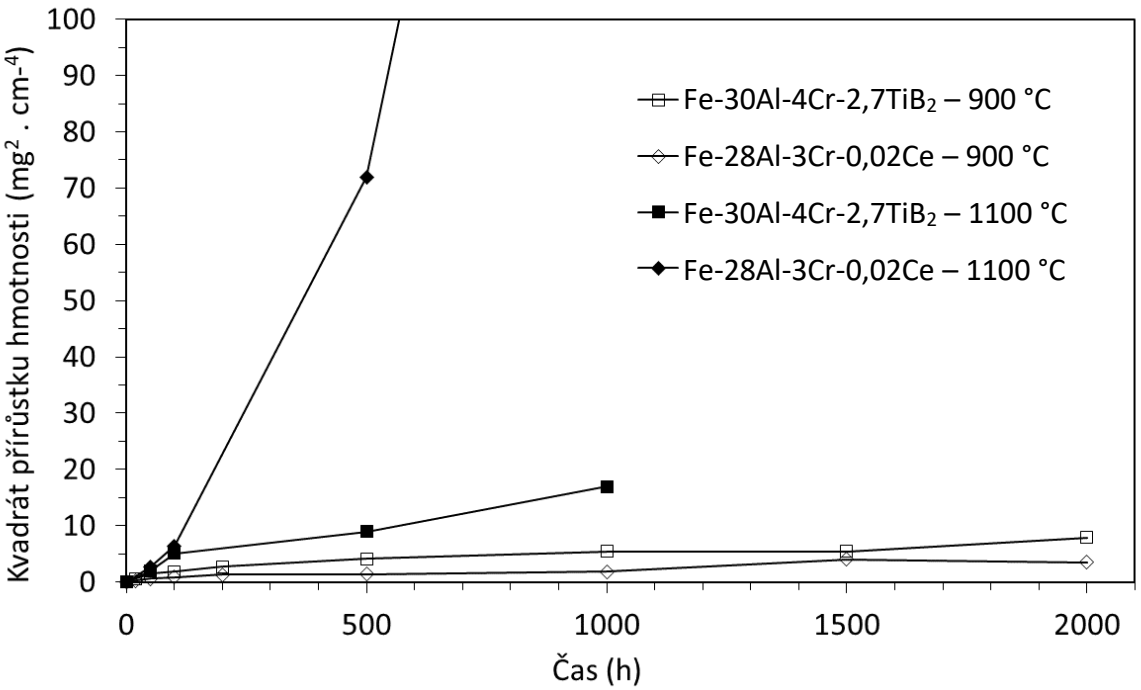

Obr. 7. Kvadrát přírůstků hmotnosti v závislosti na čase slitin Fe-28Al-3Cr-0,02Ce a Fe-30Al-4Cr-2,7TiB_2 po cyklické oxidaci při teplotách 900 a 1100 °C v laboratorním vzduchu

3. Korozní odolnost aluminidů železa na bázi Fe-Al v roztavené sklovině

V mnoha aplikacích ve sklářském průmyslu se používají kovové materiály v přímém kontaktu se sklovinou. Jedná se například o elektrody, držáky elektrod, termočlánkové trubky, součásti feedrů, výtokové trubky, plunžry, součásti strojů pro tvarování skla atd. Vlivem extrémních podmínek mají používané materiály limitovanou životnost [53, 54]. Navíc jsou vyvíjeny, především z důvodů ekologických, nové druhy sklovin, které v mnoha případech vytvářejí agresivnější prostředí vůči stávajícím kovovým materiálům. Na tyto podněty je nutné reagovat vývojem a testováním nových materiálů, které vydrží vysoké teploty a budou lépe odolávat korozním účinkům sklovin. Obecně jsou na materiály přicházející do kontaktu se sklovinou kladeny tyto požadavky [54]:

1. materiály musí mít vysokou odolnost vůči sklovině při požadované pracovní teplotě (maximálně do 1200 °C) - z hlediska plošné koroze menší než 4-8 mm/rok
2. rozpouštění materiálu musí být rovnoměrné
3. při interakci kovového materiálu se sklovinou nesmí vznikat bubliny a nesmí docházet k intenzivnímu zbarvení skloviny
4. materiály musí mít dostatečnou odolnost vůči oxidaci v pecní atmosféře
5. materiály musí mít dostatečnou pevnost při požadované teplotě.

Velmi dobrá oxidační odolnost slitin na bázi Fe-Al i testy Pyroferalu v padesátých letech minulého století v podmínkách sklářského průmyslu [11] prokázaly, že slitiny na bázi aluminidů železa mohou najít uplatnění i v kontaktu se sklovinou. Navíc, slitiny vyvíjené na katedře materiálu na Technické univerzitě v Liberci obsahují výrazně menší množství uhlíku než má slitina Pyroferal. Uhlík ve slitinách (i vázaný v karbidech) totiž způsobuje během reakcí se sklovinou vznik velkého množství bublin, dochází k tzv. „zpěnění“. Soustavný výzkum korozního chování a korozní odolnosti aluminidů železa započal na Technické univerzitě v Liberci v roce 2000 a to v rámci projektů i ve spolupráci s průmyslem (Preciosa a.s.), výsledky jsou shrnuty v [55].

Od roku 2004 se další výzkum soustředil především na korozní chování aluminidů železa v sodnovápenaté sklovině (ploché sklo, obalové sklo), která se vyrábí v celosvětovém měřítku v největším množství [P3-1, P3-2 a P3-3], a také v olovnatém křišťálu [P3-2, P3-4]. Výzkum korozního chování slitin na bázi Fe-Al byl prováděn na vzorcích vystavených korozním účinkům skloviny v laboratorních podmínkách (statické korozní zkoušky). Korozní odolnost slitin byla

stanovena měřením změn hmotnosti a nově i změn „drsnosti“ povrchu, viz kapitola 4. Pro objasnění chemických procesů mezi slitinou a sklovinou byla provedena chemická analýza zbarveného skla a povrchových partií vzorků.

[P3-1]	HOTAŘ, A. a P. KRATOCHVÍL. The corrosion resistance of iron aluminide Fe28Al3Cr0.02Ce (at%) in a molten glass. *Intermetallics*. 2007, 15(3), 439-441.
[P3-2]	HOTAŘ, A., P. KRATOCHVÍL a V. HOTAŘ. The corrosion resistance of Fe_3Al-based iron aluminides in molten glasses. *Kovove Mater*. 2009, 47(4), 247-252. ISSN 1338-4252.
[P3-3]	HOTAŘ, A., V. HOTAŘ a F. NOVOTNÝ. Corrosion behaviour of Fe-40Al-Zr at.% alloy in molten soda-lime glass. *Kovove Mater*. 2014, 52(03), 149-155.
[P3-4]	HOTAŘ, A., V. HOTAŘ a J. DROBEČEK. Corrosion resistance of heat-resistance alloys in molten lead crystal at 1200 °C. In: *METAL 2012 - Conference Proceedings, 21st International Conference on Metallurgy and Materials*. Ostrava: TANGER, 2012, s. 1467-1470. ISBN 978-808729431-4.

3.1 Korozní odolnost aluminidů železa v roztavené sodnovápenaté sklovině a v olovnatém křišťálu

V pracích [P3-1, P3-2, P3-3, P3-4] byla hodnocena korozní odolnost aluminidů železa (viz Tab. 4) vůči roztaveným sklovinám (sodnovápenaté sklovině a olovnatém křišťálu). Byly stanoveny korozní úbytky (Obr. 8 a 9), které lze přepočítat na korozní rychlost v mm/rok (Tab. 4) a nově také parametry drsnosti povrchů před a po korozním testu, viz kapitola 4. Výsledky aluminidů železa pak byly porovnávány s naměřenými hodnotami u chromniklové oceli (EN X8CrNi25-21), která se hojně užívá v kontaktu se sklovinou.

Tab. 4. Korozní rychlost rozpouštění ve sklovinách při teplotě 1200°C, počítáno z hmotnostních úbytků po 168 hodinách

Slitina	v sodnovápenaté sklovině (mm/rok)	v olovnatém křišťálu (mm/rok)
Fe-40Al-Zr	2,1*	-
Fe-28Al-3Cr-0,5Zr	x	X
Fe-28Al-3Cr-0,02Ce	1,2	0,8
Fe-25Al-5Cr	0,9	0,5
EN X8CrNi25-21	1,9	1,0

*po 96 hodinách
x…nelze stanovit (ulpívaly zbytky skla)
-… nebylo stanoveno

Vývoj korozních úbytků aluminidů železa po interakci se sodnovápenatou sklovinou je patrný z obrázku 8. Nejnižší úbytky byly naměřeny u slitiny Fe-25Al-5Cr. Legování aluminidů železa zirkoniem i malým přídavkem céru se projevilo z hlediska korozní odolnosti jako škodlivé. Přesto i tyto aluminidy mají nižší korozní úbytky než chromniklová ocel. Vyšší korozní odolnost, při porovnání s chromniklovou ocelí, mají také aluminidy železa v roztaveném olovnatém křišťálu (Obr. 9). Nejnižší úbytky byly opět naměřeny u aluminidu železa Fe-25Al-5Cr. Celkově nižší korozní úbytky slitin vlivem interakce s olovnatým křišťálem jsou způsobené odlišným složením a také vyšší viskozitou skloviny při teplotě 1200 °C.

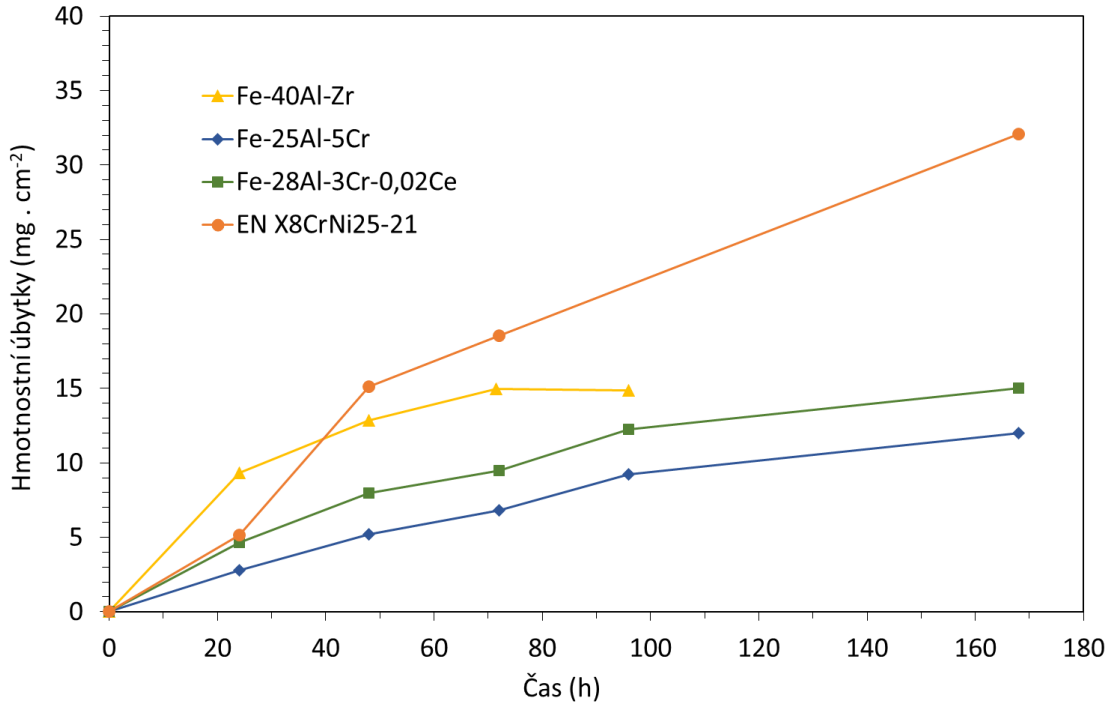

Obr. 8. Hmotnostní úbytky aluminidů železa a chromniklové oceli v roztavené sodnovápenaté sklovině při teplotě 1200 °C

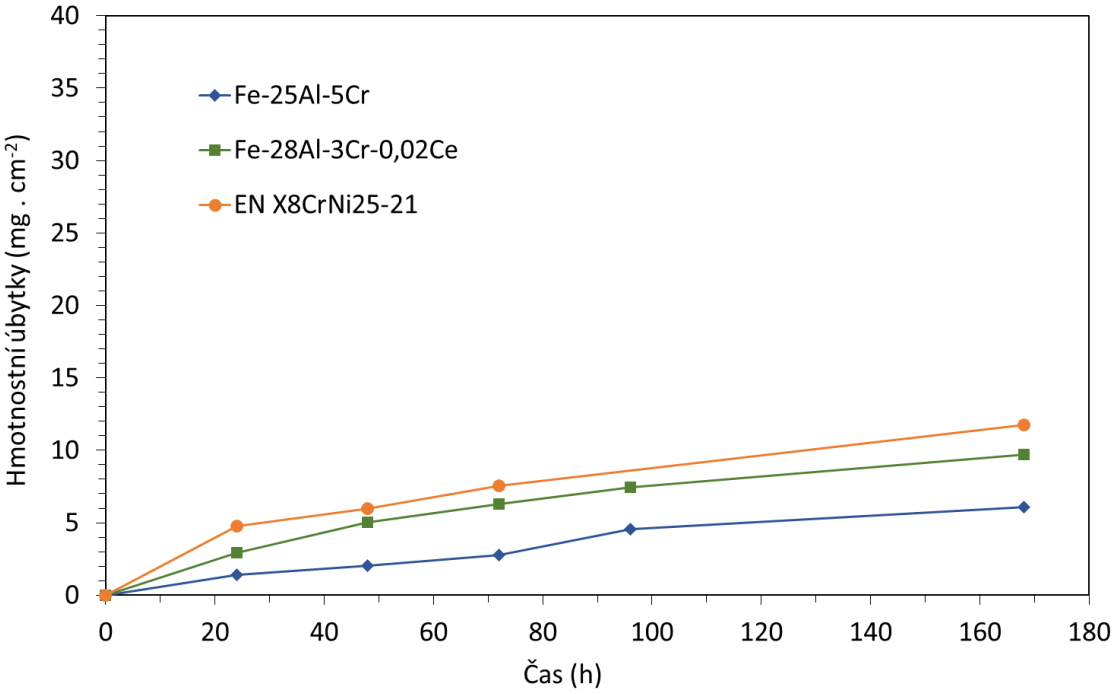

Obr. 9. Hmotnostní úbytky aluminidů železa a chromniklové oceli v roztaveném olovnatém křišťálu při teplotě 1200 °C

3.2 Mechanismus koroze aluminidů železa v roztavené sodnovápenaté sklovině a v olovnatém křišťálu

Během korozních testů byl objasněn mechanismus koroze aluminidů železa v sodnovápenaté sklovině [P3-2, P3-3]. Pro všechny testované aluminidy železa (Tab. 4) je typická přednostní difuse hliníku k povrchu vzorku a jeho oxidace. Hliník reaguje s SiO_2 za vzniku Al_2O_3 a Si. Zvýšený výskyt Al_2O_3 v blízkosti povrchu zvyšuje viskozitu skloviny a tím dochází ke zpomalení rozpouštění slitiny na bázi Fe-Al. Křemík vytváří v okolí aluminidů železa malé částice, které způsobují šedé zbarvení skloviny (Obr. 10, vlevo). Kromě šedého zbarvení bylo pozorováno také žluto-hnědé zbarvení (ambrové) sodnovápenaté skloviny způsobené redukcí síry a železa. Výskyt drobných bublinek v blízkosti vzorků lze vysvětlit reakcí Al s SO_3 za vzniku SO_2.

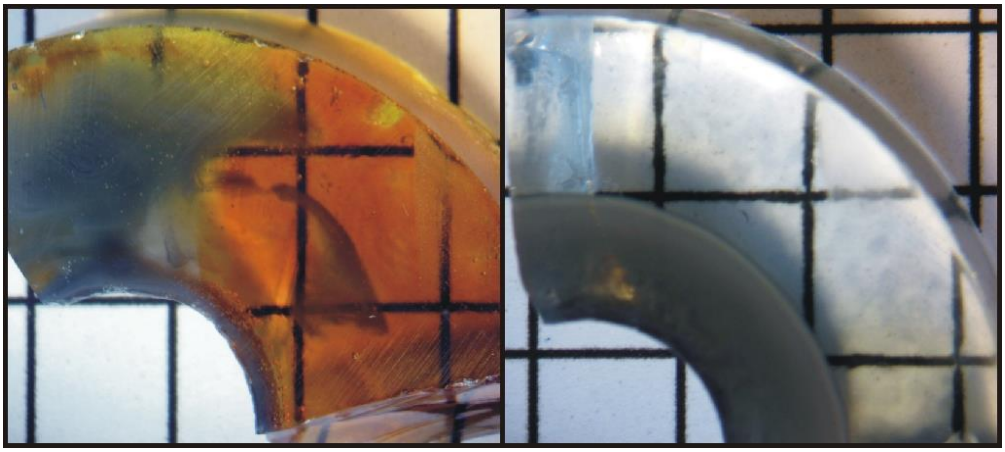

Obr. 10. Zbarvení sodnovápenaté skloviny (vlevo) a olovnatého křišťálu (vpravo) vlivem interakce se slitinou Fe-25Al-5Cr, místo kontaktu slitiny se sklovinou je vlevo dole

I v případě olovnatého křišťálu dochází k přednostnímu rozpouštění hliníku. Hliník v olovnatém křišťálu reaguje nejen s SiO_2, ale i s PbO za vzniku Si a Pb. Drobné kuličky Si a Pb pak způsobují typické šedé zbarvení (Obr. 10, vpravo).

Navíc u obou sklovin po interakci s aluminidy železa nebyly naměřeny zvýšené hodnoty železa a v případě slitiny Fe-25Al-5Cr ani chromu. Z toho lze usuzovat, že rozpouštění hliníku ve sklovinách je zcela primární a tím hliník „chrání“ železo, případně chrom, před rozpouštěním.

Z hlediska technologie výroby je jakékoliv zbarvení skloviny vlivem interakce kovových materiálů nežádoucí. Aluminidy železa sice také způsobují zbarvení (viz Obr. 10), ale intenzita zbarvení je výrazně nižší než tmavě zelené zbarvení, které způsobuje chromniklová ocel (EN X8CrNi25-21) [P3-2].

4. Využití fraktální geometrie při hodnocení korozní a oxidační odolnosti aluminidů železa na bázi Fe_3Al

Fraktální geometrie a další statistické nástroje se začaly využívat na Technické univerzitě v Liberci pro hodnocení korozní odolnosti aluminidů železa na bázi Fe_3Al i dalších kovových materiálů vůči sklovinám [55, P3-1 až P3-4]. Pro kvantifikaci korozní odolnosti se běžně využívá měření hmotnostních úbytků a pro stanovení mechanismu rozpouštění slitin ve sklovinách chemická analýza jak vzorků po interakci se sklovinou, tak i samotné skloviny po korozním testu, viz kapitola 3. V některých případech však měření korozních úbytků není možné, protože nelze z povrchu vzorků odstranit zbytky skla [P3-2]. Vyvinutá metodika, která kvantifikuje změny drsnosti povrchu po interakci slitiny se sklovinou, dokáže snadno porovnat korozní odolnost slitin odlišného složení i těch, na kterých zbytky skla ulpívají [P4-1, P4-2]. Tato metodika byla také úspěšně aplikována pro stanovení oxidační odolnosti aluminidů železa [P4-3]. Je však nutné poznamenat, že pro ucelené vyhodnocení korozní či oxidační odolnosti slitin je nejvhodnější stanovit všechny parametry jak standardní (měření úbytků/přírůstků hmotnosti), tak i parametry využívající fraktální geometrii.

4.1 Popis metodiky

Po dokončení korozních testů a analýze korozních či oxidačních produktů na povrchu byly vzorky testovaných slitin šetrně rozříznuty a následně z nich byly vyrobeny metalografické výbrusy. Metalografický výbrus samozřejmě nebyl použit pouze pro tuto metodiku, ale i pro posouzení korozního nebo oxidačního chování, např. pomocí SEM. Po důkladném vyleštění (bez škrábanců) a vyčištění bylo na optickém mikroskopu pořízeno minimálně 10 snímků rozhraní slitina/okolní prostředí (okuje, korozní produkty se sklovinou nebo pryskyřice pro zapouzdření) na různých místech vzorku, viz Obr. 11 a. Na základě kontrastu mezi oxidačně nenapadenou slitinou a okolním prostředí byla pomocí software (Matlab) vygenerována křivka

rozhraní (Obr. 11 b). Křivky rozhraní jsou následně analyzovány a kvantifikovány parametry drsnosti povrchu (Obr. 11 c-e).

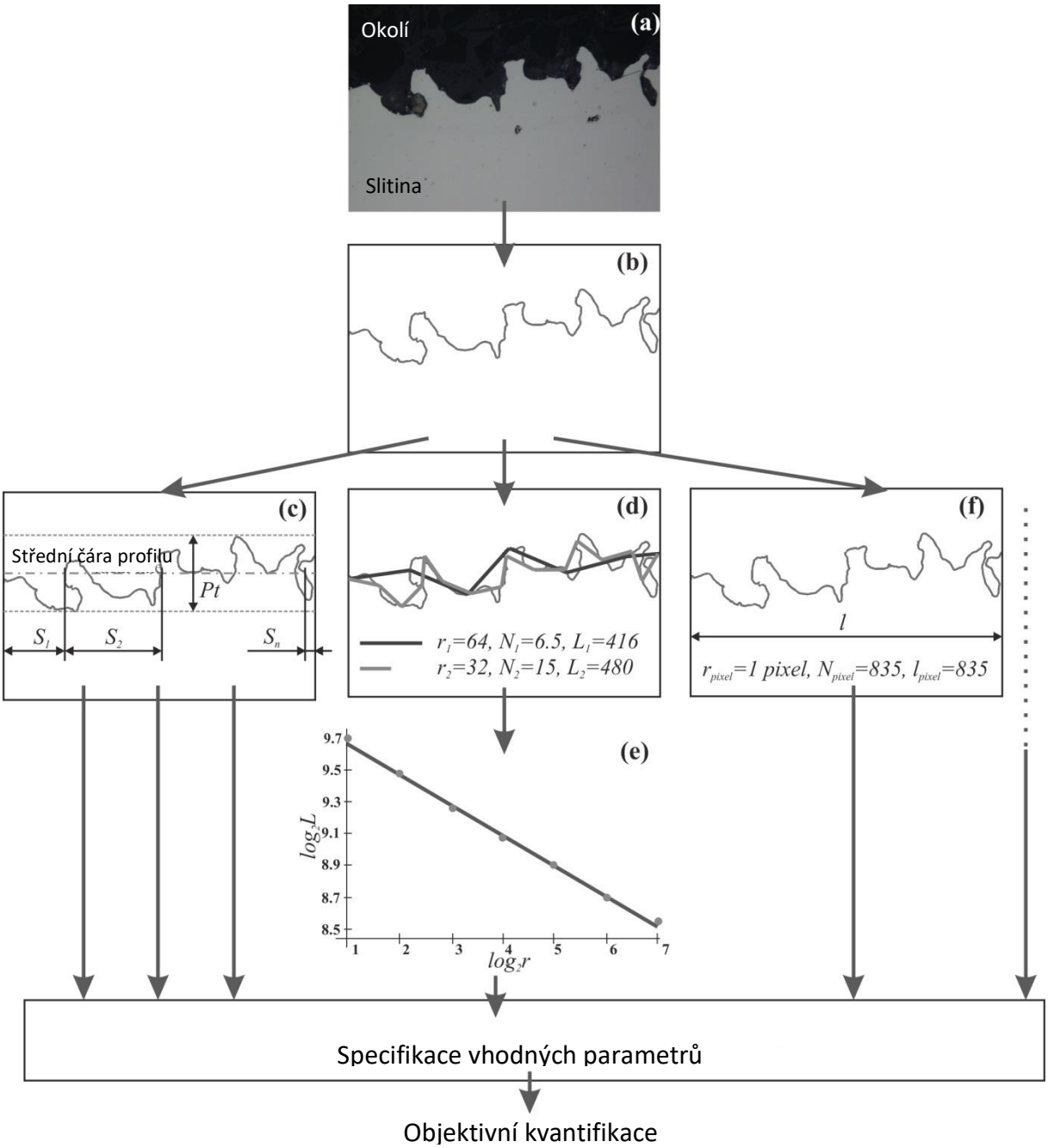

Obr. 11. Zpracování a vyhodnocení křivky rozhraní; a) snímek rozhraní z optického mikroskopu, b) softwarově vygenerovaná křivka rozhraní, c) stanovení maximální výšky profilu P_t (parametr amplitudy) a střední rozteče nerovnosti profilu Sm (parametr frekvence), d) a e) výpočet obvodové dimenze D_{C1000}, f) výpočet relativní délky L_R

Dlouholetým vývojem metodiky byly parametry popisující rozhraní slitina/okolní prostředí rozděleny do třech základních skupin:

1. Parametry amplitudy – charakterizují hloubku průniku koroze či oxidace (např. Pa – střední aritmetická úchylka, Std – směrodatná odchylka, Pt – maximální výška profilu. Vhodnější je používat označení s písmenem P (Pa, Pt) nežli označení písmenem R, protože P popisuje změny profilu místo vlastní drsnosti.
2. Parametry frekvence – zohledňují vzdálenost výstupků a slouží k charakterizaci vlnové frekvence (např. Sm – střední rozteč nerovnosti profilu)
3. Parametry složitosti – popisují složitost křivky rozhraní (např. D_{C1000} – obvodová dimenze vynásobená tisícem, L_R – relativní délka profilu)

Parametry amplitudy a frekvence (Pa, Pt, Sm) jsou definovány normou ISO 4287-1997 a používají se standardně v průmyslové praxi. Nejpoužívanějším parametrem je střední *aritmetická úchylka profilu Pa.* Pa je počítána z 5-ti intervalů a přibližně lze stanovit z (4).

$$Pa = \frac{1}{n}\sum_{i=1}^{n}|z_i| \quad (4)$$

Dalším používaným parametrem je *maximální výška profilu Pt*. Stanovení parametru Pt je graficky znázorněno na obrázku 11 c.

Výpočet *střední rozteče nerovnosti Sm* je dán (Obr. 11 c) podílem sumy vzdáleností mezi jednotlivými vrcholky (S_1, S_2 …S_n) a počtem vrcholků – linie vrcholků musí překročit střední čáru profilu a vrátit se zpět.

$$Sm = \frac{1}{n}\sum_{i=1}^{n} S_i \quad (5)$$

Stanovení *obvodové dimenze* D_C, jakožto parametru složitosti křivky, je znázorněno na obrázku 11 d. Obvodová dimenze je založená na měření délky křivky profilu různou velikostí měřítek ve shodě se vzorcem (6)

$$L_i(r_i) = N_i(r_i).r_i \quad (6),$$

kde L_i je délka v i-kroku měření, r_i je velikost měřítka a N_i je počet kroků potřebných pro změření délky křivky. Logaritmická závislost $\log_2 N(r_i)$ a $\log_2 r_i$ je nazýván Richardson-Mandelbrotův graf (Obr. 11 e) Obvodová dimense je pak stanovená ze sklonu *s* regresní čáry (7).

$$D_C = 1 - s = 1 - \frac{\Delta log_2 L(r)}{\Delta log_2 r} \quad (7)$$

Další parametr, který popisuje rychle a spolehlivě složitost křivky rozhraní, je *relativní délka* L_R. Výpočet je dán poměrem délky křivky rozhraní změřené nejkratším měřítkem l_{pixel} (1 pixelem) a celkové projekční délky l (Obr. 11 f), viz vzorec 8.

$$L_R = \frac{l_{pixel}}{l} \quad (8)$$

Jelikož výsledkem metodiky je mnoho parametrů (více než 20 parametrů), je pro popis korozního nebo oxidačního napadení vhodnější použít pouze vybrané parametry. Zúžení počtů parametrů se provádí pomocí Pearsonova korelačního koeficientu, který stanovuje míru lineární korelace mezi jednotlivými parametry. Pro posouzení korozní a oxidační odolnosti slitin většinou postačí tři vybrané parametry, které vůči sobě mají nejmenší vzájemný vztah (nejméně korelují) a tím popisují křivku rozhraní z více „úhlů".

[P4-1]	HOTAŘ, V. a A. HOTAŘ. Aplikace nekonvenčních metod pro hodnocení dat ve sklářství. *Sklář a keramik*. 2006, 56(9), 179-184. ISSN SSN 0037-637X.
[P4-2]	HOTAŘ, A. a V. HOTAŘ. Fractal geometry used for evaluation of corrosion resistence of Fe-14Al-6Cr wt. % againts molten glass. *Manufacturing Technology*. J. E. Purkyne University in Usti nad Labem, 2015, 15(4), 534-541. ISSN ISSN 1213–2489.
[P4-3]	HOTAŘ, V. a A. HOTAŘ. Fractal dimension used for evaluation of oxidation behaviour of Fe-Al-Cr-Zr-C alloys. *Corrosion Science*. 2018, 133, 141-149.

4.2 Kvantifikace korozní odolnosti aluminidů železa po interakci se sklovnou při teplotě 1200 °C

V pracích [P3-2 až P3-4] bylo kvantifikováno korozní napadení aluminidů železa pomocí vyvinuté metodiky po nejdelší době vystavení účinkům skloviny tj. po 96 h nebo po 168 h. Výsledky korozní odolnosti aluminidů železa odlišného složení a porovnávací oceli pak byly porovnávány se stavem povrchu před korozním testem (broušený povrch) a hlavně mezi jednotlivými slitinami. Hodnoty parametrů získané po devadesátišestihodinovém korozním testu v sodnovápenaté sklovině při teplotě 1200 °C jsou shrnuty v Tab. 5. Z hodnot vyplývá, že slitina Fe-25Al-5Cr se rozpouští velmi rovnoměrně (nízká komplikovanost povrchu = nízká hodnota D_{C1000}), po 96 hodinách je sice její povrch charakteristický větším počtem výstupků (nízká hodnota Sm), ale jejich velikost je malá (nízká hodnota P_t). Jinými slovy, povrch

Fe-25Al-5Cr je z měřených slitin nejhladší (Obr. 12). Vliv legování aluminidu železa zirkoniem se projevil negativně a to hlubokými ostrými průniky koroze pod povrch. Rozsáhlé korozní napadení Fe-28Al-3Cr-0,5Zr dokumentuje vysoká hodnota P_t a D_{C1000}. Z pohledu parametrů změn drsnosti povrchu má ocel EN X8CrNi25-21 nižší korozní odolnost než Fe-25Al-5Cr, ale výrazně vyšší než Fe-28Al-3Cr-0,5Zr.

Tab. 5**.** Parametry drsnosti získané z křivky rozhraní slitin po korozním testu v sodnovápenaté sklovině při teplotě 1200 °C/96 h [3-2]

Parametry (průměrná hodnota z deseti úseků)	Fe-28Al-3Cr-0,5Zr	Fe-25Al-5Cr	EN X8CrNi25-21
P_t – maximální výška profilu (μm)	127,7	8,1	28,4
Sm – střední rozteč nerovností profilu (μm)	25,6	14,6	18,4
D_{C1000} – obvodová dimenze, odhad Fraktální dimenze (-)	1203	1017	1090

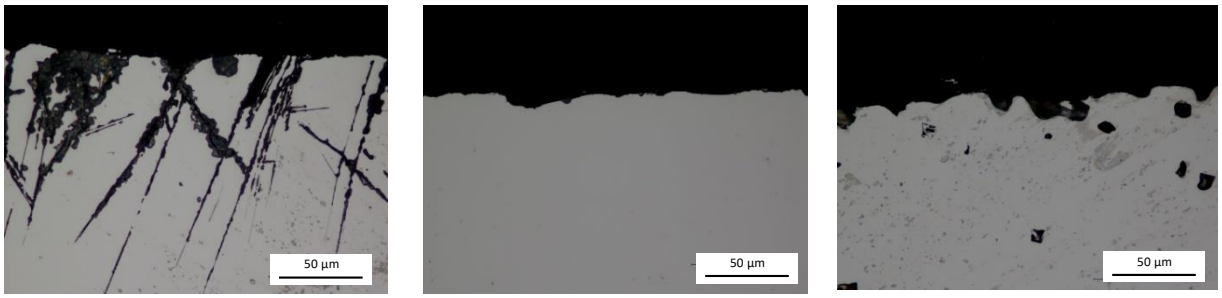

Fe-28Al-3Cr-0,5Zr Fe-25Al-5Cr EN X8CrNi25-21

Obr. 12. Rozhraní (světlá část-slitina, černá-sklovina) mezi slitinou a sklovinou v řezu kolmém na povrch po korozním testu v sodnovápenaté sklovině při teplotě 1200 °C/96 h

Měření parametrů drsnosti proběhlo na stejných materiálech i po korozním testu v olovnatém křišťálu [3-4]. I z pohledu změn drsnosti se potvrdil nižší korozní účinek roztaveného olovnatého křišťálu vůči všem testovaným slitinám. Opět největší korozní odolnost má slitina Fe-25Al-5Cr a nejnižší Fe-28Al-3Cr-0,5Zr.

4.3 Kvantifikace korozního napadení aluminidů železa sklovinou při teplotě 1200 °C v závislosti na čase

V práci [P4-2] byla věnována pozornost časovému vývoji korozního napadení slitin Fe-25Al-5Cr a EN X8CrNi25-21 sodnovápenatou sklovinou při teplotě 1200 °C. Pro popis korozního napadení testovaných materiálů byly vybrány na základě Pearsonova korelačního keoficientu tyto parametry: Pt, Pa, Sm, D_{C1000} a L_R. Časový vývoj parametrů Pt, Sm a D_{C1000} je zobrazen na obrázku 13.

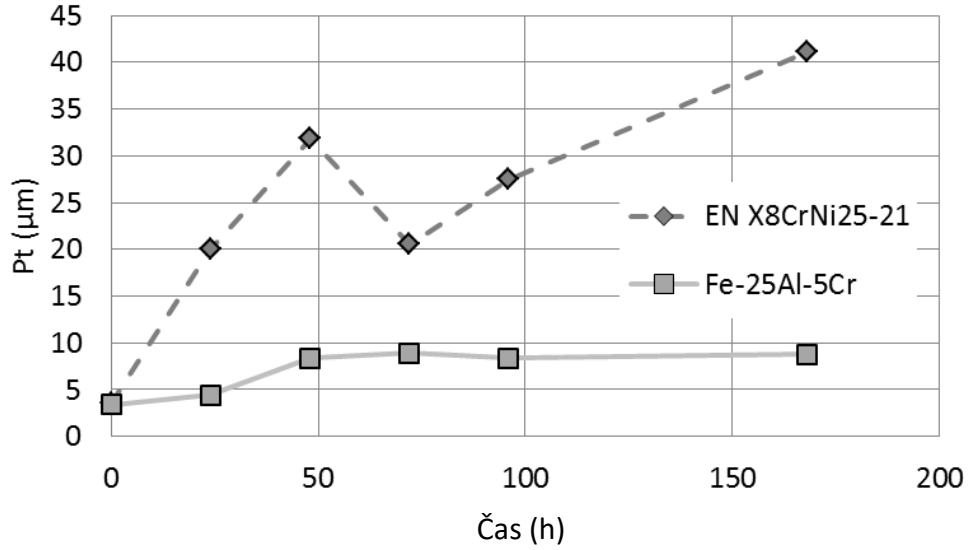

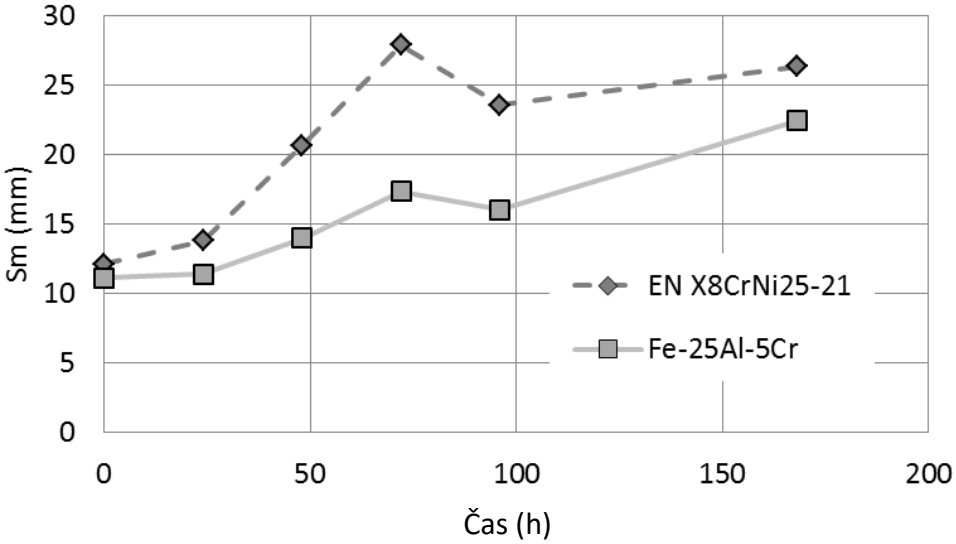

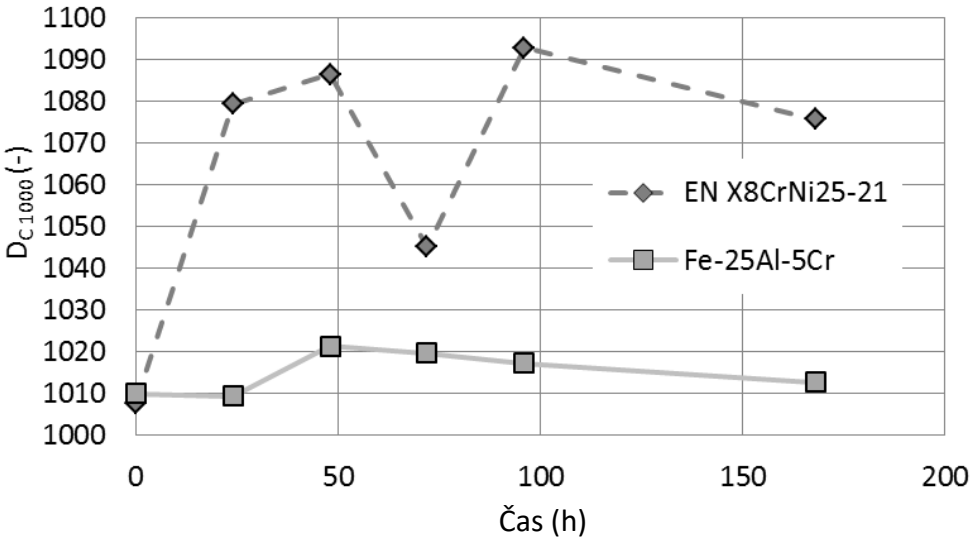

Obr. 13. Změna vybraných parametrů drsnosti vlivem interakce se sodnovápenatou sklovinou při teplotě 1200 °C v závislosti na čase

Průběhy všech parametrů prozrazují, že aluminid železa se v sodnovápenaté sklovině rozpouští velmi rovnoměrně (Obr. 13 a 14). Nízké hodnoty D_{C1000} prokazují, že křivka rozhraní je hladká a časem se složitost křivky rozhraní výrazně nezvyšuje. Během interakce Fe-25Al-5Cr se sklovinou dokonce klesá počet výstupků (roste střední rozteče nerovnosti profilu Sm) a jejich velikost neroste (nízká hodnota Pt), viz Obr. 13.

	Fe-25Al-5Cr	EN X8CrNi25-21
Před testem	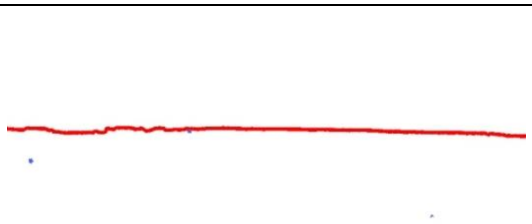	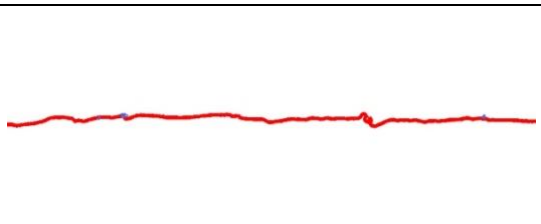
po 48 h	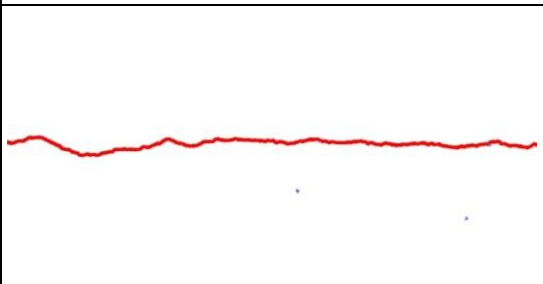	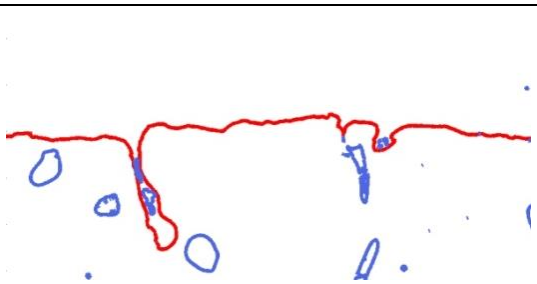
po 72 h	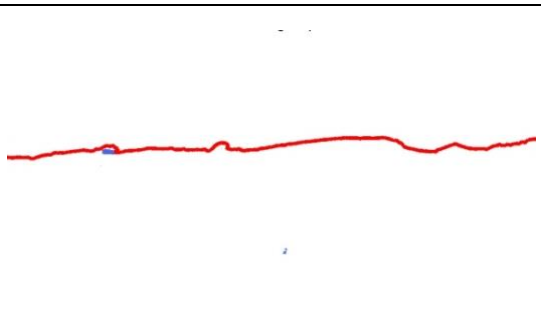	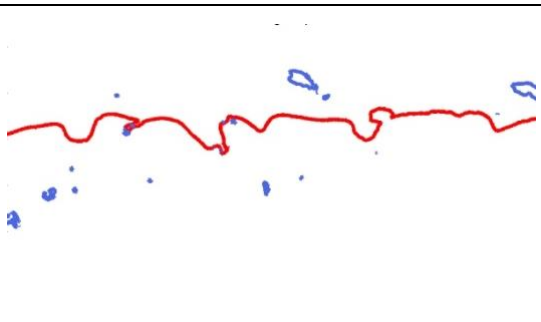
po 168 h	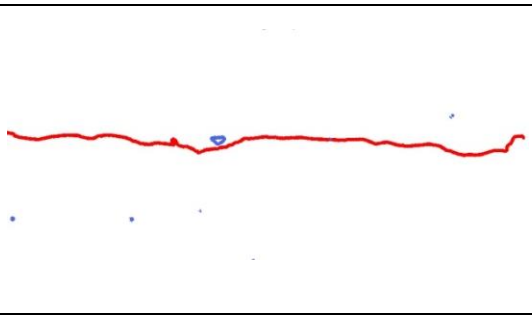	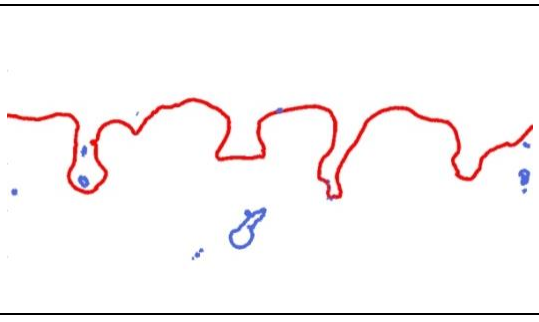

Obr. 14. Příklady křivek rozhraní (červená křivka), ze kterých byly počítány parametry drsnosti

Naopak u oceli EN X8CrNi25-21 všechny tři parametry dosahují vyšších hodnot v celém časovém intervalu. Nárůst maximální výšky profilu Pt dokládá, že koroze proniká do větší

hloubky pod povrch již po 48 hodinách než do aluminidu železa. Koroze proniká do oceli nerovnoměrně a tím roste složitost křivky rozhraní D_{C1000}. Nerovnoměrné rozpouštění ve sklovině se také projevilo vzrůstem parametru Sm. Po 72 hodinách dochází k vyhlazení povrchu oceli, klesá složitost křivky rozhraní a hloubka průniku koroze. Po 96 hodinách však parametry D_{C1000} a Pt opět vzrůstají.

4.4 Využití metodiky pro kvantifikaci odolnosti aluminidů železa po vysokoteplotní oxidaci na vzduchu

Metodika využívající poznatků fraktální geometrie a statistických nástrojů byla aplikována na komplexní slitiny Fe-Al-Cr-Zr-C, vystavené vysokoteplotní oxidaci [P4-3]. Získané výsledky vhodně doplňují poznatky o kinetice oxidace a oxidačního chování, které byly studovány „standardními postupy“ (měření přírůstků hmotnosti, analýza chemického a fázového složení pomocí EDX a XRD atd.) v [P2-1].

Pro porovnání oxidační odolnosti slitin Fe-29,7Al-3,8Cr-0,3Zr-0,2C, Fe-26,4Al-2,8Cr-0,2Zr-0,6C při teplotě 900 a 1000 °C byly použity parametry: směrodatná odchylka Std, střední rozteč nerovnosti profilu Sm a obvodová dimenze D_{C1000}, které mezi sebou měly nejmenší lineární korelaci. Parametry drsnosti shrnují grafy na Obr. 15. Slitina Fe-29,7Al-3,8Cr-0,3Zr-0,2C po oxidaci při teplotě 900 °C má mírně vyšší hodnoty Std a D_{C1000}, které jsou způsobeny především přítomností prasklin i oxidických výstupků, viz Obr. 16. Na druhou stranu, vyšší parametr Sm ukazuje, že prasklin či oxidických výstupků je méně, ovšem jsou hlubší a křivka rozhraní (povrch) je komplikovanější než u slitiny Fe-26,4Al-2,8Cr-0,2Zr-0,6C. Masivnější průběh oxidace při teplotě 1000 °C se projevil nárůstem parametrů drsnosti u obou slitin (Obr. 15). Růst Std a D_{C1000} je způsoben tvorbou hlubších oxidických výstupků, které vznikají přednostní oxidací fází bohatých na Zr (viz kapitola 2.1). Jelikož oxidace slitiny Fe-26,4Al-2,8Cr-0,2Zr-0,6C kvůli přítomnosti ZrC [P2-1] probíhá rychleji a do větších hloubek (Obr. 16), má tato slitina výrazně vyšší hodnotu Std i složitost křivky rozhraní (povrchu) reprezentované parametrem D_{C1000}. Vyšší hodnota střední rozteče nerovnosti profilu Sm u slitiny Fe-26,4Al-2,8Cr-0,2Zr-0,6C ukazuje, že výstupků má méně, ale jsou výrazně hlubší (Obr. 16).

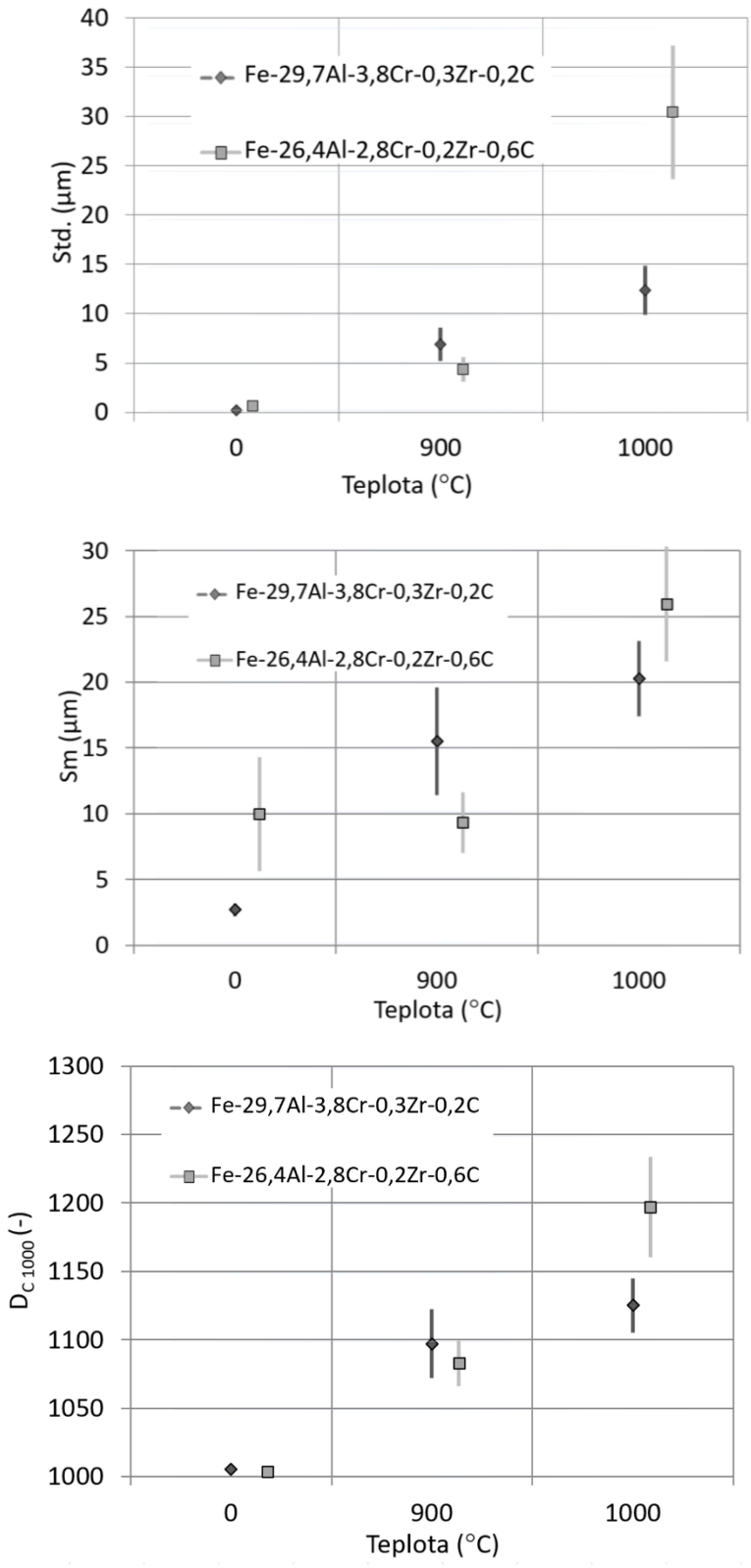

Obr. 15. Směrodatná odchylka Std, střední rozteč nerovnosti profilu Sm a obvodová dimenze D_{C1000} po oxidaci aluminidů železa při teplotě 900 °C a 1000 °C, 0 – broušený povrch

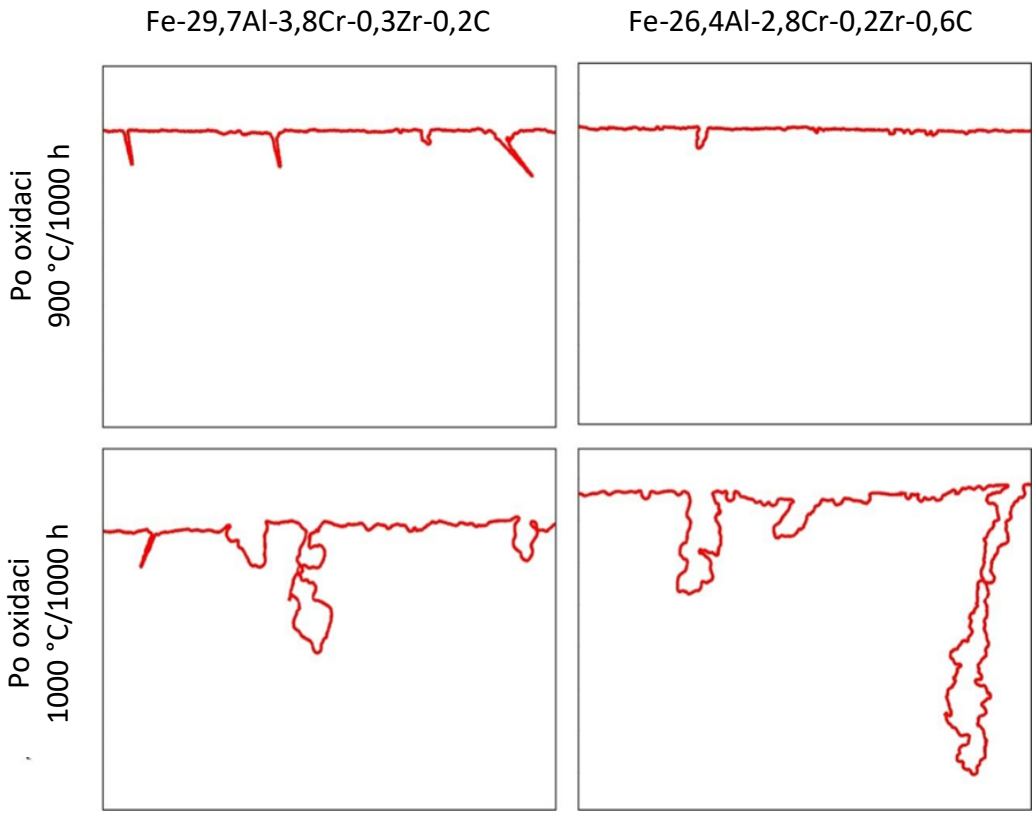

Obr. 16. Příklady křivek rozhraní použitých pro výpočet parametrů drsnosti

Rozsah oxidačního napadení v závislosti na teplotě oxidace byl stejnou metodikou kvantifikován u slitiny Fe-26,4Al-2,8Cr-0,2Zr-0,6C. Vhodné parametry (viz Obr. 17) byly opět vybrány pomocí Personova korelačního koeficientu, jedná se o: Pa – střední aritmetickou úchylku, Sm – střední rozteč nerovnosti profilu a L_R – relativní délku profilu. Mírný nárůst střední aritmetické úchylky a relativní délky profilu po oxidaci při teplotě 900 °C dokládá nízké porušení povrchu (Obr. 18). Oxidické výstupky jsou malé a je jich více (pokles Sm – střední rozteč nerovnosti profilu). Se vzrůstající teplotou oxidace až na 1100 °C dochází k většímu průniku oxidace do hloubky podél karbidů zirkonia, a proto výrazně vzrůstají hodnoty střední aritmetické úchylky a relativní délky profilu. Snižuje se také četnost výstupků (roste Sm - střední rozteče nerovnosti profilu). Při teplotě 1200 °C se oxidace neomezuje pouze na precipitáty ZrC, ale napadá i matrici Fe-Al, proto se oxidické výstupky propojují a větví. Propojování a větvení se projevilo především nárůstem hodnot L_R (nárůst složitosti křivky rozhraní). Četnost výstupků se oproti oxidaci při teplotě 1100 °C výrazně nemění.

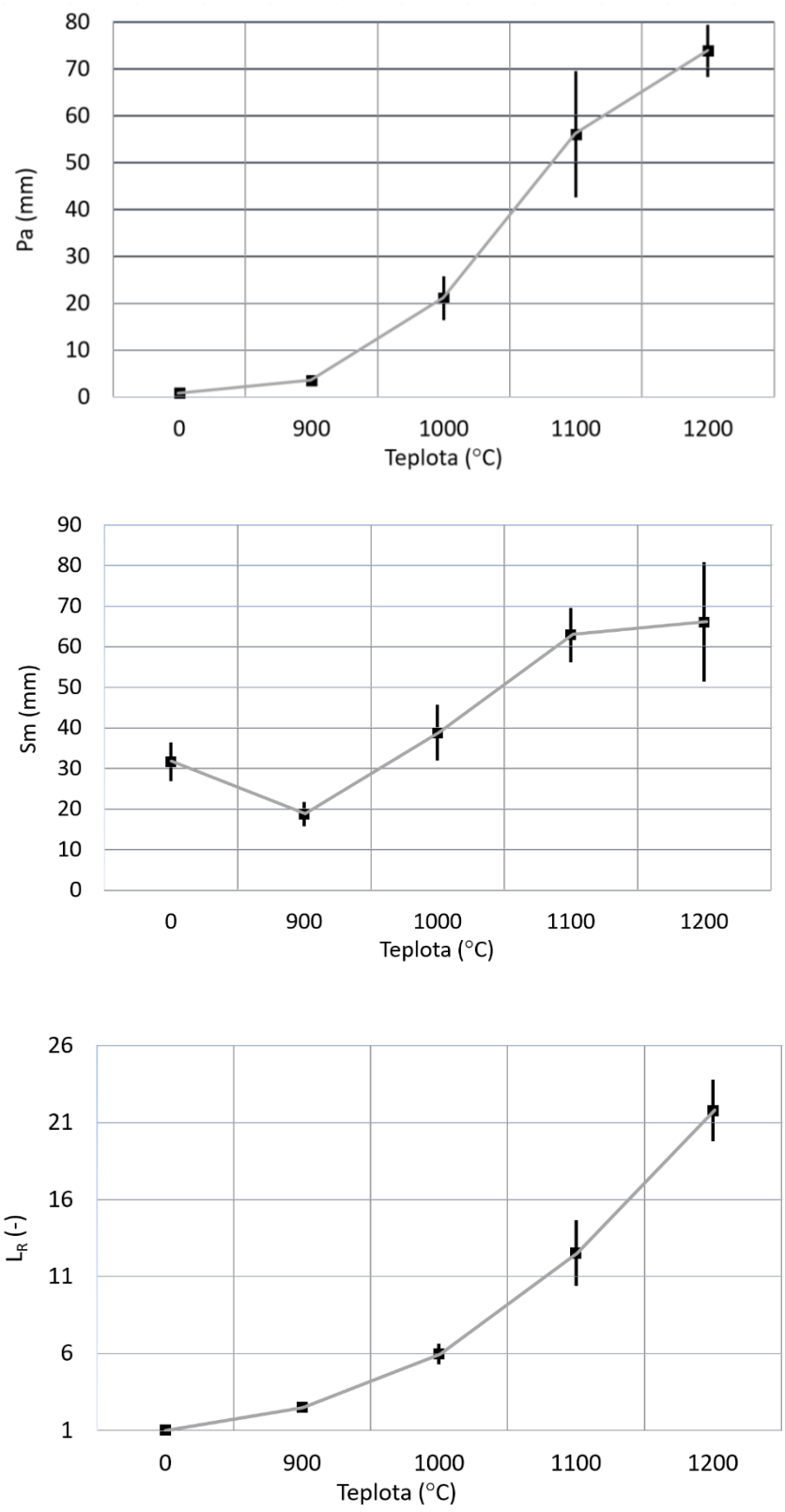

Obr. 17. Závislost parametrů střední aritmetické úchylky (Pa), střední rozteče nerovnosti profilu (Sm) a relativní délky profilu (L_R) na teplotě oxidace slitiny Fe-26,4Al-2,8Cr-0,2Zr-0,6C, 0 – broušený povrch

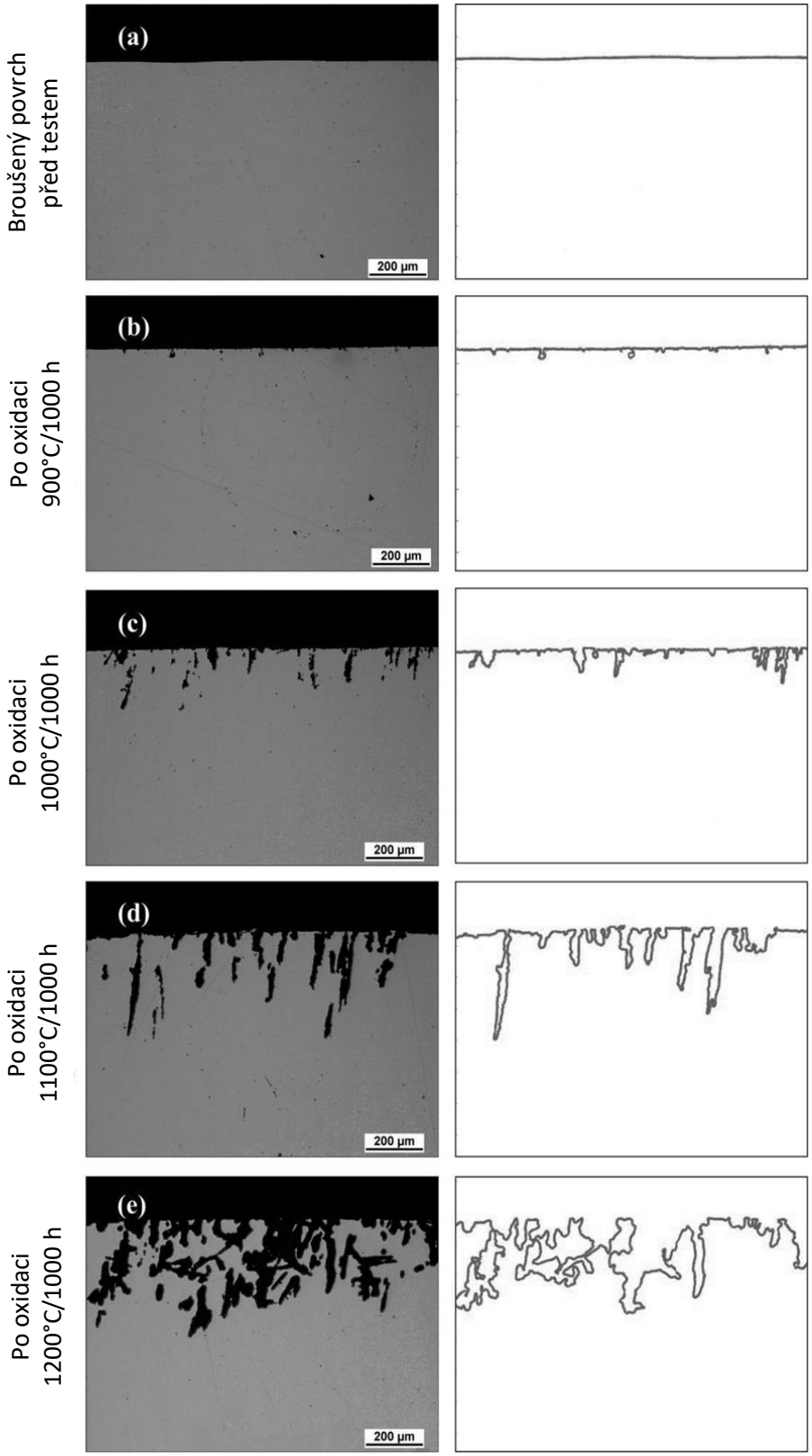

Obr. 18. Příklady křivek rozhraní slitiny Fe-26,4Al-2,8Cr-0,2Zr-0,6C použitých pro výpočet parametrů drsnosti

5. Shrnutí a závěry

Výsledky předkládané habilitační práce lze shrnout:

1. Při vysokoteplotní oxidaci aluminidů železa legovaných různým obsahem zirkonia hraje významnou roli struktura, tj. přítomnost těchto fází: Lavesova fáze (Fe, Al)$_2$Zr, eutektikum (Lavesova fáze + Fe-Al a karbidy ZrC. Je popsán vliv obsahu Zr na fázové složení okují, na kinetiku oxidace a na vstupní oxidaci. Okuje nejčastěji obsahují Al_2O_3, Fe_2O_3 a ZrO_2 a jejich podíl se mění s chemickým složením slitiny a podmínkami oxidace. Byla zjištěna přítomnost dvou modifikací ZrO_2 – tetragonální a monoklinická. Přítomnost zirkonia nad 0,1 at. % způsobuje zhoršení oxidační odolnosti binární slitiny Fe-Al a s rostoucím obsahem Zr oxidační odolnost klesá. Při teplotách nad 1000 °C je negativní vliv Zr ještě výraznější. Na oxidační odolnost má vliv fázové složení slitin. Jestliže ve slitině převažuje Lavesova fáze, proniká oxidace do materiálu pomaleji. Naopak přítomnost ZrC oxidaci urychluje. Nicméně, ternární (Fe-Al-Zr) i komplexní slitiny (s přídavkem chromu a uhlíku) s obsahem max. 0,4 at. % Zr si během isotermické i cyklické oxidace při teplotě 900 °C zachovávají velmi dobrou oxidační odolnost.

2. Výzkum se také zaměřil na vliv tantalu, céru a titanboridu na vysokoteplotní oxidaci aluminidů železa. Během isotermické oxidace se slitina Fe-25Al-2Ta pokrývá oxidickou vrstvou obsahující Al_2O_3, Fe_2O_3 a Ta_2O_5. Fázová analýza na povrchu prokázala již při teplotě 700 °C přítomnost Lavesovy fáze Fe_2Ta. Do teploty 800 °C je však výskyt Lavesovy fáze na povrchu nízký, proto se na slitině Fe_3Al s 2 at. % tantalu vytváří tenká a přilnavá vrstva složená převážně z Al_2O_3. Při vyšších teplotách (nad 900 °C) tloušťka okují výrazně roste. Proto při teplotě 1000 °C byl naměřen lineární až hyperbolický přírůstek hmotnosti. Při ochlazení z těchto teplot však dochází k odlupování oxidické vrstvy pravděpodobně vlivem precipitace Fe_2Ta pod vrstvou oxidů. Velmi dobrou oxidační odolností při teplotách nad 900 °C vyniká komplexní slitina Fe-30Al-4Cr-2,7TiB_2, pro kterou je charakteristická homogenní a jemnozrnná struktura.

3. Byla zjištěna vynikající korozní odolnost slitiny Fe-25Al-5Cr v sodnovápenaté sklovině a v olovnatém křišťálu. Po interakci slitiny Fe-25Al-5Cr s oběma typy sklovin má nižší korozní úbytky než austenitická ocel. Byl objasněn mechanismus rozpouštění

aluminidů železa ve sklovinách. Pro obě skloviny je charakteristická přednostní rekce hliníku s SiO_2 za vzniku Al_2O_3 a Si. V případě olovnatého křišťálu Al navíc reaguje s PbO za vzniku částic Pb. Křemík a olovo (Pb jen v případě olovnatého křišťálu) způsobují šedé zbarvení skloviny v blízkosti povrchu Fe-Al slitiny. Pro sodnovápenatou sklovinu je navíc charakteristické žluto-hnědé (ambrové) zbarvení, které je způsobené redukcí síry a železa. Intenzita nežádoucího zabarvení vlivem interakce aluminidů železa s testovanými sklovinami je však výrazně nižší než zbarvení, které způsobuje chromniklová ocel.

4. Pro kvantifikaci oxidačního a korozního napadení byla vyvinuta a úspěšně aplikována metodika, která využívá poznatků fraktální geometrie a také standardní nástroje statistiky. Pro kvantifikaci rozhraní (křivky rozhraní) mezi slitinou a okolním prostředím (vzduch, sklovina) byly použity parametry amplitudy, frekvence a složitosti. Bylo porovnáváno korozní napadení aluminidů železa a austenitické oceli po interakci se sodnovápenatou sklovinou a také s olovnatým křišťálem za stejných korozních podmínek. Byl kvantifikován průnik koroze při interakci se sklovinou pod povrch slitin v závislosti na čase. Metodika byla také použita pro porovnání oxidačního napadení aluminidů železa odlišného složení nebo pro kvantifikaci vlivu teploty na vstupní oxidaci aluminidů železa.

6. Literatura

[1] MCKAMEY, C. G., J. H. DEVAN, P. F. TORTORELLI a V. K. SIKKA. A review of recent developments in Fe_3Al-based alloys. *Journal of Materials Research*. 1991, 6(8), 1779-1805.

[2] TORTORELLI, P. F. a J. H. DEVAN. Behavior of iron aluminides in oxidizing and oxidizing/sulfidizing environments. *Materials Science and Engineering: A*. 1992, 153(1-2), 573-577.

[3] NATESAN, K. a P. F. TORTORELLI. High-temperature corrosion and applications of nickel and iron aluminides in coal-conversion power systems. In: DEEVI, S.C., eds. *International Symposium on nickel and iron aluminides: processing, properties, and applications: conference proceedings.* ASM International, 1997, ISBN 0871705907

[4] TORTORELLI, P. F. a J. H. DEVAN. Compositional influences on the high-temperature corrosion resistance of iron aluminides. In: SCHNEIBEL, J.H. – CRIMP, M.A., eds. *Processing, properties, and applications of iron aluminides: conference proceedings.* TMS, 1994, ISBN 13: 9780873392402

[5] BERNST, R., A. SCHNEIDER a M. SPIEGEL. Metal dusting of binary iron aluminium alloys at 600 °C. *Materials and Corrosion*. 2006, 57(9), 724-728.

[6] LI, Y.S., M. SPIEGEL a S. SHIMADA. Corrosion behaviour of various model alloys with NaCl–KCl coating. *Materials Chemistry and Physics*. 2005, 93(1), 217-223.

[7] LI, Y. S. a M. SPIEGEL. Internal Oxidation of Fe–Al Alloys in a KCl-Air Atmosphere at 650 °C. *Oxidation of Metals*. 2004, 61(3/4), 303-322.

[8] HOTAŘ, A. a P. KRATOCHVÍL. The corrosion resistance of iron aluminide Fe28Al3Cr0.02Ce (at%) in a molten glass. *Intermetallics*. 2007, 15(3), 439-441.

[9] PLUHAŘ, J. a M. VYKLICKÝ. Vlastnosti žáruvzdorné slitiny ČSN 42 2484 (Pyroferal) a její použití. Technická zpráva č. 189. Místo vydání: Praha, Ministerstvo těžkého strojírenství, 1959

[10] KRATOCHVÍL, P. The history of the search and use of heat resistant Pyroferal© alloys based on FeAl. *Intermetallics*. 2008, 16(4), 587-591.

[11] UXA, V. Nové žáruvzdorné slitinové materiály ve sklářském průmyslu. *Sklář a keramik*. 1956, 6(9-10), 225-228.

[12] KRATOCHVÍL, P., V. VODIČKOVÁ, J. HAKL, T. VLASÁK, P. HANUS a J. PEŠIČKA. High temperature mechanical properties of Fe28Al4Cr alloy with additives TiB_2 and Zr. *Intermetallics*. 2010, 18(7), 1365-1368.

[13] KRATOCHVÍL, P., P. KEJZLAR, R. KRÁL a V. VODIČKOVÁ. The effect of Zr addition on the structure and high temperature strength of Fe-30 at.% Al type alloys. *Intermetallics*. 2012, 20(1), 39-46.

[14] KRATOCHVÍL, P., V. VODIČKOVÁ, R. KRÁL a M. ŠVEC. The Effect of Laves Phase $(Fe,Al)_2Zr$ on the High-Temperature Strength of Carbon-Alloyed Fe_3Al Aluminide. *Metallurgical and Materials Transactions A*. 2016, 47(3), 1128-1131.

[15] KRATOCHVÍL, P., M. ŠVEC a V. VODIČKOVÁ. The Effect of Low Concentrations Nb and C on the Structure and High-Temperature Strength of Fe_3Al Aluminide. *Metallurgical and Materials Transactions A*. 2017, 48(9), 4093-4096.

[16] PRESCOTT, R., M. J. GRAHAM, H. KÖHNE, K. LUCKA, S. RICHTER a J. MAYER. The formation of aluminum oxide scales on high-temperature alloys. *Oxidation of Metals*. 1992, 38(3-4), 233-254.

[17] NATESAN, K. Corrosion performance of iron aluminides in mixed-oxidant environments. *Materials Science and Engineering: A*. 1998, 258(1-2), 126-134.

[18] DEVAN, J. H. a P. F. TORTORELLI. The oxidation-sulfidation behavior of iron alloys containing 16–40 AT% aluminum. *Corrosion Science*. 1993, 35(5-8), 1065-1071.

[19] TORTORELLI, P. F. a K. NATESAN. Critical factors affecting the high-temperature corrosion performance of iron aluminides. *Materials Science and Engineering: A*. 1998, 258(1-2), 115-125.

[20] PINT, B. A., J. LEIBOWITZ a J. H. DEVAN. The Effect of an Oxide Dispersion on the Critical Al Content in Fe-Al Alloys. *Oxidation of Metals*. 1999, 51(1/2), 181-197.

[21] QUADAKKERS, W. J. a K. BONGARTZ. The prediction of breakaway oxidation for alumina forming ODS alloys using oxidation diagrams. *Materials and Corrosion/Werkstoffe und Korrosion*. 1994, 45(4), 232-241.

[22] GRABKE, H. J. Oxidation of NiAl and FeAl. *Intermetallics*. 1999, 7(10), 1153-1158.

[23] HOTAŘ, A., M. PALM, P. KRATOCHVÍL, V. VODIČKOVÁ a S. DANIŠ. High-temperature oxidation behaviour of Zr alloyed Fe_3Al-type iron aluminide. *Corrosion Science*. 2012, 63, 71-81.

[24] ROMMERSKIRCHEN, I., B. ELTESTER a H. J. GRABKE. Oxidation of β-FeAl and Fe-Al alloys. *Materials and Corrosion/Werkstoffe und Korrosion*. 1996, 47(11), 646-649.

[25] BABU, N., R. BALASUBRAMANIAM a A. GHOSH. High-temperature oxidation of Fe_3Al-based iron aluminides in oxygen. *Corrosion Science*. 2001, 43(12), 2239-2254.

[26] CHEVALIER, S., P. JUZON, G. BORCHARDT, A. GALERIE, K. PRZYBYLSKI a J. P. LARPIN. High-Temperature Oxidation of Fe_3Al and Fe_3Al–Zr Intermetallics. *Oxidation of Metals*. 2010, 73(1-2), 43-64.

[27] LEE, W.H. a R.Y. LIN. Oxidation, sulfidation and hot corrosion of intermetallic compound Fe_3Al at 605°C and 800 °C. *Materials Chemistry and Physics*. 1999, 58(3), 231-242.

[28] NOWAK, K. a M. KUPKA. High-temperature oxidation behaviour of B2 FeAl based alloy with Cr, Zr and B additions. *Materials Chemistry and Physics*. 2012, 132(2-3), 902-908.

[29] WAMBACH, K., J. PETERS a H. J. GRABKE. Behaviour of Al_2O_3 scales on Fe-Al and Fe-Ni-Al alloys with small additions of titanium, zirconium, niobium and vanadium on thermal cycling and creep in oxidizing and carburizing atmospheres. *Materials Science and Engineering*. 1987, 88, 205-212.

[30] DEVAN, H. J., TORTORELLI, P. F. a M. J. BENNETT. Environmental effects on iron aluminides. In: COLE, N. C. – JUDKINS, R. R. eds. Proceedings of the Eight Annual Conference on Fossil Energy Materials. U.S. Department of Energy, August 1994, pp. 309-320

[31] JIANSEN, N., W. XIAOJING, W. QING, C. XIAOYING, L. WEIMIN a Z. XINGYAO. The cyclic oxidation behaviors of Fe_3(Al, Cr, Zr) and Fe_3(Al, Cr, Nb) intermetallic compound at high temperature. *Journal of Shanghai University (English Edition)*. 1997, 1(1), 79-82.

[32] STEIN, F., G. SAUTHOFF a M. PALM. Phases and phase equilibria in the Fe–Al–Zr system. *Zeitschrift für Metallkunde*. 2004, 95(6), 469-485.

[33] KRATOCHVÍL, P., P. KEJZLAR, R. KRÁL a V. VODIČKOVÁ. The effect of Zr addition on the structure and high temperature strength of Fe-30 at.% Al type alloys. *Intermetallics*. 2012, 20(1), 39-46.

[34] PINT, B. A., P. F TORTORELLI a I .G. WRIGHT. Long-term oxidation performance of ingot-produced Fe_3Al alloys. *Materials at High Temperatures*. 2014, 16(1), 1-13.

[35] JANDA, D., H. FIETZEK, M. GALETZ a M. HEILMAIER. The effect of micro-alloying with Zr and Nb on the oxidation behavior of Fe_3Al and FeAl alloys. *Intermetallics*. 2013, 41, 51-57.

[36] KRATOCHVÍL, P., P. MÁLEK, M. CIESLAR, P. HANUS, J. HAKL a T. VLASÁK. High-temperature mechanical properties of Zr alloyed Fe_3Al-type iron aluminide. *Intermetallics*. 2007, 15(3), 333-337.

[37] NOURBAKHSH, S., O. SAHIN, W. H. RHEE a H. MARGOLIN. A structural study of oxidation in a zirconia-toughened alumina fiber-reinforced Fe_3Al composite. *Metallurgical Transactions A*. 1993, 24(2), 435-443.

[38] CHEVALIER, J., L. GREMILLARD, A. V. VIRKAR a D. R. CLARKE. The Tetragonal-Monoclinic Transformation in Zirconia: Lessons Learned and Future Trends. *Journal of the American Ceramic Society*. 2009, 92(9), 1901-1920.

[39] KELLY, J. a I. DENRY. Stabilized zirconia as a structural ceramic: An overview. *Dental Materials*. 2008, 24(3), 289-298.

[40] MILENKOVIC, S. a M. PALM. Microstructure and mechanical properties of directionally solidified Fe–Al–Nb eutectic. *Intermetallics*. 2008, 16(10), 1212-1218.

[41] HANUS, P., E. BARTSCH, M. PALM, R. KREIN, K. BAUER-PARTENHEIMER a P. JANSCHEK. Mechanical properties of a forged Fe–25Al–2Ta steam turbine blade. *Intermetallics*. 2010, 18(7), 1379-1384.

[42] RISANTI, D. D. a G. SAUTHOFF. Strengthening of iron aluminide alloys by atomic ordering and Laves phase precipitation for high-temperature applications. *Intermetallics*. 2005, 13(12), 1313-1321.

[43] KREIN, R. a M. PALM. The influence of Cr and B additions on the mechanical properties and oxidation behaviour of L21-ordered Fe–Al–Ti-based alloys at high temperatures. *Acta Materialia*. 2008, 56(10), 2400-2405.

[44] YANGSHAN, S., Y. ZHENGJUN, Z. ZHONGHUA a H. HAIBO. Mechanical properties of Fe_3Al-based alloys with cerium addition. *Scripta Metallurgica et Materialia*. 1995, 33(5), 811-817.

[45] KRATOCHVÍL, P., V. VODIČKOVÁ a I. ŠEDIVÁ. Struktura a mechanické vlastnosti aluminidu železa Fe28Al5Cr s přísadami céru a titanboridu. *Hutnické listy*. 2000, (9), 19-21.

[46] KARLÍK, M. a M. CIESLAR. Precipitation in the Fe–28Al–4Cr intermetallic alloy with Ce addition. *Materials Science and Engineering: A*. 2002, 324(1-2), 5-10.

[47] YU, X. a Y. SUN. The oxidation improvement of Fe_3Al based alloy with cerium addition at temperature above 1000 °C. *Materials Science and Engineering: A*. 2003, 363(1-2), 30-39.

[48] NOVÁK, P. a K. NOVÁ. Oxidation behavior of Fe–Al, Fe–Si and Fe–Al–Si intermetallics. *Materials*. 2019, 12(11), 1748.

[49] PINT, B. A., I. G. WRIGHT, W. Y. LEE, Y. ZHANG, K. PRÜSSNER a K. B. ALEXANDER. Substrate and bond coat compositions: factors affecting alumina scale adhesion. *Materials Science and Engineering: A*. 1998, 245(2), 201-211.

[50] KUENZLY, J. D. a D. L. DOUGLASS. The oxidation mechanism of Ni_3Al containing yttrium. *Oxidation of Metals*. 1974, 8(3), 139-178.

[51] WRIGHT, I. G., PINT, B. A., LEE, W. Y., ALEXANDER, K. B. a K. PRÜßNER. Some effects of metallic substrate composition on degradation of thermal barrier coatings. Technical Report n. ORNL/CP-95674, Place of issue: Oak Ridge (stát Tennessee, Spojené státy americké), Oak Ridge National Lab.,1997

[52] PINT, B. A., A. J. GARRATT-REED a L. W. HOBBS. Possible Role of the Oxygen Potential Gradient in Enhancing Diffusion of Foreign Ions on α-Al_2O_3 Grain Boundaries. *Journal of the American Ceramic Society*. 1998, 81(2), 305-314.

[53] Kirsch, R. *Kovy ve sklářství*, Informatorium Praha, 1992. ISBN 80-85427-13-3

[54] SMRČEK, A. a J. SMRČEK. Žáruvzdorné ocele pro přímý styk s tekutou sklovinou – část II. *Sklář a keramik*. 1966, 16(12), 351-356.

[55] HOTAŘ, A. *Korozní odolnost aluminidu železa Fe28Al3Cr0,02Ce ve sklovině*. Liberec, 2004. Disertační práce. Technická univerzita v Liberci. Vedoucí práce Prof. RNDr. Petr Kartochvíl, DrSc.

7. Soubor komentovaných publikací

[P2-1] HOTAŘ, A., M. PALM, P. KRATOCHVÍL, V. VODIČKOVÁ a S. DANIŠ. High-temperature oxidation behaviour of Zr alloyed Fe_3Al-type iron aluminide. *Corrosion Science*. 2012, 63, 71-81.

[P2-2] HOTAŘ, A., P. KEJZLAR, M. PALM a J. MLNAŘÍK. The effect of Zr on high-temperature oxidation behaviour of Fe3Al-based alloys. *Corrosion Science*. 2015, 100, 147-157.

[P2-3] HOTAŘ, A. a M. PALM. Oxidation resistance of Fe–25Al–2Ta (at.%) in air. *Intermetallics*. 2010, 18(7), 1390-1395.

[P2-4] HOTAŘ, A., P. KRATOCHVÍL a J. CÍZNER. Oxidation resistance of Fe28Al3Cr0.02Ce and Fe30Al4Cr2.7TiB_2 (at. %) in air. In: *METAL 2010 - 19th International Conference on Metallurgy and Materials*. Ostrava: TANGER, 2010, s. 915-919. ISBN 978-808729417-8.

[P3-1] HOTAŘ, A. a P. KRATOCHVÍL. The corrosion resistance of iron aluminide Fe28Al3Cr0.02Ce (at%) in a molten glass. *Intermetallics*. 2007, 15(3), 439-441.

[P3-2] HOTAŘ, A., P. KRATOCHVÍL a V. HOTAŘ. The corrosion resistance of Fe_3Al-based iron aluminides in molten glasses. *Kovove Mater*. 2009, 47(4), 247-252. ISSN 1338-4252.

[P3-3] HOTAŘ, A., V. HOTAŘ a F. NOVOTNÝ. Corrosion behaviour of Fe-40Al-Zr at.% alloy in molten soda-lime glass. *Kovove Mater*. 2014, 52(03), 149-155.

[P3-4] HOTAŘ, A., V. HOTAŘ a J DROBEČEK. Corrosion resistance of heat-resistance alloys in molten lead crystal at 1200 °C. In: *METAL 2012 - Conference Proceedings, 21st International Conference on Metallurgy and Materials*. Ostrava: TANGER, 2012, s. 1467-1470. ISBN 978-808729431-4.

[P4-1] HOTAŘ, V. a A. HOTAŘ. Aplikace nekonvenčních metod pro hodnocení dat ve sklářství. *Sklář a keramik*. 2006, 56(9), 179-184. ISSN SSN 0037-637X.

[P4-2] HOTAŘ, A. a V. HOTAŘ. Fractal geometry used for evaluation of corrosion resistence of Fe-14Al-6Cr wt. % againts molten glass. *Manufacturing Technology*. J. E. Purkyne University in Usti nad Labem, 2015, 15(4), 534-541. ISSN ISSN 1213–2489.

[P4-3] HOTAŘ, V. a A. HOTAŘ. Fractal dimension used for evaluation of oxidation behaviour of Fe-Al-Cr-Zr-C alloys. *Corrosion Science*. 2018, 133, 141-149.

Corrosion Science 63 (2012) 71–81

Contents lists available at SciVerse ScienceDirect

Corrosion Science

journal homepage: www.elsevier.com/locate/corsci

High-temperature oxidation behaviour of Zr alloyed Fe_3Al-type iron aluminide

A. Hotař [a,*], M. Palm [b], P. Kratochvíl [c], V. Vodičková [a], S. Daniš [c]

[a] Technical University of Liberec, Faculty of Engineering, Department of Material Science, Studentská 2, CZ 46117 Liberec, Czech Republic
[b] Max-Planck-Institut für Eisenforschung GmbH, Max-Planck-Strasse 1, D-40237 Düsseldorf, Germany
[c] Charles University of Prague, Faculty of Mathematics and Physic, Ke Karlovu 5, CZ 12116 Prague 2, Czech Republic

ARTICLE INFO

Article history:
Received 6 January 2012
Accepted 26 May 2012
Available online 9 June 2012

Keywords:
A. Intermetallics (based on Fe_3Al)
B. XRD
B. SEM
B. EPMA
C. Oxidation
C. Kinetic parameters

ABSTRACT

The oxidation behaviour of two Fe_3Al-based Fe–Al–Cr–Zr–C alloys has been evaluated between 900 and 1200 °C. The alloys contained either $(Fe,Al)_2Zr$ Laves phase or ZrC carbide. The alloys were oxidised for up to 1000 h in synthetic air using thermogravimetric analysis (TGA). Scales that formed on the surfaces of the sample as well as cross sections were analysed by light optical microscopy (LOM), X-ray diffraction (XRD), scanning electron microscopy (SEM), and energy-dispersive X-ray spectrometry (EDS).

At 900 °C parabolic growth and low weight gains for both tested alloys were observed. The scales are predominantly formed by Al_2O_3 with minor amounts of ZrO_2. Some Fe_2O_3 was observed after oxidation at 900 °C. At 1000 °C oxidation ingresses into the samples along grain boundaries due to preferential oxidation of the Zr-rich precipitates, becoming more severe at higher temperatures. Ingress of oxidation into the sample is more pronounced for the alloy containing ZrC where at 1200 °C it is not any longer limited to the carbide but extends markedly into the Fe_3Al matrix.

1. Introduction

Fe_3Al-based alloys have been studied as materials for high-temperature structural applications because they have low material costs (compared with corrosion and heat resistant steels), low density (5.8–6.3 g/cm^3) and a very good corrosion resistance at high temperatures in a variety of aggressive environments [1,2]. The good corrosion resistance of Fe–Al-based alloys is caused by the formation of protective α-Al_2O_3 (alumina) scales in oxidising environments [1,2]. However, depending on alloy composition (especially the Al content in the base Fe–Al), exposure time and temperature, iron oxides and metastable γ-, δ- and θ-Al_2O_3 can form. All these oxides grow faster and are more voluminous and porous than α-Al_2O_3 and are therefore less protective [3–6].

Additions of ternary alloying elements influence the mechanical properties and corrosion resistance of Fe–Al-based alloys. The addition of Cr increases ductility and ultimate strength but also increases the oxidation rate [1,7,8]. On the other hand, the oxidation resistance can be improved by addition of small Zr levels [2,9–11]. Doping of Fe_3Al with Zr results in flatter scales and the outward diffusion of Al through the scale is suppressed (for details see [12] and references therein). Specifically, it has been shown that addition of Zr in the range 0.05–0.1 at.% to Fe_3Al–Cr alloys improves the adherence of the α-Al_2O_3 scale [11,13–17]. Apparently, doping with Zr inhibits the formation of voids at the metal/scale interface [16].

The purpose of the present paper is to investigate the high-temperature oxidation behaviour of two Fe–Al–Cr–Zr–C alloys. Their composition is similar to the composition of an alloy tested in [18], which in view of its strength is promising for high-temperature applications.

2. Experimental

Two Fe–Al–Cr–Zr–C alloys were molten in a vacuum furnace and ingots were produced by investment casting. The composition of the alloys (in at.%) is given in Table 1. The ingots with dimension $30 \times 40 \times 350$ mm^3 were rolled at 1200 °C to sheets with a final thickness of 13 mm. For oxidation tests as-rolled samples with dimension $10 \times 10 \times 1$ mm^3 were cut by electrical discharge machining (EDM). The surfaces of the samples were ground to 1200 grit. The oxidation behaviour was investigated using a Setaram SETSYS 16/18 thermobalance with continuous recording of the mass gains and with a mass sensitivity of 1 μg. Samples of both alloys were oxidised in synthetic air (20.5% O_2, 79.5% N_2) at a flow rate of 1.54×10^{-6} m^3/s at temperatures from 900 to 1200 °C.

All scales and microstructures were inspected by light optical microscopy (LOM) and scanning electron microscopy (SEM). For observation of the ingress of the oxidation and the microstructures, cross sections of the samples were prepared by cutting with a precision saw and embedding them in a conductive resin. Metallographic samples were ground by diamond suspensions and

* Corresponding author. Tel.: +420 485 353 136; fax: +420 485 353 631.
E-mail address: adam.hotar@tul.cz (A. Hotař).

0010-938X/$ - see front matter © 2012 Elsevier Ltd. All rights reserved.
http://dx.doi.org/10.1016/j.corsci.2012.05.027

Table 1
Chemical composition of alloys in at.%.

Alloy	Al	Zr	Cr	C	Fe
A	29.7	0.3	3.8	0.2	Bal.
B	26.4	0.2	2.8	0.6	Bal.

subsequently polished by a suspension of non-crystallising colloidal silica. The phases in the oxide scales were determined by X-ray diffraction (XRD) and grazing incidence X-ray diffraction (GI-XRD). Measurements were performed on a Seifert XRD 7 diffractometer with Bragg–Brentano geometry using Cu Kα radiation. The compositions of the phases of the scales were evaluated

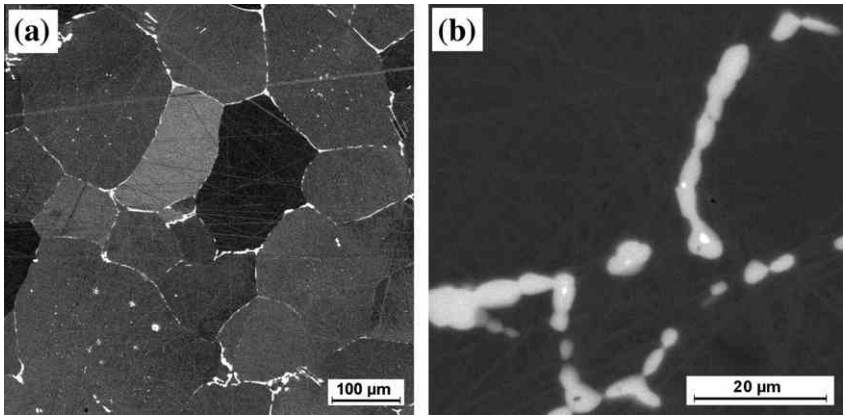

Fig. 1. SEM micrograph (backscatter electron (BSE) contrast) of alloy A (Fe–29.7Al–3.8Cr–0.3Zr–0.2C) in the as rolled condition. (a) Overview showing the Fe_3Al matrix (black) and $(Fe,Al)_2Zr$ Laves phase particles (light phase); (b) Magnification of (a) showing small ZrC nuclei (white) within the Laves phase (grey).

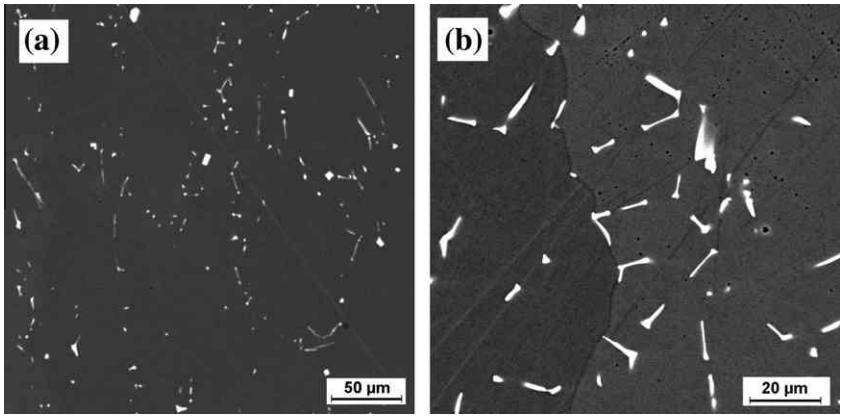

Fig. 2. SEM-BSE micrograph of alloy B (Fe-26.4Al-2.8Cr-0.2Zr-0.6C) in the as rolled condition. (a) Overview showing the Fe_3Al matrix (black) and ZrC particles (light phase) (b) Detail of ZrC particles on the grain's boundary.

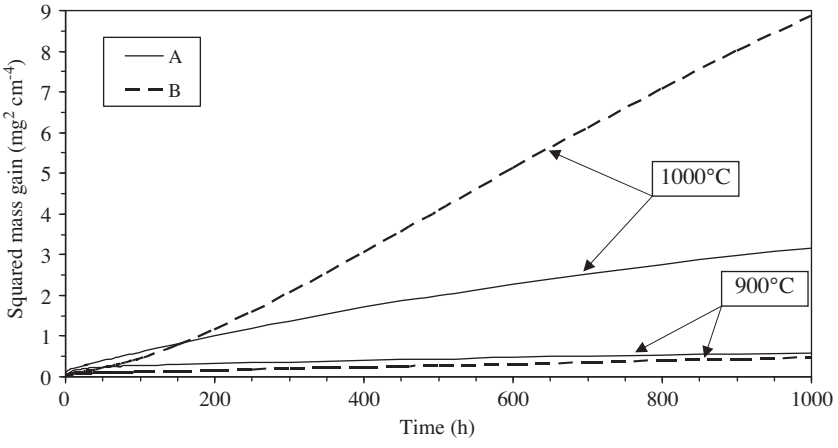

Fig. 3. Squared mass gain versus exposure time for alloys A and B at 900 and 1000 °C in synthetic air.

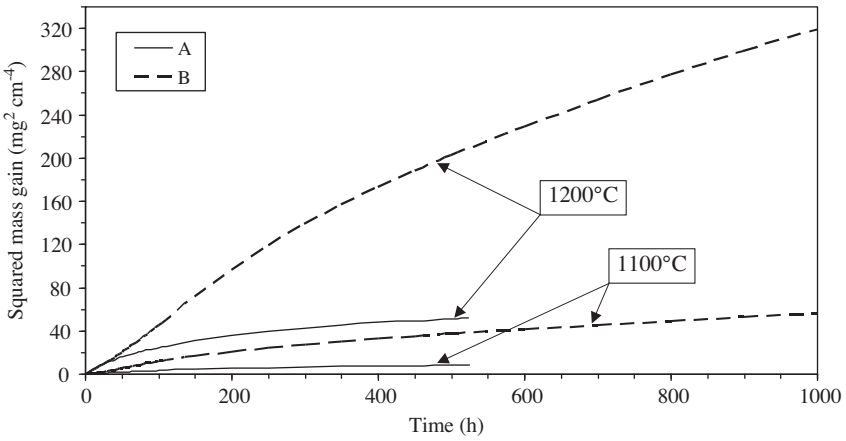

Fig. 4. Squared mass gain versus exposure time for alloys A and B at 1100 and 1200 °C in synthetic air.

Table 2
Apparent parabolic rate constants k_p of selected Fe–Al alloys oxidised in air. The current data for k_p were calculated from the TGA curves omitting the initial 200 h.

Alloy (at.%)	k_p (g^2 cm^{-4} s^{-1})				Reference
	900 °C	1000 °C	1100 °C	1200 °C	
A Fe–29.7Al–3.8Cr–0.3Zr–0.2C	8.3×10^{-14}	7.5×10^{-13}	2.7×10^{-12}	1.3×10^{-11}	This work
B Fe–26.4Al–2.8Cr–0.2Zr–0.6C	1.1×10^{-13}	[c]	1.2×10^{-11}	7.6×10^{-11}	This work
Fe–27.2Al–5.1Cr–0.1Zr[a]				6.0×10^{-12}7.4 $\times 10^{-12}$	[12][12]
Fe–28Al–5Cr–0.05Zr–0.03C[b]	–	3.3×10^{-15}	1.6×10^{-13}	6.1×10^{-12}	[11]
Fe–28Al–5Cr–0.03C[b]	–	1.4×10^{-13}	1.5×10^{-11}	3.8×10^{-11}	[11]
Fe–20Al–0.1Zr	9×10^{-14}				[20]
Fe–32Al–0.8Zr	4×10^{-13}	–	–	–	[20]
Fe–28Al–3Cr–0.02Ce	4.2×10^{-13}	–	[c]	–	[23]
Fe–30Al–4Cr–2.7TiB2	6.9×10^{-13}	–	4.3×10^{-12}	–	[23]
Fe–25Al	1.0×10^{-13}	–	–	–	[24]
Fe–27Al–15Ti	1.4×10^{-13}	–	–	–	[22]

[a] Oxidation in dry O_2.
[b] Short term oxidation for 100 h.
[c] No parabolic oxidation behaviour.

through energy-dispersive X-ray spectrometry (EDS; Bruker) on a TESCAN SEM.

3. Results and discussion

The two selected alloys have been designed for applications at high temperatures. They differ in that two different phases have been related to their corrosion behaviour. After hot rolling at 1200 °C, the microstructure of alloy A (Fe–29.7Al–3.8Cr–0.3Zr–0.2C) consists of a Fe_3Al matrix with a grain size of about 500 μm with elongated particles of the Laves phase $(Fe,Al)_2Zr$ (Fig. 1) which has been identified by EDS and XRD. The Laves phase is mostly observed along grain boundaries. Within the Laves phase light nuclei are observed which have been identified as ZrC by SEM-EDS (Fig. 1b).

The main difference in the composition of alloy B (Fe–26.4Al–2.8Cr–0.2Zr–0.6C) is a considerably higher carbon content. While the Fe_3Al matrix has about the same grain size than alloy A, alloy B does not any longer contain Laves phase but instead ZrC particles are observed. They are distributed inside the grains as well as along grain boundaries (Fig. 2).

The results of the oxidation tests performed in synthetic air at 900, 1000, 1100 and 1200 °C are summarised in Figs. 3 and 4. After an initial transition period parabolic mass gains are observed with

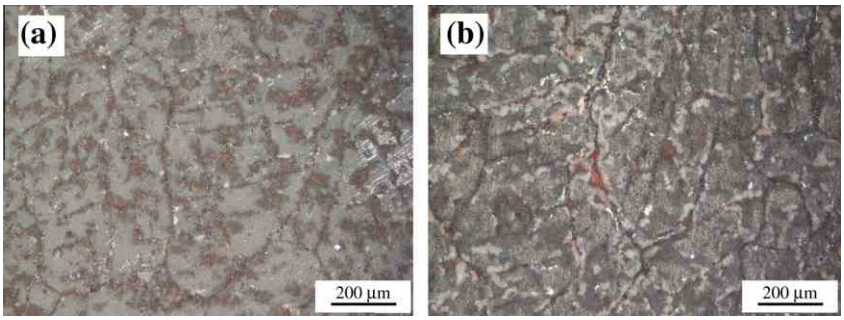

Fig. 5. LOM micrographs of scales formed on alloy A at 900 °C (a) and 1000 °C (b).

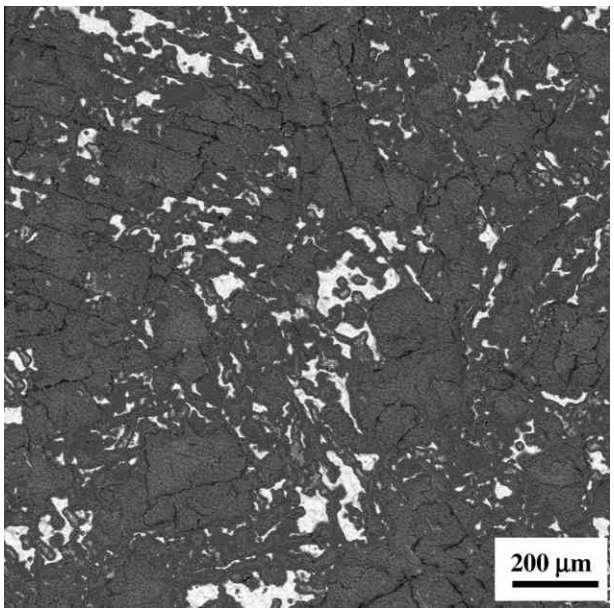

Fig. 6. SEM-BSE micrograph of the surface of alloy A oxidised at 1200 °C/500 h. The oxide scale (grey) has spalled markedly during cooling (light areas).

the exception of alloy B, where linear or even hyperbolic growth is observed at 1000 °C. With increasing temperature the mass gain increases for both alloys. However, for alloy B the increase with time is markedly higher above 900 °C than for alloy A. No drops in the mass gain curves (Figs. 3 and 4) are observed which indicates that no spallation took place during isothermal oxidation. The initial transition period, which is characterised by a higher oxidation rate, is due to the formation of transient Al_2O_3 phases [3–6]. Their transformation to α-Al_2O_3 and the effect of Zr on that is discussed in [11,19].

Parabolic rate constants (k_p) evaluated from the parabolic rate law

$$(\Delta m/A)^2 = k_p t \quad (1)$$

where $\Delta m/A$ is the weight gain per unit area (mg/cm^2) and t is the time (s) are usually employed to compare the oxidation behaviour of different alloys. Strictly, not only parabolic growth but also the formation of an even scale is a prerequisite for the determination of k_p. Because of the ingress of oxidation into the sample, determination of k_p in its true sense is not possible for the present alloys. However, in cases where no true parabolic growth of the scales has been observed but where the weight gains show a parabolic curve shape, "apparent" parabolic rate constants have been determined in order to judge the oxidation behaviour [20–22]. At 900 °C alloys A and B both have low apparent parabolic rate constants (Table 2) comparable to those of binary Fe_3Al [24] and lower than those of other Fe_3Al-type iron aluminides [20,22,23]. At higher temperatures k_p values seem to be at the high side of reported data, possibly due to increasing ingress of oxidation of the present alloys. However, data are scarce as these temperatures are already quite high for the application of Fe–Al alloys and also difficult to compare because of varying experimental conditions (Table 2).

The inspection of the scales by LOM and SEM revealed that thin adherent oxide scales formed on the surfaces of alloys A and B at 900 °C. Scales formed on alloy B at higher temperatures are dense and adherent. In contrast, scales formed on alloy A between 1000 and 1200 °C were porous and spalled easily during or after cooling to room temperature (22 °C). Fig. 5 shows LOM micrographs of the scales formed on alloy A at 900 and 1000 °C. They are dense and adherent though cooling from 1000 °C lead to the formation of cracks. In contrast, scales on alloy A oxidised at 1100 and 1200 °C spalled during cooling (Figs. 6 and 7). The element mappings in Fig. 7b–f) show that the scale mainly consists out of Al_2O_3 with small amounts of ZrO_2 scattered on top of the Al_2O_3 scale. It also reveals that Cr is only present in the matrix and does not enter into the scale in any detectable amounts.

The scales formed on alloy B during oxidation at 900–1200 °C did not spall during cooling and also they did not show cracking as was observed in case of alloy A (Fig. 5b). Fig. 8 shows the intact scale on alloy B after oxidation and cooling from 1200 °C. In contrast to the scale formed on alloy A at the same temperature (Fig. 6) the oxide scale has not spalled during cooling. SEM-EDS revealed that the scale mainly consist out of Al_2O_3 with small amounts of ZrO_2 scattered on the surface (Fig. 9), i.e. comparable to the scale that formed on alloy A at the same temperature.

Specifically the scales formed on alloy A at 900 and 1000 °C showed brown patches indicative of the presence of iron oxides (Fig. 5).

In order to characterise further the oxide scales they were analysed in detail by XRD and GI-XRD (Table 3). Scales formed on both alloys at 900 °C consisted of Al_2O_3 and minor amounts of ZrO_2 and Fe_2O_3 while at 1200 °C scales are formed by Al_2O_3 and ZrO_2 (Figs. 10 and 11). In general, while the amount of Fe_2O_3 decreases with increasing temperature the volume fraction of ZrO_2 increases (Ta-

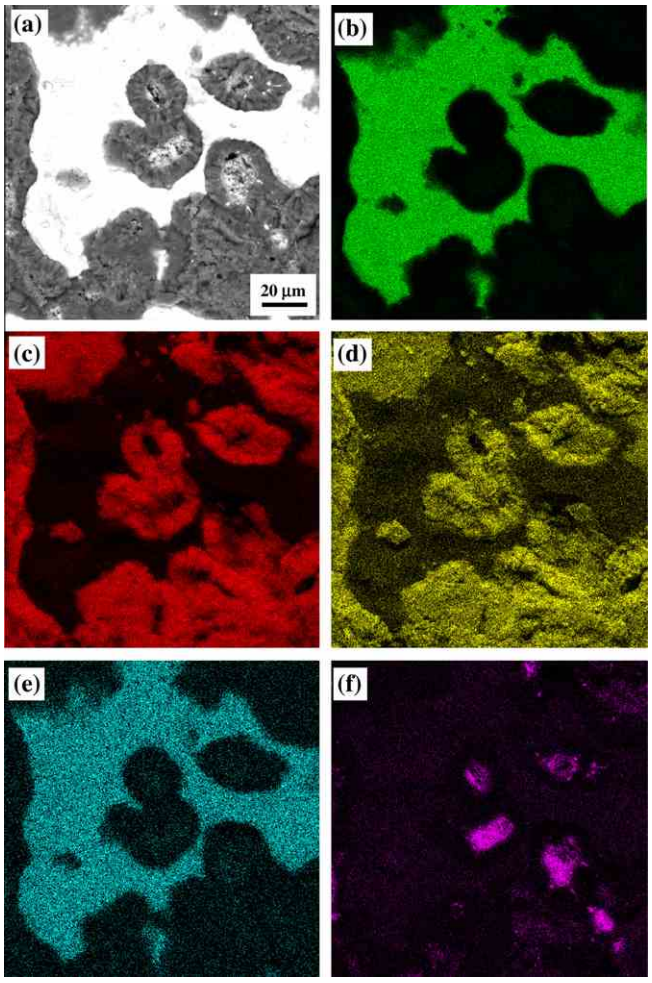

Fig. 7. SEM-BSE micrograph of the surface of alloy A oxidised at 1200 °C (a) and mappings of elements: Fe (b), Al (c), O (d), Cr (e) and Zr (f).

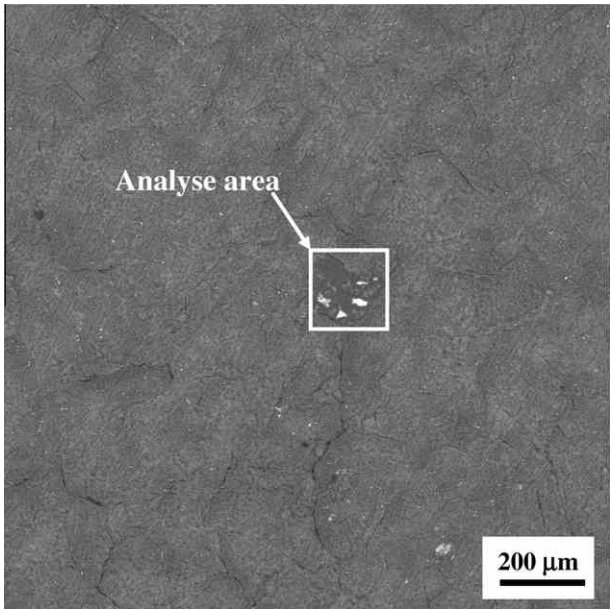

Fig. 8. SEM-BSE micrograph of the scale on alloy B oxidised at 1200 °C/1000 h. Fig. 9 shows SEM-EDS analysis of the marked area.

Table 3
Phases detected by GI-XRD (or XRD) and EDS in the oxide scales of alloys A and B after isothermal oxidation between 900 and 1200 °C.

Temperature (°C)	A	B
900	Al_2O_3, few ZrO_2, minor amounts of Fe_2O_3	Al_2O_3, few Fe_2O_3, minor amounts of ZrO_2
1000	Al_2O_3, few ZrO_2, Fe_2O_3?	Al_2O_3, ZrO_2
1100	Al_2O_3, ZrO_2	Al_2O_3, ZrO_2
1200	Al_2O_3, ZrO_2	Al_2O_3, ZrO_2

ble 3). The formation of iron oxides is typical for the initial stage of the oxidation before the thermodynamically stable Al_2O_3 can develop a continuous scale and therefore these transient iron oxides are specifically observed at lower temperatures [6,25]. It is noteworthy, that ZrO_2 is present in two polymorphs, the monoclinic and the tetragonal one. Below about 1170 °C tetragonal ZrO_2 should transform into the monoclinic polymorph by a martensitic reaction. However, it is well known that tetragonal ZrO_2 can be stabilised at lower temperatures by impurities, particle size or strain energies [26–29].

The formation of ZrO_2 maybe partly associated with enrichment in Zr at the metal/scale interface during oxidation. For Fe–28Al–5Cr–0.1Zr (at.%) Alexander et al. [30] observed such enrichment after isothermal oxidation at 1000 °C for 96 h. For an alloy of nominally the same composition oxidised at 1100 °C for 100 h Chevalier et al. [11,19] established the presence of nm-sized ZrO_2 particles located close to the scale/alloy interface through transmission electron microscopy (TEM) which hints to ZrO_2 formation by Zr enrichment at the metal/scale interface. On the other hand they also detected ZrO_2 particles near the scale/gas interface [19] which should have formed by active diffusion of Zr toward the gas interface (see [12] and Refs. therein). The present results also show the presence of ZrO_2 on the surface of the scales, i.e. at the scale/gas interface (Fig. 7).

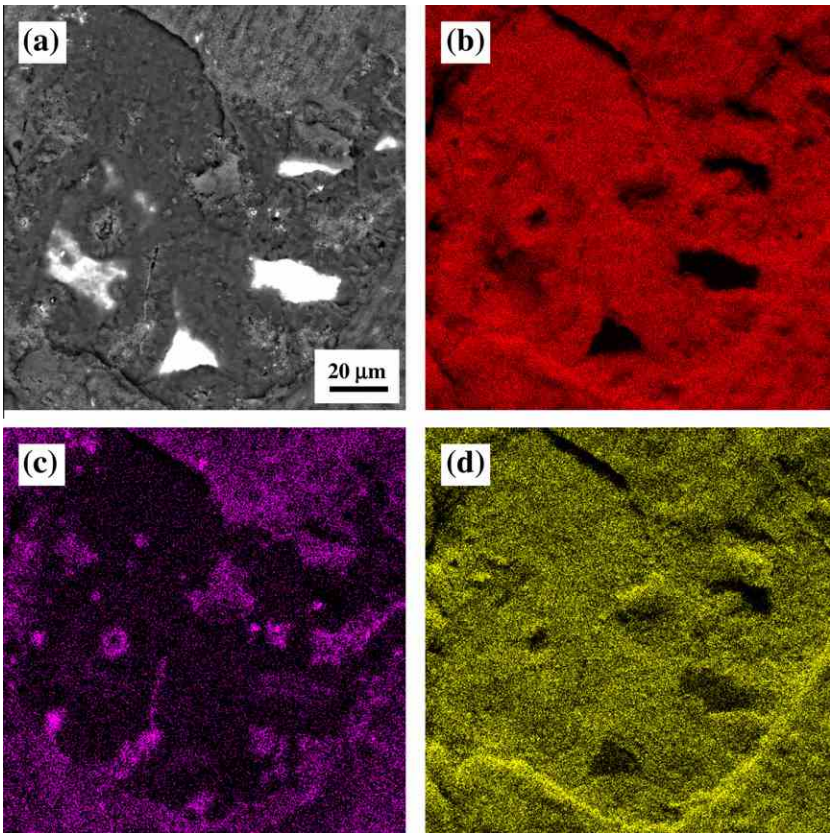

Fig. 9. SEM-BSE micrograph of the surface of alloy B oxidised at 1200 °C (a) and mappings of elements: Al (b), Zr (c) and O (d). The analysed area is marked in Fig. 8.

For alloys with low Zr contents usually only the presence Al_2O_3 in the scales has been reported, e.g. for Fe–28Al–5Cr–0.05Zr–0.03C (at.%) after cyclic oxidation at 1000 °C and cooling to RT for 500 h [15] only scales consisting out of Al_2O_3 were observed. However, in scales formed on Fe–27.2Al–5.1Cr–0.1Zr–0.04C (at.%) during cyclic oxidation between upper 1000–1300 °C and RT for up to 5000 h Pint et al. [16] observed Al_2O_3 scales with frequent ZrO_2 particles on the surface of the scales, i.e. at the gas interface. Fe–Al alloys with higher Zr contents of 0.3 and 0.8 at.% showed even larger volume fractions of zirconium oxide in the scales [31]. Therefore it is reasonable that the present alloys also show a larger volume fraction of ZrO_2 in the scales as they contain 0.2 and 0.3 at.% Zr compared to Fe–28Al–5Cr (at.%) alloys with 0.05–0.1 at.% Zr which may show scales only consisting out of Al_2O_3.

Inspection of cross sections of the oxidised samples revealed that after oxidation at 900 °C only oxide scales on the surfaces have formed while all samples oxidised at or above 1000 °C show ingress of the oxidation into the samples. For alloy A the oxidation after 1000 h at 1000 °C is limited to oxidation of Laves phase particles along grain boundaries (Fig. 12a) while after oxidation for 500 h at 1200 °C oxides protrude more frequently from the surface into the sample (Fig. 12c). Ingress of oxidation into the sample is even more pronounced in case of alloy B. Already after oxidation for 1000 h at 1000 °C oxides penetrate into the sample (Fig. 12b) and presumably this is the reason for the increased weight gain of alloy B compared to that of alloy A at the same temperature (Fig. 3). The oxides are not limited to former ZrC particles, but propagate into the Fe_3Al matrix. After oxidation at 1200 °C for 1000 h massive oxidation is observed in alloy B (Fig. 12d) where not only ZrC particles but also a large volume of the Fe_3Al matrix has already been oxidised.

The chemical composition of the oxides was analysed using SEM-EDS mappings and line scans. The EDS mapping of alloy A oxidised at 1000 °C reveals that the Zr-rich Laves phase particles at the grain boundaries are preferentially oxidised (Fig. 13). The majority of the oxide is Al_2O_3 but also some ZrO_2 is always present in the core of the oxides (Fig. 13c and d). The EDS mapping of alloy B also oxidised at 1000 °C shows the formation of Al_2O_3 and ZrO_2 as well (Fig. 14). The Zr oxide is more spread within the oxidised area, i.e. not limited to the core as observed in case of alloy A, and the oxidised areas are also larger compared to alloy A (Fig. 13). However, after oxidation at 1200 °C for 1000 h the EDS line scan (Fig. 15) reveals that also in alloy B oxidised areas are Zr rich in the core and more Al rich in the outer rim.

It has been shown before that apparently the presence of the Laves phase $(Fe,Al)_2Zr$ and the phase $(Fe,Al)_{12}Zr$ (τ_1) have a detrimental effect on the oxidation behaviour of Fe–Al–Zr alloys [20]. The current results suggest that also ZrC deteriorates the oxidation

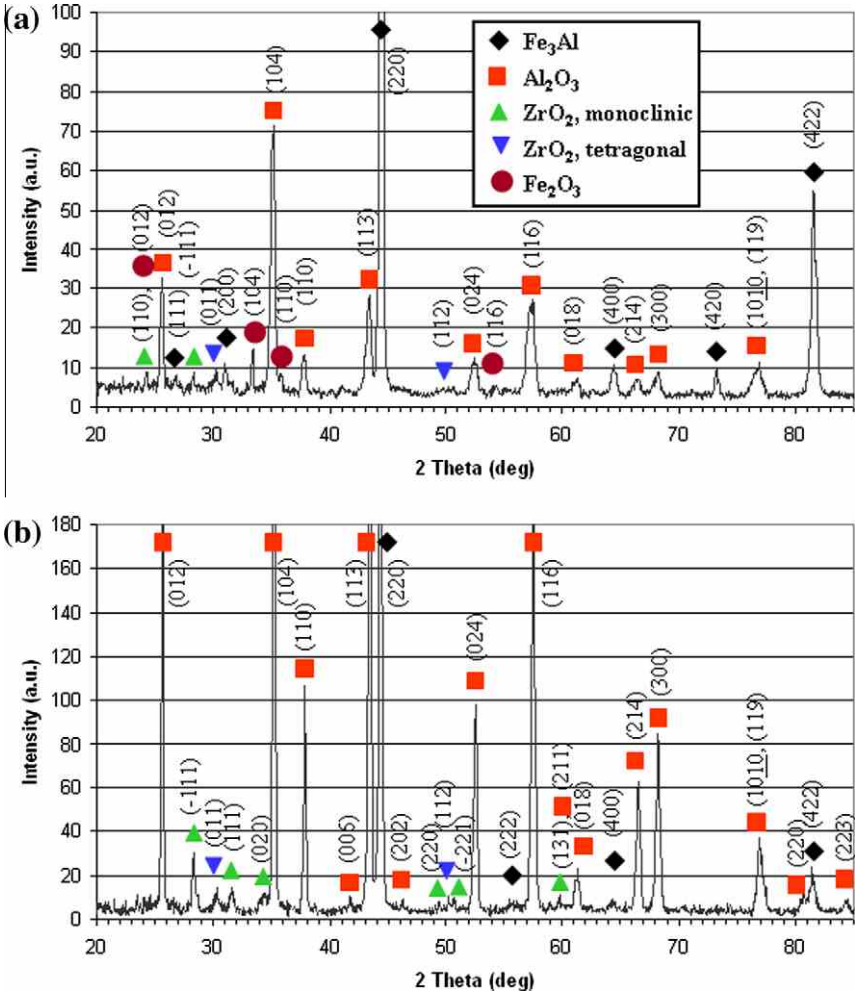

Fig. 10. XRD patterns of the oxidised surface of alloy A after oxidation at 900 °C/1000 h (a) and 1200 °C/500 h (b).

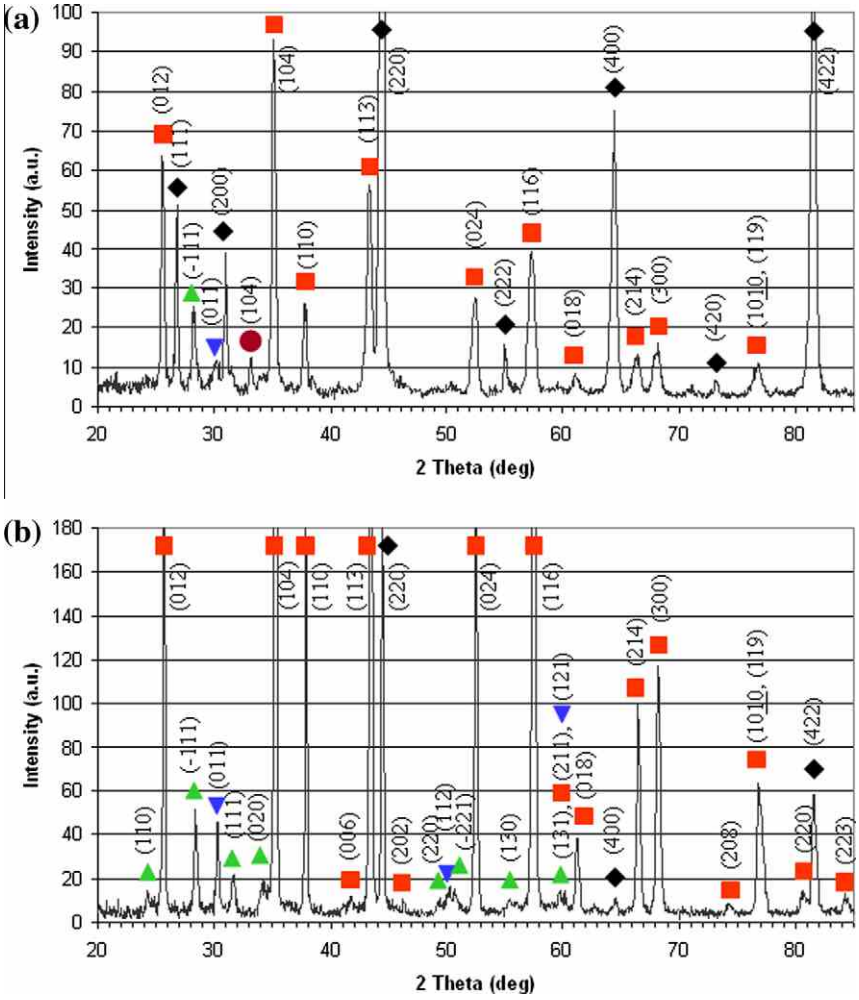

Fig. 11. XRD patterns of the oxidised surface of alloy B after oxidation at 900 °C/1000 h (a) and 1200 °C/1000 h (b).

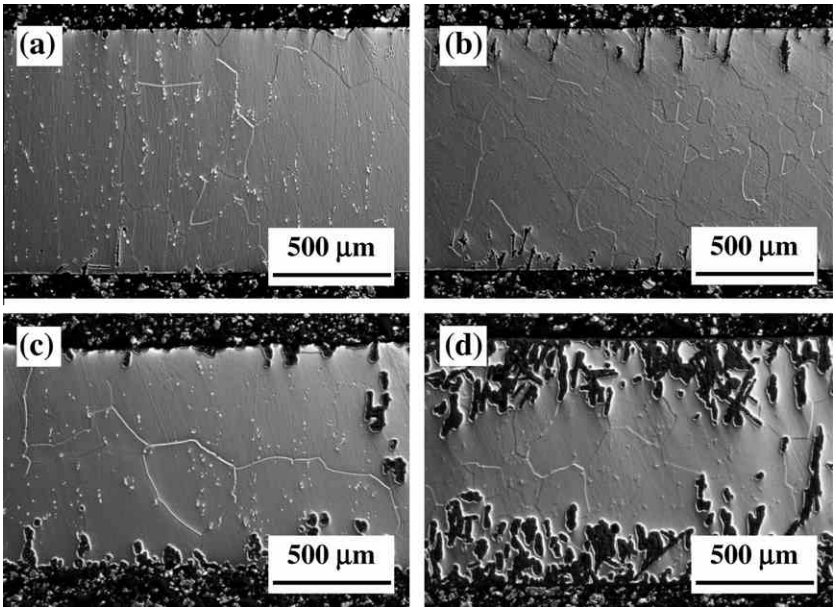

Fig. 12. LOM micrographs of cross sections showing the amount of oxide protrusions into the samples after oxidation at 1000 °C for 1000 h (a and b) and 1200 °C for 500 h (c), for 1000 h (d) of alloys A (left) and B (right).

behaviour of Fe–Al alloys, at least above 900 °C. It is well known that ZrC oxidises rapidly above about 500 °C by the reactions [32–35].

$$ZrC + O_2 \leftrightarrow ZrO_2 + C \quad (2)$$

or

$$ZrC + 2O_2 \leftrightarrow ZrO_2 + CO_2 \quad (3)$$

Actually, the EDS mapping of carbon reveals that carbon is enriched within the oxide (Fig. 13e), i.e. as expected according to Reaction (2). The volume of CO_2 generated by Reaction (3) is rather large and it has been suggested that therefore it should lead to the formation of spherical pores within the oxide [33,35]. That no gas pores are observed within the oxides also suggests that oxidation of ZrC happened according to Eq. (2).

From oxidation experiments carried out by other groups only in one case oxide penetration into a Fe–Al–Cr–Zr alloy has been reported. While no protrusions of oxides into the sample were observed for Fe–28Al–5Cr–0.1Zr–0.05B (at.%) after isothermal oxidation for 96 h at 1000 °C [30], an alloy of nominally the same composition showed deep oxide penetrations after cyclic oxidation between upper 1100–1300 °C and RT [16].

However, for explanation of some of the current results observations by Nourbakhsh et al. [35] are of great relevance. During pressure casting of a zirconia-toughened alumina (Al_2O_3) fibre-reinforced Fe_3Al-based intermetallic composite double layers of ZrC and $(Fe,Al)_2Zr$ Laves phase (denoted as Fe_2AlZr in [35]) formed at the fibre/matrix interface. These double layers were unintentionally oxidised when the composite was annealed at 1100 °C for 24 or 240 h in air. From an elaborate TEM study of the oxidised ZrC/Laves phase double layers the authors found that ZrC is more

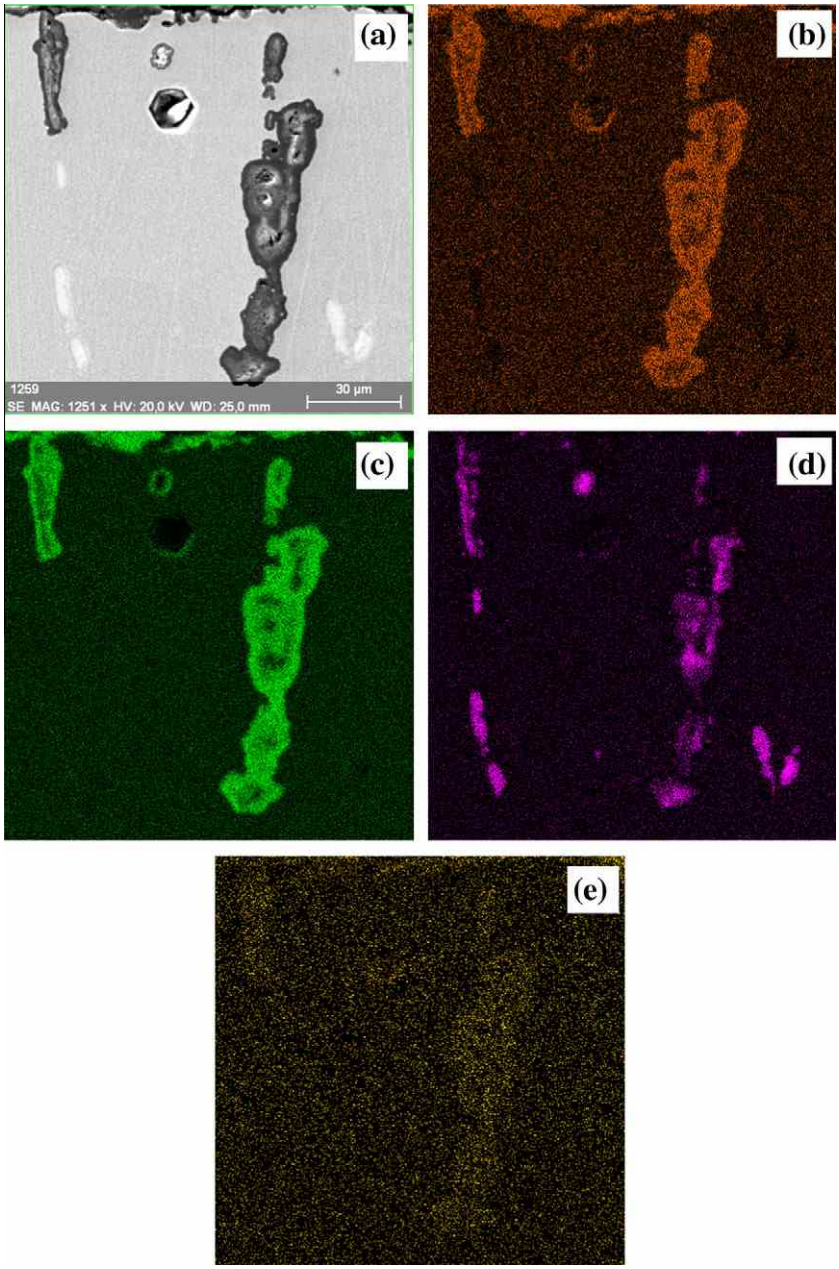

Fig. 13. SEM (secondary electron (SE) contrast) micrograph of the cross section of alloy A after oxidation at 1000 °C for 1000 h (a) and mappings of elements: O (b), Al (c), Zr (d), and C (e).

readily oxidised than the Laves phase $(Fe,Al)_2Zr$ and that Al_2O_3 grew preferentially where ZrO_2 had formed, enveloping the ZrO_2. From the latter observation the authors inferred that Al_2O_3 may have difficulty in nucleating on its own and that ZrO_2 may have a catalytic effect in enhancing Al_2O_3 formation [35].

The above observations are inline with the present results. Comparison of the cross sections of the oxidised samples reveals that at temperatures above 900 °C alloy B, which contains ZrC, is more readily oxidised than alloy A, which contains the Laves phase $(Fe,Al)_2Zr$ (Fig. 12). Also the pronounced zoning of the oxidised areas is observed for the present alloys (Figs. 13 and 15). That the initial formation of ZrO_2, by preferential oxidation of ZrC, may promote the formation Al_2O_3 would explain, why at 1100 and 1200 °C a massive ingress of oxidation into the sample takes place, which is not any longer limited to the phases richer in Zr than the matrix, but which markedly affects the otherwise much more oxidation resistant matrix (Fig. 12). It is noted that the presence of Zr in the alloys has an influence on the grain structure of Al_2O_3 in that columnar grains of Al_2O_3 are formed instead of equiaxed grains [2,12,14,16]. In case of the present alloys, comparable columnar grain structures of Al_2O_3 were observed around Zr-particles (Fig. 16).

Precipitates like Laves phases or carbides are frequently employed for strengthening Fe–Al-based alloys. The oxidation behav-

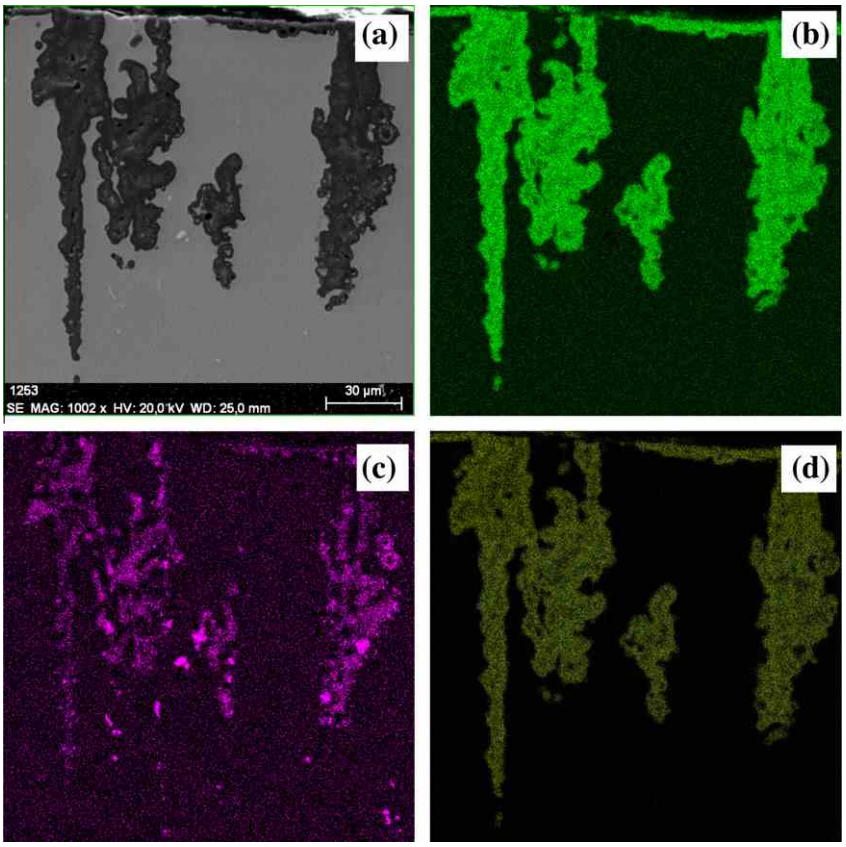

Fig. 14. SEM-SE micrograph of the cross section of alloy B after oxidation at 1000 °C for 1000 h (a) and mappings of elements: Al (b), Zr (c) and O (d) showing the distribution of Al_2O_3 and ZrO_2.

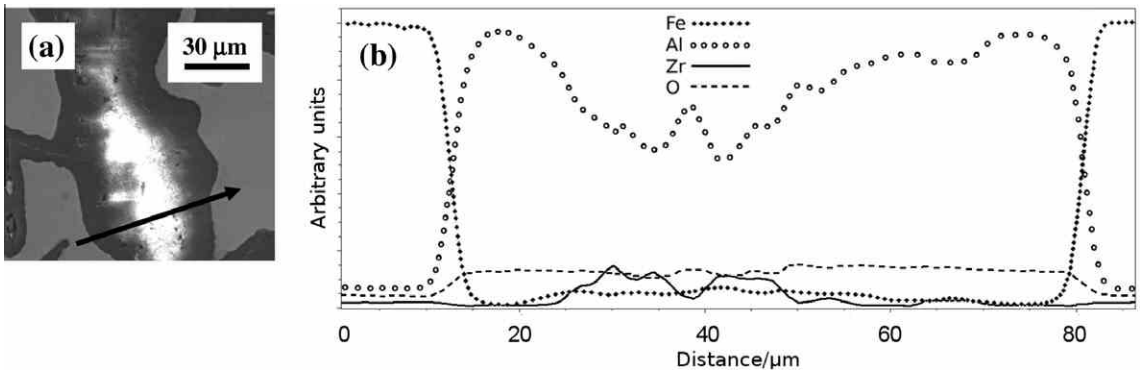

Fig. 15. SEM-SE micrograph of the cross section of alloy B after oxidation at 1200 °C for 1000 h (a); light phase: ZrO_2, dark: Al_2O_3, grey: Fe_3Al. The phases were identified through EDS line scans (b).

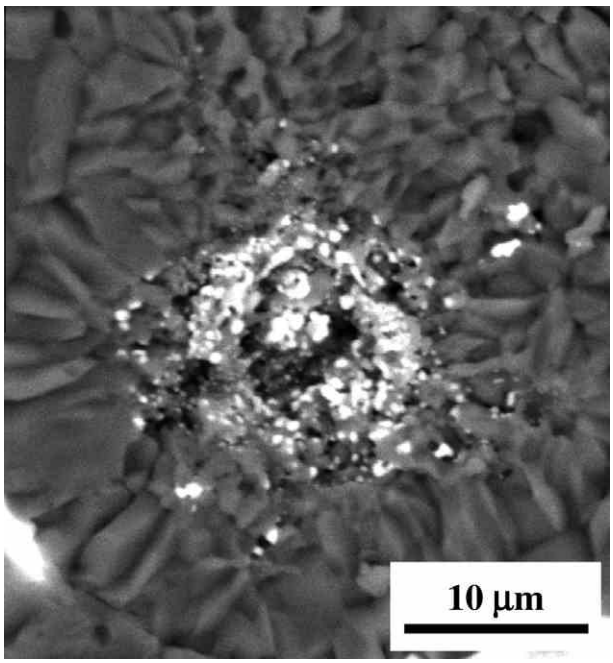

Fig. 16. SEM-BSE micrograph of the columnar grain microstructure of Al_2O_3 (grey) around the Zr-particles (white); the surface detail of alloy A oxidised at 1200 °C was observed at the metal/scale interface.

iour of the present alloys is therefore compared with other Fe–Al-based alloys designed for applications at high temperature. Recently, Janda et al. [36] reported the cyclic oxidation behaviour between upper 750–1050 °C and RT of a series of alloys including Fe–27Al–0.4Nb–0.19Zr (at.%). The alloy showed parabolic oxidation behaviour at 750 and 900 °C but spallation of the scales at 1050 °C. However, preferential oxidation of carbides and borides was already observed at 900 °C.

In Fig. 17 the squared mass gains versus exposure time for various iron aluminides at 900 °C in synthetic air are shown. It can be seen that the present alloys compare favourably to the other alloys in that they show lower mass gains.

In case of Fe–28Al–3Cr–0.02Ce and Fe–30Al–4Cr–2.7TiB_2 (at.%) thin and homogeneous oxide scales formed at 900 °C resulting in a parabolic growth of the scales [23]. In contrast, oxidation at 1100 °C resulted in a hyperbolic growth of the scales. Investigation of cross sections revealed marked intergranular oxidation in case of Fe–28Al–3Cr–0.02Ce.

A quite different oxidation behaviour was observed for Fe–Al–Ta alloys [21]. Under isothermal conditions they only showed parabolic oxidation behaviour between 600 and 800 °C. Above 800 °C scales cracked or spalled due to the formation of Laves phase precipitates at the sample/scale interface. On the other hand, isothermal oxidation tests on Fe–Al–Ti alloys with and without Laves phase precipitates as a strengthening phase revealed that the presence of a Laves phase itself a priori does not have a detrimental effect on the oxidation behaviour [22].

4. Summary and conclusions

The oxidation behaviour of two Fe–Al–Cr–Zr–C alloys designed for applications at high temperatures has been evaluated between 900 and 1200 °C. While both alloys showed a very good oxidation resistance at 900 °C, which compared favourably to those of other Fe_3Al-based alloys, they show increasing weight gains at higher temperatures due to ingress of the oxidation into the sample. While the alloy with $(Fe,Al)_2Zr$ Laves phase (alloy A) showed limited oxide protrusions at 1000 °C the alloy with zirconium carbide ZrC (alloy B) showed a marked ingress of oxidation already at this temperature, which led to a much higher weight gain and a linear oxidation behaviour. Above 1000 °C both alloys showed extensive oxide protrusions due to preferential attack of the strengthening precipitates but while for alloy A oxidation is limited to the Laves phase, oxidation in alloy B is not limited to the ZrC precipitates but extends into the matrix.

The oxidation behaviour of Fe–Al–Cr–(C) alloys with Zr and containing second phases such as carbides or Laves phase mainly along grain boundaries is compared to Fe–Al–Zr alloys with higher Al contents. The oxidation behaviour of the present alloys is less favourable as all other alloys do not show ingress of oxidation into the sample or only under cyclic conditions.

It may therefore be concluded that the present Fe_3Al-based Fe–Al–Cr–Zr–C alloys which have been prepared for application at high temperatures do have an excellent oxidation resistance up to 900–1000 °C. However, starting at 1000 °C the Zr-rich precipitates are preferentially oxidised, ZrC more readily than the Laves phase $(Fe,Al)_2Zr$.

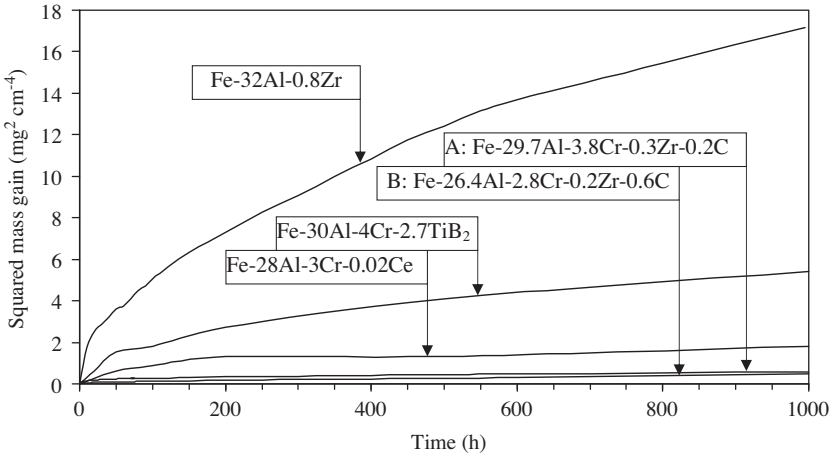

Fig. 17. Squared mass gain versus exposure time for various iron aluminides at 900 °C in synthetic air. Fe–28Al–3Cr–0.02Ce and Fe–30Al–4Cr–2.7TiB_2 (at.%): [35]; Fe–32Al–0.8Zr (at.%): [27].

Acknowledgements

The authors would like to thank Mr T. Schildheuer for help with oxidation testing and Mr G. Bialkowski for sample preparation. This research was supported by The Czech Science Foundation GACR (P 108/12/1452).

References

[1] C.G. McKamey, J.H. DeVan, P.F. Tortorelli, V.K.J. Sikka, A review of recent developments in Fe_3Al-based alloys, Mat. Res. 6 (1991) 1779–1805.
[2] P.F. Tortorelli, K. Natesan, Critical factors affecting the high-temperature corrosion performance of iron aluminides, Mat. Sci. Eng. A258 (1998) 115–125.
[3] R. Prescott, M.J. Graham, The oxidation of iron–aluminum alloys, Oxid. Met. 38 (1992) 73–87.
[4] I. Rommerskirchen, B. Eltester, H.J. Grabke, Oxidation of β-FeAl and Fe–Al alloys, Mat. Corros. 47 (1996) 646–649.
[5] A. Velon, I. Olefjord, Oxidation behavior of Ni_3Al and Fe_3Al: II early stage oxide growth, Oxid. Met. 56 (2001) 425–451.
[6] B. Pöter, F. Stein, R. Wirth, M. Spiegel, Early stages of protective oxide layer growth of binary iron aluminides, Z. Phys. Chem. 219 (2005) 1489–1503.
[7] P.F. Tortorelli, J.H. DeVan, Behavior of iron aluminides in oxidizing and oxidizing/sulfidizing environments, Mat. Sci. Eng. A153 (1992) 573–577.
[8] D.B. Lee, G.Y. Kim, G.J. Kim, The oxidation of Fe_3Al–(0%, 2%, 4%, 6%)Cr alloys at 1000 °C, Mat. Sci. Eng. A339 (2003) 109–114.
[9] J.H. DeVan, P.F. Tortorelli, Environmental effects on iron aluminides, Proc. 7th Annual Conf. on Fossil Energy Materials, Department of Energy DOE (1993) 277–288.
[10] K. Natesan, Corrosion performance of iron aluminides in mixed-oxidant environments, Mat. Sci. Eng. A258 (1998) 126–134.
[11] S. Chevalier, P. Juzon, G. Borchardt, A. Galerie, K. Przybylski, J.P. Larpin, High-temperature oxidation of Fe_3Al and Fe_3Al-Zr, Oxid. Met. 73 (2010) 43–64.
[12] B.A. Pint, Experimental observations in support of the dynamic-segregation theory to explain the reactive-element-effect, Oxid. Met. 45 (1996) 1–37.
[13] B.A. Pint, J.R. Regina, K. Prüßner, L.D. Chitwood, K.B. Alexander, P.F. Tortorelli, Effect of environment on the oxidation of ingot-processed iron aluminides, Intermetallics 9 (2001) 735–739.
[14] B.A. Pint, P.F. Tortorelli, I.G. Wright, The oxidation behavior of ODS iron aluminides, Mat. Corros. 47 (1996) 663–674.
[15] J. Ni, X.J. Wan, Q. Wang, X.Y. Cheng, W.M. Liu, X.Y. Zhang, The cyclic oxidation behaviors of Fe_3(Al, Cr, Zr) and Fe_3(Al, Cr, Nb) intermetallic compound at high temperature, J. Shanghai Univ. 1 (1997) 79–82.
[16] B.A. Pint, P.F. Tortorelli, I.G. Wright, Long-term oxidation performance of ingot produced Fe_3Al alloys, Mater. High Temp. 16 (1999) 1–13.
[17] B.A. Pint, K.L. More, P.F. Tortorelli, W.D. Porter, I.G. Wright, Optimizing the imperfect oxidation performance of iron aluminides, Mater. Sci. Forum 369–372 (2001) 411–418.
[18] P. Kratochvil, P. Malek, M. Cieslar, P. Hanus, J. Hakl, T. Vlasak, High-temperature mechanical properties of Zr alloyed Fe_3Al-type iron aluminide, Intermetallics 15 (2007) 333–337.
[19] K. Przybylski, S. Chevalier, P. Juzon, Effect of Zr on the oxidation properties of Fe_3Al intermetallic compound, J. Chin. Soc. Corros. Prot. 29 (2009) 286–292.
[20] F. Stein, M. Palm, G. Sauthoff, Mechanical properties and oxidation behaviour of two-phase iron aluminium alloys with Zr(Fe, Al)2 Laves phase or Zr(Fe, Al)12 τ_1 phase, Intermetallics 13 (2005) 1275–1285.
[21] A. Hotař, M. Palm, Oxidation resistance of Fe–25Al–2Ta (at.%) in air, Intermetallics 18 (2010) 1390–1395.
[22] M. Palm, G. Sauthoff, Deformation behaviour and oxidation resistance of single-phase and two-phase $L2_1$-ordered Fe–Al–Ti alloys, Intermetallics 12 (2004) 1345–1359.
[23] A. Hotař, P. Kratochvíl, J. Cizner, Oxidation resistance of Fe28Al3Cr0.02Ce and Fe30Al4Cr2.7TiB_2 (at.%) in air, Proc. 19th Int. Conf. on Metallurgy and Materials, METAL 2010, (2010), paper no. 127, online available at http://www.nanocon.cz/data/metal2010/sbornik/lists/papers/337.pdf.
[24] B. Pöter, F. Stein, M. Spiegel, reported in S. Milenkovic, M. Palm, Microstructure and mechanical properties of directionally solidified Fe–Al–Nb eutectic, Intermetallics 16 (2008) 1212-18.
[25] K. Natesan, P.F. Tortorelli, High-temperature corrosion and applications of nickel and iron aluminides in coal-conversion power systems, in: S.C. Deevi, P.J. Maziasz, V.K. Sikka, R.W. Cahn (Eds.), Int. Symp. on Nickel and Iron aluminides: Processing, Properties, and Applications, ASM, International, 1997, pp. 265.
[26] T. Mitsuhashi, M. Ichihara, U. Tatsuke, Characterization and stabilization of metastable ZrO2, J. Am. Ceram. Soc. 57 (1974) 97–104.
[27] R.C. Garvie, Stabilization of the tetragonal structure in zirconia microcrystals, J. Phys. Chem. 82 (1978) 218–224.
[28] J.R. Kelly, I. Denry, Stabilized zirconia as a structural ceramic: an overview, Dental Mat. 24 (2008) 289–298.
[29] J. Chevalier, L. Gremillard, The tetragonal-monoclinic transformation in zirconia: Lessons learned and future trends, J. Am. Ceram. Soc. 92 (2009) 1901–1920.
[30] K.B. Alexander, K. Prüssner, P.Y. Hou, P.F. Tortorelli, Microstructure of alumina scales and coatings on zirconium-containing iron aluminide alloys, in: J.A. Little, S.B. Newcomb (Eds.), Microscopy of Oxidation 3, Maney, 1997, p. 246.
[31] C.H. Xu, W. Gao, H. Gong, Oxidation behaviour of FeAl Intermetallics. The effects of Y and/or Zr on isothermal oxidation kinetics, Intermetallics 8 (2000) 769–779.
[32] R.W. Bartlett, M.E. Wadsworth, I.B. Cutler, The oxidation kinetics of zirconium carbide, Trans. Met. Soc. AIME 227 (1963) 467–472.
[33] R.F. Voitich, E.A. Pugach, High-temperature oxidation of ZrC and HfC, Powder Met. Met. Ceram. 12 (1973) 916–922.
[34] S. Shimada, A thermoanalytical study on the oxidation of ZrC and HfC powders with formation of carbon, Solid State Ionics 149 (2002) 319–326.
[35] S. Nourbakhsh, O. Sahin, W.H. Rhee, H. Margolin, A structural study of oxidation in a zirconia-toughened alumina fibre-reinforced Fe_3Al composite, Metall. Trans. A24 (1993) 435–443.
[36] D. Janda, M. Galetz, M. Schütze, M. Heilmaier, The effect of micro-alloying with Zr and Nb on the oxidation behavior of Fe_3Al and FeAl alloys, in: Proc. Sixth Discussion Meeting on the Development of Innovative Iron Aluminium Alloys FEAL2011, (2011) 133–136.

Corrosion Science 100 (2015) 147–157

Contents lists available at ScienceDirect

Corrosion Science

journal homepage: www.elsevier.com/locate/corsci

The effect of Zr on high-temperature oxidation behaviour of Fe_3Al-based alloys

A. Hotař[a,*], P. Kejzlar[a], M. Palm[b], J. Mlnařík[c]

[a] Technical University of Liberec, Faculty of Engineering, Department of Materials Science, Studentská 2, CZ 46117 Liberec, Czech Republic
[b] Max-Planck-Institut für Eisenforschung GmbH, Max-Planck-Strasse 1, d-40237 Düsseldorf, Germany
[c] SVÚM a.s – Research and Testing Center, Corrosion Laboratory, Tovární 2053, CZ 25088 Čelákovice, Czech Republic

ARTICLE INFO

Article history:
Received 19 February 2015
Received in revised form 1 July 2015
Accepted 28 July 2015
Available online 30 July 2015

Keywords:
A. Intermetallics (based on Fe_3Al)
B. EPMA
B. SEM
B. XRD
C. Oxidation
C. Kinetic parameters

ABSTRACT

The cyclic oxidation of Fe–30Al–*x*Zr and Fe–25Al–*x*Zr (*x* = 0.3–5.2 at.%) has been investigated at 900 °C and 1100 °C in laboratory air. Scales, oxide protrusions and structural changes were analysed by LOM, XRD, SEM and EDS. The oxidation rate increases with increasing Zr content as well as with increasing temperature. Spallation of thin scales formed at 900 °C on the Zr lean alloys is observed, while thicker scales formed on Zr-rich alloys or at 1100 °C show cracking but do not spall. At both temperatures the scales on all alloys consist of Al_2O_3, Fe_2O_3 and ZrO_2 and oxide protrusions penetrate into the samples. These protrusions form by preferential oxidation of Zr rich phases.

1. Introduction

Fe_3Al-type iron aluminides are known for their excellent oxidation and corrosion resistance and they do have a low density compared to other Fe-based materials [1–3]. However, limited ductility at ambient temperature is a concern and sufficient high-temperature strength and creep properties for structural applications have to be attained through alloying [4–8].

By alloying Fe–Al with Zr, the oxidation behaviour and the strength at high temperatures both can be improved and therefore ternary Fe–Al–Zr alloys as well as higher order alloys have been extensively investigated, e.g. Refs. [9–19]. Fe–Al alloys with Al contents exceeding about 16–19.5 at.% Al owe their good oxidation and corrosion resistance to the fact that they form adherent α-Al_2O_3 scales in oxidising atmospheres [20,21]. However, in the initial stages of oxidation metastable γ- and θ-Al_2O_3 form, which are porous and less adherent and therefore less protective and which persist the longer the lower the temperature is [22].

It has been shown that doping Fe–Al with up to 0.1 at.% Zr accelerates the formation of stable α-Al_2O_3 [19,23] and that also at high temperatures (1000–1200 °C) oxidation behaviour improves through better adherence of α-Al_2O_3 scales [14,17,24,25]. In the case of alloying with 0.1–1.0 at.% Zr, only small mass gains were observed at 900 °C, but at temperatures above 1000 °C oxidation rates increased due to significant ingress of oxides into the alloys [15,19,26]. E.g. investigation of Fe–Al–Cr–Zr–C alloys revealed preferential oxidation of the Zr-rich phases such as Laves phase $Zr(Fe,Al)_2$ and ZrC, which were located mainly along grain boundaries [26]. Whether higher levels of Zr above 1.0 at.% may have a detrimental effect on the corrosion resistance of iron aluminides is not quite clear. Increased mass gains were observed for Fe–20Al–2.5Zr during isothermal oxidation at 900 °C [15]. As the Al content of this alloy is close to the lower limit for the formation of protective Al_2O_3 scales in binary Fe–Al [21] it could also be therefore that this alloy showed an inferior oxidation behaviour. Fe–39Al–5Zr and Fe–47Al–5Zr showed massive growth with large linear weight gains during cyclic oxidation at 1200 °C [27], though this temperature may already be a little bit high for application of iron aluminides. Also less protective mixed $Al_2O_3 + ZrO_2$ oxide scales formed on Fe–Al–Cr–Zr and Fe–Al–Cr–Zr–C alloys, where the volume fraction of ZrO_2 increased with increasing temperature [14,17,26].

Alloying Fe–Al with Zr for strengthening at high temperatures is well feasible. Because the solid solubility of Zr in Fe–Al is quite limited [28], already small additions of Zr cause formation of strengthening Zr-rich particles such as Laves phase $Zr(Fe,Al)_2$

* Corresponding author. Fax: +420 485 353 631.
E-mail address: adam.hotar@tul.cz (A. Hotař).

http://dx.doi.org/10.1016/j.corsci.2015.07.016
0010-938X/

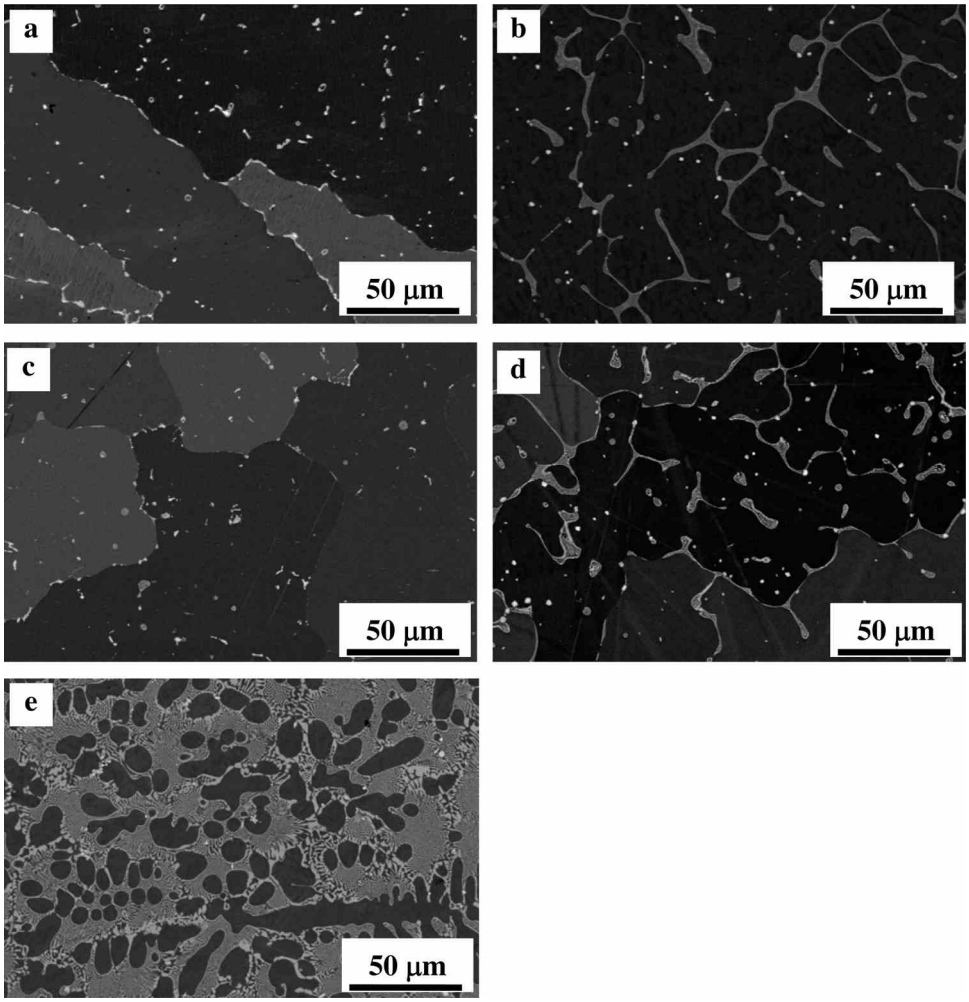

Fig. 1. SEM micrographs (back-scatter electron (BSE) contrast) of the as-cast microstructures of alloys Fe–25Al–*x*Zr (a) 25–0; (b) 25–1 and Fe–30Al–*x*Zr (c) 30–0; (d) 30–1; (e) 30–5. Dark phase: Fe–Al matrix; grey: eutectic Laves phase + Fe–Al; small bright particles are ZrC.

and τ_1 phase $Zr(Fe,Al)_{12}$ or ZrC in C containing alloys [29]. Therefore, alloying with higher amounts of Zr is desirable for improving strength at high temperatures but it has to be checked whether this deteriorates the oxidation behaviour [15].

In view of the above, Fe–25Al–*x*Zr ($x = 0.5$, 1, 5; all compositions are in at.%) and Fe–30Al–*x*Zr ($x = 0.5$, 1) alloys were prepared and cyclic oxidation tests at 900 °C and 1100 °C were performed. Though a couple of investigations on cyclic oxidation of Fe–Al–Zr(-X-Y) alloys have been performed, these were mostly confined to a single alloy and Al and Zr contents of the investigated alloys varied over a wide range of compositions [17,19,23,25,27,30,31]. The aim of the present paper is to evaluate the effect of different amounts of Zr and Al on the apparent oxidation rates and microstructure of Fe_3Al-based alloys at cyclic oxidation and to compare it to previous results on cyclic oxidation of Fe_3Al based alloys.

2. Experimental

Alloys were produced by a vacuum induction melting. Dimensions of the ingots were approximately $20 \times 40 \times 150$ mm. The chemical compositions of the investigated alloys are given in Table 1. From the raw metals used for the preparation of the alloys the following technical impurities result: 0.1 at.% Cr, 0.01 at.% B, 0.1 at.% Mn, 0.06 at.% C.

For cyclic oxidation tests, cylinders of 19 mm height with a diameter of 7 mm were cut by electrical discharge machining (EDM). The surface of the cylinders was carefully ground to 1200 grid. Cyclic oxidation tests were performed at 900 and 1100 °C in laboratory air up to 500 h in a muffle furnace containing air inlets at the front and in the back. Samples were placed in an alumina crucible and the tests were performed with of heating and cooling rates of 10 °C/min. and 2 °C/min, respectively. Mass gains were measured by weighing the alumina crucible with the sample on an electronic laboratory balance with a precision of 10^{-4} g after 25, 50, 100, 200, 300, 400 and 500 h. The mass gain for each alloy was determined as an average of two specimens' weight gains. In this way any spalled oxides are collected and measured and therefore this set up is considered as the correct method to determine the total mass gain during cyclic oxidation [32]. Pint et al. [32] also observed that for times $\geq$ 500 h the cycle frequency has little effect on the results.

Characterisation of microstructures and scales has been performed by light optical microscopy (LOM) and scanning electron

Table 1
Designations and analysed chemical compositions of the investigated alloys.

Alloy designation	Al (at.%)	Zr (at.%)	Fe
25–0	25.7	0.3	Bal.
25–1	25.7	1.0	Bal.
30–0	29.3	0.4	Bal.
30–1	29.2	0.9	Bal.
30–5	30.1	5.2	Bal.

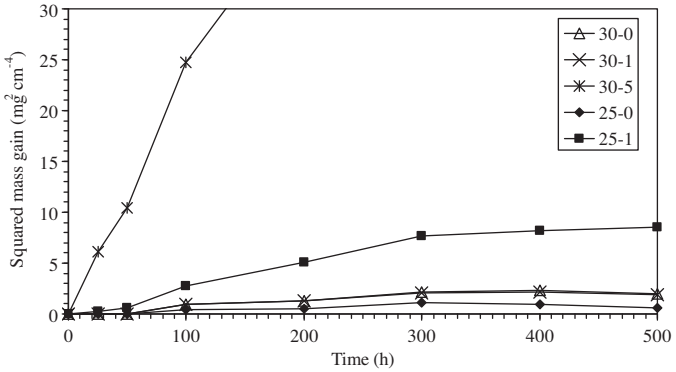

Fig. 2. Squared mass gain as a function of time for cyclic oxidation of Fe–Al–Zr alloys in laboratory air at 900 °C.

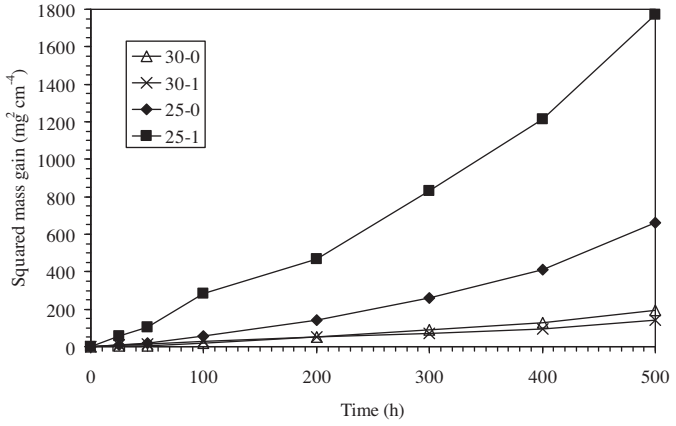

Fig. 3. Squared mass gain as a function of time for cyclic oxidation of Fe–Al–Zr alloys in laboratory air at 1100 °C.

microscopy (SEM). SEM was carried out using a Zeiss Ultra Plus equipped with energy-dispersive spectrometry (EDS; Oxford X-MAX 20 mm^2). The oxide scales were characterised by EDS and by X-ray diffraction (XRD) using a Seifert XRD 7 diffractometer with Bragg–Brentano geometry employing Cu Kα radiation.

3. Result and discussion

The alloys were investigated in the as-cast state and with increasing Zr content their microstructures can be divided into three groups [33]. The alloys 25–0 and 30–0 consist of a Fe–Al matrix with precipitates of the hexagonal C14 Laves phase $Zr(Fe,Al)_2$ at the grain boundaries (Fig. 1a,c). By increasing the Zr content the grains of the Fe–Al matrix are surrounded by a fine lamellar eutectic of Fe–Al and Laves phase (Fig. 1b,d). The volume fraction of the eutectic increases with increasing Zr content and in alloy 30–5 islands of primary Fe–Al are embedded within the eutectic (Fig. 1e). In all alloys a few small cubic particles of ZrC are observed, which formed because of the high affinity of Zr to carbon [34], which was present as an impurity in the raw iron used for casting. The changes in the microstructures after 500 h of oxidation at both temperatures are identical to changes caused by annealing at 1000 °C for 200 h [33]. The Laves phase in the eutectic coarsens and partially transforms from hexagonal C14 to cubic C15 structure. In the alloys containing 30 at.% Al the phase τ_1 $Zr(Fe,Al)_{12}$ formed in addition. The as-cast microstructures of the Fe–Al–Zr alloys as well as changes in the microstructure after annealing at 1000 °C for 200 h are described in detail in Ref. [33].

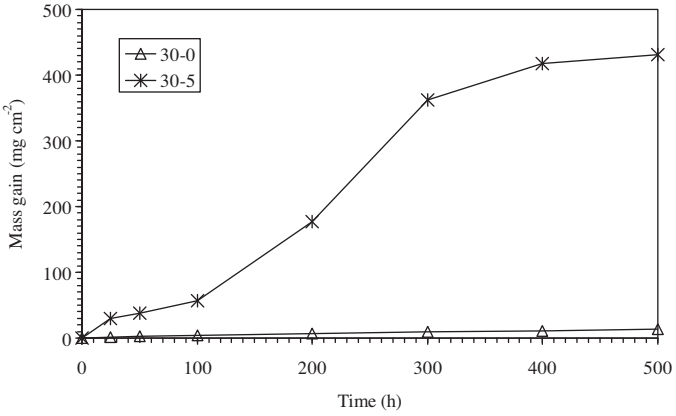

Fig. 4. Total mass gain as a function of time for 30–5 and 30–0 after cyclic oxidation at 1100 °C in laboratory air.

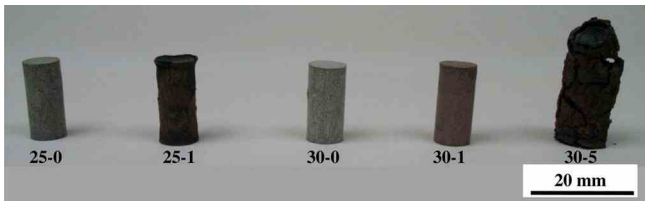

Fig. 5. Fe–Al–Zr samples after cyclic oxidation in laboratory air at 1100 °C.

Figs. 2–4 show the mass gain during cyclic oxidation in laboratory air at 900 °C and 1100 °C. Squared mass gain values at 900 °C (Fig. 2) almost show parabolic behaviour except for 30–5 alloy, which shows a linear increase. The mass gains of the other alloys increases up to 300 h, then tends to flatten and no significant mass changes are evident. In contrast, all alloys show a linear or hyperbolic growth of the scales at 1100 °C (Figs. 3, 4). At both temperatures for alloys with the same Al content mass gains increase with increasing Zr content. In case of the alloy with the highest Zr content (alloy 30–5) even disintegration due to extensive ingress of the oxidation is observed after cyclic oxidation at 1100 °C (Figs. 4 and 5). Fig. 5 also reveals that alloy 25–1 shows a pronounced scale formation after cyclic oxidation at 1100 °C.

For comparison of the oxidation behaviour of the investigated alloys, "apparent" parabolic rate constants were determined. The prerequisite for the evaluation of parabolic rate constants in strict sense is that dense adherent oxide scales of constant thickness form on the metal surface. For the present alloys this is not the case as will be shown later. However, in order to compare the present results with data published previously, in those cases where the squared mass gains show a more or less parabolic behaviour with time, parabolic rate constants (k_p) have been calculated from the

Table 2
Apparent parabolic rate constants k_p of Fe–Al– Zr alloys after cyclic oxidation in air at 900 °C. For comparison data for isothermal oxidation (*) of Fe–Al(-Zr-X) alloys at 900 °C are shown as well.

Alloy (in at.%)	k_p (g^2 cm^{-4} s^{-1})	Reference
25–0 (Fe–25.7Al–0.3Zr)	2.8×10^{-14}	This work
25–1 (Fe–25.7Al–1.0Zr)	3.1×10^{-12}	This work
30–0 (Fe–29.3Al–0.4Zr)	6.4×10^{-13}	This work
30–1 (Fe–29.2Al–0.9Zr)	5.8×10^{-13}	This work
*Fe–25Al	7.3×10^{-15}	[37]
*Fe–25.7Al	7.5×10^{-14}	[38]
*Fe–30Al	1.1×10^{-14}	[37]
*Fe–20Al–0.1Zr	9×10^{-14}	[15]
*Fe–20Al–2.5Zr	2×10^{-12}	[15]
*Fe–32Al–0.8Zr	4×10^{-13}	[15]

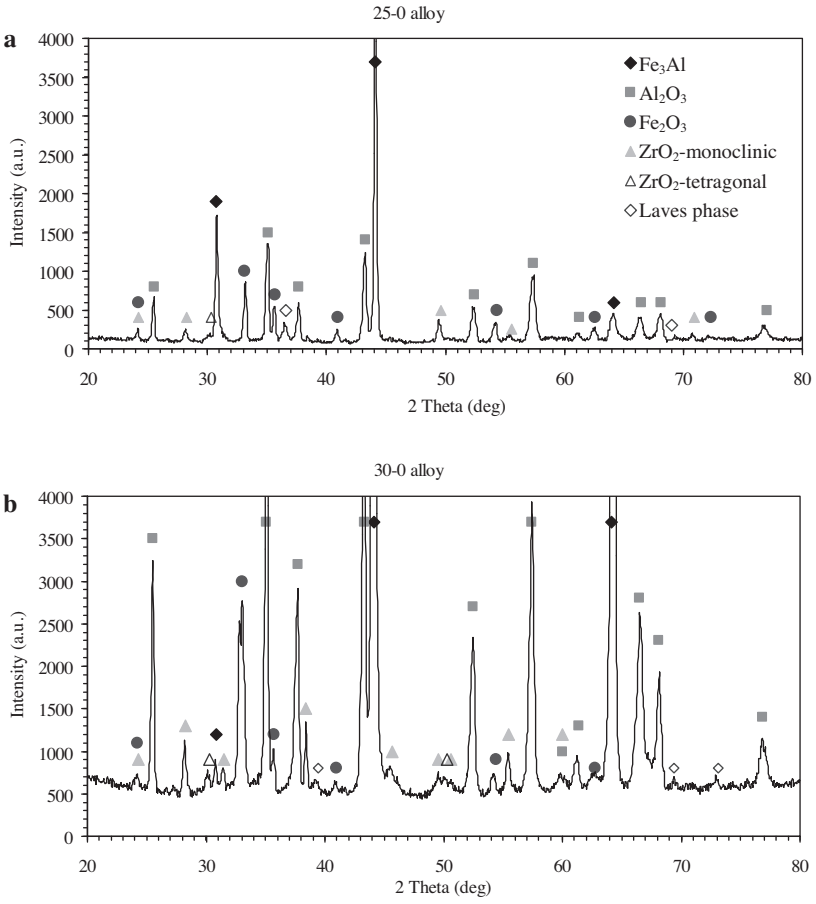

Fig. 6. XRD patterns of the oxidised surface of alloys 25–0 (a) and 30–0 (b) after cyclic oxidation at 900 °C/500 h.

Table 3
Oxides detected by XRD and EDS in the scales after cyclic oxidation at 900 °C and 1100 °C.

Alloy	900 °C	1100 °C
25–0 (Fe–25.7Al–0.3Zr)	Al_2O_3, Fe_2O_3, few ZrO_2	Al_2O_3, few Fe_2O_3, few ZrO_2
25–1 (Fe–25.7Al–1.0Zr)	Al_2O_3, Fe_2O_3, few ZrO_2	Al_2O_3, few Fe_2O_3, few ZrO_2
30–0 (Fe–29.3Al–0.4Zr)	Al_2O_3, Fe_2O_3, few ZrO_2	Al_2O_3, few ZrO_2
30–1 (Fe–29.2Al–0.9Zr)	Al_2O_3, Fe_2O_3, ZrO_2	Al_2O_3, few Fe_2O_3, few ZrO_2
30–5 (Fe–30.1Al–5.2Zr)	Al_2O_3, Fe_2O_3, ZrO_2	Sample disintegrated—not measured

weight gain per unit area $\Delta m/A$ (mg/cm^2) and time t (s) by the following relation:

$$\left(\frac{\Delta m}{A}\right)^2 = k_p t \quad (1)$$

As the scales on the present alloys actually do not show a parabolic growth in strict sense, the rate constants are designated as "apparent".

Because all alloys showed linear or hyperbolic mass gains at 1100 °C, apparent parabolic rate constants are only evaluated for 900 °C with the exception of alloy 30–5 (Table 2). For the evaluation of k_p, only the range above 200 h has been considered to exclude metastable phase growth in the initial stages of oxidation of Fe–Al alloys, which is observed up to 100–150 h at 900 °C [35,36]. In Table 2 the apparent parabolic rate constants of the present alloys are summarised and k_p values for isothermal oxidation at 900 °C of alloys of similar compositions [15] and of binary alloys of the same Al content [37,38] are given for comparison. k_p for the present alloys increases markedly with increasing Zr content, as has been observed in the case of isothermally oxidised Fe–Al–Zr alloys [15]. Also for comparable Zr contents, apparent parabolic rate constants for cyclic and isothermal oxidation match each other. This indicates that similar oxides scales formed under both conditions. Moreover, for alloy 25–0 with 0.3 at.% Zr k_p matches that of binary Fe–25Al isothermally oxidised at 900 °C, showing that this alloy has an excellent oxidation behaviour under cyclic oxidation conditions up to this temperature. However, if the Zr content is increased from 0.3 to 1 at.% in alloy 25–1 k_p already increases by two orders of magnitude. Finally, in case of Fe–Al–Zr–Nb–C–B alloys a negative effect on cyclic oxidation by increasing the Al content has been reported [19], which is not observed for the present alloys.

Oxide scales formed at 900 °C and 1100 °C were analysed in detail by XRD and EDS. The results of the XRD and EDS analyses are summarised in Table 3. Scales after cyclic oxidation at 900 °C consist of Al_2O_3, Fe_2O_3 and ZrO_2 and the volume fractions of these oxides are dependent on the Zr content of the alloys. In case of alloys with the lowest Zr content – 25–0 and 30–0 – the scales consist predominately of Al_2O_3, Fe_2O_3 and minor amounts ZrO_2 (Fig. 6, Table 4). For the alloys with higher Zr contents, the amount of Al_2O_3 decreases while the fractions of Fe_2O_3 and ZrO_2 increase (Fig. 7, Table 4). In case of cyclic oxidation at 1100 °C, the same trend is observed (Tables 3 and 4; Figs. 8 and 9) in that for alloys of the

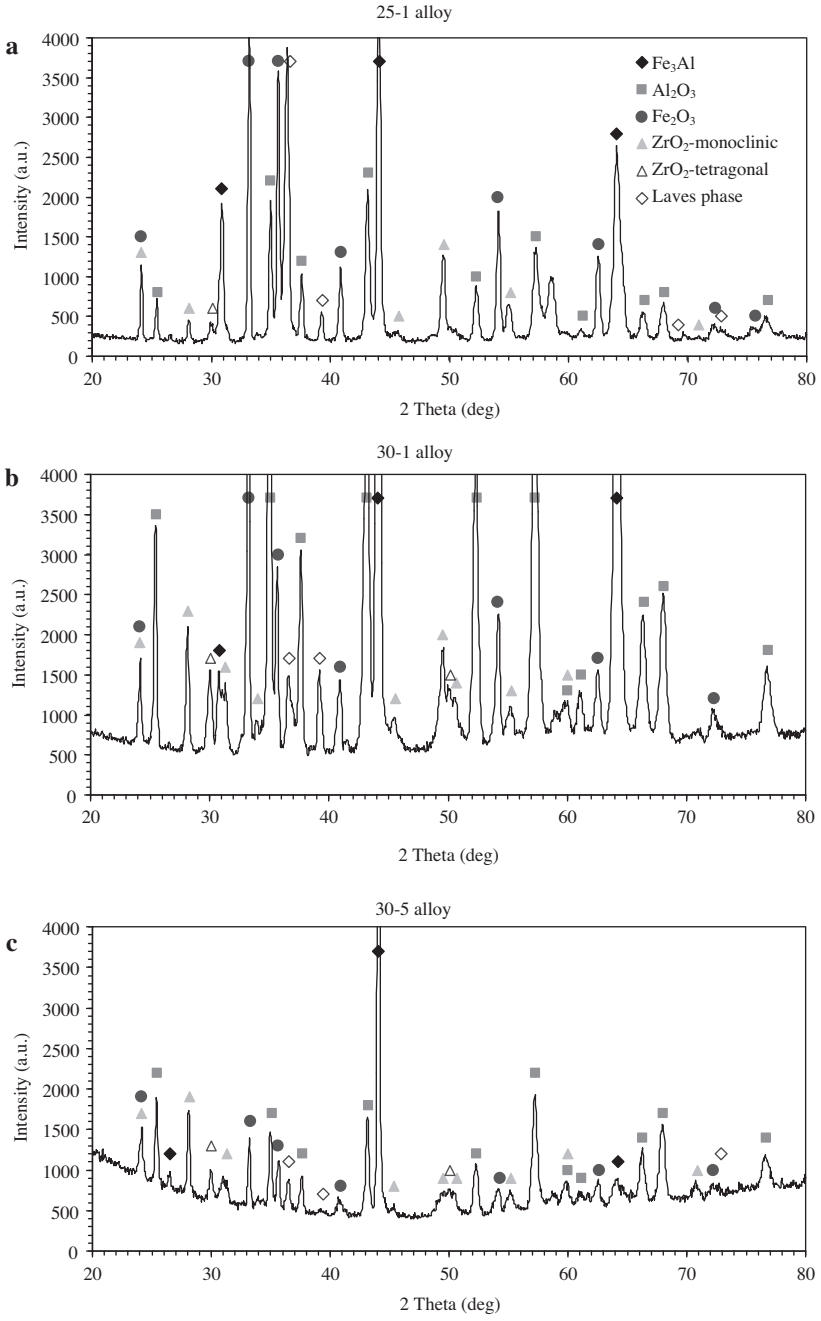

Fig. 7. XRD patterns of the oxidised surface of alloys 25–1 (a), 30-1 (b) and 30–5 (c) after cyclic oxidation at 900 °C/500 h.

Table 4
Composition of the surface scales determined by the EDS analysis at 10 kV after oxidation at 1100 °C for 500 h.

Alloy	at.% Fe	at.% Al	at.% Zr	at.% O
25–0	2.6	37.0	0.77	59.6
25–1	7.1	36.0	1.28	55.6
30–0	1.32	38.7	0.88	59.1
30–1	3.8	37.2	1.43	57.6
30–5	9.4	29.5	2.46	58.6

same Al content an increase of Zr promotes formation of ZrO_2 and Fe_2O_3 and decreases the amount of Al_2O_3. However, for all alloys the fraction of Al_2O_3 is higher at 1100 °C compared to that at 900 °C (Table 3).

Above results are supported and can be explained by studying the cross sections. Figs. 10 and 11 exemplary show cross sections of alloys 30–5 and 25–1 after cyclic oxidation at 900 °C and 1100 °C, respectively. EDS analysis of the oxide scales (analysis area A in Figs. 10 and 11) confirms that both consist out of mixtures of Al_2O_3, Fe_2O_3 and ZrO_2, but that the fraction of Al_2O_3 is markedly higher after oxidation at 1100 °C. It is noted that detailed EDS analysis of the scales did not reveal any layering of the oxides but that in all cases they form a uniform mixture. Underneath the scale (analysis area B and C) the samples are, compared to the initial composition of the alloys, depleted in Al but enriched in Fe. The difference between area B and area C is in the Zr content, which is markedly lower in area B compared to the initial composition but higher in area C. The formation of the zones is apparently through formation of Al_2O_3, which causes outward diffusion of Al. Thereby the area underneath

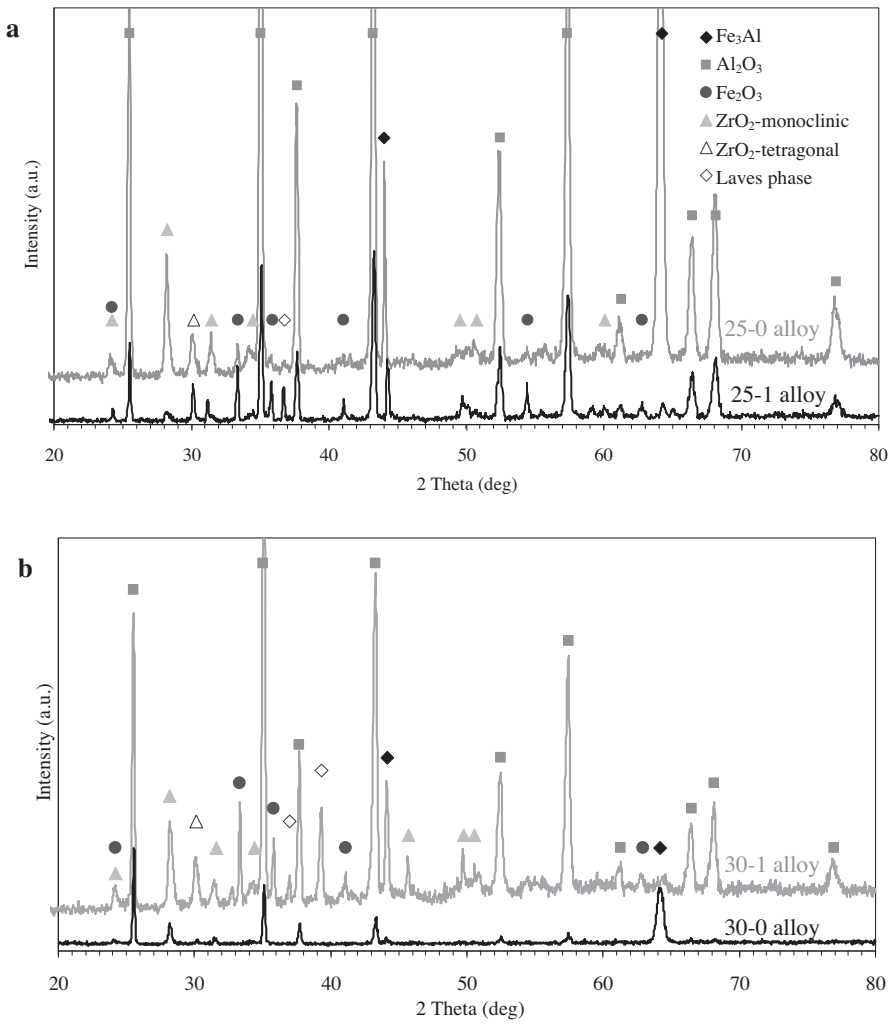

Fig. 8. XRD patterns of the oxidised surface of alloys 25–0 and 25–1 (a), 30–0 and 30–1 (b) after cyclic oxidation at 1100 °C/500 h.

the scale becomes depleted in Al. This zone is much broader at 1100 °C than at 900 °C (Figs. 10 and 11) due to the higher diffusivity at the higher temperature. This also explains why the fraction of Al_2O_3 is higher after cyclic oxidation at 1100 °C than at 900 °C. Though besides Al_2O_3, ZrO_2 and Fe_2O_3 form, the Al content in the alloy is still high enough for the predominant formation of Al_2O_3. However, the fraction of Al_2O_3 decreases with decreasing Al and/or increasing Zr content of the alloys (Tables 3 and 4). Formation of ZrO_2 also leads to a depletion in Zr underneath the scale (analysis area B), but because of the considerably lower diffusivity of Zr this zone is less extended than the Al depleted zone. The larger width of the Al depleted zone is also the reason for the increase of Zr in analysis area C (Figs. 10 and 11), where the Zr content is higher than in the initial composition of the alloys.

The substantially lower diffusivity of Zr could be one possibility for the flattening of the weight gain curves at 900 °C, which is observed for alloys 25–0, 25–1, 30–0 and 30–1 at 900 °C (Fig. 2). With increasing oxidation time the fraction of Al_2O_3 may increase due to the sluggish diffusion of Zr and the flattening of the weight gain curves above 300 h could be related to a higher fraction of well protective Al_2O_3 in the scales. However, the scales formed at 900 °C are too thin to detect any changes in the volume fractions of the oxides. The flattening of the weight gain curves (Fig. 2) resembles a parabolic oxidation behaviour, which actually is not the case for the present alloys as they show formation of mixed oxide scales and oxide protrusions (Fig. 12). In case of 25–0 even a slight decrease in weight above 400 h was observed and the reason therefore is currently not clear. It is noted, that the flattening/decrease of the weight gain after prolonged cyclic oxidation has in all cases been observed on both samples of the alloys tested at 900 °C. Further studies are necessary for understanding of the weight decrease of the 25–0 alloy.

The weight gain curve for alloy 30–5 oxidised at 1100 °C flatten off above 300 h (Fig. 4) can be explained by the rapid oxidation of the samples. The samples showed spallation of the scales after about 100 h and after 300 h almost the whole volume of the samples is composed of oxides and therefore the weight gain curve tends to flatten off.

Compared to isothermal oxidation of alloys containing about the same Al and Zr contents but small amounts of Cr and C [26], cyclic oxidation of alloys 25–0 and 30–0 yielded only slightly different results. In both cases predominant formation of Al_2O_3 in the temperature range 900–1100 °C is observed and the additional presence of a small amount of Fe_2O_3 after oxidation at 900 °C and of ZrO_2 after oxidation at 1100 °C. However, after isothermal oxidation no ZrO_2 was observed at 900 °C and in case of cyclic oxidation of alloy 25–0 few Fe_2O_3 is still observed after cyclic oxidation at 1100 °C which is not the case for isothermal oxidation [26]. These small differences may relate to the addition of Cr in the isothermally oxidised alloys, which should further enhance oxidation resistance.

The XRD patterns of the oxide scales also reveal the presence of two ZrO_2 polymorphs, the monoclinic and the tetragonal

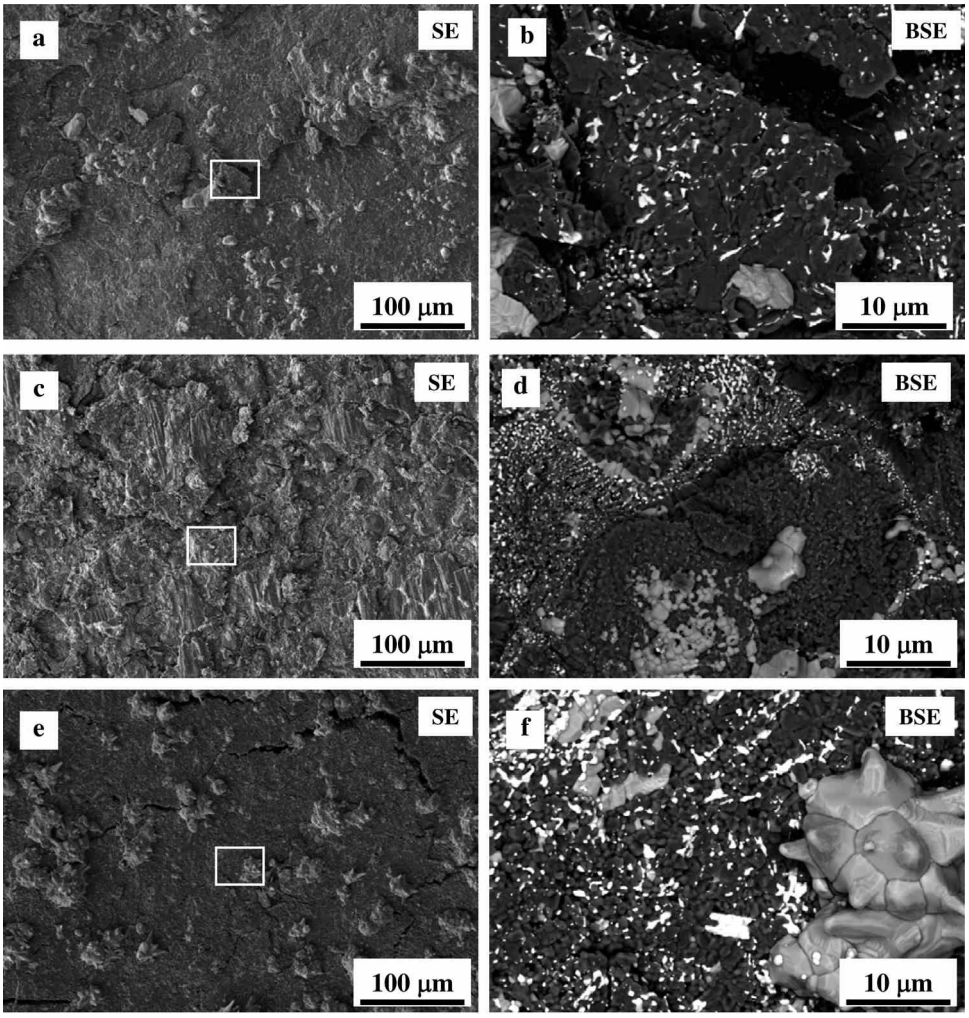

Fig. 9. SEM micrographs of the oxidised surfaces of alloys 25–1 (a,b), 30–1 (c,d) and 30–5 (e,f) after cyclic oxidation at 1100 °C/500 h. Areas marked in the SEM micrographs obtaind by secondary electron (SE) contrast (a,c,f) are shown in higher magnification by SEM BSE (b,d,e), revealing the composition of the oxides; dark grey: Al_2O_3, grey: iron oxides, white: ZrO_2.

(Figs. 6–8). The formation of tetragonal ZrO_2 below its transformation temperature of about 1170 °C has been observed within oxide scales of isothermally oxidised Fe–Al–Zr–Cr–C alloys before [26]. The metastable occurrence of tetragonal ZrO_2 has been explained by stabilisation through impurities, particle size or strain energies [39–42]. Inspection by SEM and EDS revealed that the oxide scales that formed during cyclic oxidation at 900 °C on alloys 25–0 and 30–0 spalled during thermal cycling (Fig. 13). Spallation is evident from "windows" in the oxide scale, which have sharp edges and corners and in which the underlying Fe–Al matrix is exposed (Fig. 13a,b). Fig. 13c shows that cracking occurs especially at the Fe–Al matrix/oxide interface, suggesting that they originate from thermal stresses caused by varying thermal expansion coefficients. In contrast, no such marked spallation is observed after cyclic oxidation at 900 °C for the alloys with higher Zr contents (Fig. 14), where specifically the scales on alloys 25–1 and 30–1 (Fig. 14a,b) show cracking but no spallation. From Fig. 14d it is apparent that these continuous oxide scales are thicker than oxide scales on 25–0 and 30–0 (Fig. 13c). Comparison of the cross sections in Figs. 13 c and 14 d shows that the thicker scales are more porous. These pores could lower the thermal stresses that build up during thermal cycling and therefore the thicker scales actually may not that readily spall although some cavities at the Fe–Al matrix/oxide interface are also visible in Fig. 14d. Also the oxides scales which formed at 1100 °C and which are even thicker than those formed at 900 °C do show cracks from thermal cycling but for none of the samples spallation of the scales is observed (Fig. 9).

Inspection of cross sections of the samples after cyclic oxidation at 900 °C also revealed marked ingress of the oxidation into all samples (Fig. 12). Comparison of the alloys with the same Al content shows, that ingress of oxidation increases with increasing Zr content. Comparison of the alloys with about the same Zr content shows, that the alloys with 25 at.% Al show a slightly more marked ingress of oxidation than their counterparts with about 30 at.% Al. For the alloys with the lowest Zr content (25–0 and 30–0) ingress of oxidation apparently follows the grain boundaries (Fig. 12a,c). As in these two alloys the grain boundaries in the initial state are covered by Laves phase (Fig. 1a,c), preferential oxidation of the Laves phase apparently facilitated the ingress. For the alloys with about 1 at.% Zr (25–1 and 30–1) oxide protrusions are much more pronounced (Fig. 12b,d) and penetrate deeper into the samples (Table 5). The initial microstructure of these two alloys showed Laves phase + Fe–Al eutectics along the Fe–Al grain boundaries (Fig. 1b,d) and these eutectics are apparently preferentially oxidised, causing a more severe ingress of the oxidation. It is noted, that the eutectics coagulated during long term cyclic oxidation at 900 °C. Therefore, now the microstructure consists of coarse Laves phase particles within the Fe–Al matrix. Presumably it is this change in the microstructure

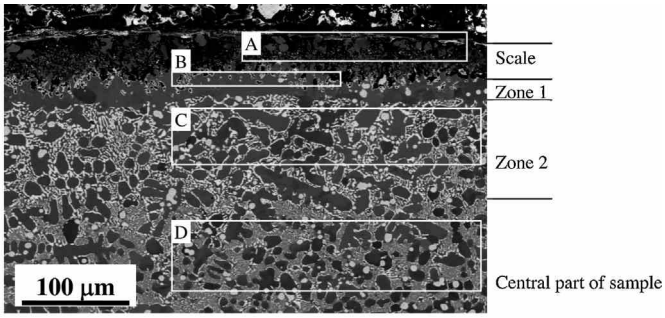

Chemical composition of zones (at.%)	O	Al	Fe	Zr
Scales – analysis area **A**	31.4	29.8	33.1	5.7
Zone 1 – analysis area **B**	6.8	25.8	63.4	4.0
Zone 2 – analysis area **C**		25.5	68.2	6.3
Central part of sample – analysis area **D**		30.4	63.5	6.1

Fig. 10. SEM–AsB micrograph of the cross section of alloy 30–5 after cyclic oxidation at 900 °C/500 h; Scale: Al_2O_3, ZrO_2, Fe_2O_3, particles of Fe–Al and Laves phase; Zone 1: Fe–Al, few Laves phase and τ_1 phase; Zone 2: Fe–Al matrix, Laves phase; Central part of sample: Fe–Al matrix, Laves phase, τ_1 phase.

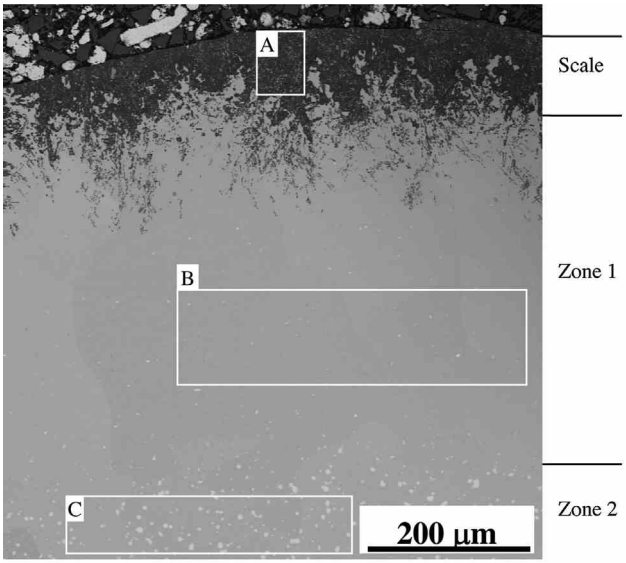

Chemical composition of zones (at.%)	O	Al	Fe	Zr
Scale – analysis area **A**	60.3	35.7	2.7	1.32
Zone 1 – analysis area **B**	0.0	18.1	81.8	0.13
Zone 2 – analysis area **C**	0.0	18.3	80.4	1.27
Central part of sample	0.0	20.5	78.4	1.20
Initial composition of sample	0.0	25.7	73.3	1.0

Fig. 11. SEM–AsB micrograph of the cross section of alloy 25–1 after cyclic oxidation at 1100 °C/500 h; Scale: particles of Fe–Al, Al_2O_3, ZrO_2, Fe_2O_3; Zone 1: Fe–Al, few Laves phase particles; Zone 2: Fe–Al matrix, Laves phase.

Table 5
Depth of ingress of oxidation into the alloys after cyclic oxidation in air at 900 °C/500 h.

Alloy	Depth of ingress (μm)
25–0 (Fe–25.7Al–0.3Zr)	44 ± 15
25–1 (Fe–25.7Al–1.0Zr)	89 ± 19
30–0 (Fe–29.3Al–0.4Zr)	36 ± 13
30–1 (Fe–29.2Al–0.9Zr)	63 ± 13
30–5 (Fe–30.1Al–5.2Zr)	106 ± 9

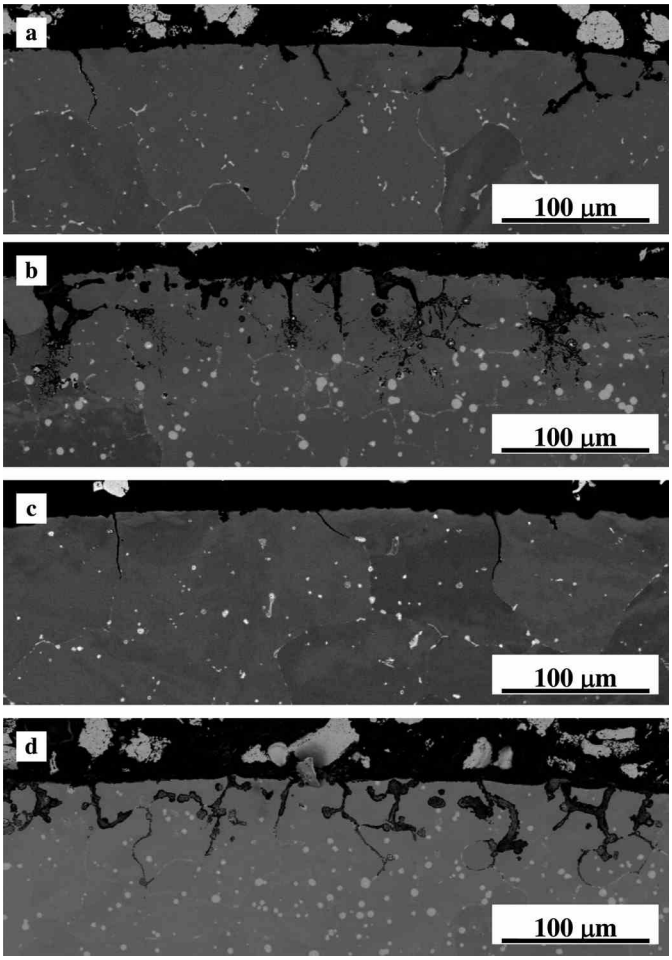

Fig. 12. SEM–AsB micrographs of cross sections showing oxide protrusions into the samples after cyclic oxidation at 900 °C/500 h; 25–0 (a), 25–1 (b), 30–0 (c) and 30–1 (d).

which causes the branching of the oxide protrusions after initially following the eutectic, which is well visible in Fig. 12b.

In contrast to the above, the cross section of alloy 30–5 after cyclic oxidation at 900 °C shows the presence of a thick scale, underneath which two zones can be identified, where the microstructure differs from that in the core of the sample (Fig. 10). Instead of single protrusions, oxidation advances quickly into the sample, which is evident in that the scale still contains a lot of metallic particles of Fe–Al and Laves phase (Fig. 10). Underneath the scale is a thin layer (zone 1, Fig. 10) which consists out of Fe–Al and which contains very few Zr-rich phases (Laves phase, τ_1 phase), because this zone is depleted in Al and Zr. In the second zone the Zr content is about the same as in the central part of the sample, only the Al content is still lower. Therefore, in accordance with the phase diagram [28], Laves phase particles are also observed in this zone (Fig. 10), but not the τ_1 phase. At a distance of approximately 150 μm from the surface the alloy has its original chemical composition and the microstructure consist of Laves phase + τ_1 + Fe–Al, as is expected for this composition after long-term annealing at 900 °C [33].

In case of cyclic oxidation at 1100 °C, the ingress of oxidation into all the samples is more pronounced than at 900 °C and considerably non-uniform (Figs. 15 and 11). Alloys 25–0, 30–0 and 30–1 show more extensive oxide protrusions (Fig. 15), which again formed through preferential attack of the eutectic areas. However, oxides protruding into alloy 25–1 are not limited to the eutectics, but the oxides also massively penetrate into the Fe–Al matrix (Fig. 11).

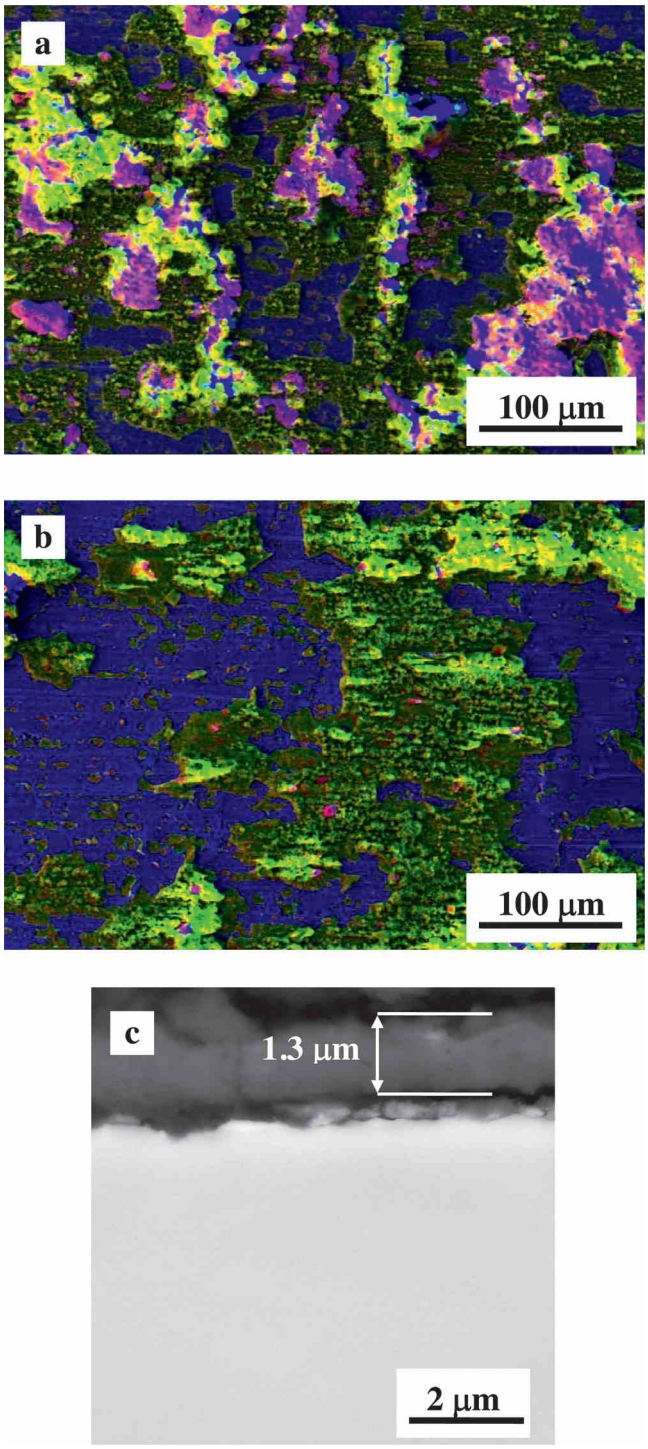

Fig. 13. Element mappings of the surface of alloys (a) 25–0 and (b) 30–0 after oxidation at 900 °C/500 h; green: alumina, violet and light blue: iron oxides, orange: ZrO_2, dark blue: matrix. (c) SEM–AsB (angle selective backscattered) of cross-section of alloy 25–0 after oxidation at 900 °C/500 h, where the beginning of spallation of the oxide scale is visible.

Comparison of the present results with data from literature is not straightforward possible, as no cyclic oxidation has been performed on ternary alloys with respective Al contents. Xu and Gao [31] performed cyclic oxidation between 1000 and 1200 °C on Fe–35.3Al–0.8Zr and Fe–36.4Al–0.3Zr. In accordance with the present results, they did not observe spallation of the scales but recorded high mass gains as well. Whether (substantial)

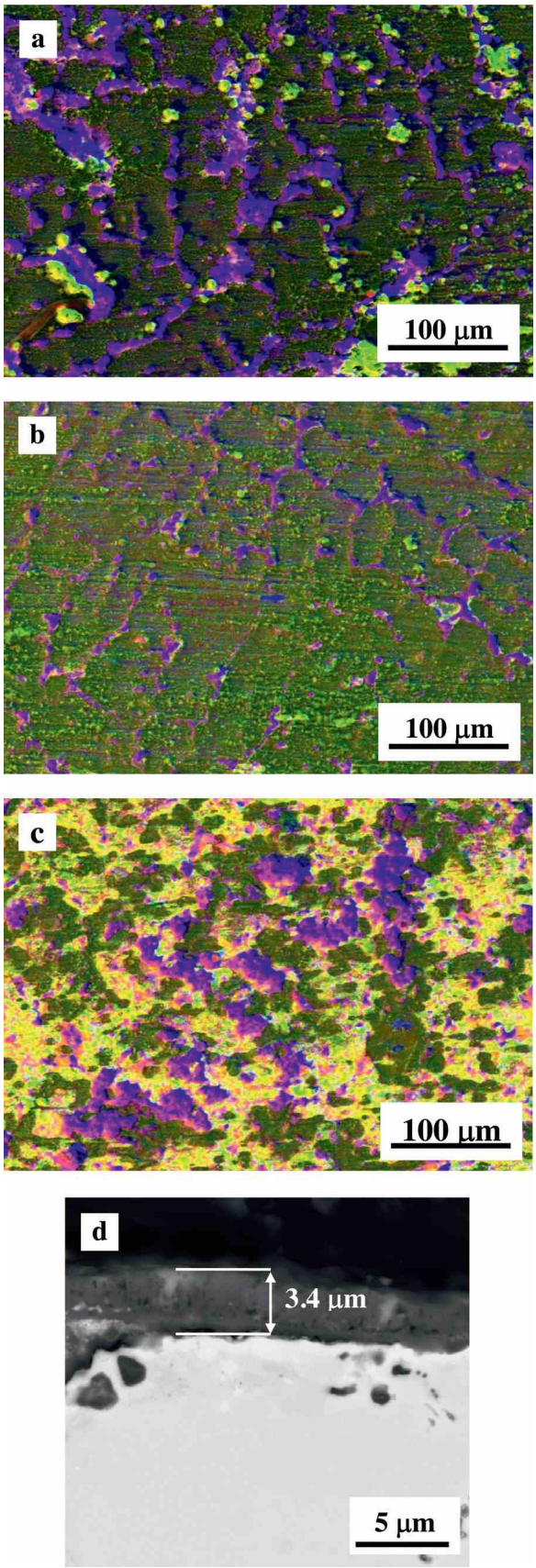

Fig. 14. Element mappings of the surface of alloys (a) 25–1, (b) 30–1 and (c) 30–5 after cyclic oxidation at 900 °C/500 h; green: alumina, violet and light blue: iron oxides, orange and yellow: ZrO_2; (d) SEM–AsB micrographs of cross section of 25–1.

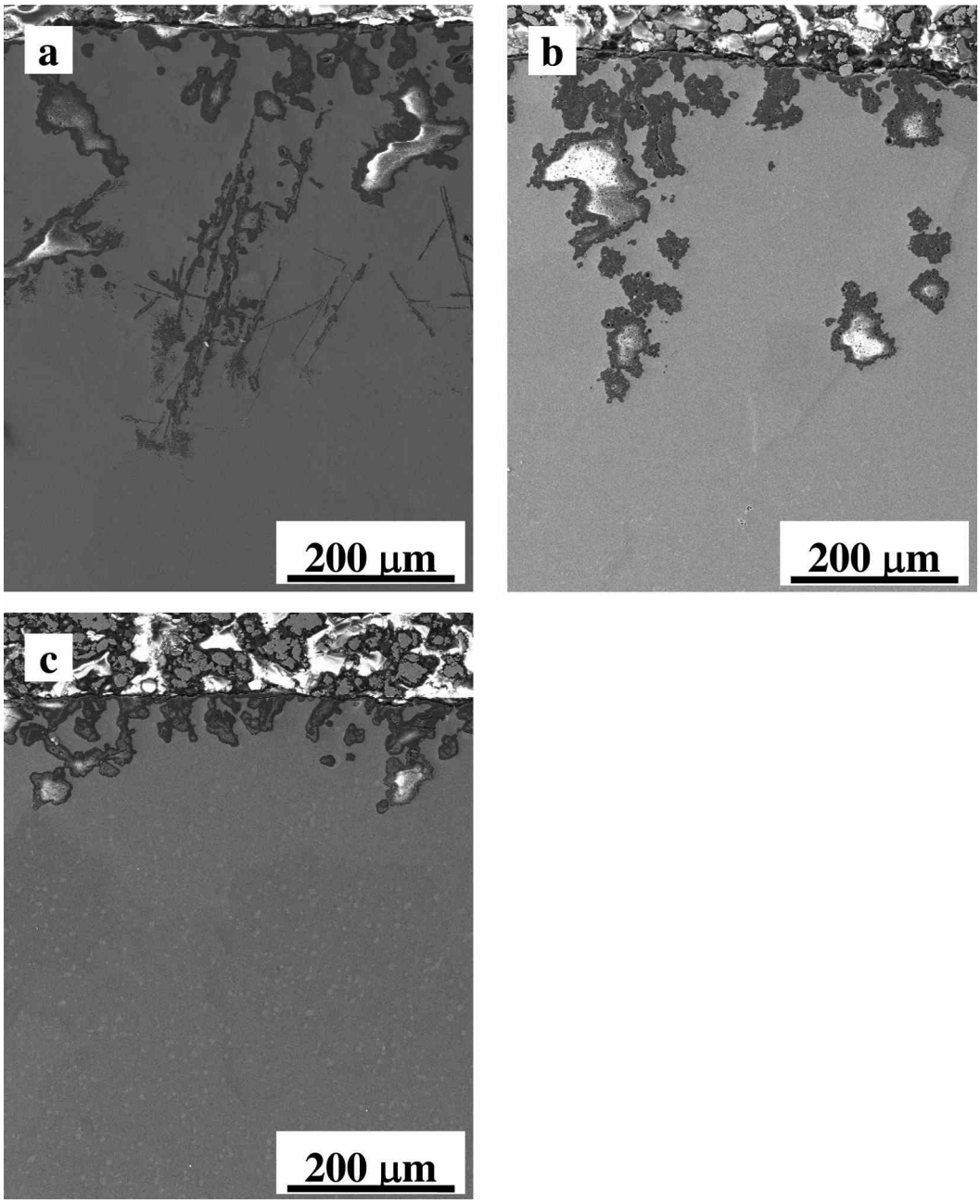

Fig. 15. SEM (mixed SE + BSE signal) micrographs of cross sections showing oxide protrusions into the samples after cyclic oxidation at 1100 °C/500 h; 25–0 (a), 30–0 (b) and 30–1 (c).

internal oxidation took place is not clear as no results from cross sections were reported. In case alloy Fe–36.4Al–0.04Zr–0.02C, cyclic testing for 100 h (1-hour cycles) at 900 °C revealed spallation of the scales and further oxidation of the uncovered material [43]. After cyclic oxidation tests on single-phase Fe–28Al–5Cr–0.05Zr [17] and Fe–28Al–5Cr–0.1Zr [25] no internal oxidation was observed in the temperature range 900–1200 °C and no spallation of the scales took place at 1000 °C [25] or was delayed at 1100 °C [17]. As the above alloys differ from the present ones in that they contain an additional amount of Cr and as they contain no precipitates of a second phase, it is not clear which of these two details may account for the differences to the present results. However, results from Janda et al. [19] hint to the latter. After cyclic oxidation at 900 °C they observed substantial internal oxidation in Fe–26.6–39Al–0.2Zr–0.4Nb–0.2C–0.07B alloys, which started at the interface between different precipitates and the Fe–Al matrix. For the alloy containing 26.6 at.% Al they evaluated the depth of the ingress after 550 h as 48 μm, which is about the same value observed for alloy 25–0 (Table 5). However, contrary to the present results they observed a markedly increasing depth of the ingress with increasing Al content of the alloys.

Comparison with isothermal experiments shows that for Fe–Al–Cr–Zr–C alloys, which show a microstructure comparable to the present alloys in that they also have Laves phase precipitates along grain boundaries, ingress of oxidation into the samples has only been observed at 1000 °C [26], while at 900 °C adherent scales formed. For a single-phase Fe–Al–Cr–Zr–C–B alloy, no ingress of oxidation was reported after isothermal oxidation between 900 and 1200 °C [44]. However, formation of Zr oxides at grain boundaries in single-phase Fe–36.4Al–0.3Zr has been reported,

though it is not clear whether this was observed at all temperatures for isothermal oxidation between 1000 and 1200 °C [45].

4. Conclusions

The effect of Zr content on the cyclic oxidation behaviour of Fe–25Al and Fe–30Al has been investigated at 900 °C and 1100 °C in laboratory air. For the investigated alloys no beneficial effect of alloying with 0.3–5.2 at.% Zr is observed. While protective Al_2O_3 scales form on binary Fe–Al alloys at these temperatures, mixed scales consisting of Al_2O_3, Fe_2O_3 and ZrO_2 formed on all Fe–Al–Zr alloys at both temperatures. Though alloys which contain 0.3 or 0.4 at.% Zr show formation of only thin scales at 900 °C, these scales readily spall during thermal cycling. In contrast, much thicker scales that formed at 1100 °C or on the alloy containing 5.2 at.% Zr oxidised at 900 °C showed cracks but did not spall. The thicker scales are more porous and probably these pores could lower the thermal stresses that build up during thermal cycling. Besides formation of scales, all alloys show ingress of oxidation along grain boundaries. Due to the low solid solubility of Zr in Fe–Al, Zr rich intermetallic phases form at comparable low Zr contents. In the present alloys they are mainly situated at the grain boundaries. Preferential oxidation of these phases leads to rapid internal oxidation of the alloys at 1100 °C.

Acknowledgements

This research was supported by The Czech Science Foundation GA ČR (GAP108/12/1452). The authors would like to thank Prof. P. Kratochvíl for valuable advice and to S. Daniš for XRD analyses. They also wish to thank to the Institute for Nanomaterials, Advanced Technologies and Innovation of the Technical University of Liberec for the use of their equipment for the study of the microstructures.

References

[1] C.G. McKamey, J.H. Devan, P.F. Tortorelli, V.K. Sikka, A review of recent developments in Fe_3Al-based alloys, J. Mater. Res. 6 (1991) 1779–1805.
[2] S.C. Deevi, V.K. Sikka, Nickel and iron aluminides: an overview on properties, processing, and applications, Intermetallics 4 (1996) 357–375.
[3] N.S. Stoloff, Iron aluminides: present status and future prospects, Mater. Sci. Eng. A 258 (1998) 1–14.
[4] C.G. McKamey, P.J. Maziasz, G.M. Goodwin, T. Zacharia, Effects of alloying additions on the microstructures, mechanical properties and weldability of Fe_3Al-based alloys, Mater. Sci. Eng. A 174 (1994) 59–70.
[5] D.G. Morris, Possibilities for high-temperature strengthening in iron aluminides, Intermetallics 6 (1998) 753–758.
[6] W.J. Zhang, R.S. Sundar, S.C. Deevi, Improvement of the creep resistance of FeAl-based alloys, Intermetallics 12 (2004) 893–897.
[7] M. Palm, Concepts derived from phase diagram studies for the strengthening of Fe–Al-based alloys, Intermetallics 13 (2005) 1286–1295.
[8] D.G. Morris, M.A. Munoz-Morris, Development of creep-resistant iron aluminides, Mater. Sci. Eng. A 462 (2007) 45–52.
[9] F. Tate, Development of Iron-aluminum Base Alloy for Gas Cooled Reactor Components: Final Report Contract at (30–3) 325, Office of Technical Services, Department of Commerce, 19591–49.
[10] G. Saintfort, P. Mouturat, P. Pépin, J. Petit, G. Cabane, M. Salesse, Propriétés mécaniques à chaud des alliages fer-aluminium à forte teneur en aluminium, Mem. Sci. Rev. Metall. 60 (1963) 125–134.
[11] R.H. Titran, K. Vedula, G.G. Anderson, High temperature properties of equiatomic FeAl with ternary additions, Mater. Res. Soc. Symp. Proc. 39 (1985) 309–317.
[12] D.J. Gaydosh, S.L. Draper, M.V. Nathal, Microstructure and tensile properties of Fe-40 at. pct Al alloys with C, Zr, Hf, and B additions, Metall. Trans. A 20 (1989) 1701–1714.
[13] J.L. Smialek, J. Doychak, D.J. Gaydosh, Oxidation behavior of FeAl + Hf, Zr, B, Oxid. Met. 34 (1990) 259–275.
[14] B.A. Pint, P.E. Tortorelli, I.G. Wright, Long-term oxidation performance of ingot-produced Fe_3Al alloys, Mater. High Temp. 16 (1999) 1–13.
[15] F. Stein, M. Palm, G. Sauthoff, Mechanical properties and oxidation behaviour of two-phase iron aluminium alloys with $Zr(Fe, Al)_2$ Laves phase or $Zr(Fe,Al)_{12}$ τ_1 phase, Intermetallics 13 (2005) 1275–1285.
[16] F. Dobes, P. Kratochvil, K. Milicka, Compressive creep of Fe_3Al-type iron aluminide with Zr additions, Strength Mater. 40 (2008) 106–109.
[17] S. Chevalier, P. Jozun, G. Borchardt, A. Galerie, K. Przybylski, J.P. Larpin, High-temperature oxidation of Fe_3Al and Fe_3Al–Zr intermetallics, Oxid. Met. 73 (2010) 43–64.
[18] P. Kratochvil, P. Kejzlar, R. Král, V. Vodičková, The effect of Zr addition on the structure and high temperature strength of Fe-30 at.% Al type alloys, Intermetallics 20 (2012) 39–46.
[19] D. Janda, H. Fietzek, M. Galetz, M. Heilmaier, The effect of micro-alloying with Zr and Nb on the oxidation behavior of Fe_3Al and FeAl alloys, Intermetallics 41 (2013) 51–57.
[20] P. Tomaszewicz, G. Wallwork, Iron–aluminium alloys: a review of their oxidation behaviour, Rev. High Temp. Mater. 4 (1978) 75–104.
[21] J.H. DeVan, P.F. Tortorelli, The oxidation–sulfidation behavior of iron alloys containing 16–40 at.% aluminium, Corros. Sci. 35 (1993) 1065–1071.
[22] K. Wefers, C. Misra, Oxides and hydroxides of aluminum, Alcoa Technical Paper (1987) 1-92.
[23] K. Wambach, J. Peters, H.J. Grabke, Behaviour of Al_2O_3 scales on Fe–Al and Fe-Ni-Al alloys with small additions of titanium zirconium, niobium and vanadium on thermal cycling and creep in oxidising and carburizing atmospheres, Mater. Sci. Eng. 88 (1987) 205–212.
[24] J.H. DeVan, P.F. Tortorelli, Environmental effects on iron aluminides, in: 7th Annual Conference on Fossil Energy Materials, Department of Energy DOE, Oak Ridge TN, USA, 1993.
[25] J. Ni, X.J. Wan, Q. Wang, X.Y. Cheng, W.M. Liu, X.Y. Zhang, The cyclic oxidation behaviors of $Fe_3(Al, Cr, Zr)$ and $Fe_3(Al, Cr, Nb)$ intermetallic compound at high temperature, J. Shanghai Univ. 1 (1997) 79–82.
[26] A. Hotař, M. Palm, P. Kratochvíl, V. Vodičková, S. Daniš, High-temperature oxidation behaviour of Zr alloyed Fe_3Al-type iron aluminide, Corros. Sci 63 (2012) 71–81.
[27] C.A. Barrett, R.H. Titran, The Cyclic Oxidation Resistance at 1200 °C of b-NiAl, FeAl and CoAl Alloys with Selected Third Element Additions, NASA Lewis Research Center, 1992, pp. 1–12.
[28] F. Stein, G. Sauthoff, M. Palm, Phases and phase equilibria in the Fe–Al–Zr system, Z. Metall. 96 (2004) 469–485.
[29] P. Kratochvíl, F. Dobeš, J. Pešička, P. Málek, J. Buršík, V. Vodičková, P. Hanus, Microstructure and high temperature mechanical properties of Zr-alloyed Fe_3Al-type aluminides: the effect of carbon, Mater. Sci. Eng. A 548 (2012) 175–182.
[30] P.F. Tortorelli, K.B. Alexander, Mechanically reliable scales and coatings, in: 9th Annual Conference on Fossil Energy Materials, Department of Energy DOE, Oak Ridge, TN, 1995, pp. 247–256.
[31] C.H. Xu, W. Gao, Oxidation behaviour of FeAl intermetallics: effects of reactive elements on cyclic oxidation properties, Mater. Sci. Technol. 17 (2001) 324–332.
[32] B.A. Pint, P.F. Tortorelli, I.G. Wright, Effect of cycle frequency on high-temperature oxidation behavior of alumina-forming alloys, Oxid. Met. 58 (2002) 73–101.
[33] P. Kejzlar, P. Kratochvíl, R. Král, V. Vodičková, Phase structure and high-temperature mechanical properties of two-phase Fe–25Al–*x*Zr alloys compared to three-phase Fe–30Al–*x*Zr alloys, Metall. Mater. Trans. A 45 (2014) 335–342.
[34] M. Cieslar, M. Karlik, Carbide formation in Zr-containing Fe3Al-based alloys, Mat. Sci. Eng. A 462 (2007) 289–293.
[35] I. Rommerskirchen, Oxidationsverhalten von b-NiAl und b-FeAl sowie Fe–Al–Legierungen, in: Fortschritt-Berichte, Reihe 5, Nr. 422, VDI Verlag, 1996, pp. 1–93.
[36] F. Lang, Z. Yu, S. Gedevanishvili, S.C. Deevi, T. Narita, Isothermal oxidation behavior of a sheet alloy of Fe–40 at.% Al at temperatures between 1073 and 1473 K, Intermetallics 11 (2003) 697–705.
[37] M. Palm, Oxidation of Fe–Al alloys (5–40 at.% Al) at 700 and 900 °C, Kovove Materialy—Metallic Materials (submitted).
[38] I. Kim, W.D. Cho, H.J. Kim, High-temperature oxidation of Fe_3Al containing yttrium, J. Mater. Sci. 35 (2000) 4695–4703.
[39] T. Mitsuhashi, M. Ichihara, U. Tatsuke, Characterization and stabilization of metastable ZrO_2, J. Am. Ceram. Soc. 57 (1974) 97–104.
[40] R.C. Garvie, Stabilization of the tetragonal structure in zirconia microcrystals, J. Phys. Chem. 82 (1978) 218–224.
[41] J.R. Kelly, I. Denry, Stabilized zirconia as a structural ceramic: an overview, Dent. Mater. 24 (2008) 289–298.
[42] J. Chevalier, L. Gremillard, The tetragonal-monoclinic transformation in zirconia: lessons learned and future trends, J. Am. Ceram. Soc. 92 (2009) 1901–1920.
[43] A. Mignone, S. Frangini, A. La Barbera, O. Tassa, High temperature corrosion of B_2 iron aluminides, Corros. Sci. 40 (1998) 1331–1347.
[44] K. Przybylski, S. Chevalier, P. Juzoń, Effect of Zr on the oxidation properties of Fe_3Al intermetallic compound, J. Chin. Soc. Corros. Protect. 29 (2009) 286–292.
[45] C.H. Xu, W. Gao, H. Gong, Oxidation behaviour of FeAl intermetallics. The effects of Y and/or Zr on isothermal oxidation kinetics, Intermetallics 8 (2000) 769–779.

Intermetallics 18 (2010) 1390–1395

Contents lists available at ScienceDirect

Intermetallics

journal homepage: www.elsevier.com/locate/intermet

Oxidation resistance of Fe–25Al–2Ta (at.%) in air

A. Hotař [a,*], M. Palm [b]

[a] Technical University of Liberec, Faculty of Engineering, Department of Materials Science, Studentská 2., CZ 46117 Liberec, Czech Republic
[b] Max-Planck-Institut für Eisenforschung GmbH, Max-Planck-Strasse 1, D-40237 Düsseldorf, Germany

ARTICLE INFO

Article history:
Received 1 October 2009
Received in revised form
17 February 2010
Accepted 18 February 2010
Available online 17 March 2010

Keywords:
A. Iron aluminides (based on Fe_3Al)
B. Oxidation at high temperatures

ABSTRACT

The high-temperature oxidation behaviour of Fe–25Al–2Ta (in at.%) has been investigated between 600 and 1000 °C using thermogravimetric analysis (TGA) in synthetic air. After oxidation for 1000 h the scales were analysed by light optical microscopy (LOM), grazing incidents X-ray diffraction (GI-XRD), scanning electron microscopy (SEM), and electron probe microanalysis (EPMA). Between 600 and 800 °C thin adherent oxide scales grew according to a parabolic rate law. At 900 °C parabolic growth was observed for several hundred hours, interrupted by sudden mass gains which are probably caused by cracking of the scales, while at 1000 °C no protective scales formed. The scales are predominantly formed by Al_2O_3 and minor amounts of Fe_2O_3. While scales formed between 600 and 800 °C are still adherent after cooling to room temperature, scales formed at higher temperatures spalled during/after cooling, possibly because the Laves phase Fe_2Ta formed on the sample surfaces underneath the oxide scales. Parabolic rate constants k_p show that compared to other Fe–Al alloys addition of 2 at.% Ta has no detrimental effect to the excellent oxidation resistance in air between 600 and 800 °C.

1. Introduction

Iron aluminide based alloys are potential materials for high-temperature structural applications because they have the advantages of low material costs (compared with corrosion and heat resistant steels), low density (5.8–6.3 g cm^{-3}) and a notable corrosion resistance at high temperatures in a variety of aggressive environments, e.g. in oxidising and sulphidising atmospheres [1–4], strongly carburising gas mixtures [5], under certain salt deposits or melts [4,6], chlorine-containing vapours [4,7] or molten glass [8]. The good corrosion resistance of Fe–Al-based alloys is caused by the formation of dense and adherent α-Al_2O_3 (alumina) layers in oxidising environments [3,9]. Depending on exposure time, temperature and alloy composition – most specifically the Al content – the formation of the α-Al_2O_3 layer is preceded by the formation of iron oxides and metastable γ-, δ- and θ-Al_2O_3, which grow faster and are more voluminous and porous than α-Al_2O_3 [10–13].

The chemical composition significantly affects the oxidation resistance of Fe–Al-based alloys. For binary Fe–Al alloys which contain at least 19.5 at.% Al oxidation rates are relatively low [14]. Additions of ternary alloying elements influence the corrosion resistance markedly. E.g., the addition of Cr increases oxidation rates of alloys containing less than 19.5 at.% Al [15,16] while Ce has a positive effect on the oxidation resistance of iron aluminides based on Fe_3Al at temperatures above 1000 °C [17].

The Fe–25Al–2Ta (in at.% - nominal composition) alloy investigated here qualifies for applications at and above 600 °C because of its high creep resistance which surpasses that of other Fe_3Al-based alloys [18]. Preliminary information on the oxidation behaviour of this alloy was obtained by measuring the weight gain of compressive yield stress specimens after testing for 45 min in air at various temperatures (Fig. 1) [19]. All specimens have the same size of 5 × 5 × 10 mm^3. The results show that the addition of Ta does not deteriorate the short-term oxidation behaviour of the as-cast alloy. However, in contrast to Fe–25Al–2Ta in the as-cast state spallation of oxide scales was observed after a previous heat treatment of the alloy at 1000 °C for 200 h. In order to get a better understanding of the oxidation behaviour of Ta containing Fe_3Al-based alloys long-term oxidation experiments have been carried out now.

2. Experimental

The Fe–25Al–2Ta (at.%) alloy was produced by levitation melting (system by Celes, Lautenbach, France) in argon of 99.999% purity. The alloy was produced using Fe of 99.98% purity, Al (99.9%) and Ta (99.999%). The melt was cast into a cylindrical Cu mould of 22 mm in diameter and about 100 mm in length. Samples with dimension 10 × 10 × 1 mm^3 were cut by electrical discharge machining (EDM). Specimens were ground to 1200 grit surface finish. Thermogravimetric analysis (TGA) was carried out using

* Corresponding author. Tel.: +420 485 353 136; fax: +420 485 353 631.
E-mail address: adam.hotar@tul.cz (A. Hotař).

0966-9795/$ – see front matter © 2010 Elsevier Ltd. All rights reserved.
doi:10.1016/j.intermet.2010.02.014

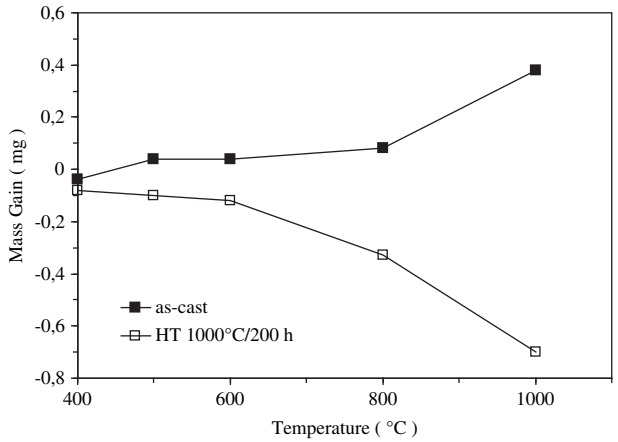

Fig. 1. Mass gain of as-cast and heat-treated (HT: 1000 °C, 200 h) Fe-25Al-2Ta during compression testing in air as a function of temperature, all specimens have the same size of 5 × 5 × 10 mm^3 [19].

a Setaram SETSYS 16/18 thermobalance with continuous recording of the mass gains with a mass sensitivity of 1μg. The oxidation behaviour was tested in synthetic air (20.5% O_2, 79.5% N_2) at a flow rate of 1.54 × 10^{-6} m^3/s. Samples of as-cast Fe–25Al–2Ta were oxidised at 600, 700, 800, 900 and 1000 °C. The oxide layers were analysed by X-ray diffraction (XRD). A Phillips diffractometer with Bragg-Brentano geometry equipped with a copper cathode ($\lambda_K\alpha$ = 0.1540598 nm) was employed for general analysis of the oxidised samples. The scales were specifically analysed by grazing incidence X-ray diffraction (GI-XRD) using Cu Kα radiation on a Bruker AXS D8 Advance equipped with a parabolic Göbel mirror and SolX detector. A 1200 microns slit aperture and incidence angles of 1.0° and 2.5° were used to achieve a suitable sensitivity towards the composition at the surface. All scales were inspected by light optical microscopy (LOM). Scanning electron microscopy (SEM) and quantitative analysis of the phases by wave-length dispersive electron probe microanalysis (EPMA) was performed on a Jeol JXA-8100 instrument.

3. Results and discussion

3.1. TGA

Figs. 2–4 illustrate the dependence of the squared mass gain during oxidation of Fe–25Al–2Ta in synthetic air on time at different temperatures. The TGA curves indicate a parabolic rate law for the growth of the oxide scale between 600 and 800 °C. It is noted that all samples show increased mass gains at the beginning of the tests for approximately 100 h which are attributed to the comparable fast growth of metastable phases (Fig. 2). At 900 °C a sudden increase in the mass gain occurred after an initially slow growth of the scales (Fig. 3). In order to verify that this is no experimental artefact the test was repeated but to the same result (Fig. 3). After an initially parabolic growth for about 370 h a sudden increase of the mass gain was observed for a few hours which was again followed by parabolic growth for another 600 h. Fig. 4 shows a linear or even hyperbolic growth at 1000 °C. Visual inspection of the scales by LOM revealed that adherent scales formed between 600 and 800 °C while the scales formed at 900 and 1000 °C show apparent signs of spallation. Because the TGA curves do not show any mass loss, spallation must have occurred during/after cooling to room temperature (RT).

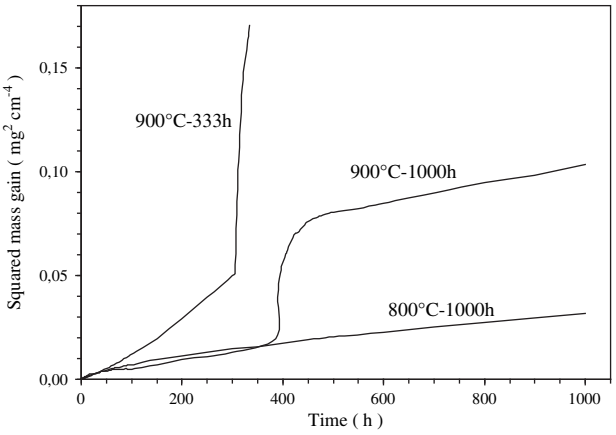

Fig. 3. Squared mass gain versus exposure time for Fe–25Al–2Ta at 900 and 800 °C (for comparison) in synthetic air.

In order to compare the oxidation behaviour with that of other Fe_3Al-based alloys the parabolic rate constant k_p was determined at 600, 700 and 800 °C, i.e. where parabolic growth and an adherent oxide scale were observed, from the parabolic rate law

$$(\Delta m/A)^2 = k_p t$$

where Δm/A is the weight gain per unit area (mg/cm^2) and t the time in s. The parabolic rate constants of Fe–25Al–2Ta are summarized

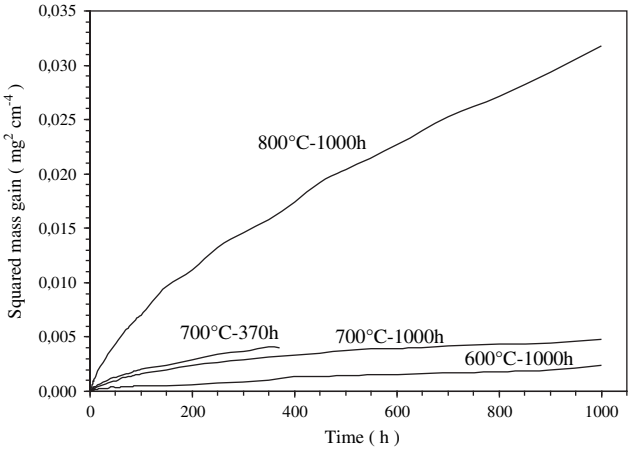

Fig. 2. Squared mass gain versus exposure time for Fe–25Al–2Ta at 600, 700 and 800 °C in synthetic air.

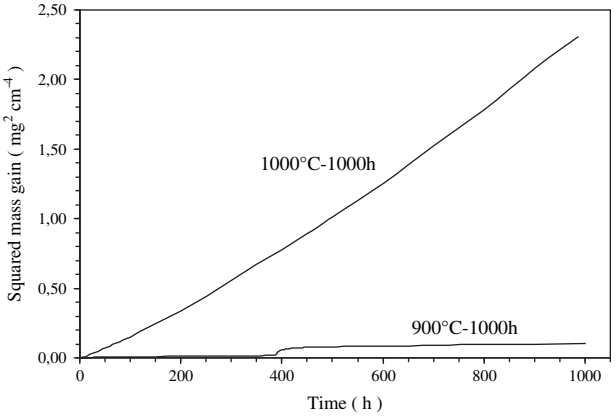

Fig. 4. Squared mass gain versus exposure time for Fe–25Al–2Ta at 1000 and 900 °C (for comparison) in synthetic air.

Table 1
Apparent parabolic rate constants k_p of selected Fe–Al alloys oxidised in air. The current data for k_p were calculated from the TGA curves omiting the initial stage where growth of metastable phases occurs.

Alloy	Temperature (°C)	k_p ($g^2\ cm^{-4}\ s^{-1}$)	Reference
Fe–25Al–2Ta	600	5.6×10^{-16}	this work
Fe–25Al–2Ta	700 (370 h)	8.3×10^{-16}	this work
Fe–25Al–2Ta	700 (1000 h)	2.2×10^{-15}	this work
Fe–25Al	700	8.6×10^{-16}	[21]
Fe–25Al–2Ta	800	8.3×10^{-15}	this work
Fe–25Al	800	2.7×10^{-15}	[21]
Fe–28Al	800	6.4×10^{-15}	[15]
Fe–52Al	800	2.6×10^{-14}	[11]
Fe–28Al–2Cr	800	3.6×10^{-15}	[15]
Fe–23Al–8.5Ti	800	3.3×10^{-15}	[22]
Fe–27Al–15Ti	800	2.0×10^{-14}	[20]

in Table 1 and compared to that of other Fe_3Al-based alloys. The results show an increase of the parabolic rate constants with increasing temperature which is related to the accelerated diffusion of the oxide forming components with increasing temperature. At 700 and 800 °C k_p for Fe–25Al–2Ta is about the same as for binary Fe–25Al and Fe_3Al-based alloys containing minor additions of Cr or Ti. However, those alloys still show the formation of protective Al_2O_3 scales at temperatures above 800 °C [11,20,21], whereas at these temperatures the scale on Fe–25Al–2Ta cracks and is not any longer protective.

3.2. Composition of the oxide scales and phases at the sample surfaces

Analysis of the oxide scales by XRD and GI-XRD revealed that they are formed by Al_2O_3, Fe_2O_3, and Ta_2O_5 (Fig. 5a). While after oxidation at the lower temperatures more Fe_2O_3 is observed (Fig. 5a), Al_2O_3 is the predominant oxide at the higher temperatures and also the amount of Ta_2O_5 increases (Fig. 5b). No difference exists between the GI-XRD with incidence angles of 1.0° and 2.5° indicating no pronounced layering of the scales. Astonishingly, the Laves phase Fe_2Ta is observed at all temperatures. According to previous descriptions of the microstructure of this alloy about 0.5 vol.% Fe_2Ta are found in the as-cast state and up to about 7 vol.% after annealing at 1000 °C [19]. Though some Fe_2Ta may precipitate in the sample during oxidation at elevated temperatures, this

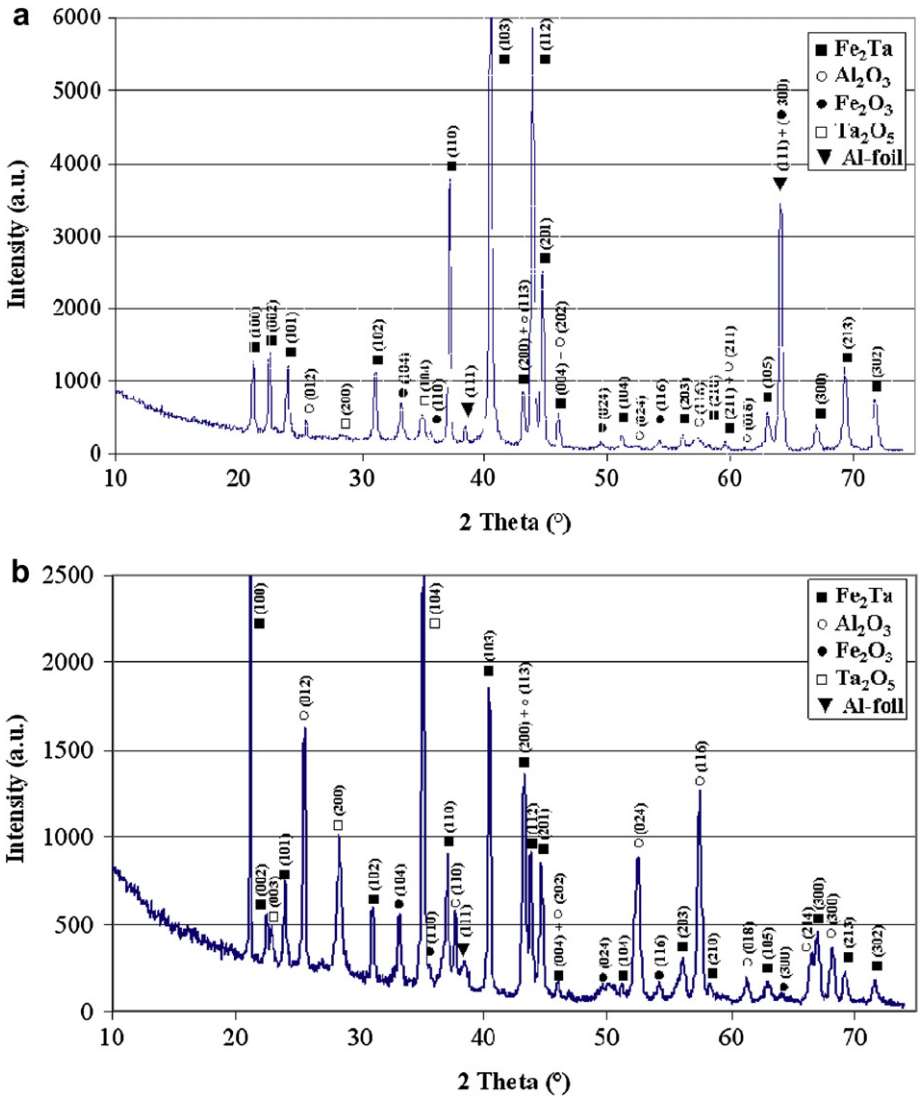

Fig. 5. GI-XRD patterns of the oxidised surface of Fe–25Al–2Ta after oxidation at 700 °C (a) and 900 °C (b) for 1000 h. Al-foil has been used as sample holder which yielded a few additional lines.

should happen in the bulk, i.e. in the sample underneath the oxide scale, and should therefore not yield such strong peaks as observed in Fig. 5.

In order to clarify the formation of the Laves phase the samples oxidised at 700 and 900 °C for 1000 h were analysed by SEM and EPMA. Fig. 6 shows the sample oxidised at 700 °C for 1000 h. The surface is covered by a thin oxide layer which is too thin (<2 μm) for EPMA (Fig. 6a). Only in a few places thicker oxides are observed which could be analysed by EPMA (Fig. 6b). In these places Al_2O_3, Fe_2O_3, and a mixture of oxides containing a Ta-rich phase were analysed. Whether the latter is the Laves phase Fe_2Ta is not clear. In some of these places the scale spalled during cooling revealing that rather large grains of up to 100 μm of Laves phase formed at the surface of the sample (Fig. 7). After oxidation at 900 °C for 1000 h a much thicker oxide scale has formed which partially spalled during/after cooling (Fig. 8). According to EPMA and in agreement with the GI-XRD results the scale is formed mainly by Al_2O_3 and few Fe_2O_3 (Fig. 8a). Where the scale has spalled the underlying surface of the sample is covered by numerous particles of the Laves phase Fe_2Ta a few microns in size (Fig. 8b). The bright contrast of Fe_2Ta in the SEM–SE micrograph shown in Fig. 8c reveals that the Laves phase Fe_2Ta is located at the surface of the sample. Ta_2O_5, which has also been identified by GI-XRD, is not found in the oxide scale which only consists out of Al_2O_3 and few Fe_2O_3 (Fig. 8a).

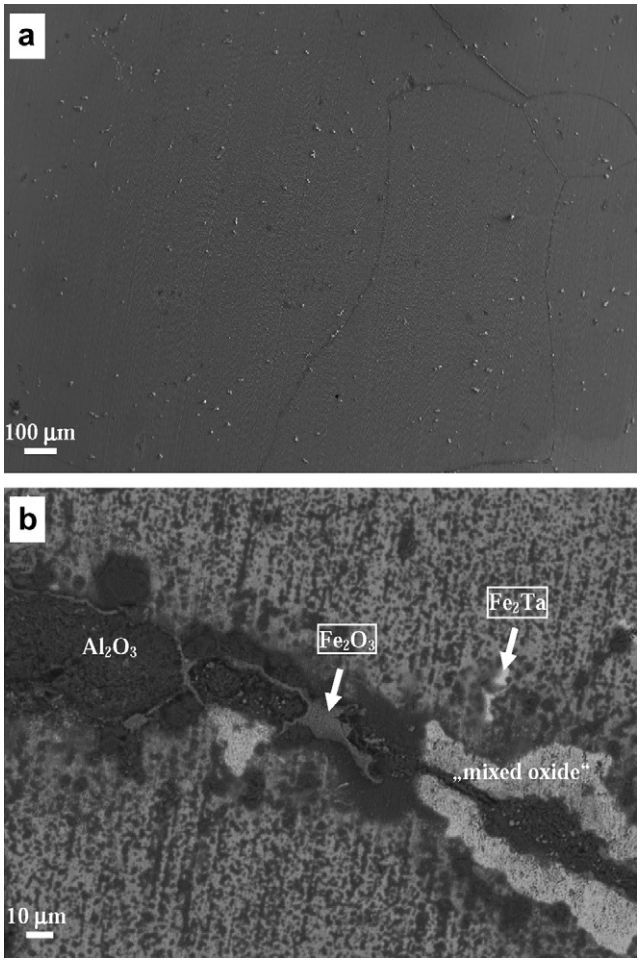

Fig. 6. SEM micrographs of the oxidised surface of Fe–25Al–2Ta after oxidation at 700 °C for 1000 h a): Overview (secondary electron (SE) contrast) showing a homogeneous thin oxide layer; b): place where thicker oxides are observed (backscatter electron (BSE) contrast; dark: Al_2O_3; grey: Fe_2O_3; light grey: mixture of oxides containing a Ta-rich phase; light: Fe_2Ta).

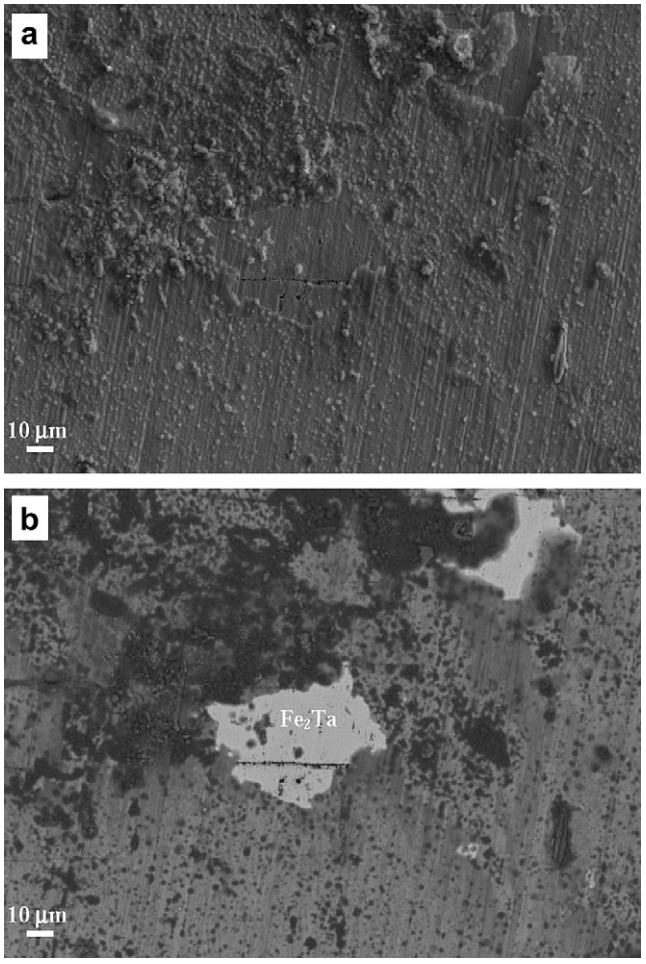

Fig. 7. SEM micrographs of the oxidised surface of Fe–25Al–2Ta after oxidation at 700 °C showing the same place in SE (a) and BSE (b) contrast. Where the oxide layer has spalled (a) the BSE micrograph (b) reveals the presence of a light phase, which was identified as the Laves Fe_2Ta phase by EPMA.

However, some EPMA measurements of the Laves phase Fe_2Ta showed oxygen contents of 4–20 at.%. Because the Laves phase does not contain so much oxygen it is assumed that these analyses were actually from mixtures of Fe_2Ta and Ta_2O_5, where Ta_2O_5 formed by oxidation of the Laves phase.

3.3. Oxidation behaviour of Fe–25Al–2Ta and comparison to other Ta containing alloys

Between 600 and 800 °C thin adherent Al_2O_3 scales form on the surface of Fe–25Al–2Ta. They also contain some Fe_2O_3 whose amount decreases with increasing temperature. The iron oxide may have formed in the initial stages of the oxidation as has been described for binary Fe–Al [13] and Fe–28Al–5Cr [15]. Because the Fe–Al matrix is supersaturated with Ta in the as-cast state [19] some Laves phase will form during the long-term oxidation at high temperatures. The additional depletion of the matrix by Al (and Fe) by the formation of Al_2O_3 and Fe_2O_3 may further support the formation of Laves phase. For Ni-base superalloys it has been shown that Ta diffuses outwards to the metal/oxide scale interface where then Ta-rich phases – in that case probably carbides – form [23,24]. It is assumed that, like in the case of other elements, the oxygen potential gradient is the driving force for the outward diffusion of Ta [23,25]. It is well possible that the formation of the

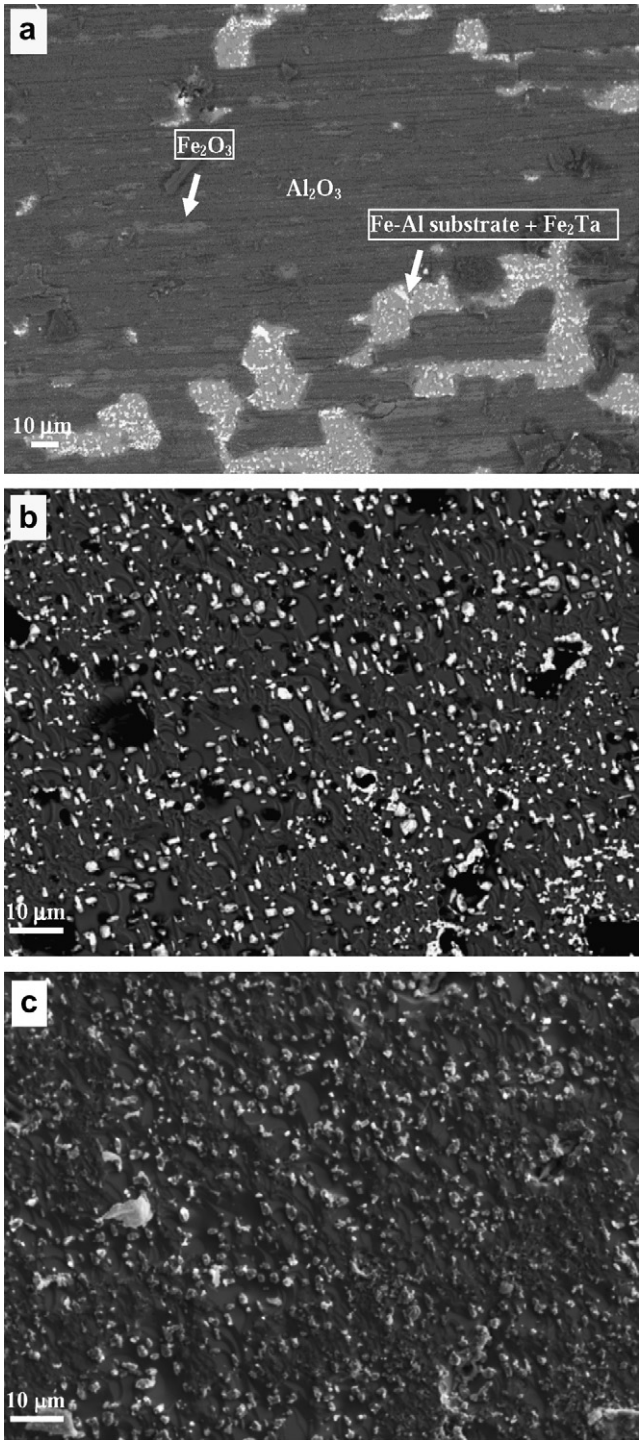

Fig. 8. SEM micrographs of the oxidised surface of Fe–25Al–2Ta after oxidation at 900 °C. a): SEM-BSE micrograph of the oxide scale (dark grey) that has partially spalled in the lower part of the micrograph; b) SEM-BSE micrograph of the surface of the sample where the oxide scale has spalled (grey matrix: Fe–Al; white particles: Fe_2Ta; black phase: Al_2O_3); c): SEM–SE micrograph of the same area as in (b) revealing by the bright contrast of Fe_2Ta and Al_2O_3 that these phases lie on top of the sample surface.

Laves phase on the surface of Fe–25Al–2Ta has the same origin. That more Laves phase particles are observed at the surface with increasing temperature is in accordance with this assumption [25].

Where Laves phase grains have formed at the sample surface the otherwise adherent scale may spall during cooling (Fig. 7b). Also from Ni-base superalloys it is known that the formation of Ta-rich particles at the metal/scale interface leads to spallation of the scales [23,24]. One mechanism that leads to spallation is that Ta-rich particles at the sample surface are undercut by the growing scale which cracks at the particle/oxide interface during cooling [24]. This mechanism seems not to be responsible for the spallation of the present scales because the Laves phase particles are not undercut by the growing scale and are still on the sample surface after the scale spalled (Figs. 7b and 8b,c). Another effect which leads to spallation during cooling are differences in the coefficients of thermal expansion (CTE). Compared to ferritic Fe–Al alloys a significant increase of the CTE is observed when Fe_3Al and FeAl form, which results in a decrease of the resistance against spallation [26]. In the present case, besides differences in the 'CTE's of the iron aluminide and the scale, also differences in the 'CTE's of the Laves phase and the scale may have caused spallation during cooling.

Also at 900 °C the formation of an oxide scale consisting out of Al_2O_3 and few Fe_2O_3 is observed. This leads again to a parabolic growth of the scale for several hundred hours but then a sudden dramatic increase of the mass gain is observed within a few hours followed again by a parabolic growth of the scales (Fig. 3). Presumably the sudden increase in the oxidation rate is caused by cracking of the protective oxide layer (Fig. 8a). After the cracks have healed, parabolic growth of the scale is observed again. Post mortem investigation of the sample oxidised at 900 °C for 1000 h revealed the presence of numerous fine Laves phase particles on the surface of the sample (Fig. 8b,c). Whether they are the reason for the cracking of the scale during the test is not clear. The growth of the particles may lead to mechanical tensions between substrate and scale and/or within the scale and these tensions may finally result in the cracking of the scale. At least these mechanical tensions seem to be responsible that the scales of the samples oxidised at 900 and 1000 °C spalled during cooling because in both cases large fractions of the scales spalled which is typical for this mechanism [27].

At 1000 °C no protective scale forms any longer but fast growth of a mixture of Al_2O_3, Fe_2O_3 and Ta_2O_5 is observed. Possibly the larger fraction of Ta_2O_5 within the alumina scale is responsible for this inferior oxidation behaviour. It has been found that formation of such second phases can lead to thermal expansion stresses and/or stress concentration sites as well as rapid oxygen transport through the scale (see e.g. [23,28]).

No comprehensive treatment on the oxidation behaviour of Ta-rich phases does exist. However, already early studies showed that Ta-rich alloys show a good oxidation resistance at high temperatures in air [29,30]. Moreover, these studies showed that Ta-rich Laves phases do not negatively influence the oxidation behaviour. E.g., of a series of Ta–Cr alloys those in the single-phase region of the Laves phase Cr_2Ta (at that time erroneously designated as Cr_3Ta_2) showed even the highest oxidation resistance at 1250 °C [29]. More recent investigations also showed that of Laves phase reinforced Cr-based Cr–(Nb, Ta) alloys those containing Cr_2Ta showed the best oxidation resistance under cyclic oxidation conditions [31]. Also for other alloy systems containing Ta-based Laves phases no deterioration of the oxidation behaviour under static and cyclic conditions has been observed [32,33]. While in Fe–25Al–2Ta no preferential oxidation of the Laves phase is observed too, the nucleation and growth of new Laves phase particles on the surface of the sample is apparently detrimental for the resistance to cyclic oxidation of this alloy. In contrast to the Ta-rich alloys investigated in [29–33], which all showed a good oxidation resistance at temperatures above 1000 °C, the present alloy already shows a fast growth of the oxide scale at 1000 °C. Moreover, the current alloy shows a different oxidation behaviour in the as-cast state and after being heat treated (Fig. 1) [19]. In view

of the present results this difference may be caused by the higher volume fraction of the Laves phase within the heat-treated alloy.

4. Summary and conclusions

The high-temperature oxidation behaviour of Fe–25Al–2Ta has been investigated between 600 and 1000 °C by TGA in synthetic air. The results can be summarized as follows:

1. Between 600 and 800 °C thin adherent oxide scales mainly consisting out of Al_2O_3 grew according to a parabolic rate law. Such oxide scales are protective against further oxidation and also in other corrosive environments.
2. Parabolic rate constants k_p show that compared to other Fe–Al alloys addition of 2 at.% Ta has no detrimental effect to the excellent oxidation resistance in air between 600 and 800 °C.
3. At 900 °C parabolic growth was observed for several hundred hours after which sudden mass gains occurred which were again followed by parabolic growth. Such a behaviour hints to cracking of the scales.
4. At 1000 °C a linear to hyperbolic mass gain was observed indicating continuous or even increased oxidation during the duration of the test.
5. Scales formed at 900 and 1000 °C spalled during/after cooling to RT, possibly because large amounts of the Laves phase Fe_2Ta formed on the sample surfaces underneath the oxide scales.

Acknowledgements

The authors would like to thank Mr T. Schildheuer for help with oxidation testing, Mr G. Bialkowski for sample preparation, Ms. I. Wossack for SEM and EPMA, and Dr. Patrick Keil for GI-XRD.

References

[1] Sykes C, Bampfylde JW. The physical properties of iron–aluminum alloys. J Iron Steel Inst 1934;130:389–418.
[2] Hardwick D, Wallwork G. Iron–aluminium alloys: a review of their feasibility as high temperature materials. Rev High-Temp Mat 1978;4:47–74.
[3] McKamey CG, DeVan JH, Tortorelli PF, Sikka VKJ. A review of recent developments in Fe_3Al-based alloys. Mat Res 1991;6:1779–805.
[4] Natesan K, Tortorelli PF. High-temperature corrosion and applications of nickel and iron aluminides in coal-conversion power systems. In: Proceedings International Symposium on nickel and iron aluminides: processing, properties, and applications. ASM 1997. p. 265–80.
[5] Bernst R, Schneider A, Spiegel M. Metal dusting of binary iron aluminium alloys at 600°C. Mat Corr 2006;57:724–8.
[6] Li YS, Spiegel M, Shimada S. Corrosion behaviour of various model alloys with NaCl–KCl coating. Mat Chem Phys 2005;93:217–23.
[7] Li YS, Spiegel M. Internal oxidation of Fe–Al alloys in a KCl-air atmosphere at 650°C. Oxid Met 2004;61:303–22.
[8] Hotař A, Kratochvíl P. The corrosion resistance of iron aluminide Fe28Al3Cr0.02Ce (at%) in molten glass. Intermetallics 2007;15:439–41.
[9] Tortorelli PF, Natesan K. Critical factors affecting the high-temperature corrosion performance of iron aluminides. Mat Sci Eng 1998;A258:115–25.
[10] Prescott R, Graham MJ. The oxidation of iron–aluminum alloys. Oxid Met 1992;38:73–87.
[11] Rommerskirchen I, Eltester B, Grabke HJ. Oxidation of β–FeAl and Fe–Al alloys. Mat Corros 1996;47:646–9.
[12] Velon A, Olefjord I. Oxidation behavior of Ni_3Al and Fe_3Al: II. Early stage oxide growth. Oxid Met 2001;56:425–51.
[13] Pöter B, Stein F, Wirth R, Spiegel M. Early stages of protective oxide layer growth of binary iron aluminides. Z Phys Chem 2005;219:1489–503.
[14] DeVan JH, Tortorelli PF. The oxidation–sulfidation behavior of iron alloys containing 16–40 AT% aluminum. Corros Sci 1993;35:1065–71.
[15] Tortorelli PF, DeVan JH. Behavior of iron aluminides in oxidizing and oxidizing/sulfidizing environments. Mat Sci Eng 1992;A153:573–7.
[16] Lee DB, Kim GY, Kim GJ. The oxidation of Fe_3Al–(0, 2, 4, 6%)Cr alloys at 1000 °C. Mat Sci Eng 2003;A339:109–14.
[17] Yu XQ, Sun YS. The oxidation improvement of Fe_3Al based alloy with cerium addition at temperature above 1000 °C. Mat Sci Eng 2003;A363:30–9.
[18] Palm M, Krein R, Milenkovic S, Sauthoff G, Risanti D, Stallybrass C, et al. Strengthening mechanisms for Fe–Al-based alloys with increased creep resistance at high temperatures. Mat Res Soc Symp Proc 2007;980:II01–01.
[19] Risanti DD, Sauthoff G. Strengthening of iron aluminide alloys by atomic ordering and Laves phase precipitation for high-temperature applications. Intermetallics 2005;13:1313–21.
[20] Palm M, Sauthoff G. Deformation behaviour and oxidation resistance of single-phase and two-phase $L2_1$-ordered Fe–Al–Ti alloys. Intermetallics 2004;12:1345–59.
[21] Pöter B, Stein F, Spiegel M. reported in Milenkovic S, Palm M. Microstructure and mechanical properties of directionally solidified Fe–Al–Nb eutectic. Intermetallics 2008;16:1212–8.
[22] Krein R, Palm M, Heilmaier M. Characterization of microstructures, mechanical properties, and oxidation behavior of coherent A2 + $L2_1$ Fe–Al–Ti. JMR 2009;24:3412–21.
[23] Pint BA, Wright IG, Lee WY, Zhang Y, Prüßner K, Alexander KB. Substrate and bond coat compositions: factors affecting alumina scale adhesion. Mater Sci Eng 1998;A245:201–11.
[24] Wright IG, Pint BA, Lee WY, Alexander KB, Prüßner K. Some effects of metallic substrate composition on degradation of thermal barrier coatings. In: Nicholls J, Rickerby D, editors. High temperature surface engineering. Institute of Materials (UK); 2000. p. 95–113.
[25] Pint BA, Garratt-Reed AJ, Hobbs LW. Possible role of oxygen potential gradient in enhancing diffusion of foreign ions on α-Al_2O_3 grain boundaries. J Am Ceram Soc 1998;81:305–14.
[26] Pint BA, Porter WD, Wright IG. The effect of thermal expansion on spallation behaviour of Fe-base alumina forming alloys. Mater Sci Forum 2008;595–598:1083–92.
[27] Pint BA, Tortorelli PF, Wright IG. Effect of cycle frequency on high-temperature oxidation behavior of alumina-forming alloys. Oxid Met 2002;58:73–101.
[28] Kuenzly JD, Douglass DL. The oxidation mechanisms of Ni_3Al containing yttrium. Oxid Met 1974;8:139–78.
[29] Kubaschewski O, Schneider A. Measurements on the oxidation-resistance of high-melting-points alloys. J Inst Met 1949;75:403–16.
[30] Kubaschewski O, Schneider A. Oxidation-resistance and some phase relationships in the system chromium-tantalum-nickel. J Inst Met 1949;75:417–30.
[31] Brady MP, Zhu JH, Liu CT, Tortorelli PF, Walker LR. Oxidation resistance and mechanical properties of Laves phase reinforced Cr in-situ composites. Intermetallics 2000;8:1111–8.
[32] Palm M, Sauthoff G. Long-term creep and oxidation behavior of a Laves phase-strengthened NiAl-Ta-Cr alloy for gas turbine applications. Mat Res Soc Symp Proc 2001;646. N.6.8.1-N.6.8.6.
[33] Brady MP, Liu CT, Zhu JH, Tortorelli PF, Walker LR. Effects of Fe additions on the mechanical properties and oxidation behavior of Cr_2Ta Laves phase reinforced Cr. Scr Mater 2005;52:815–9.

OXIDATION RESISTANCE OF Fe28Al3Cr0.02Ce AND Fe30Al4Cr2.7TiB$_2$ (at.%) IN AIR

Adam HOTAŘ[a], Petr KRATOCHVÍL[a], Josef CÍZNER[b]

[a] *Technical University of Liberec, Faculty of Engineering, Department of Materials Science, Studentská 2., 46117 Liberec, Czech Republic, adam.hotar@tul.cz, pekrat@met.mff.cuni.cz*

[b] *Research Institute SVÚM a.s. 190 11 Praha – Běchovice, Czech Republic, cizner@svum.cz*

Abstract

The high-temperature oxidation behaviour of Fe28Al3Cr0.02Ce and Fe30Al4Cr2.7TiB$_2$ (in at.%) has been investigated at 900 and 1100 °C for up to 2000 h. in air. The corrosion resistance was determined by measurement of weight gains. After oxidation the surface layer and the scales were analysed by light optical microscopy (LOM), electron probe microanalysis (EDX) and X-ray diffraction (XRD). Parabolic rate constants k_p was compared with other Fe$_3$Al alloys.

At 900 °C thin oxide scales of both alloys grew according to a parabolic rate law. In the case of oxidation at 1100°C, thicker scales and attack on the surface layer of both alloys were observed.

Keywords: Iron Aluminides (based on Fe$_3$Al), oxidation at high temperatures

1. INTRODUCTION

Fe$_3$Al – based iron aluminides are potential materials for structural applications at high-temperature. The advantages are low material costs (compared with corrosion and heat resistant steels), low density (5.8 – 6.3 g.cm^{-3}) and a corrosion resistance at high temperatures in a variety of aggressive environments [1,2]. The good corrosion resistance of Fe–Al-based alloys is caused by the formation of continuous and adherent α-Al$_2$O$_3$ (alumina) layers in oxidising environments [1,2]. The formation of the α-Al$_2$O$_3$ layer is preceded by the formation of iron oxides and metastable γ-, δ- and θ-Al$_2$O$_3$, which grow faster and are more voluminous and porous than α-Al$_2$O$_3$ [3,4]. The formation of Al$_2$O$_3$ metastable phases depends on exposure time, temperature and alloy composition. The content of Al and ternary alloying elements significantly affect the corrosion resistance Fe$_3$Al alloys. For binary Fe–Al alloys which contain at least 19.5 at.% Al oxidation rates are relatively low [5]. The addition of Ce has a positive effect on the oxidation resistance of iron aluminides based on Fe$_3$Al at temperatures above 1000°C [6] and Ti hasn't detrimental effect on the oxidation behaviour [7,8]. On the other hand, the Cr content (within the range of 2 to 4 at.%) slightly increases oxidation rates of Fe$_3$Al alloys [9].

The aim of the present paper is to describe the long-term oxidation behaviour of Fe28Al3Cr0.02Ce and Fe30Al4Cr2.7TiB$_2$ alloys in air at 900 and 1100°C. Mechanical properties of these alloys were tested recently [10, 11]. Very good oxidation resistance of the Fe28Al3Cr0.02Ce against molten glasses was also observed at 1200°C [12].

2. EXPERIMENTAL

The alloys were melted in a vacuum furnace and cast in an argon atmosphere by the Research Institute of Metals, Ltd. Panenské Břežany. Consequently, the original ingots (thickness 40 mm) of Fe28Al3Cr0.02Ce were rolled to the final sheets (13 mm) at 1200°C. For preparation of Fe30Al4Cr2.7TiB$_2$ the powder of rods 10μ long was used. The samples were cut from tubes (ϕ 30 x 7 mm prepared by extrusion of rods (ϕ 117

mm) at 1140°C at FERRA, Inc. Hrádek u Rokycan. Samples for an oxidation test were cylinders - ϕ 7 x 30 mm. Chemical compositions of studied alloys are in **Table 1**.

Table 1. - Chemical compositions of tested alloys

The alloy (at.%)	Al	Cr	Mn	TiB_2	Ce	Fe
Fe28Al3Cr0.02Ce	28.44	2.64	0.40	-	0.02	Balance
Fe30Al4Cr2.7TiB_2	30.2	3.9	0.2	2.7	-	Balance

The test samples were placed in alumina boats and oxidation tests were carried out in the furnace at 900°C and 1100°C. After each time period samples mass gain was measured. Changes of sample surface were determined by light optical microscopy (LOM) and electron probe microanalysis (EDX). The oxide layers were analysed by X-ray diffraction (XRD).

3. RESULTS AND DISCUSSION

3.1 Thermogravimetric analyse

The dependences of the squared mass gain during oxidation of both alloys in air on time at different temperatures are illustrated on **Figs. 1-2**. At 900°C the curves indicated a parabolic rate low for the growth of the oxide scale. However, the increased mass gains were determined at the beginning of the oxidation test for approximately 200 h. For the initial oxidation the fast growth of metastable phases is typical (**Fig. 1**). **Figs. 1-2** also show a linear or even hyperbolic (especially Fe28Al3Cr0.02Ce) growth of oxide scales at 1100°C. In the case of Fe28Al3Cr0.02Ce very high levels of mass gain were observed at 1100°C.

The parabolic rate constant k_p was determined at 900°C for comparing with other Fe_3Al-based alloys. The parabolic rate constant was calculated from the parabolic rate law:

$$\left(\frac{\Delta m}{A}\right)^2 = k_p \times t$$ where Δm/A is the weight gain per unit area (mg/cm^2) and t the time in s.

Table 2. - Apparent parabolic rate constants k_p of selected Fe_3Al alloys oxidised in air at 900°C. The parabolic rate constants of tested alloys were calculated from the TGA curves omitting the initial oxidation (up to 200 h).

Alloy	k_p ($g^2\ cm^{-4}\ s^{-1}$)	Reference
Fe28Al3Cr0.02Ce	4.17×10^{-13}	This work
Fe30Al4Cr2.7TiB_2	6.94×10^{-13}	This work
Fe27Al15Ti	1.37×10^{-13}	[7]
Fe23Al15Ti	3.51×10^{-14}	[7]
Fe20Al2.5Zr	2×10^{-13}	[13]
Fe25Al	1.0×10^{-13}	[14]
Fe26Al9.5Nb (at 850°C)	1.3×10^{-13}	[14]

The parabolic rate constants of both iron aluminides are summarized in **Table 2** and compared to that of other Fe_3Al-based alloys.

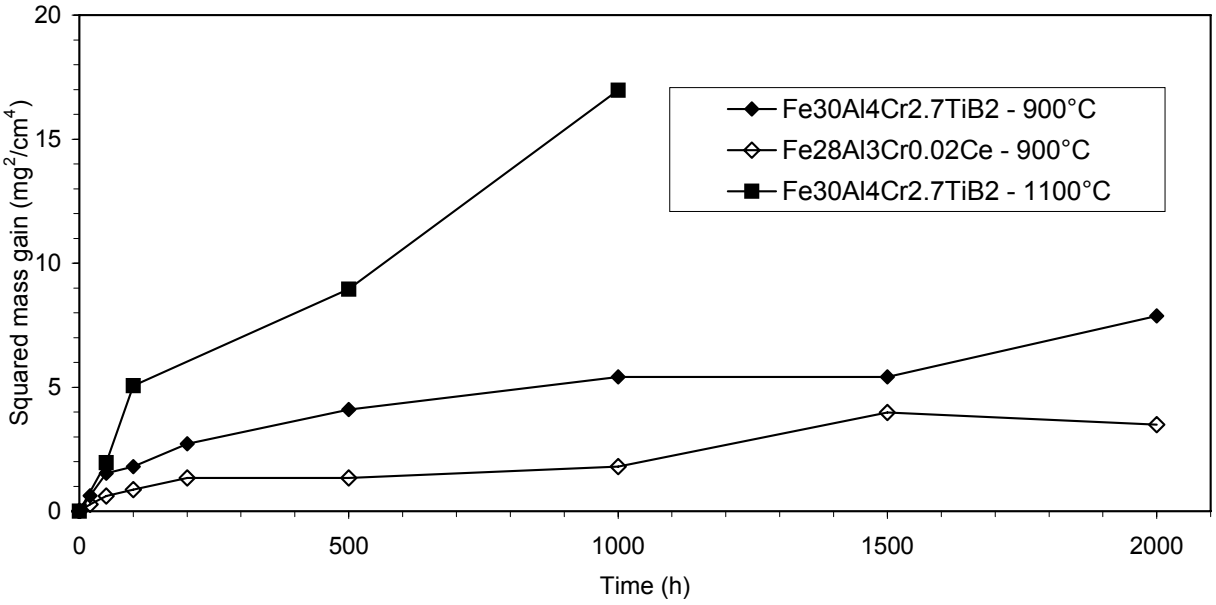

Fig. 1. Squared mass gain versus exposure time for $Fe30Al4Cr2.7TiB_2$ at 900 and 1100 °C in air (Fe28Al3Cr0.02Ce for comparison)

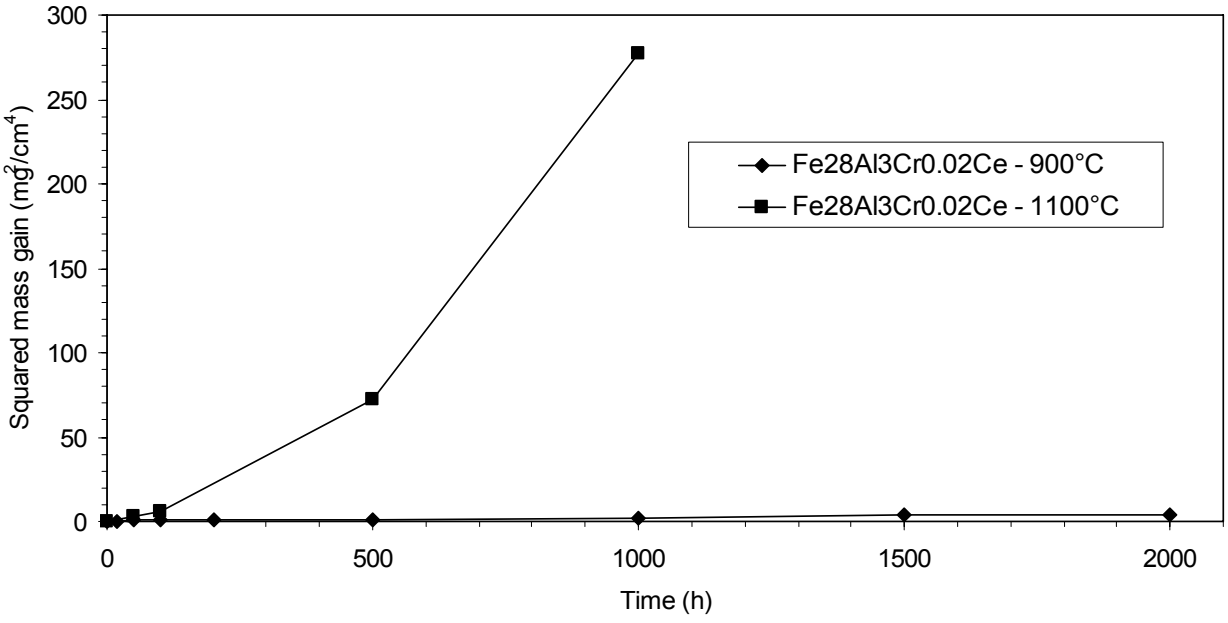

Fig. 2. Squared mass gain versus exposure time for Fe28Al3Cr0.02Ce at 900 and 1100 °C in air

Parabolic rate constants k_p for both tested alloys are about the same as for binary Fe25Al and other Fe_3Al-based alloys at 900 °C (Table 2). Even if the difference between k_p of Fe28Al3Cr0.02Ce and $Fe30Al4Cr2.7TiB_2$ is low at 900°C, mass gains of Fe28Al3Cr0.02Ce are significantly higher than $Fe30Al4Cr2.7TiB_2$ at 1100°C. In the case of Fe28Al3Cr0.02Ce, the beneficial influence of cerium on Fe_3Al oxidation behavior, which the previous investigation reported [6], wasn't found. For this tested alloy the high oxidation rate and the growth of porous and no protective scales were observed at 1100°C. Nevertheless,

these are the corrosion behaviour of this alloy is similar to oxidation of other Fe_3Al-based alloys, e.g. Fe28Al, Fe50Al at 1100°C and Fe25Al2Ta at 1000°C [3, 6, 15]. Presumably, the lower corrosion resistance of Fe28Al3Cr0.02Ce at 1100°C was caused by lower amount of Ce (ten times lower as Fe28Al4Cr0.25Ce [6]). The higher content of cerium in Fe_3Al-based alloys improved adhesion oxide scale, refined oxide grains and reduced cracks and content of iron and chromium in the alumina scale [6].

3.2 Investigations of the oxide scale and the sample surface layer

Fig. 3 reveals surface structure of Fe30Al4Cr2.7TiB_2 and Fe28Al3Cr0.02Ce at 1100°C. Fe30Al4Cr2.7TiB_2 alloy has fine grains and the surface is less damage, see Fig. 3 - A. The stable fine grain structure of the alloy with Ti_2B reduced intergranular oxidation and surface damage during long-term oxidation test at 1100°C. This investigation is in agreement with low mass gain (Fig.1). Vice-versa, the granular structure of Fe28Al3Cr0.02Ce alloy causes of significant intergranular oxidation (Fig. 3 – B) thereby probably high mass gains were measured (Fig. 2). In the case of oxidation test at 900°C, the intergranular oxidation of surface wasn't observed.

Results of EDX analyse clearly show that the oxide scales are composed of Al_2O_3. Oxide layer is thin and compact at 900°C (see Fig. 4). The structure was controlled by XRD. On the other hand, significantly thicker and more porous oxide layer was formed on the surface both tested alloys at 1100°C. The scales of Fe30Al4Cr2.7TiB_2 were more adherent than scales on the surface of Fe28Al3Cr0.02Ce and didn't spall during/after cooling to RT (see the cross section, Fig. 3 – A).

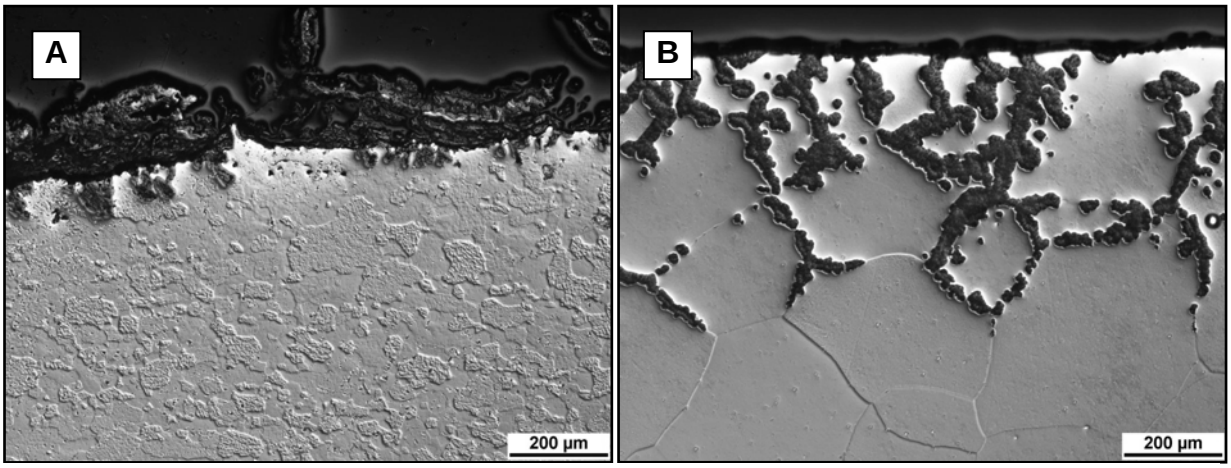

Fig. 3. Light optical micrographs of surface structure of Fe30Al4Cr2.7TiB_2 (A) and Fe28Al3Cr0.02Ce (B) after 1000 h oxidation in air at 1100°C

4. CONCLUSION

The high-temperature oxidation behaviours of Fe28Al3Cr0.02Ce and Fe30Al4Cr2.7TiB_2 have been investigated at 900 and 1100°C in air. The results of oxidation tests can be summarized as follows:

1. For the both tested iron aluminides parabolic growth was observed at 900 °C. Thin and homogeneous oxide scales were formed. The oxide layer is mainly composed of alumina.
2. For both tested alloys, parabolic rate constants k_p are about the same as for other Fe_3Al-based alloys at 900 °C.

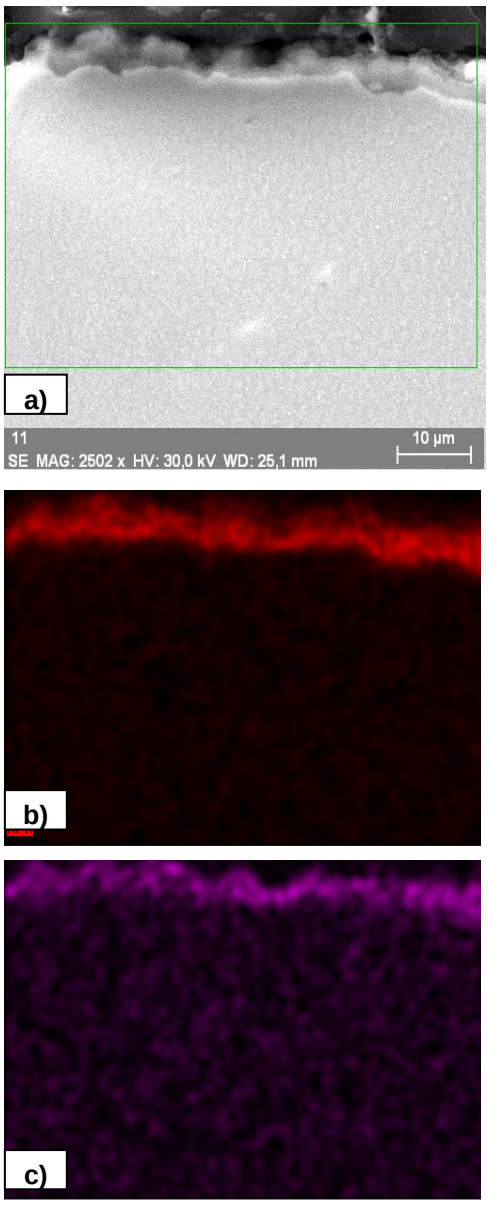

Fig. 4. EDX analyse of cross section of Fe28Al3Cr0.02Ce after 2000 h of oxidation in air at 900°C, a) SEM – SE, b) EDX – mapping of Al, c) EDX – mapping of O

3. The oxidation resistance of Fe30Al4Cr2.7TiB_2 at 1100°C is better than Fe28Al3Cr0.02Ce because of the fine grain structure of iron aluminide with TiB_2 which reduced intergranular oxidation.

5. ACKNOWLEDGEMENTS

The authors would like to thank Ing. P. Kejzlar for sample preparation and for SEM and EDX analyse. This work was supported by the Research Plan MSM 4674788501.

REFERENCES

[1] McKamey CG. Iron Aluminides, in Physical Metallurgy and processing of Intermetallic compounds, eds. Stoloff NS, Sikka VK, 1994; 351-91.

[2] Tortorelli PF, Natesan K. Critical factors affecting the high-temperature corrosion performance of iron aluminides. Mat Sci Eng 1998;A258:115-25.

[3] Rommerskirchen I, Eltester B, Grabke H.J. Oxidation of β–FeAl and Fe–Al alloys. Mat Corros 1996;47:646-9

[4] Natesan K. Corrosion performance of iron aluminides in mixed-oxidant environments. Mat Sci Eng 1998;A258:126-34.

[5] DeVan JH, Tortorelli PF. The oxidation–sulfidation behavior of iron alloys containing 16–40 at% aluminum. Corros Sci 1993;35:1065-71.

[6] Yu XQ, Sun YS. The oxidation improvement of Fe_3Al based alloy with cerium addition at temperature above 1000 °C. Mat Sci Eng 2003;A363:30-9.

[7] Palm M, Sauthoff G. Deformation behaviour and oxidation resistance of single-phase and two-phase $L2_1$-ordered Fe–Al–Ti alloys. Intermetallics 2004;12:1345-59.

[8] Krein R, Palm M. The influence of Cr and B additions on the mechanical properties and oxidation behaviour of $L2_1$-ordered Fe-Al-Ti-based alloys at high temperatures. Acta Mater 2006;56:2400-5.

[9] Lee DB, Kim GY, Kim GJ. The oxidation of Fe_3Al–(0, 2, 4, 6%)Cr alloys at 1000 °C. Mat Sci Eng 2003;A339:109-14.

[10] Kratochvíl P, Pešička J, Hakl J, Vlasák T, Hanus P. Creep behaviour of intermetalic Fe-28Al-3Cr alloy with Ce addition. J. Alloys Compd. 2004;378;258-62

[11] Dobeš F, Milička K, Kratochvíl P. Small punch creep in Fe28Al3Cr0.02Ce alloy. Intermetallics 2004;12:1397–1401.

[12] Hotař A, Kratochvíl P, Hotař V. The corrosion resistance of Fe_3Al-based iron aluminides in molten glasses. Kovove Mater. 2009;47;247:52.

[13] Stein F, Palm M, Sauthoff G. Mechanical properties and oxidation behaviour of two-phase iron aluminium alloys with $Zr(Fe,Al)_2$ Laves phase or $Zr(Fe,Al)_{12}$ τ_1 phase. Intermetallics 2005;13:1275-85.

[14] Milenkovic S, Palm M, Microstructure and mechanical properties of directionally solidified Fe-Al-Nb eutectic. Intermetallics 2008; 16:1212-18.

[15] Hotař A, Palm M, Oxidation resistance of Fe-25Al-2Ta (at.%) in air, Intermetallics 18 (2010), in press

Available online at www.sciencedirect.com
ScienceDirect
Intermetallics 15 (2007) 439–441
Intermetallics
www.elsevier.com/locate/intermet

Short communication

The corrosion resistance of iron aluminide Fe28Al3Cr0.02Ce (at%) in a molten glass

A. Hotař [a,*], P. Kratochvíl [b]

[a] Technical University of Liberce, Faculty of Engineering, Department of Materials Science, Hálkova 6, Liberec CZ-46117, Czech Republic
[b] Charles University, Faculty of Mathematics and Physics, Department of Metal Physics, Prague CZ-12116, Czech Republic

Received 10 July 2006; accepted 11 July 2006
Available online 11 September 2006

Abstract

Corrosion resistance of iron aluminides was investigated in molten glass. Iron aluminide with cerium additive (Fe28Al3Cr0.02Ce) and comparative steels (AISI 446, AISI 314) were tested and compared. The corrosion resistance was determined using measurement of weight loss. The tinting of molten glass is important to describe the interaction between the molten glass and the investigated materials. The corrosion resistance of aluminide against soda-potash glass was observed to be better than that of the compared steels.

Keywords: A. Iron aluminides, based on Fe_3Al; B. Corrosion

The advantages of Fe_3Al-based iron aluminides (for example, low material costs, low density and corrosion resistance at high temperature) may enable their use as structural elements in glass making [1]. Materials based on Fe 40–45 at% Al were tested in the Czech republic for corrosion resistance in molten glass in the early fifties of the last century, see e.g. [2]. Results of corrosion resistance were very good, but material was used only in cast state because of poor room-temperature ductility and bad machinability. High content of carbon was also a disadvantage for using in molten glass. Therefore this material was used for elements outside molten glass (for example, burners, holders, etc.).

Special requirements necessary for the use of metals and alloys in molten glass are namely high corrosion resistance at high temperatures (to 1200 °C), low tint of glass, low generation of bubbles and high enough values of mechanical properties at high temperature.

The solution of metal in molten glass has mostly the character of oxidation [3]. The oxidation in molten glass differs from oxidation in gaseous environment because protective scales are not formed on the surface during corrosion in molten glass. The process of corrosion can be measured as a weight loss (weight change), while the formed oxides immediately dissolve in the neighbouring molten glass where their concentration may increase up to saturation level. The diffusion of impurities into molten glass is therefore reduced. This is the process which takes place near metallic parts inserted into the molten glass.

The iron aluminide (composition in at% Fe–28Al–3Cr–0.12C–0.3Mn–0.02Ce) was tested for corrosion resistance and the corrosion resistance was compared to steels AISI 314 and AISI 446 (both with Cr contents over 20 at%). The samples of iron aluminide as well as of steels for testing were cylinders (∅;12 × 18 mm long) machined from sheets of 13 mm thick, which were prepared by rolling at 1200 °C. The grains are elongated in the rolling direction. After corrosion tests (holding at 1250 °C and 1350 °C) structure is recrystallized.

The test samples were placed in alumina crucibles, which were prior filled with scrap glass. Soda-potash glass (container ware), which is 60% from all produced glass, was used for corrosion test. The conditions (time, temperature) of corrosion tests are summarized in Fig. 1, where the extent of molten

* Corresponding author. Tel.: +420 485 353 136; fax: +420 485 353 631.
E-mail address: adam.hotar@tul.cz (A. Hotař).

0966-9795/$ - see front matter © 2006 Elsevier Ltd. All rights reserved.
doi:10.1016/j.intermet.2006.07.006

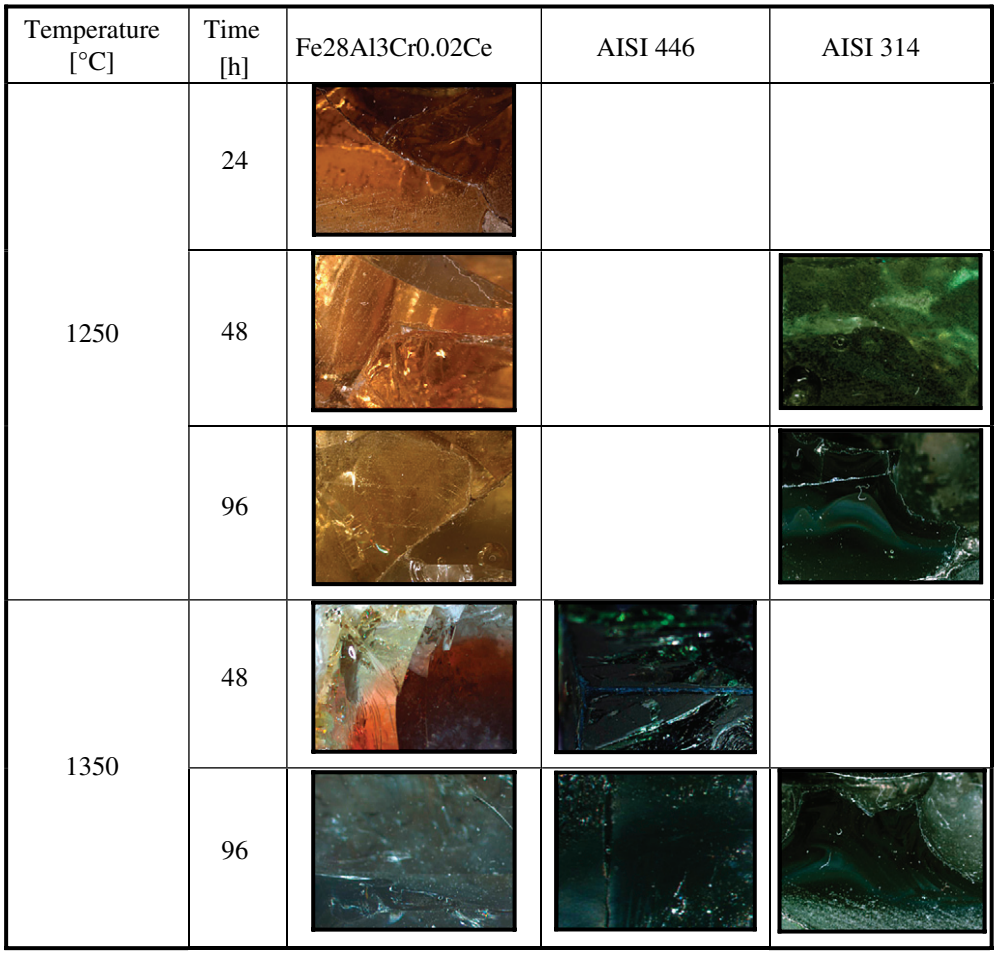

Fig. 1. The summary of tinting during corrosion tests in molten glass (temperature, time of interaction), photography area is 7 × 5 mm.

glass tinting by iron aluminide and by steels up to 1350 °C and 96 h is obvious too. It is less intensive than for steels. The tint of glass by interaction with iron aluminide is due mainly to the dissolution of Al_2O_3 (especially) and of Fe_2O_3. Cr_2O_3 (very intensive green tint) dissolves very quickly from steels to molten glass.

The corrosion resistance was determined by measurement of weight loss. The iron aluminide obviously behaves better than comparative steel under all corrosion conditions (Table 1). The difference between iron aluminide and steels at 1250 °C/48 h is very pronounced. Corrosion resistance is 9 times higher than austenitic steel. The corrosion in the molten glass is compared with that in air, e.g. at 1200 °C in Fig. 2.

These results show that iron aluminide has better corrosion resistance against molten glass (soda-potash type) than the steels compared. Therefore iron aluminides could replace

Table 1
Weight loss after corrosion test in soda-potash molten glass at 1350 °C and 1250 °C

Temperature [°C]	Time [h]	Fe28Al3Cr0.02Ce [mg/cm^2]	AISI 446 [mg/cm^2]	AISI 314 [mg/cm^2]
1250	24	2.2	–	–
	48	2.1	17.8	–
	96	5.5	21.7	–
1350	48	10.6	–	–
	96	18.8	103.3	97.1

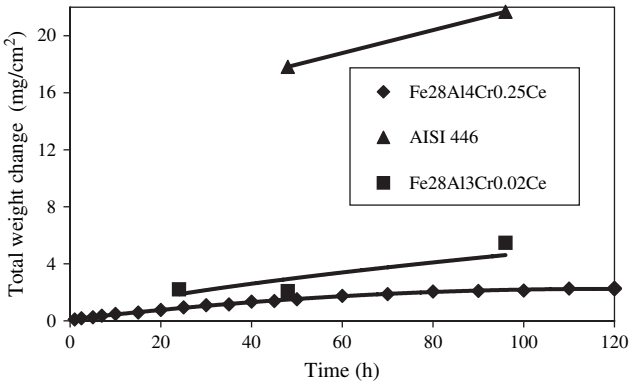

Fig. 2. Comparison of the total weight gain of Fe28Al4Cr0.25Ce (scales) during corrosion in air at 1200 °C [4]and weight loss of Fe28Al3Cr0.02Ce – this paper (dissolution of oxides) and AISI 446 – this paper (dissolution of oxides) in soda-potash molten glass at 1250 °C.

heat resistant steels for applications in soda-potash molten glass to 1200 °C. Feeder plungers, parts of gatherer and elements for mechanical homogenizing of molten glass are the prospective applications.

The results can be summarized as follows:

1 The tested iron aluminide tints molten glass (up to 1350 °C/96 h.) less intensively and its dissolution is much slower than that of steels AISI 314 and 446.
2 Corrosion tests demonstrate that corrosion properties of iron aluminides in soda-potash molten glass are better than comparative steels.
3 The iron aluminides could replace heat resistant steels, which are used mainly in soda-potash molten glass to 1200 °C.

Acknowledgements

The authors wish to thank the late Roland Kirsch, Ph.D. for important advice and comments on metals in glassmaking. Special thanks go to Gréta Nováková, M.Sc. This work was supported by the Czech Science Foundation (GA CR 106/05/P167).

References

[1] McKamey CG, DeVan JH, Tortorelli PF, Sikka VKJ. Mater Res 1991;6:1779–805.
[2] Uxa V. Sklář a keramik 1956;6:225–8 [in Czech].
[3] Kirsch R. Metals in glassmaking. Elsevier Science Ltd; 1993.
[4] Xinquan Y, Yangshan S. Mater Sci Eng 2003;A363:30–9.

The corrosion resistance of Fe_3Al-based iron aluminides in molten glasses

A. Hotař[1]*, P. Kratochvíl[1], V. Hotař[2]

[1] *Technical University of Liberec, Faculty of Engineering, Department of Materials Science, Studentská 2, CZ 46117 Liberec, Czech Republic*
[2] *Technical University of Liberec, Faculty of Engineering, Department of Glass Producing Machines and Robotics, Studentská 2, CZ 46117 Liberec, Czech Republic*

Received 7 August 2008, received in revised form 19 February 2009, accepted 23 March 2009

Abstract

Corrosion resistance of iron aluminides was investigated in molten soda-lime glass and molten lead glass. Iron aluminides with different additives and comparative steel (EN X8CrNi 25-21) were tested in laboratory conditions and compared. The corrosion resistance was determined using measurement of weight change and change of surface. The tinting of molten glasses is important to describe the interaction between the molten glass and the investigated materials. The alloys Fe25Al5Cr and Fe28Al3Cr0.02Ce have very good corrosion resistance against both glasses. The preferential oxidation of aluminium is typical for all tested iron aluminides and generated alumina slows down corrosion of these alloys. The plunger for molten glass output control was produced from Fe25Al2Cr and the application plant test of plunger has been running in lead molten glass. Damage of the surface is typical for doped Zr iron aluminide.

K e y w o r d s: iron aluminide (Fe_3Al type), corrosion resistance, molten soda-lime glass, molten lead glass

1. Introduction

Fe_3Al-based iron aluminides have been studied as candidates for high-temperature structural applications in glass making. The main advantages of Fe_3Al-type iron aluminides compared to chromium-nickel steels are low material costs, low density and corrosion resistance at high temperature [1]. On the other hand, these alloys have low ductility at room temperature and low high-temperature strength. However, these disadvantages can be partly suppressed by off-stochiometric composition (e.g. 28 at.% Al) and ternary additives (especially chromium) in combination with grain refinement agents such as Ce.

Alloys based on Fe_3Al and FeAl have excellent oxidation resistance at high temperatures. High-temperature corrosion resistance of alloys based on Fe-Al in oxidation media is caused by creation, maintenance of intact and adherent layer of Al_2O_3 [2]. Minimum aluminium content for pure binary Fe-Al alloy is approx. 16–19 at.%. Aluminium content of investigated iron aluminides is satisfactory to originate continuous aluminium oxide layer. The temperatures for the formation of high-quality protective of α-Al_2O_3 layer are 800–900 ℃. Alloying can influence corrosion resistance of iron aluminides, too. Chromium addition in amount greater as 4 at.% deteriorates corrosion resistance [3]. Vice-versa, cerium has positive effect on corrosion resistance of iron aluminides based on Fe_3Al at temperatures above 1000 ℃ [4].

The corrosion resistance of materials based on Fe40–45at.%Al in molten glass was tested in the Czech Republic in the early fifties of the last century, see e.g. [5]. Results of corrosion resistance were very good but high content of carbon was a disadvantage for using in molten glass. Therefore this material was used for parts of furnaces, which were not in contact with molten glass (for example burners, holders etc.).

Special requirements necessary for the use of metals and alloys in molten glass are namely high

*Corresponding author: tel.: +420 485 353 136; e-mail address: adam.hotar@tul.cz

Table 1. Chemical composition of the alloys

Materials		Chemical composition							
		Al	C	Ce	Zr	Cr	Mn	Ni	Fe
Fe25Al5Cr	wt.%	14.20	0.02	–	–	5.63	max. 0.45	–	Bal.
	at.%	25.41	0.08	–	–	5.23	max. 0.40	–	Bal.
Fe28Al3Cr0.02Ce	wt.%	16.13	0.04	0.06	–	2.85	0.46	–	Bal.
	at.%	28.39	0.16	0.02	–	2.60	0.40	–	Bal.
Fe28Al3Cr0.5Zr	wt.%	17.39	0.05	–	0.47	3.72	0.20	–	Bal.
	at.%	28.06	0.2	–	0.53	2.85	0.26	–	Bal.
EN X8CrNi25-21 (ČSN 417 255)	wt.%	–	max. 0.20	–	–	24.00–26.00	1.50	19.00–22.00	Bal.
	at.%	–	max. 0.92	–	–	25.37–27.48	1.50	17.79–20.60	Bal.

corrosion resistance at high temperatures (to 1200 °C), low tint of glass, low generation of bubbles and proper values of mechanical strength [6] and creep properties at high temperatures [7].

The solution of metal in molten glass has mostly the character of oxidation [8]. The oxidation in molten glass differs from oxidation in gaseous environment because generally protective scales are not formed on the surface during corrosion in molten glass. The process of corrosion can be measured as a weight loss (weight change), while the formed oxides immediately dissolve in the neighbouring molten glass where their concentration may increase up to saturation level. This is the process, which takes place near metallic parts inserted into the molten glass.

The aim of the present paper is to describe corrosion resistance of alloys based on Fe_3Al (with different composition) in molten soda-lime glass and molten lead crystal. The results are compared with steel EN X8CrNi25-21, which is now frequently used in molten glasses.

2. Experimental procedure

The iron aluminides of different composition (Table 1) were tested for corrosion resistance and that was compared to steel EN X8CrNi25-21. The samples were cylinders (ø 12 mm × 18 mm long) machined from sheets 13 mm thick, which were prepared by rolling at 1200 °C. The grains are elongated in the rolling direction (Fig. 1). The structure after corrosion tests (holding at 1200 °C) is recrystallized.

The test samples were placed in alumina crucibles, which were prior filled with scrap glass, in the furnace. All tests were carried out at 1200 °C. The corrosion tests were performed in different mol-

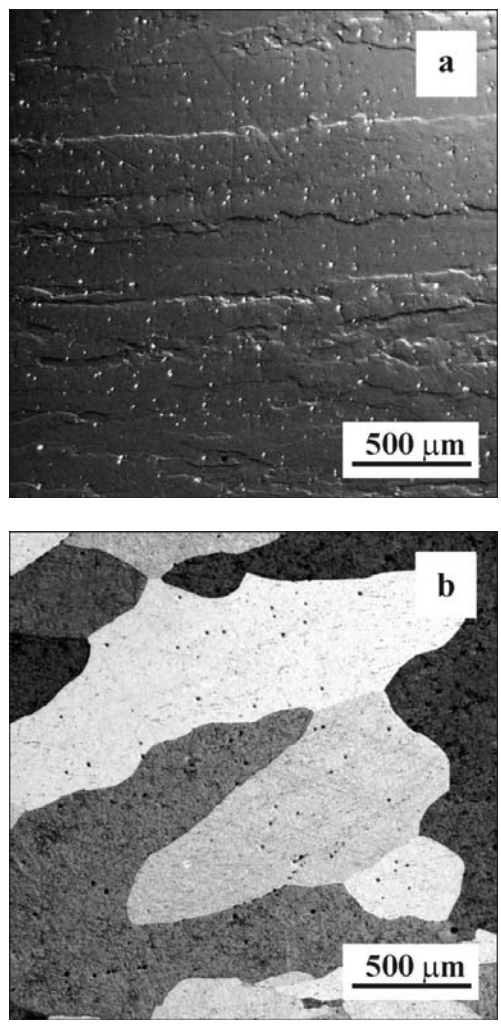

Fig. 1. (a) Structure of Fe28Al3Cr0.02Ce – Mastermet reagent, (b) structure of Fe28Al3Cr0.02Ce (to the right) after corrosion test in molten lead glass at 1200 °C/72 h – Rollason's reagent.

Table 2. Chemical composition of the glasses before tests; viscosities of molten glasses at 1200 °C

Composition (wt.%)	SiO_2	Al_2O_3	Fe_2O_3	CaO	MgO	K_2O	Na_2O	SO_3	Viscosity log η (dPa)
Soda-lime glass (transparent container glass)	74.03	1.67	0.05	10.08	0.54	0.62	12.68	0.13	2.67
Composition (wt.%)	SiO_2	Na_2O	K_2O	BaO	PbO	ZnO	As_2O_3	Er_2O_3	Viscosity log η (dPa)
Lead crystal	53.0	2.5	10.8	0.7	32.0	0.7	0.2	0.018	3.28

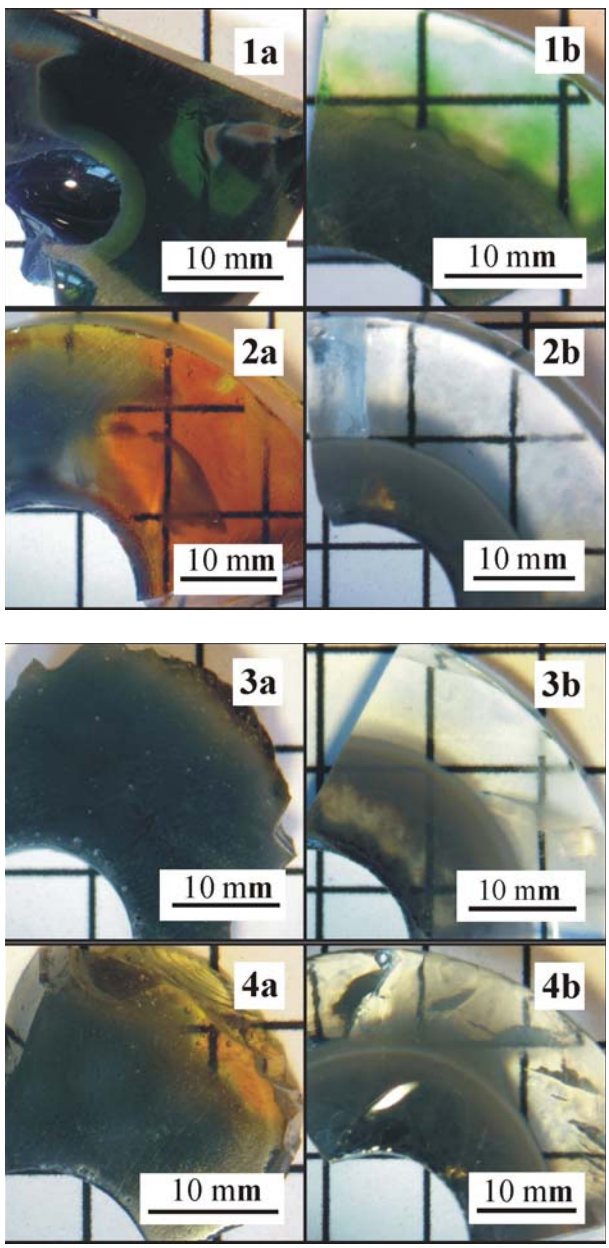

Fig. 2. The tinting of soda-lime glass (a) and lead crystal (b) after interaction with alloys, time interval 168 h; 1 – EN X8CrNi25-21, 2 – Fe25Al5Cr, 3 – Fe28Al3Cr0.02Ce, 4 – Fe28Al3Cr0.5Zr.

ten glasses (Table 2) for time intervals: 24, 48, 72, 96, 168 hours. After each test the crucibles were cooled down in furnace, subsequently carefully broken and the glass separated from surface of alloys except for Fe28Al3Cr0.5Zr. The corrosion resistance was determined using measurement of the weight change and change of surface roughness. Change of chemical composition of glasses was measured by EDX.

3. Results and discussion

3.1. Corrosion resistance of tested alloys

Describing of tinting by the interaction between alloys and glasses is very important. The tinting of both glasses after 168 hours is obvious in Fig. 2. (colour version on the website). The cylindrical samples were situated (tinting the glass) in lower left corner. Soda-lime glass is tinted more intensively than lead crystal after interaction with alloys.

Iron aluminides tint glasses mainly to grey. Yellow-brown tint of soda-lime glass was also observed after corrosion test with iron aluminides. This colour is little intensive (glass is still transparent) and it is typical for soda-lime glass after interaction with Fe25Al5Cr. On the contrary, comparative steel tinted both glasses to dark green. The dark green tint of steel was caused especially by Cr_2O_3, which dissolves very quickly from steels to molten glass. Only a small quantity of Cr_2O_3 tints very intensively [8]. In the picture you can see bubbles in the scrap of soda-lime glass. In preference carbon reacted with SO_3 during interaction steel with soda-lime glass and gases (CO_2 and SO_2) generated.

The corrosion resistance was determined by measurement of weight change. Weight loss is typical for all alloys with the exception of iron aluminide alloyed by Zr. Weight gain of iron aluminide alloyed by Zr is due to glued-on thin layer of glass on the surface of specimen, therefore the corrosion cannot be quantified. Other specimens for iron aluminides have lower weight loss than comparative steel (Figs. 3 and 4). The rate of solution in molten glass is very important parameter. The slopes of curve show that alloys Fe25Al5Cr and Fe28Al3Cr0.02Ce have smaller rate of solution in

Table 3. The rate of solution in molten glasses

Glass	Temperature (°C)	Fe25Al5Cr (mm/year)	Fe28Al3Cr0.02Ce (mm/year)	EN X8CrNi25-21 (mm/year)
Lead crystal	1200	0.5	0.8	1.0
Soda-lime glass	1200	0.9	1.2	1.9
	1350	No measurement	2.6	11.2

Table 4. The roughness parameters of boundaries between alloys and glasses, D_{C1000} average compass dimension (multiplied by 1000), STD average standard deviation and R_t average maximum roughness

Glass, time period	Fe25Al5Cr			Fe28Al3Cr0.02Ce			Fe28Al3Cr0.5Zr			EN X8CrNi25-21		
	D_{C1000} (–)	STD (μm)	R_t (μm)	D_{C1000} (–)	STD (μm)	R_t (μm)	D_{C1000} (–)	STD (μm)	R_t (μm)	D_{C1000} (–)	STD (μm)	R_t (μm)
Before the test	1016	0.8	3.7	1018	0.8	4.7	1017	0.7	3.2	1012	0.6	3.3
Lead crystal, 168 h	1010	1.7	7.6	1017	2.6	11.0	1057	8.4	36.2	1042	2.5	12.1
Soda-lime glass, 168 h	1020	2.0	8.3	1023	2.7	13.1	1037	10.8	46.1	1036	8.8	34.0

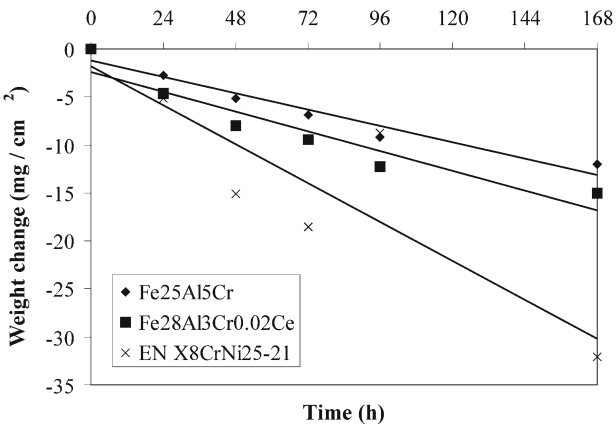

Fig. 3. The dependence of weight loss on time in soda-lime glass at 1200 °C.

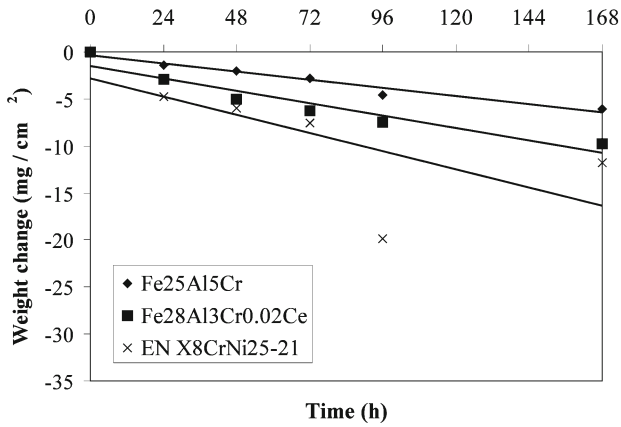

Fig. 4. The dependence of weight loss on time in lead crystal at 1200 °C.

both glasses than comparative steel. The difference of solution rate is greater at 1350 °C in soda-lime glass, see Table 3.

The surface roughness of samples was measured after the exposure to molten glass. The corroded surface was observed using light optical microscopy. The boundary curve (see Fig. 5) was described by a software tool. For a quantification of the metal roughness fractal geometry and statistic tools were used. The dividing curve generated is described by a fractal dimension (a compass dimension multiplied by 1000, D_{C1000}, for details see [9]) that expresses the degree of complexity of the interface between alloy and glass by means of a single number. Also average standard deviation (STD) of all the curves and average maximum roughness of all the curves (R_t) are used for the statistical description [10]. These parameters are given in Table 4.

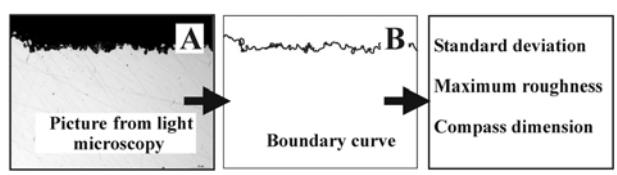

Fig. 5. Description of boundary curve.

The values of roughness parameters show that all testing materials are less damaged after interaction in lead molten glass than in molten soda-lime glass. Low roughness parameters of iron aluminides (Fe25Al5Cr, Fe28Al3Cr0.02Ce) are obvious from all

results. Austenitic steel (EN X8CrNi25-21) has similar values as Fe28Al3Cr0.02Ce after interaction in lead molten glass but surface of this steel is more damaged after interaction in soda-lime molten glass. In the case of Fe28Al3Cr0.5Zr, the damaged surface layer is very thick. Probably this is caused by selective surface corrosion. The detrimental effect of Zr on oxidation resistance of iron aluminides is realized also in [11].

3.2. Corrosion mechanism of iron aluminides

Diffusion of aluminium from samples and preferential oxidation of aluminium are typical for all tested iron aluminides. The reaction of Al with SiO_2 causes a formation of Al_2O_3 and Si in both glasses. Al_2O_3 layer is formed at the glass/alloy interface, which is partially protected against further solution of iron aluminides. In addition alumina, which is concentrated near the surface of samples, increases viscosity and also slows down corrosion of these alloys.

The generated Si small particles cause grey tint of soda-lime glass. If a reducing effect of aluminium is lower, aluminium reacts with SO_3 and Fe_2O_3 and the yellow-brown tint of soda-lime glass generates. Small bubbles in soda-lime glass are caused by the reaction Al with SO_3, too.

In the case of a lead crystal, Al reacts especially with PbO and the reaction causes a formation of Al_2O_3 and Pb. The reaction of aluminium with SiO_2 also takes place at the same time. Small particles of Pb and Si formed grey area around the sample.

Higher corrosion rates of all tested alloys in soda-lime glass are caused by different chemical composition, especially by the content of SO_3 (Table 2) because corrosion resistance of majority of metals decreases with increasing content of SO_3 [8]. Viscosity of glasses also has influence on rates of alloy solution because diffusion and glass flow are slowed down with increasing viscosity. But lower viscosity of lead crystal than that of soda-lime glass does not increase solution rate of alloys in lead crystal too much (see Table 2).

All tested iron aluminides have sufficient content of aluminium for good corrosion resistance in molten glass. Differences of aluminium content in iron aluminides are small and lower content of Al can cause only shorter oxidation lifetime of iron aluminides in molten glasses. Therefore alloying elements (Cr, Zr, Ce) probably have an effect on corrosion rate. For understanding of the effect of alloying elements on corrosion mechanism of iron aluminides in tested molten glasses, further studies and analysis are necessary.

3.3. Application plant tests

The application plant tests also run in lead molten glass at present because alloys Fe25Al5Cr and Fe28Al3Cr0.02Ce have very good corrosion resistance. The plungers for molten glass output control from glass furnace were casted from iron aluminide base on Fe_3Al. Final shapes of plungers were produced by investment casting to save cost production. The as-cast plunger from Fe25Al2Cr is cyclically heated up from room temperature to working temperature. The working temperature of molten glass is 900–1050 ℃ and temperature of furnace atmosphere is 1130–1150 ℃. The plunger is now used without damage for 79 cycles (i.e. 312 hours at service temperature) under these conditions.

4. Conclusions

1. Alloy Fe25Al5Cr has better corrosion resistance against both molten glasses (soda-lime molten glass and lead molten glass) than the steel EN X8CrNi25--21. The alloy Fe25Al5Cr tinted less intensively both glasses and the rate of solution and damage of surface were the lowest.

2. Alloy Fe28Al3Cr0.02Ce offers better resistance also to soda-lime glass than EN X8CrNi25-21. It dissolves slower and the surface is smoother. On the other hand, the corrosion resistance of iron aluminide with Ce to lead molten glass is comparable to steel EN X8CrNi25-21.

3. The alloy Fe28Al3Cr0.5Zr has different results of corrosion resistance. Thin layer of glass is glued on the samples of iron aluminides with Zr therefore the corrosion cannot be quantified. Large damage of samples surface is typical for this type of iron aluminide.

4. The preferential oxidation of aluminium is typical for all tested iron aluminides. Generated alumina formed a layer at the glass/alloy interface, which partially protected iron aluminides against further solution. In addition, alumina around samples increases viscosity and it also slows down corrosion of these alloys.

5. Tested iron aluminides have sufficient content of aluminium for good corrosion resistance in molten glass. Small differences among corrosion rates of tested iron aluminides are probably caused by alloying elements (Cr, Zr, Ce).

6. The good laboratory results stimulated the application plant tests of iron aluminide based on Fe_3Al run in lead molten glass. Iron aluminides (especially Fe25Al5Cr) could replace heat resistant steels for applications in soda-lime molten glass to 1200 ℃. Feeder plungers, parts of gatherer and elements for mechanical homogenizing of molten glass are the prospective applications.

Acknowledgements

The authors would like to thank A. Smrček for help with describing of corrosion mechanism.

This work was supported by the Research Plan of Ministry of Education MSM 4674788501.

References

[1] McKAMEY, C. G.—DeVAN, J. H.—TORTORELLI, P. F.—SIKKA, V. K. J.: Mater Res, *6*, 1991, p. 1779.
[2] TORTORELLI, P. F.—NATESAN, K.: Mat. Sci. Eng., *A258*, 1998, p. 115.
[3] LEE, D. B.—KIM, G. Y.—KIM, G. J.: Mat. Sci. Eng., *A339*, 2003, p. 109.
[4] XINQUAN, Y.—YANGSHAN, S.: Mat. Sci. Eng., *A363*, 2003, p. 30.
[5] UXA, V.: Sklář a keramik, *6*, 1956, p. 225 (in Czech).
[6] HOTAŘ, A.—KRATOCHVÍL, P.: Kovove Mater., *40*, 2002, p. 45 (in Czech).
[7] KRATOCHVÍL, P.—HANUS, P.—HAKL, J.—VLASÁK, T.: Kovove Mater., *42*, 2004, p. 73.
[8] KIRSCH, R.: Metals in Glassmaking. Amsterdam, Elsevier Science Ltd. 1993.
[9] MANDELBROT, B. B.: The Fractal Geometry of Nature. 2nd ed. New York, Freeman WH and Co. 1982.
[10] HOTAŘ, V.—NOVOTNÝ, F.: In.: Proceedings of 11th International Conference on Fracture. Ed.: Carpinteri, A. Turin, CCI Centro Congressi Internazionale s.r.l. 2005, p. 588.
[11] STEIN, F.—PALM, M.—SAUTHOFF, G.: Intermetallics, *13*, 2005, p. 1275.

Kovove Mater. 52 2014 149–155
DOI: 10.4149/km_2014_3_149

Corrosion behaviour of Fe-40Al-Zr (at.%) alloy in molten soda-lime glass

A. Hotař[1]*, V. Hotař[2], F. Novotný[3]

[1] *Technical University of Liberec, Faculty of Engineering, Department of Material Science, Studentská 2, 461 17 Liberec, Czech Republic*
[2] *Technical University of Liberec, Faculty of Engineering, Department of Glass Producing Machines and Robotics, Studentská 2, 461 17 Liberec, Czech Republic*
[3] *Institute of Chemical Technology, Department of Glass and Ceramics, Technická 5, 166 28 Prague 6, Czech Republic*

Received 11 December 2013, received in revised form 29 January 2014, accepted 12 February 2014

Abstract

The corrosion behaviour of Fe-40Al-Zr (at.%) has been investigated in molten soda-lime glass at 1200 °C. The measurement of weight loss and surface change were used for explanation of the corrosion resistance. The alloying by 0.09 at.% Zr reduces the corrosion resistance of Fe-40Al-Zr against molten soda-lime glass in comparison with earlier tested Fe-25Al-5Cr alloy. The corrosion mechanism of Fe-40Al-Zr alloy in molten soda-lime glass was also described. During reactions between tested iron aluminide and glass oxides, Al_2O_3 was generated and preferential oxidation of Zr-rich precipitates occurred.

K e y w o r d s: iron aluminide (FeAl type), corrosion behaviour, molten soda-lime glass

1. Introduction

Fe-Al and Fe_3Al based alloys are of interest as possible replacement for various stainless steels because their high-temperature oxidation resistance is very good [1–3]. Other advantages of Fe-Al and Fe_3Al based alloys are low material cost and their low density compared to that of steels. However, high-temperature strength and creep properties of binary Fe-Al alloys are insufficient for structural applications. One of the ways to improve strength at high-temperature is alloying by elements, which cause formation of second phases as strengthening particles (for example Zr, Nb or Ta), or solid solution strengthening (for example Ti) [4–7].

Iron aluminides are generally regarded as very oxidation resistant because dense and adherent oxide scales of α-Al_2O_3 form on the surface [1–3]. However, the phase composition of scales can change depending on the chemical composition of the alloy, temperature and exposure time. In addition to α-Al_2O_3, scales can also contain metastable γ-, δ-, θ-Al_2O_3 and iron oxides and oxides of ternary alloying elements, which cause an increase of the oxidation rate in many cases. The Zr content influences the oxidation behaviour of Fe_3Al alloys very significantly. The positive effect of small Zr concentrations on the oxidation behaviour of Fe_3Al alloys was already discussed [2, 8–10]. The addition of Zr in the range 0.05–0.1 at.% is used as reactive element, which improves especially the adherence of the α-Al_2O_3 scales on the Fe_3Al-Cr alloys [8, 10, 11]. If the Fe_3Al-Cr alloy's content of Zr is in the range 0.1–1.0 at.%, very good oxidation resistance was observed only up to 900 °C [12, 13]. The temperature increase above 1000 °C causes the penetration of oxides into the samples what increases the oxidation rate [12, 13]. Large amounts of Zr (above 1 at.%) have detrimental effect on the oxidation behaviour even at 900 °C [6].

Testing of the corrosion resistance against molten glasses has been stimulated by the very good oxidation resistance of iron aluminides in air. First test of alloys based on Fe-Al (with 40–45 at.% Al) in the glass industry was performed by Uxa [14] in the early fifties of the 20th century. This alloy was used specifically for burners, valves, holders, etc., and replaced the elements from cast iron. The corrosion resistance of iron

*Corresponding author: tel.: +420 485 353 136; e-mail address: adam.hotar@tul.cz

Table 1. Chemical composition of the alloys in at.%

Alloy	Al	Cr	Zr	Mn	B	Mo	Fe
Fe-40Al-Zr	40.61	0.02	0.09	0.15	0.05	0.01	Bal.

aluminides based on Fe_3Al type alloys against soda-lime glass and molten lead crystal was reported in [15, 16]. The results were compared with austenitic steel (EN X8CrNi25-21), which is frequently used in molten glasses.

It is the purpose of this paper to present corrosion tests of Fe-40Al-Zr (at.%) in molten soda-lime glass. The findings extend the knowledge about corrosion resistance and behaviour of iron aluminides in molten soda-lime glass, which is used for the production of flat and container glass.

2. Experimental

The composition of the tested material is given in Table 1. The alloy contained also carbon as technical impurity coming from the raw metal, which was used for the preparation of the alloys. A vacuum induction furnace was used for melting of the alloy. The ingot (approximately 19 mm × 33 mm in cross section) was subsequently hot rolled at 1200 °C in ten passes to a sheet of 5.3 mm thickness. Rolling of the ingot was performed in a protective capsule as described in [17]. Small cuboids were cut from the sheet and the sample surfaces were ground using SiC papers up to 1200 grit.

The corrosion experiments were performed in soda-lime glass (Table 2) at 1200 °C. Each sample was placed (on the smallest side of cuboid) in an alumina crucible and the crucible was subsequently filled with glass scrap. Then the crucible was heated to 1200 °C in a muffle furnace. The corrosion tests were carried out for 24, 48, 72 and 96 h. After each time interval, the crucible was cooled down slowly in the furnace. The cold crucible was carefully broken and the glass separated from the surface of the samples. The corrosion behaviour in molten glass was investigated by measuring the weight loss and the change of surface roughness. For each time interval, weight loss is an arithmetic average of three measurements. Chemical analysis of the samples surface was carried out by energy-dispersive X-ray spectrometry (EDS; Bruker). For the determination of the chemical composition of the glass, an ARL 9400 XP sequential WD-XRF spectrometer was used.

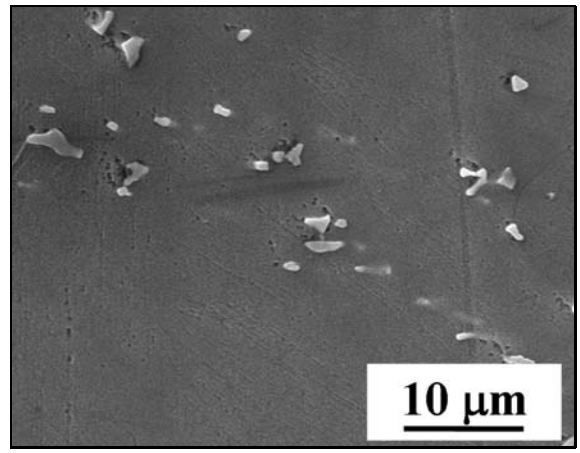

Fig. 1. SEM-SE micrograph of Fe-40Al-Zr alloy in the as rolled condition; detail of ZrC particles (light phase) in FeAl matrix (dark gray).

3. Results and discussion

The microstructure of Fe-40Al-Zr alloy consists of FeAl matrix and ZrC particles after hot rolling at 1200 °C. The phase analysis has been performed by EDS (Fig. 1).

The behaviour of Fe-40Al-Zr alloy in contact with molten soda-lime glass was determined by measurements of mass loss, roughness change and chemical analysis of samples surface and glass. Figure 2 reveals the corrosion kinetics of the tested alloy in molten soda-lime glass at 1200 °C. The slope of the curves shows that Fe-40Al-Zr dissolves faster in the early stage. The slowing down of solution of Fe-40Al-Zr after 72 and 96 h of interaction is probably caused by an increased concentration of corrosion products (probably iron disilicide or oxides of the alloy) near the surface of samples. This saturated area presumably partially reduces chemical reaction between the alloy and the molten glass. However, the corrosion rate of Fe-40Al-Zr in molten soda-lime glass is the highest

Table 2. Chemical composition of soda-lime glass determined using XRF analysis

Composition (wt.%)	SiO_2	Al_2O_3	Fe_2O_3	CaO	MgO	K_2O	Na_2O	SO_3	TiO_2
Before corrosion test	72.359	0.982	0.087	8.411	4.237	0.221	13.426	0.121	0.063
After corrosion test at 1200 °C/96 h	71.587	1.234	0.098	8.407	4.388	0.209	13.707	0.231	0.063

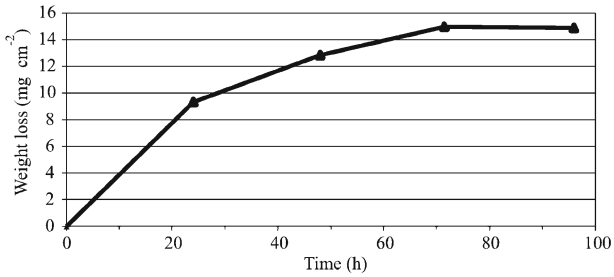

Fig. 2. Weight loss of Fe-40Al-Zr as a function of time during interaction with soda-lime glass at 1200 °C.

Table 3. Corrosion rates of iron aluminides in soda-lime glass at 1200 °C, calculated from weight loss after 96 h

Alloys	Corrosion rates (mm/year)	Reference
Fe-40Al-Zr	2.1	This work
Fe-28Al-3Cr-0.5Zr*	x	[16]
Fe-25Al-5Cr	1.4	[16]
EN X8CrNi25-21	1.8	[16]

*weight gain was measured

among the compared iron aluminides (Table 3). Iron aluminides and steel from [16] were tested in different molten soda-lime glass (container glass instead of flat glass), but the composition of both glasses is very similar, therefore it is possible to compare the corrosion rates.

Corrosion rate R was evaluated from

$$R = 87.6\frac{W}{ATd}, \tag{1}$$

where W is the weight loss (mg), A is the area of a sample (cm^2), T is time of exposure (h) and d is the density of alloy (g cm^{-3}).

The corrosion resistance of the tested alloy may be described also using the roughness of the surface. The surface roughness of samples was measured after 96 h exposure to molten glass. The cross section of the surface was investigated using light optical microscopy, see Fig. 3a. The shape of the surface – dividing line between the alloy and glass (boundary curve) was evaluated (Fig. 3b) and described by image analysis using a software tool developed in Matlab [18]. Many types of parameters can be used for a quantification of the metal roughness. The parameters can be divided into three groups:

(i) *parameters of amplitude,* useful for corrosion depth characterization, Rt – maximum roughness is used as an example in Table 4 (Fig. 3c), the parameter is surface profile parameter defined by standard ISO 4287-1997;

(ii) *parameters of frequency,* used to describe surface profile spacing parameters and for corrugation frequency characterization, an example in the Table 4 is Sm – mean spacing used (Fig. 3c), the parameter is defined by equation:

$$\mathrm{Sm} = \frac{1}{n}\sum_{i=1}^{n} S_i; \tag{2}$$

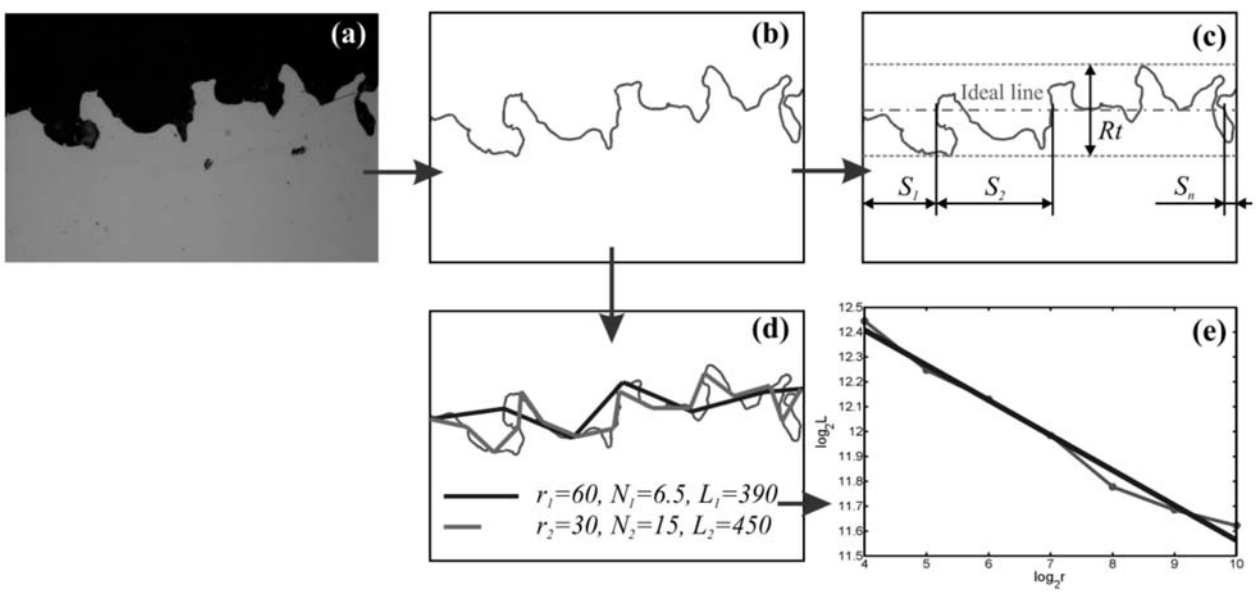

Fig. 3. Image analysis: gray scale image from light optical microscopy (a), evaluated dividing line between the alloy and glass (boundary curve) (b), parameter of amplitude (Rt – maximum roughness) and parameter of frequency (Sm – mean spacing) (c), computing of compass dimension: measurement of profile length by different ruler r_i (d), generation of Richardson-Mandelbrot plot, a compass dimension computing D_C from slope (e).

Table 4. The roughness parameters of boundary curves of alloys after corrosion test at 1200 °C/96 h

Parameters (average of ten measured sections)	Fe-40Al-Zr	Fe-28Al-3Cr-0.5Zr	Fe-25Al-5Cr	EN X8CrNi25-21
Rt – Maximum roughness (μm)	36.0	127.7	8.1	28.4
Sm – Mean spacing (μm)	38.5	25.6	14.6	18.4
D_C 1000 – Compass dimension, estimated Fractal dimension (–)	1072	1203	1017	1090

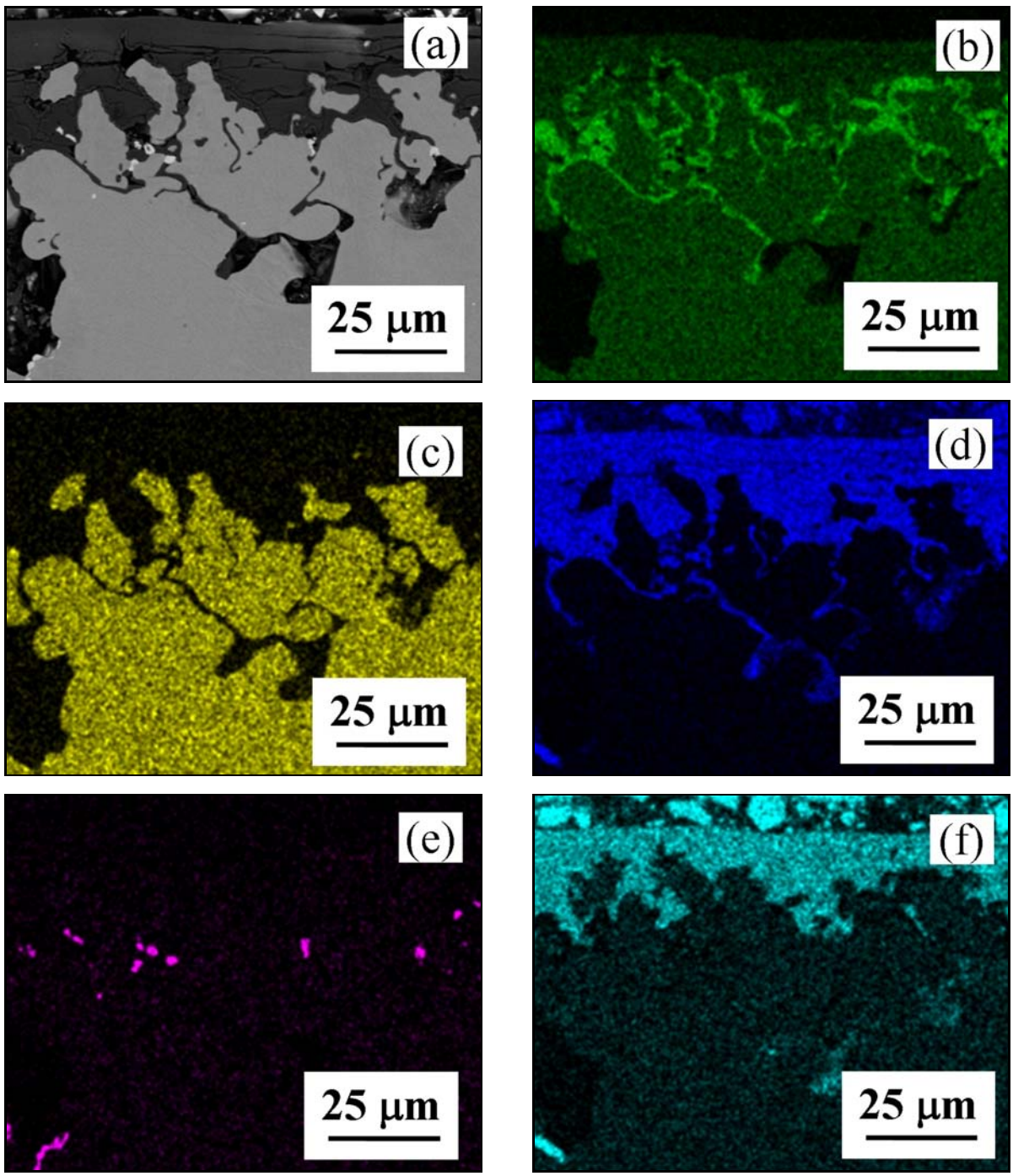

Fig. 4. The cross section of glass/metal interface after interaction Fe-40Al-Zr (at.%) with soda-lime glass at 1200 °C/96 h, SEM-BSE micrograph (a) and mappings of elements: Al (b), Fe (c), O (d), Zr (e) and Si (f).

(iii) *parameters of complexity and deformation,* estimating of fractal dimension by compass dimension (D_C).

The estimated compass dimension expresses the degree of complexity of the interface between alloy and glass by means of a single number [19]. A compass method [19, 20] is based on measuring the dividing line (roughness profile) using different sizes of rulers (Fig. 3d) according to the equation:

$$L_i(r_i) = N_i(r_i) \cdot r_i, \tag{3}$$

where L_i is the length in i-th step of the measurement, r_i is the ruler size and N_i is the number of steps needed for the measurement that is given by the power law:

$$N(r_i) = \text{const} \cdot r_i^{-D_C}. \tag{4}$$

If the line is fractal and hence the estimated fractal dimension is larger than the topological dimension, the length measured increases as the ruler size is reduced. Using previously mentioned equations it will be obtained

$$L_i(r_i) = N_i(r_i) r_i = \text{const} \cdot r_i^{-D_C} \cdot r_i = \text{const} \cdot r_i^{1-D_C}, \tag{5}$$

where D_C is the estimated dimension: the compass dimension.

The logarithmic dependence between $\log_2 N(r_i)$ and $\log_2 r_i$ is called the Richardson-Mandelbrot plot (Fig. 3e). The compass dimension is then determined from the slope s of the regression line:

$$D_C = 1 - s = 1 - \frac{\Delta \log_2 L(r)}{\Delta \log_2 r}. \tag{6}$$

The dimension is multiplied by 1000 (D_C 1000). The fractal dimension can be also estimated by the use of many other methods [19, 20].

The roughness parameters of Fe-40Al-Zr were compared with previously tested alloys under the same corrosion conditions (Table 4). The tested material Fe-40Al-Zr has a deeper surface disruption than the austenitic steel and Fe-25Al-5Cr (Rt – maximum roughness). On the other hand, an uneven and very deep penetration of oxygen into the sample was observed in the case of Fe-28Al-3Cr-0.5Zr. The mean spacing parameter shows that the surface of alloy Fe-40Al-Zr has most peaks and holes compared to the ideal line. However, the oxidation proceeds more uniformly (low value of D_C 1000) than austenitic steel and Fe-28Al-3Cr-0.5Zr.

EDS analyses of the glass/metal interface of Fe-40Al-Zr alloy reveal an oxidation behaviour, which is similar to that of iron aluminides based on Fe_3Al [16]. The generation of alumina was the result of reactions between FeAl matrix of tested alloy and glass oxides (especially with SiO_2), see Fig. 4. The generated alumina dissolved in the molten glass (Table 2) in contrast to the oxidation of iron aluminides in air, which is characterized by formation a thin protective layer of Al_2O_3 [1–3]. However, amount of alumina in the molten glass near the sample surface increases during the interaction and the saturated molten glass reduces further reaction between iron aluminide and the molten glass (unsaturated). In addition to alumina, the reaction between FeAl and SiO_2 generates FeSi and Fe_3Si, which are inert. It is assumed that an increased concentration of FeSi and Fe_3Si partially protects the alloy against further dissolution of alloy similarly as alumina.

On the other hand, the presence of Zr-rich particles in Fe-40Al-Zr alloy has detrimental effect on the oxidation rate in soda-lime glass (Table 3). Post mortem investigation of the sample after interaction with the molten glass for 96 h revealed an increased amount of ZrO_2 at the alloy/glass interface (Table 5). The formation of ZrO_2 was caused by the preferential oxidation of zirconium from Zr-rich precipitates during reactions with sulphate ions or other oxides of the glass (for example SiO_2). The preferential oxidation probably caused the non-uniform attack of the sample surface (the greater waviness of the boundary curve), see Fig. 5. Similar preferential oxidation behaviour was observed after oxidation in air [12, 13, 21].

Figure 6 (colour version on the website) shows the

Table 5. Chemical composition of interface alloy/glass, area EDS analyses

Elements	O	Na	Al	Si	S	Fe	Zr
(wt.%)	41.24	0.16	43.39	1.22	1.15	0.74	12.09
(at.%)	58.35	0.16	36.40	0.98	0.81	0.30	3.00

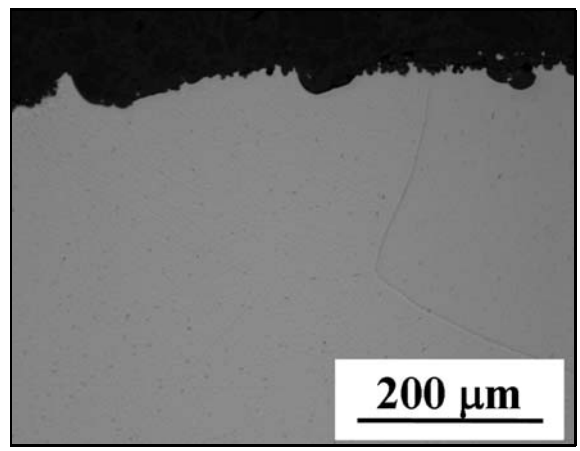

Fig. 5. LOM micrographs of the cross section of Fe-40Al-Zr (at.%) after interaction with soda-lime glass at 1200 °C/96 h.

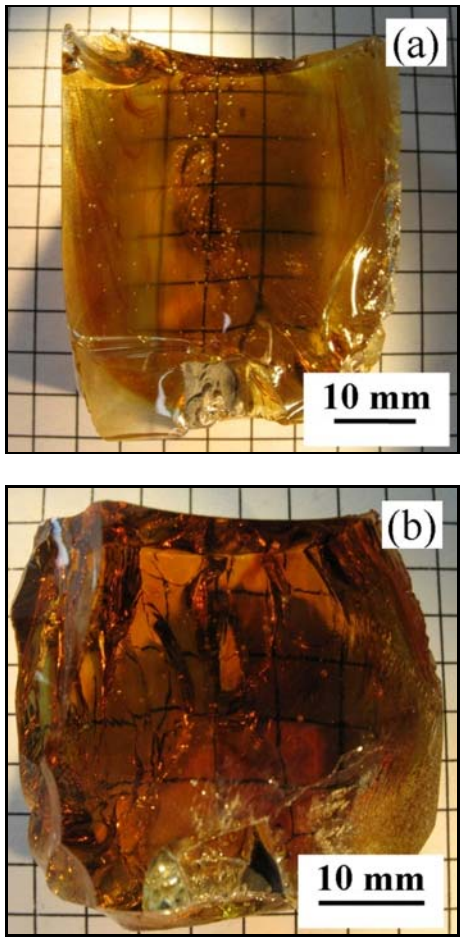

Fig. 6. The tinting of soda-lime glass after interaction with Fe-40Al-Zr (at.%) at 1200 °C after time interval 24 h (a) and 96 h (b).

tinting of the glass after interaction with Fe-40Al-Zr. The yellow-brown tint is caused by the presence of the polysulphide of iron. The polysulphide of iron is a product of the reaction between the sulphate ions and Fe_2O_3, which occurs under reducing conditions. The yellow-brown tint of soda-lime glass due to interaction with iron aluminides was already observed earlier [16]. In case of Fe-40Al-Zr, the soda-lime glass has no grey areas, which were observed in glass after interaction with Fe-28Al-3Cr-0.5Zr or Fe-25Al-5Cr. The grey tinting was caused by a formation of Si small particles.

The interaction between Fe-40Al-Zr and molten soda-lime glass also results in the generation of bubbles (Fig. 6). The bubbles mainly contain SO_2. The source of SO_2 bubbles is the reaction between Al and SO_3 that is contained in the soda-lime glass.

4. Conclusions

The corrosion behaviour of Fe-40Al-Zr in molten soda-lime glass has been studied at 1200 °C and the results were compared with previously tested alloys. The results can be summarized as follows:

1. The corrosion resistance of Fe-40Al-Zr alloy against molten soda-lime glass is lower compared to austenitic steel (EN X8CrNi25-21), because this alloy was dissolved faster and the surface of the sample is more disrupted.

2. The corrosion resistance of Fe-40Al-Zr is also lower than that of iron aluminide without Zr. It is obvious, that the presence of 0.09 % Zr reduces the corrosion resistance of iron aluminides against molten soda-lime glass as in the case of high-temperature oxidation of iron aluminides with Zr addition in air.

3. The corrosion mechanism of Fe-40Al-Zr alloy is characterized by the formation of alumina, FeSi and Fe_3Si. It seems that the saturation of molten glass by these products reduces further reaction between Fe-40Al-Zr alloy and the molten glass (unsaturated). The preferential oxidation of Zr was also observed. The preferential oxidation of Zr in particles causes a non-uniform attack of the sample surface and the increase of the oxidation rate.

Acknowledgements

The authors wish to thank P. Novák (Institute of Chemical Technology) for XRF analysis and P. Kejzlar (Technical University of Liberec) for EDS analyses. This work was supported by the Czech Science Foundation (GAČR P107/10/0438).

References

[1] McKamey, C. G., De Van, J. H., Tortorelli, P. F., Sikka, V. K. J.: Mater Res, *6*, 1991, p. 1779. doi:10.1557/JMR.1991.1779
[2] Tortorelli, P. F., Natesan, K.: Mat. Sci. Eng. A, *258*, 1998, p. 115. doi:10.1016/S0921-5093(98)00924-1
[3] Prescott, R., Graham, M. J.: Oxid Met, *38*, 1992, p. 73. doi:10.1007/BF00665045
[4] Risanti, D. D., Sauthoff, G.: Intermetallics, *13*, 2005, p. 1313. doi:10.1016/j.intermet.2004.12.029
[5] Palm, M., Sauthoff, G.: Intermetallics, *12*, 2004, p. 1345. doi:10.1016/j.intermet.2004.03.017
[6] Stein, F., Palm, M., Sauthoff, G.: Intermetallics, *13*, 2005, p. 1275. doi:10.1016/j.intermet.2004.08.013
[7] Milenkovic, S., Palm, M.: Intermetallics, *16*, 2008, p. 1212. doi:10.1016/j.intermet.2008.07.007
[8] Chevalier, S., Juzon, P., Borchardt, G., Galerie, A., Przybylski, K., Larpin, J. P.: Oxid Met, *73*, 2010, p. 43. doi:10.1007/s11085-009-9168-8
[9] Natesan, K.: Mat Sci Eng A, *258*, 1998, p. 126. doi:10.1016/S0921-5093(98)00925-3
[10] Pint, B. A., Tortorelli, P. F., Wright, I. G.: Mater High Temp, *16*, 1999, p. 1. doi:10.3184/096034099783641236
[11] Ni, J., Wan, X. J., Wang, Q., Cheng, X. Y., Liu, W. M., Zhang, X. Y.: J Shanghai Univ, *1*, 1997, p. 79. doi:10.1007/s11741-997-0049-6

[12] Janda, D., Galetz, M., Schütze, M., Heilmaier, M.: In: Proceedings of 6th Discussion Meeting on the Development of Innovative Iron Aluminium Alloys FEAL 2011. Eds.: Trujillo, F. J. P., Morris, D. G. Madrid, Spain, Department of Physical Metallurgy, CENIM-CSIC 2011, p. 133.
[13] Hotař, A., Palm, M., Kratochvíl, P., Vodičková, V., Daniš, S.: Corr. Sci., *63*, 2012, p. 71. doi:10.1016/j.corsci.2012.05.027
[14] Uxa, V.: Sklář a keramik, *6*, 1956, p. 225 (in Czech).
[15] Hotař, A., Kratochvíl, P.: Intermetallics, *15*, 2007, p. 439. doi:10.1016/j.intermet.2006.07.006
[16] Hotař, A., Kratochvíl, P., Hotař, V.: Kovove Mater., *47*, 2009, p. 247.
[17] Schindler, I., Kawulok, P., Fabík, R.: In: Proceedings of 2nd International Conference on Recent Trends in Structural Materials. Ostrava, Tanger Ltd. 2012. ISBN 978-80-87294-34-5, http://www.comat.cz/files/proceedings/11/reports/992.pdf
[18] Hotař, V., Novotný, F.: In: Proceedings of 11th International Conference on Fracture. Ed.: Carpinteri, A. Turin, CCI Centro Congressi Internazionale s.r.l 2005, p. 58.
[19] Mandelbrot, B. B.: The fractal geometry of nature. 2nd ed. New York, Freeman WH and Co. 1982.
[20] Peitgen, H. O., Juergens, H., Saupe, D.: Chaos and Fractals: New Frontiers of Science. New York, Berlin, Heidelberg, Springer-Verlag 1992. doi:10.1007/978-1-4757-4740-9
[21] Xu, C. H., Gao, W., Gong, H.: Intermetallics, *8*, 2000, p. 769. doi:10.1016/S0966-9795(00)00007-8

CORROSION RESISTANCE OF HEAT-RESISTANCE ALLOYS IN MOLTEN LEAD CRYSTAL AT 1200℃

Adam HOTAŘ[1], Vlastimil HOTAŘ[2], Jan DROBEČEK[1]

[1]*Department of Material Science, Technical University of Liberec, Liberec, Czech Republic*

[2]*Department of Glass Producing Machine and Robotics, Technical University of Liberec, Liberec, Czech Republic*

Abstract

The important parameter for using heat-resistance alloys in the glass industry is the corrosion resistance of alloys in molten glass. The corrosion resistance of the alloy depends on the chemical composition of the glass and alloy and the temperature. The corrosion tests of iron aluminide Fe14Al5Cr, austenitic steel EN X8CrNi25-21 and nickel alloy were carried out in a lead crystal at 1200℃. The cor rosion kinetic of the test alloys was determined by the measurement of weight loss. The changes of sample surface layers were quantified by the surface roughness. The most suitable alloy for application in molten lead crystal is the iron aluminide Fe14Al5Cr. The alloy Fe14Al5Cr has had the lowest weight loss and parameters of roughness, tinted the molten glass at the least. The corrosion resistance of the austenitic steel against the molten lead crystal is also very good.

Key words:

iron aluminide (Fe_3Al type), austenitic steel, nickel alloy, corrosion resistance, molten lead crystal

1. INTRODUCTION

Metals and their alloys are used increasingly for applications in molten glasses [1]. Electrodes, holders of electrodes, parts of feeders (like plungers), parts of gatherer and elements of mechanical homogenizing of molten glass are often produced from metal materials for example stainless steels (austenitic, feritic steels), precious metals (platinum), nickel alloys etc. Fe_3Al-based alloys, which are characterized by an excellent corrosion resistance at high temperatures in a variety of aggressive environments [2, 3], have been also studied as materials for high-temperature structural applications in the glass making [4].

Corrosion resistance of heat-resistance alloys against a molten glass depends on type of glass (chemical composition of glass) and temperature. Therefore laboratory tests in molten glass are necessary for choice the most suitable heat-resistant alloy.

The aim of the present paper is to describe and compare the corrosion resistance of the iron aluminide Fe14Al6Cr, the austenitic steel EN X8CrNi25-21 and the nickel alloy in the molten lead crystal at 1200℃. Very good corrosion resistance of the iron aluminide Fe14Al6Cr and the austenitic steel EN X8CrNi25-21 was already observed in a soda-lime glass and a lead crystal with different composition [4].

2. EXPERIMENTAL

Three types of metal materials were tested in the molten lead crystal (Table 1). Chemical compositions of the test alloys are reported in Table 2. Cuboid samples of the iron aluminide and the nickel alloy were cut by electro-discharge machining. Surface layers of samples were manually removed using SiC abrasive papers, down to grit 1200 (five steps). In case of the austenitic steel, samples were machined from bars and the sample surface was also ground using SiC abrasive papers (same grit as cuboid samples). Then sample dimensions and the weight were measured.

Corrosion tests were carried out at 1200℃ for up to 96 h. Samples put into alumina crucibles, which subsequently filled with cullet. After alumina crucibles with the samples and cullet were placed in a furnace. After each test crucibles were cooled down in the furnace. Cold crucibles were carefully broken and the glass separated from the surface of alloys. The corrosion resistance was evaluated using of the weight change and the change of surface roughness. Changes of the surface were observed on the sample cross-sections and were quantified using fractal geometry and statistic tools (a compass dimension – $D_{C\ 1000}$, standard deviation – STD and an average maximum roughness of all the curves – R_t). The surface roughness of samples was measured before and after the corrosion test in the molten glass. In addition, the tinting of glass and the change of sample surface were visually described.

Table 1 Chemical composition of the lead crystal before corrosion tests

[wt.%]	SiO_2	PbO	ZnO	Al_2O_3	B_2O_3	CaO	Sb_2O_3	K_2O	Na_2O	Er_2O_3	Nd_2O_3
Lead crystal	51.36	32.00	0.71	0.1	0.77	1.96	0.21	6.58	6.31	0.2	0.002

Table 2 Chemical composition of alloys

Alloy	Chemical composition [wt.%]											
	C	Al	Mn	Si	Cr	Fe	Nb	Ta	W	Co	Cu	Ni
141 I	0.34	-	0.58	0.55	26.9	7.97	0.99	0.93	4.94	4.47	0.05	Bal.
Fe14Al6Cr	0.02	14.20	max. 0.45	-	5.63	Bal.	-	-	-	-	-	-
EN X8CrNi25-21	max. 0.02	-	1.50	1.00	24 – 26	Bal.	-	-	-	-	-	19 – 22

3. RESULT AND DISCCUSION

Due to interaction between the molten glass and alloys the molten lead crystal was tinted and sample surface and eventually shape was changed. Fig. 1 shows samples after 96 h. in the molten lead crystal. Samples of the iron aluminide and the austenitic steel keep their original shape and dimensions.

Fe14Al6Cr 10.1x8.4x17.8 mm | EN X8CrNi25-21 ϕ16x12.3 mm | 141 I 13.3x11x15 mm

Fig. 1 – Samples (with original dimensions) after the corrosion test in the molten lead crystal at 1200℃ for 96 h.

However residuals of a dark green glass on the surface of the steel are observed. On the other hand, the sample of the nickel alloy is covered by metal phases, which probably has high content of lead.

The tinting of the glass after 96 h. is obvious in Fig. 2. The iron aluminide tinted the molten glass less intensively; the glass is only lightly grey near the sample (lower right corner). The glass is green after interaction with the austenitic steel. Dark green up to black color of the glass is caused by interaction between the molten lead crystal and the nickel alloy.

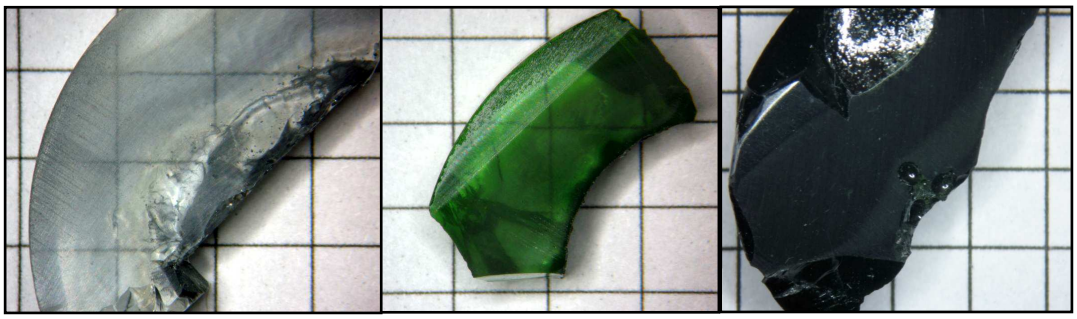

Fe14Al6Cr EN X8CrNi25-21 141 I

Fig. 2 – The tinting of the lead crystal after interaction with test alloys at 1200℃, time interval 96 h.; samples were situated in lower right corner; dimension of squares is 5 mm

The corrosion resistance of the test alloys was determined by measurement of weight change. The results reveal Table 3. For the iron aluminide and the austenitic steel up to 48 h. weight loss the after corrosion test are characteristic. The iron aluminide has lower weight loss than the steel. The weight gains of austenitic steel were caused by residuals of glass on the samples (Fig. 1) for time periods 72 and 96 h. In case of the nickel alloy weight of samples significantly increased due to a metal phases on the sample therefore the results cannot be compared.

Table 3 Weight change of samples after corrosion tests in lead crystal at 1200℃;

+…weight gain, - …weight loss

Time intervals [h.]	Fe14Al6Cr [mg/cm^2]	EN X8CrNi25-21 [mg/cm^2]	141 I [mg/cm^2]
0	0.00	0.00	0.00
5,5	-	-	+144.77
13	- 3.07	- 6.75	-
24	- 4.69	- 7.49	+888.35
48	- 4.70	- 10.32	+1282.92
72	- 15.49	+ 0.37	+1433.68
96	- 16.22	+ 7.32	+1484.05

The similar behavior of the iron aluminide and the steel was observed in [4]. Same iron aluminide and same austenitic steel were tested in the lead crystal with different chemical composition. The austenitic steel has also the lower corrosion resistance than the iron aluminide (Fig. 3). Fig. 3 shows that test alloys have better corrosion resistance against the lead crystal in [4].

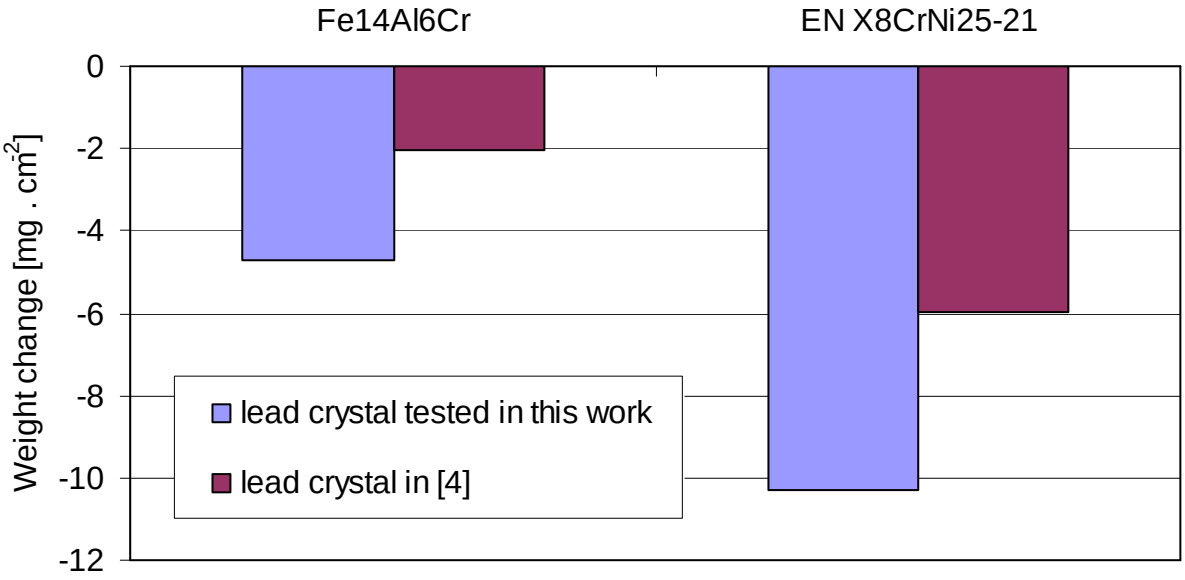

Fig. 3 – Weight change of the iron aluminide and the austenitic steel after interaction with the lead crystals at 1200℃ for time interval 96 h.

Table 4 reveals surface parameters of test alloys. The iron aluminide and the austenitic steel are less damage due to corrosion reactions with the molten glass. The iron aluminide surface has a more complex structure, whereas the austenitic steel is wavier. On the other hand the surface of the nickel alloy is very damage therefore it cannot be quantified.

Table 4 Roughness parameters of boundaries between alloys and the lead crystal, $D_{C\,1000}$ average compass dimension (multiplied by 1000), STD average standard deviation and R_t average maximum roughness

	Fe14Al6Cr			EN X8CrNi25-21			141 I		
	D_{C1000} [-]	STD [µm]	R_t [µm]	D_{C1000} [-]	STD [µm]	R_t [µm]	D_{C1000} [-]	STD [µm]	R_t [µm]
before tests	1023	0.56	3.55	1017	0.43	2.92	1007	0.29	1.99
Lead crystal after 96 h.	1038	0.88	4.65	1020	2.51	10.56	Cannot be quantified	Cannot be quantified	Cannot be quantified

4. CONCLUSIONS

1. The iron aluminide Fe14Al6Cr has the best corrosion resistance against the molten lead crystal than comparable alloys. The alloy Fe14Al6Cr tinted less intensively the glass, and the rate of solution and damage of the surface are lowest.
2. The good corrosion resistance of the austenitic steel was also observed in the molten lead crystal.
3. the nickel alloy is not suitable for applications in molten lead crystal.

ACKNOWLEDGEMENTS

This work was supported by the by the SGS project „Innovations in Material Engineering“.

REFERENCES

[1] KIRSCH, R.: Metals in glassmaking, Elsevier Science Ltd. 1993

[2] McKAMEY, C.G., DeVAN, J.H., P.F. TORTORELLI, SIKKA, V.K.J.: A review of recent developments in Fe_3Al-based alloys, Mat Res, 6, 1991, 1779-1805.

[3] TORTORELLI, P.F., NATESAN, K.: Critical factors affecting the high-temperature corrosion performance of iron aluminides, Mat Sci Eng, A258, 1998, 115-25.

[4] HOTAŘ, A., KRATOCHVÍL P., HOTAŘ, V.: The corrosion resistance of Fe_3Al based iron aluminides in molten glasses, Kovove Mater.,47, 2009, 247-52.

APLIKACE NEKONVENČNÍCH METOD PRO HODNOCENÍ DAT VE SKLÁŘSTVÍ

Vlastimil HOTAŘ
Technická univerzita v Liberci, Katedra sklářských strojů a robotiky
Adam HOTAŘ
Technická univerzita v Liberci, Katedra materiálu

NON-CONVENTIONAL METHODS APPLICATION FOR DATA EVALUATION IN GLASS INDUSTRY

Possibilities of use new tolls as fractal dimension and statistics for evaluation some types of data were first mentioned in this journal before three years. The article [1] was intended to a preliminary familiarization with fractal geometry and to possibilities of use in glass industry. The research is now shifted to the applications and to an expansion to the other types of data.

Před třemi lety byly v tomto časopise poprvé zmíněny možnosti využití nových nástrojů, jako je fraktálová dimenze, ale i statistika pro hodnocení některých typů dat. Článek [1] byl zaměřen na úvodní seznámení s fraktálovou geometrií a vytyčení možností pro aplikace ve sklářském průmyslu. Výzkum se nyní posunul směrem k aplikacím, nasazením v průmyslové praxi a k expanzi na hodnocení dalších typů dat. Možnosti prezentovaného přístupu k hodnocení dat však nejsou zdaleka vyčerpány.

1. Úvod

Aplikace jsou zaměřeny na tři typy dat: digitální nebo skenované fotografie (2D snímky), rozhraní povrchů a časové řady. Základním principem metodiky hodnocení dat je využití vždy několika vypočtených parametrů získaných pomocí různých principů (především statistiky a fraktálové geometrie). Výsledné hodnocení může pak být shrnuto přepočtem do výsledné jakosti nebo užito jako řídící veličina pro výrobní proces anebo jako samostatná informace pro statistické zpracování měřených výsledků. Cílem článku je krátce shrnout pokroky ve výzkumu a představit praktickou ukázku nasazení metody hodnocení dat v praxi.

2. Hodnocení povrchových struktur

Hodnocení povrchových struktur ve formě snímků dírek píchaného zboží z elektronového mikroskopu bylo ukázáno již v článku [1]. Vady dírek se projevují především mléčným zakalením dírky a po zvětšení jako rozpraskání povrchu, které může mít hrubší nebo jemnější strukturu. Kontrola jakosti povrchu dírek je prováděna subjektivně, což je nespolehlivé.

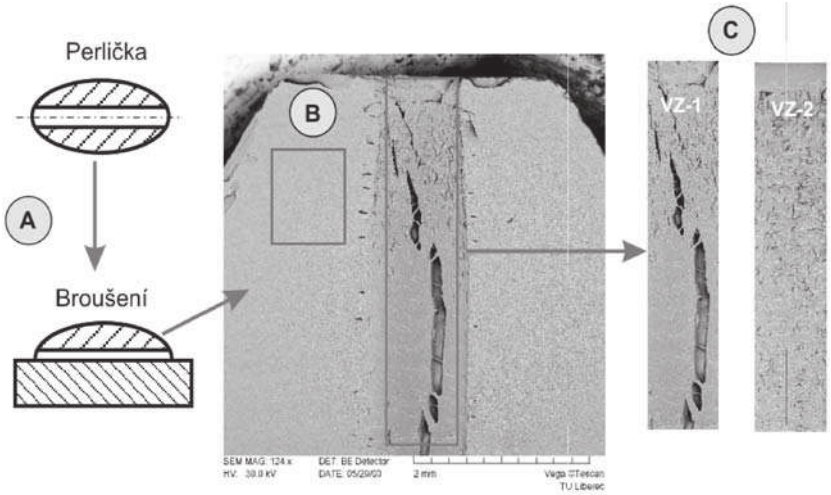

Obr. 1 - Broušení perličky, výběr okna snímku a okna brusu, analyzovaná oblast vzorku VZ-1, VZ-2

Při vývoji vhodné metodiky objektivního hodnocení byla cílem jednoznačná kvantifikace povrchu, jejíž výsledky lze použít pro zařazení vzorků do tříd jakosti pro obchodní účely, pro posílení systému jakosti, i při studiu vztahu kvality povrchu ve vazbě na fyzikální podmínky jeho vzniku, tedy vyhodnocení vlivu technologických změn na charakter povrchu. Kvantifikace by obecně měla být jednoduchá, rychlá a výsledek srozumitelně vyjádřen, nejlépe ve stejné jakostní škále, která je již užívána.

Proces hodnocení tohoto typu vzorků lze rozdělit do následujících kroků:

1. Příprava vzorku - zbroušení vzorku na 1/3 průměru dírky tak, aby se odhalila dírka, **obr.1 A**.

2. Získání snímků - snímání vzorku na elektronovém mikroskopu a získání datového obrazu.

3. Zpracování snímků - softwarové zpracování datových obrazů (ořezání datového obrazu a přepočet na konstantní jas), **obr. 1 B**.

4. Analýza datového obrazu povrchu dírky, **obr. 1 C**.

5. Vyhodnocení snímku a případné posouzení vztahu mezi strukturou a fyzikální podstatou jejího vzniku.

K přesnému a jasnému definování charakteru povrchu se jeví jako nutné zvolit minimálně dvě analýzy, kdy každá popíše spolehlivě jeden ze dvou typů vad, již zmíněnou hrubší (hluboké praskliny), **obr. 1**, VZ-1 a jemnější (mělké rozpraskání) strukturu, **obr. 1**, VZ-2.

Pro detekci hlubokých prasklin se ukázala jako nejvhodnější vyvinutá metoda pracovně nazvaná: stanovení procentuálního zastoupení počtu sousedních pixelů stejné velikosti - detekce trhlin [2, 3], která vychází z prahování, kdy snímek ve stupních šedi (0 až 255) je převáděn pomocí jednoduchého pravidla na binární obrazy - snímky složené ze dvou hodnot barev, z bílé (hodnota 1) a černé (hodnota 0). Například při zavedení prahu na úrovni 100, jsou pixely s hodnotou nižší nebo rovnou 100 převáděny na pixely s hodnotou

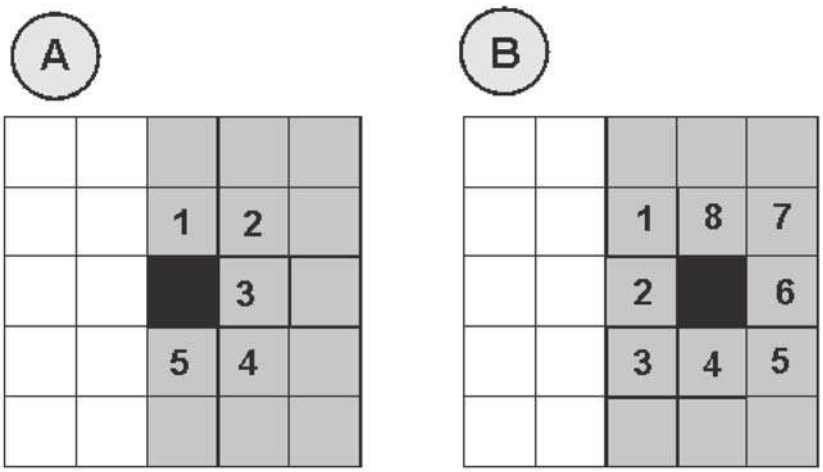

Obr. 2 - Hraniční pixely, které zobrazují prasklinky

0 a vyšší než 100 na pixely s hodnotou 1. V binárním obraze jsou hledány pixely, které mají více než 5 sousedů s hodnotou 0 - tedy černé pixely prezentující vady. Černý pixel na **obr. 2 A** má právě 5 sousedů a 5 sousedů budou mít také všechny číslované pixely, obr. 2 A. Číslo 5 a více bylo zvoleno, protože minimálně 5 sousedů mají pixely na hranici trhlinek a uvnitř trhlinek mají 8 sousedů (což je limitní hodnota), **obr. 2 B**. Na snímku se vypočte procentuálně kolik pixelů má 5 a více sousedů vzhledem k celkovému počtu. Pro výpočet bylo užito vyvinutého programu v prostředí Matlab.

Pro detekci mělkého rozpraskání je používáno odhadu fraktálové dimenze pomocí mřížkové metody [2, 3, 4, 5, 11]. Touto metodou je počítána box dimenze (nazývaná též mřížková dimenze), která se jeví jako silná pro popis vysoké strukturovanosti digitálních snímků. Analýza je uplatněna na binární snímek, který je získán opět prahováním. Lze tak získat spektrum pro nalezení prahu s nejvyšší citlivostí na danou složitost struktury. Ve výzkumu bylo užito software HarFa [6] a dalších nástrojů pro zpracování výsledků. Box dimenze je vynásobena tisícem, aby rozdíly v dimenzi byly zřejmé a je označována D_{BD1000}. Výběr ze snímků s získanými hodnotami je uveden na **obr. 3**.

Na základě experimentálně daných váhových koeficientů, jsou výsledky obou metod shrnuty do jednoho komplexního hodnocení, které je přepočítáno na třídy jakosti.

Zde prezentovaný popis povrchu dírky vyžaduje složitou přípravu vzorku a zručnost při snímání na elektronovém mikroskopu. Jedná se tak o dva významné vlivy, které mohou negativně ovlivnit výsledky analýzy. Samotnou analýzu lze automatizovat a uzavřít před vnějším zásahem, ale kroky předcházející analýze je nutné zjednodušit a zautomatizovat. Celé metodice by pomohlo získání snímku dírky bez nutnosti zbroušení. Bez tohoto zjednodušení nelze kontrolu široce využít v provozních podmínkách a automatizovat. Existují však ideové návrhy, které by při snímání povrchu nevyužívaly zbroušeného vzorku.

3. Identifikace a kvantifikace vad ve skle

V rámci výzkumu byla včetně analýzy povrchu dírek zkoušena citlivost vyvinuté metodiky na různé typy vad ve skle. Byl analyzován soubor 26 různých typů vad ve formě skenovaných snímků z [7]. Výběr vad nebyl dán jejich četností v běžných sklech, ale především jejich rozmanitostí. Nebyla také sledována jejich velikost, která je dalším relativně snadno zjistitelným parametrem. Cílem bylo specifikovat nástroje, které by vedle velikosti vady byly schopny detekovat složitost vady a její strukturu. Tím by mělo dojít ke kvantifikaci a automatickému odlišení jednotlivých typů vad. Cílem experimentu bylo tedy specifikovat citlivost analýz na rozmanité typy vad.

Snímky byly zpracovány v šedé škále a bylo použito metod:

- fraktálové geometrie - box dimenze (popsáno výše);
- statistického popisu histogramu - ořezání histogramu na úrovni 5%. To se ukazuje ze statistického popisu histogramu jako nejvhodnější, vzhledem k charakteru získaných snímků;
- výpočtu procentuálního zastoupení poruch v obraze - v binárním obraze je vypočteno procentuální zastoupení černé. Vychází se přitom z předpokladu, že větší strukturovanost snímku (větší množství vad) a jejich větší velikost, představuje větší množství černých ploch či bodů na obraze;
- stanovení procentuálního zastoupení počtu sousedních pixelů stejné velikosti (popsáno výše).

Na **obr. 4** je uvedeno hodnocení několika typů vad spolu s výslednými parametry pro daný práh. U box dimenze byl zvolen práh 35, u procentuálního zastoupení černé práh 205, u počtu sousedů stejné velikosti se osvědčilo nastavení na 5 a více sousedů na prahu 50.

Výsledky experimentů prokazují, že pomocí 2 parametrů (box dimenze a procentuálního zastoupení počtu sousedních pixelů) lze jednoznačně odlišit typy vad. Znamená to, že pokud se stanoví prahové hodnoty pro dané parametry odpovídající dané vadě, lze vady automaticky detekovat. V další fázi výzkumu bude vhodné parametry přesněji nastavit a doplnit o výsledky spektrální analýzy, která by mohla specifikovat určitou pravidelnost na snímcích.

Snímek	Box dimenze DB_{D1000}	Detekce trhlin
	344	0,022
	1074	0,793
	1622	0,336
	1467	3,322

Obr. 3 - Ukázka hodnocení povrchů dírek píchané skleněné bižuterie

4. Objektivizace testu zvlnění plochého skla

Přestože se v tomto případě jedná o obrazovou analýzu, získávané křiv-

ky rozhraní jsou hodnoceny pomocí nástrojů pro analýzu topologicky jednodimenzionálních křivek.

Kvalita plochého skla vyráběného technologií FLOAT je sledována souborem metod posuzujících vady plochého skla od kamínků, šlír, přes konstantní tloušťku až po optické zvlnění. Úkolem kontroly jakosti skla je charakterizovat tyto vady a podle smluvně daných kritérií zařadit sklo do tříd jakosti.

soubor	snímek	Box dimenze (práh 35)	Počet sousedních pixelů stejné velikosti (5 a více)	Oříznutí histogramu na 5%	Procentuální zastoupení černé (práh 205)
samostatný krystal cristobalitu	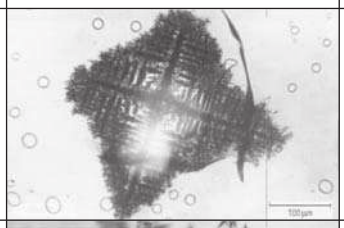	1566	9.64	213	32.20
krystaly $Ba[BeF_4]$		1570	8.63	207	41.62
kulově formované shluky krystalů cristobalitu	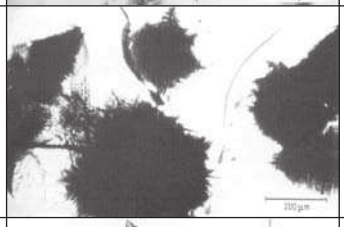	1314	42.80	255	51.18
krystaly $Ca_3(PO_4)_2$	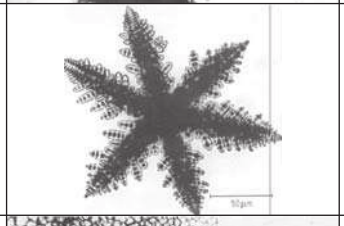	1623	22.84	255	37.52
část krystalu tridymitu	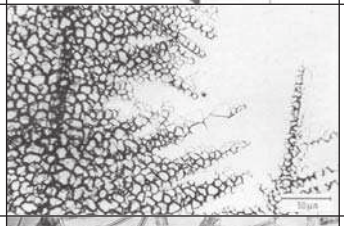	1470	18.27	253	31.19
krystaly $Ca[BeF_4]$		1438	4.78	158	23.39
tyčinkovité krystaly BaO_2-TiO_2-$3SiO_2$		1659	5.93	183	20.47

Obr. 4 - Identifikace a popis vad ve skle

Významným měřítkem kvality skla je tzv. Corrugation test (test zvlnění), který hodnotí optickou jakost (zvlnění) skla a je prováděn subjektivně offline srovnáním s etalony obsluhou. Cílem výzkumu bylo tento test objektivizovat. K tomuto účelu bylo použito nástrojů statistiky a fraktálové geometrie, a na základě váhových koeficientů je stanovena výsledná kvalita, která využívá zavedené škály tříd jakosti pro subjektivní hodnocení.

Test je založen na odrazu světla na vzorcích ze 4 m vzdálené šikmo pruhované desky (zebra-desky, **obr. 5 C**), což je matovaná skleněná tabule o rozměru 2 x 1 m s černými pruhy o šíři 25 mm svírajícími úhel 45 stupňů. Pozorovatel (obr. 5 A) je od stolu se vzorky (obr. 5 B) vzdálen další 4 m a subjektivně porovnává kvalitu vzorků s etalony. Vzorky se řadí do stupňů jakosti od 1 do 3,5. Podle pracovních etalonů se ohodnotí celá šíře pásu.

Pro objektivizaci byla odzkoušena a navržena metodika hodnocení, která využívá digitálních snímků, které jsou dále softwarově zpracovány nikoliv jako celé snímky, ale jsou z nich generovány křivky rozhraní a ty jsou hodnoceny. V následujícím výzkumu byl na základě výsledků experimentů navržen systém objektivního měření a software pro analýzu Vlnitost, který je nyní ve verzi 1.4. Celý postup zpracování lze rozdělit do jednotlivých kroků:

1. Nastavení hodnoceného vzorku do předem určené polohy.

2. Snímkování odrazu zebra-desky od vzorku digitálním fotoaparátem v černobílém módu (**obr. 6 A**) a převod do počítače (**obr. 6 D**). Snímek vzorku je na **obr. 6 E**.

3. Digitální výřez vybrané části snímku (**obr. 6 E** - šedivý obdélník).

4. Analýza vzorku, které předchází *prahování*, získání a výběr úplných *křivek rozhraní* (**obr. 6 F**).

5. Zařazení do třídy jakosti na základě výsledků výpočtu statistických parametrů a odhadu fraktálové dimenze kompletních *křivek rozhraní.*

V kroku 1 musí obsluha přesně nastavit vzorek do požadované polohy tak, aby nedocházelo ke zkreslení analýzy natočením vzorku. Tato fáze objektivního hodnocení je nejvíce citlivá na práci obsluhy, protože kroky 2 až 5 je již možné automatizovat a minimalizovat tak subjektivní vlivy. Nyní se pracuje na odstranění, případně zmírnění této podmínky.

Snímkování vzorku v kroku 2 je

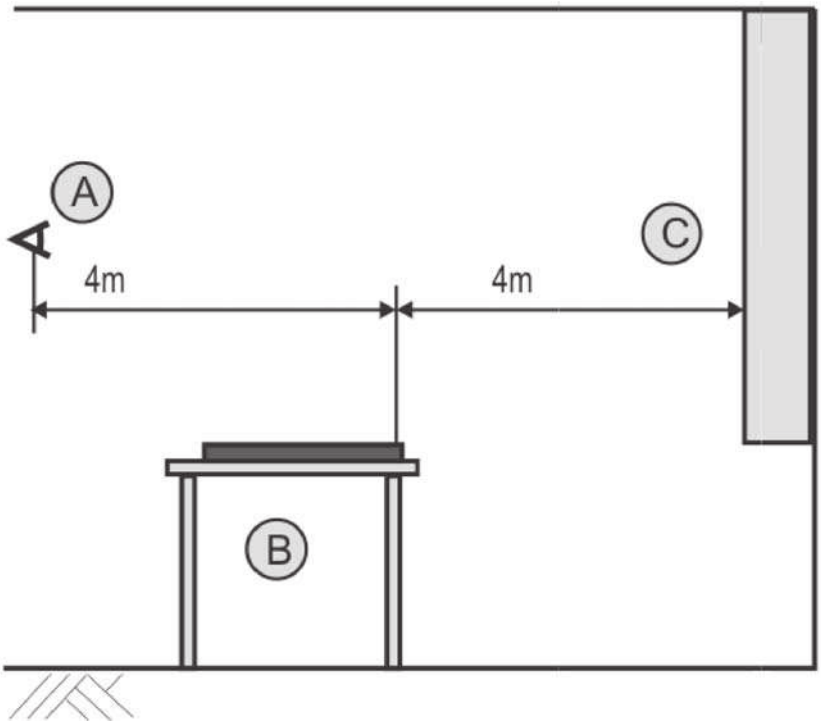

Obr. 5 - Schéma Corrugation testu

nutné provádět z pevně daného místa a pevně lokalizovaným umístěním fotoaparátu, daným pěti parametry: polohou ve třech osách, horizontálním a vertikálním natočením.

Digitální vyříznutí vybrané části snímku se provádí pro získání té části obrazu, která je důležitá pro analýzu (**obr. 6 E**).

Prahováním je získán binární snímek a z něj jsou získány křivky rozhraní (**obr. 6 F**). Pro každou křivku je provedena analýza a výsledky pro všechny kompletní křivky jsou prezentovány pro jeden vzorek jako průměrná hodnota, rozpětí výsledků a směrodatná odchylka.

Pro analýzu křivek rozhraní vzorků byly využity tři metody:

- statistické nástroje;
- odhad *fraktálové dimenze* pomocí *obvodové metody,* kdy výsledkem je tzv. *obvodová dimenze;*
- délky křivek.

Metody jsou popsány v [2, 8]. Nyní se také ověřuje možnost využití spektrální analýzy.

Jak se ukazuje, je nutné použít vždy několika parametrů, které jsou získány diametrálně odlišnými metodami. Důvodem je vnímání lidského oka, které vnímá jak pravidelné struktury, tak i složitost. Klasické nástroje popisu křivek (jako je rozpětí, rozptyl, směrodatná odchylka, variační koeficient, ...) jsou však často nepostačující. Jako vhodné se jeví užití statistických nástrojů v kombinaci s nástroji fraktálové geometrie a dalšími nástroji, jako jsou tzv. délky křivek. Dále vlivem technologie výroby lze na většině vzorků skla pozorovat dvě zvlnění. Primární, jako jasné zvlnění odražených pruhů a sekundární, které se jeví jako nejasná "rozpitá" hranice primárního zvlnění, **obr. 6 F**. Různý poměr primárního a sekundárního zvlnění mají i jednotlivé etalony odpovídající daným třídám.

Výsledná třída jakosti je dána nyní subjektivním posouzením míry pravidelnosti, složitosti a váhy mezi oběma zvlněními. K tomu, aby bylo možno objektivní výsledky přiblížit současné škále jakosti, je nutné vypočtené parametry přepočítat pomocí váhových koeficientů.

Dalším limitujícím faktorem je rychlost analýzy. Vzhledem k rozsahu obrazové analýzy a nutné přímé komunikaci mezi počítačem a fotoaparátem, je třeba dbát i na optimalizaci výpočtů a programu jako celku.

Na základě výsledků z experimentů [2, 8] byl vyvinut systém, který se skládá z hardwarové části, obsahující zařízení a nutné minimální úpravy v místnosti, kde se test provádí a část softwarovou, umožňující jednoduše objektivně vyhodnotit míru vlnitosti a jakost vzorku.

Princip hardware je zřejmý z obr. 6. Základním know-how je software vyvinutý speciálně pro tyto účely. Analýza byla vyvinuta v prostředí Matlab 7 a kompilovaná pomocí programu Matlab-Compiler 4 do samospustitelného programu nazývaného Vlnitost. To znamená, že program není závislý na prostředí Matlab, ale pouze na jeho tzv. knihovnách, které jsou spolu s programem nainstalovány na přenosném počítači systému. K běhu celého systému je potřeba, aby byl spuštěn program PSRemote 1.4, který umožňuje přímou komunikaci mezi fotoaparátem

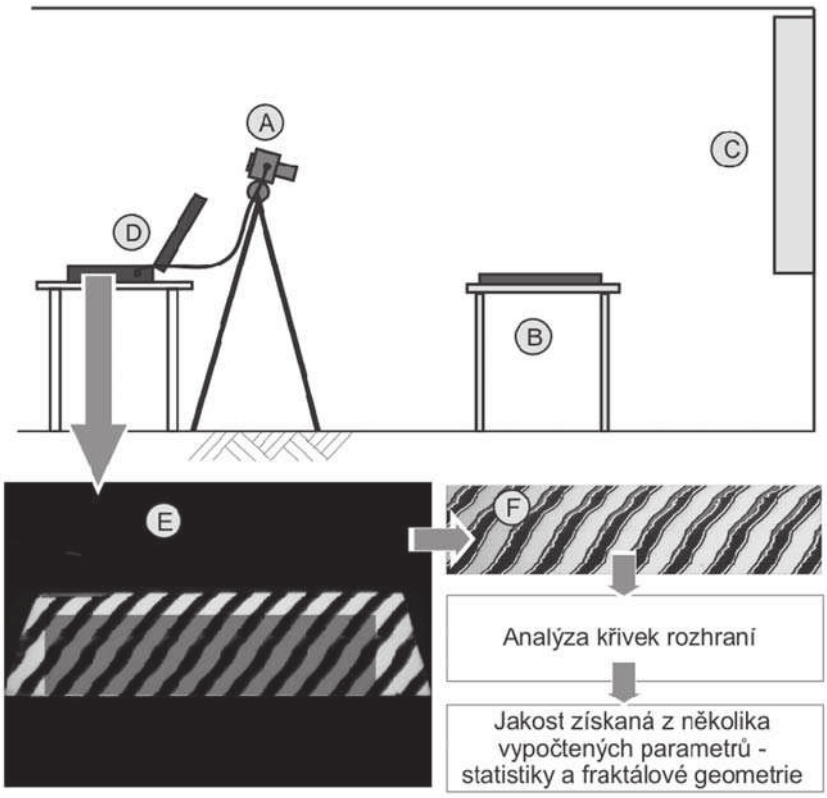

Obr. 6 - Princip analýzy snímků vzorků plochého skla

a počítačem. Většina úkonů v počítači je automatizována a celá analýza včetně automatického vyfocení je odstartována jediným tlačítkem. Operátor zadá standardní parametry vzorku a po analýze se mu v okně objeví výsledná jakost. Výsledky a zadané parametry vzorku jsou ukládány tak, aby bylo možno sledovat změny v čase.

Program je průběžně zdokonalován na základě požadavků z praxe a analýza je také urychlována. Nespornou výhodou celého systému je možnost uchovávat v počítači nejen výsledky hodnocení, ale i snímky prakticky po libovolně dlouhou dobu, pouze s nárokem na odpovídající místo na pevném disku kontrolního počítače.

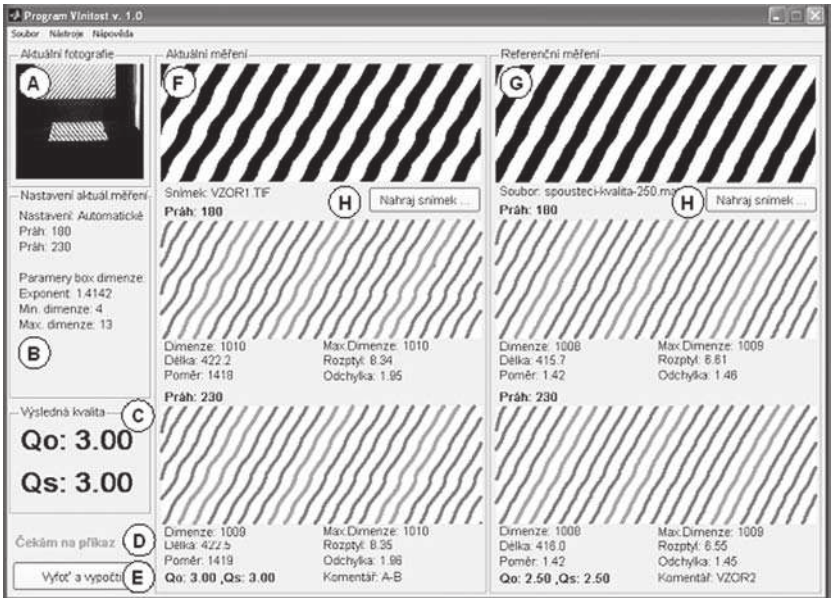

Obr. 7 - Okno programu Vlnitost 1.0

Okno programu Vlnitost 1.0 je zobrazeno na **obr. 7** a je rozděleno na několik podčástí:

• aktuální fotografie - zobrazující aktuální analyzovanou fotografii s vyznačením rámce - výřezu analyzované části - A;

• nastavení aktuálního měření - které zobrazuje nastavení (aktuální, vlastní), nastavené prahy a nastavení výpočtu *fraktálové dimenze* - B;

• výsledná kvalita - zobrazuje vypočtenou (objektivní) kvalitu Qo a subjektivně posouzenou (subjektivní) kvalitu Qs - C;

• příkazový řádek (Čekám na příkaz) - zobrazuje stav programu a průběh výpočtu - D;

• tlačítko pro spuštění programu "Vyfoť a vypočti" - spouští program na vyfocení vzorku a následně výpočet kvality, při běžném běhu programu stačí stlačit toto tlačítko pro vyfocení vzorku a start analýzy - E, případně zmáčknout klávesovou ;zkratku Ctrl+F

• aktuální měření - zobrazuje analyzovanou část fotografie, *křivky rozhraní* pro oba prahy a výsledky analýz - F;

• referenční měření - zobrazuje referenční část fotografie, *křivky rozhraní* pro oba prahy a výsledky analýz, zde je možné nahrát výsledky předchozích měření (tlačítkem H) a porovnat tak s aktuálním měřením - G.

Cílem dalšího výzkumu je již zmíněné zrychlení analýz, zvýšení komfortu pro obsluhu, zpřesňování dalších parametrů a zapracování připomínek z praxe. Tato aplikace fraktálové geometrie spolu se statistikou a dalšími nástroji je zatím nejdále v zavedení do praxe, je navržena jako vhodná metoda pro kontrolu jakosti i na jiných linkách a je důkazem možností využití těchto přístupů v průmyslovém prostředí.

5. Hodnocení míry koroze kovových materiálů sklovinou

Aplikace popisu křivek rozhraní je také vhodná pro popis povrchů a rozhraní dvou materiálů s vyšší mírou strukturovanosti. Příkladem může být užití fraktálové geometrie a statistických nástrojů pro popis korozního napadení kovových materiálů sklovinou, uvedený v tomto časopise před 3 lety v [1]. V rámci výzkumu aplikací nových kovových materiálů na bázi intermetalik ve sklářství je mimo jiné porovnávána korozní odolnost aluminidů železa (Fe28Al4Cr0,1Ce) a běžných austenitických ocelí, jako je ocel označovaná Poldi AKC (ČSN 417 255) a feritických, jako je ocel ČSN 417 153. K tomuto účelu je také používáno popisu křivek rozhraní.

Analýza byla provedena destruktivní metodou - rozborem digitálních fotografií rozhraní na metalografickém výbrusu z optického mikroskopu získaných fotoaparátem ve formátu TIF. Snímky v šedé škále byly převedeny na prahu 150 na binární snímky, ze kterých byly následně získány jednoznačně definované křivky rozhraní (jedna pro každý snímek, obr. 8). Tyto křivky byly následně analyzovány parametry:

• drsnosti: Ra, Rt, Rz, Rz(JIS), Sm;

• statistiky: směrodatná odchylka křivky profilu, rozsah křivky profilu, počet výstupků a prohlubní;

• fraktálové geometrie: obvodová dimenze ($D_{C\ 1000}$);

• délek a jejich poměrů: délka povrchu na 1 mm, poměr křivky profilu ku křivce definované maximy a minimy.

Blíže je popsána metodika v [2, 10]. Parametry drsnosti jsou určeny především pro popis materiálů s mnohem menší a do jisté míry pravidelnější strukturou, přesto některé parametry mohou být zajímavé i pro hodnocení velice strukturovaných materiálů.

Cílem užití více parametrů je popsat kvalitativně lépe a objektivně změny povrchů materiálů, které se projeví po intenzivním vystavení materiálů korozním účinkům roztavené skloviny. K popisu těchto povrchů bude stačit jen několik nejcitlivějších parametrů (2 až 4), které budou určeny na základě dlouhodobého výzkumu a po proměření velkého množství vzorků (celkem 500 a více).

Ukázka hodnocení a výsledných parametrů aluminidu železa (Fe28Al4Cr0,1Ce) a feritické oceli je na **obr. 9** (test v čiré obalové sklovině při teplotě 1350 °C 48 a 96 hodin), kde jsou uvedeny pouze parametry: obvodová dimenze ($D_{C\ 1000}$), směrodatná odchylka (STD) a rozpětí - maximální nerovnosti profilu (R).

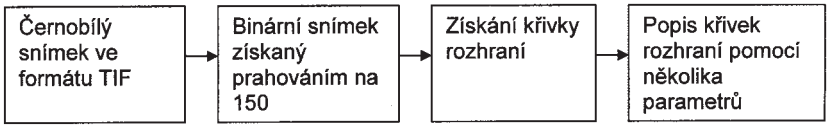

Obr. 8 - Metodika zpracování snímků pomocí vyvinutých softwarů

Vedle zde uvedeného hodnocení korozního napadení je prováděno i hodnocení korozních úbytků. Aluminidy železa v něm vykazují výrazně lepší výsledky než srovnávané oceli. V uvedených podmínkách má aluminid železa výrazně vyšší (pětinásobně) korozní odolnost než austenitická a feritická ocel [9].

Z **obr. 9** vyplývá, že složitost povrchu aluminidu železa je vyšší než u oceli. Z nízkého korozního úbytku na aluminidu železa vyplývá, že se tento materiál rozpouští nerovnoměrně, ale podstatně pomaleji než oceli. Tyto výsledky ukazují, že testovaný aluminid železa je ve sklovině sodnovápenatého typu korozně odolnější než srovnávací oceli. Proto by aluminid železa mohl nahradit žárovzdorné oceli pro aplikace do 1200 ° ve sklovině sodnovápenatého typu. Výzkum užití materiálů na bázi aluminidů železa ve sklářském průmyslu je také zmíněn v [9].

Možnosti aplikace popisu křivky rozhraní pro stanovení korozní odolnosti materiálů (ve spojení s dalšími metodami) jsou reálné a přinášejí další informace o korozním působení. Rozšíření metodiky je dáno i rozšířením užívaných softwarových nástrojů, které jsou v současné době jednoúčelové a komplikované. Cílem je proto vyvinout uživatelsky orientovaný program pro analýzu křivek rozhraní.

Křivku rozhraní lze také získat z profiloměrů a drsnoměrů. Lze tak nedestruktivně porovnávat povrchy materiálů, které vykazují vyšší strukturovanost. V této oblasti také probíhá výzkum a vývoj uživatelsky orientovaného software je pro tento typ dat také cílem.

6. Analýza časových řad

Analýza časových řad pomocí fraktálové geometrie je ve světě nejvíce propracována (především v ekonomii) a má tak největší potenciál na využití v průmyslové praxi. Vzhledem k danému prostoru pro tento článek a dalšímu vývoji v této oblasti, bude příspěvek na toto téma otištěn v některém dalším čísle tohoto časopisu.

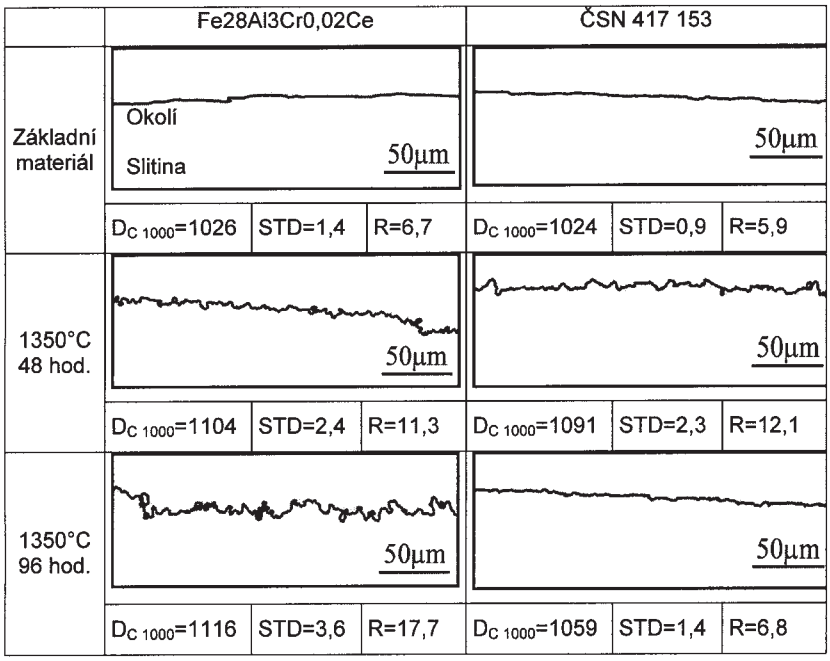

Obr. 9 - Rozhraní mezi slitinou a sklem před a po korozních testech, obvodová dimenze (průměr, $D_{C\ 1000}$), směrodatná odchylka (průměr, STD) a průměr maximální nerovnosti profilu (R)

7. Závěr

Po třech letech se výzkum nových metod hodnocení dat zdokonalil, byly použity další metody pro vyhodnocování, výzkum expandoval do dalších oblastí a v některých případech se dostal do fáze průmyslového nasazení. Přístup kombinace několik metod citlivých na rozdílné charakteristiky popisovaných dat se ukázal jako velice užitečný a vhodný pro popis dat nejenom ve sklářských aplikacích, ale i v dalších odvětvích průmyslu a výzkumu.

Poděkování:

Práce vznikla v rámci výzkumného záměru č. MSM 4674788501, finančně podporovaného Ministerstvem školství, mládeže a tělovýchovy České republiky.

LITERATURA

[1] HOTAŘ, V. - NOVOTNÝ, F., HOTAŘ, A.: Vyhodnocování výrobních dat užitím fraktálových a statistických analýz. Sklář a keramik, **53** [2003], č. 7-8, s. 148-154. ISSN 0037-637.

[2] HOTAŘ, V.: Hodnocení průmyslových dat pomocí fraktálové geometrie. In: Disertační práce, Liberec: Technická univerzita v Liberci, 2005. 123 s.

[3] HOTAŘ, V. - NOVOTNÝ, F.: Evaluation of Surface Defects by Fractal Geometry and Statistical Analysis. In Proceedings of the Norbert Kreidl Memorial Conference, Glastech. Ber. Glass Sci. Technol. Vol. 77 C. 2004. p. 230-237. ISSN 0946-7475.

[4] MANDELBROT. B. B.: The fractal geometry of nature. New York: W. H. Freeman and Co.,1982.

[5] PEITGEN, H.O. - JUERGENS, H. and SAUPE, D. Chaos and Fractals: New Frontiers of Science. New York; Berlin; Heidelberg: Springer-Verlag, 1992.

[6] ZMESKA, O. - NEZADAL, M. - BUCHNICEK, M. AND SEDLAK, O.: HarFA and HARFA: E-JOURNAL. http://www.fch.vutbr.cz/lectures/imagesci/ Brno: Ústav fyzikální a spotřební chemie, 2002.

[7] WOGEL, W.: Glasfehler. Berlin: Spinger-Verlag, 1993. ISBN 3-540-55633-8.

[8] HOTAŘ, V.: Objektivní hodnocení vlnitosti povrchu plochého skla. Sklář a keramik, **55 C** [2005]. s. 29-34. ISSN 0037-637X.

[9] HOTAŘ, A.: Možné aplikace aluminidu železa na bázi Fe3Al ve sklářství. In Sborník přednášek 12. mezinárodní konference sklářské stroje. Liberec: ČSS, Technická univerzita v Liberci. 2006. ISBN 80-7372-092-2.

[10] HOTAŘ, V. - NOVOTNÝ, F.: Surface Profile Evaluation by Fractal Dimension and Statistic Tools. In Proceedings of 11th International Conference on Fracture. Turin (Italy): CCI Centro Congressi Internazionale s.r.l., 2005., p. 588.

[11] HOTAŘ, V.: Fraktálová geometrie [online]. Liberec: Technická univerzita v Liberci, 2006. Dostupný z WWW: < http://www.ksr.tul.cz/fraktaly/ >.

Došlo: 25. 6. 2006

Lektor: doc. RNDr. Miroslav Brzezina, CSc.

[2] ALEŠ, Z., PEXA, M., PAVLŮ, J. (2012). Tribotechnical diagnostics of agricultural machines, Engineering for Rural Development conference Jelgava, 24.-25.05.2012, [online]. [cit.2014-05.01] Available at www: http://www. http://tf.llu.lv.

[3] CELEBRANT, F., ZIEGLER, J., MARASOVÁ, D. (1996). *Technická diagnostika a spolehlivost I.* Tribodiagnostika. 1. vydání. pp. 110 – 138. VŠB-TU, Ostrava. Czech Republic.

[4] HÖNIG, V., HROMÁDKO, J. (2014). Possibilities of using vegetable oil to power diesel engines as well as their impact on engine oil, *Agronomy Research* Vol. 12, No. 8, pp. 323 – 332. Estonian Agricultural University. Estonia.

[5] HÖNIG, V., MIHOLOVÁ, D., ORSÁK, M. (2014) Measurement of Wear Metals in Engine Oils by Atomic Absorption Spektrometry Method. *Manufacturing Technology,* Vol. 14, No. 3, PP. 317 – 322, J. E. Purkyne University in Ústí nad Labem nad Labem. Czech Republic.

[6] HÖNIG, V., SMRČKA, L., HORNÍČKOVÁ, Š. (2014) Application of discriminant analysis in monitoring the wear particles in the engine oil. *Manufacturing Technology,* Vol. 14, No. 3, pp. 322 – 326, J. E. Purkyne University in Ústí nad Labem nad Labem. Czech Republic.

[7] KEJZLAR, P. (2012). Structure and mechanical properties of Fe-25Al-5Zr and Fe-30Al-5Zr intermetallic alloys. *Manufacturing Technology,* Vol. 12, No. 13, pp. 131 – 135, J. E. Purkyne University in Ústí nad Labem nad Labem. Czech Republic.

[8] MIHALČOVÁ, J., HEKMAT, H. (2008). Tribotechnická diagnostika v prevádzke použitých olejov I. metódy hodnotenia častíc opotrebovania v olejoch, *Chemické listy* Vol. 102, pp. 358 – 362. Czech Society of Chemical Engineering, Prague, Czech Republic.

[9] Ministry of Defence CZ. (2007). Instruction for Tribodiagnostics of Engines, Gear and Hydraulic Systems, No. 79: 27/2007:3042, Logistics Division. Prague, Czech Republic

[10] STŘIHAVKOVÁ, E., WEISS, V. (2012) The Identification of the structures new type Al-Si-Mg Ca alloys with different Ca content using of the color metallography. *Manufacturing Technology,* Vol. 12, No. 13, pp. 248 – 251, J. E. Purkyne University in Ústí nad Labem nad Labem. Czech Republic.

[11] STODOLA, J., MACHALÍKOVÁ, J. Spolehlivost a diagnostika BSV. Část: Provozní hmoty a materiály pro MVT. Skriptum. Brno: Vydavatelská skupina UO, Brno. Univerzita obrany, p. 132, ISBN 80-7231-167-0, (2006).

[12] VESELÁ, K.., PEXA, M., MAŘÍK, J. (2014) The effect of biofuels on the quality and purity of engine oil. *Agronomy Research,* Vol. 12, No. 2, pp. 425 – 430, Estonian Agricultural University. Estonia.

Paper number: M201591

Fractal Geometry Used for Evaluation of Corrosion Resistance of Fe-14Al-6Cr Wt. % against Molten Glass

Adam Hotar[1], Vlastimil Hotar[2]
[1]Department of Material Science, Technical University of Liberec, Studentska 2, 461 17 Liberec, Czech Republic, E-mail: adam.hotar@tul.cz
[2]Departmet of Glass Producing Machines and Robotics, Technical University of Liberec, Studentska 2, 461 17 Liberec, Czech Republic, E-mail: vlastimil.hotar@tul.cz

Corrosive attack of metals and alloys by molten glass can be described by parameters of surface roughness. Fractal geometry and statistic tools were used for surface roughness quantification. The obtained parameters of fractal geometry and statistics were determined on boundary curves between alloys and glass which had been generated from the digital photography of sample cross-section. This methodology was successfully used for quantification of surface changes of iron aluminides Fe-14Al-6Cr and austenitic steel during corrosion test in molten soda-lime glass at 1200°C.

Keywords: Fractal geometry, corrosion, molten soda-lime glass, iron aluminide, austenitic steel

1 Introduction

The fractal dimension is closely connected to fractals that were defined by Benoit Mandelbrot [1], though scientists found some geometric problems with specific objects (e.g. the measurement of coast lines using different lengths of rulers by Richardson). A potentially powerful property of the fractal dimension is the ability to describe complexity by using a single number that defines and quantifies structures [2, 3]. The number is mostly a non-integer value and the fractal dimension is higher than the topological dimension. For example, the Koch curve (one of the most famous mathematical deterministic fractals) has the topological dimension $D_T = 1$, but the fractal dimension $D_F = 1.2619$. A smooth curve as a line has the topological dimension $D_T = 1$ and the fractal dimension $D_F = 1$. The fractal dimension can be computed or estimated for a set of points, curves, surfaces, topological 3D objects, etc. and if the fractal dimension is higher than the topological dimension, we name the objects fractals.

Fractal dimension is part of a wider theory, fractal geometry. Fractal geometry is closely connected to chaos theory. Furthermore, the obtained structures were produced by real dynamic systems, and the obtained data was influenced by these dynamic systems [2, 4, 5]. The data can also be tested to chaotic properties and also simulated. Chaotic system can be identified by standard tools like Lyapunov coefficient, Hurst coefficient and also by fractal dimension.

Even though applications of fractal dimension in industry are quite rare and experimental [6], it is possible to find a promising test and applications [7, 8, 9, 10]. Fractal dimension in conjunction with statistics can be used as a useful and powerful tool for an explicit, objective and automatic description of production process data (laboratory, off-line and potentially on-line). Fractal dimension does not substitute other tools like statistics and should be used with other parameters for complete analysis. Here, we carry out research into the mentioned tools on a methodology that uses standard and non-standard parameters to evaluate complex data from industrial practice [11, 12] and laboratories [13, 14, 15]. The methodology finds suitable parameters for a complete analysis of the data from a set of parameters. Only the chosen parameters should be used in order to reduce processing time in industrial practice. The chosen parameters can also be recalculated to one number, and the number can be used in quality assessment, for example [12].

The main aim of the article is to show the developed objective methodology for quantification of surface roughness of alloys (with different chemical compositions) after corrosion attack by molten glass. The selected parameters of fractal dimension and statistics tools were used early in [16, 17] for quantification of the corrosion resistance against molten glass. However, these parameters were evaluated only for comparison between the state of sample surface before and after corrosion test. The present paper describes the methodology application for corrosion attack of Fe-14Al-6Cr in molten soda-lime glass depending on time. In additional, the corrosion attack of iron aluminide was compared with austenitic steel because iron aluminides have been studied as candidates for high-temperature structural applications [18, 19]. The methodology was applied to boundary curve between alloy and glass. The surface roughness was measured after 0 to 168 hour exposure to molten glass. The article does not answer a corrosion mechanism of tested samples and structural changes of sample surfaces in time.

2 Experiment and samples

The chemical compositions of the investigated alloys are summarised in Tab. 1. The samples were cylinders of 18 mm height with a diameter of 12 mm. The surface of samples was carefully polished by using SiC paper grit 1200. The corrosion test was performed at 1200°C in molten soda-lime glass (Tab. 2). Each sample was placed (on the base of cylinder) in an alumina crucible. Then the crucible was filled with glass scrap. The crucible was subsequently heated to 1200°C in a muffle furnace. The corrosion tests were carried out for time intervals: 24, 48, 72, 96 and 168 hours. After each time interval, the crucible was cooled down slowly in the furnace and the crucible was carefully broken. The corrosion resistance of both alloys, including the samples before the test (in raw state, time: 0), was determined and compared using the developed methodology.

The methodology uses statistic tools (like Standard Deviation, Average Roughness, Mean Spacing, etc.), fractal geometry (estimation of fractal dimension), and others tools (like measurement of lengths). The methodology use 22 parameters, however the article shows only some of them.

Tab. 1 *Chemical composition of alloys*

Alloys		Chemical composition					
		Al	C	Cr	Mn	Ni	Fe
Fe-14Al-6Cr	wt.%	14.20	0.02	5.63	max. 0.45	-	Bal.
	at.%	25.41	0.08	5.23	max. 0.40	-	Bal.
EN X8CrNi25-21	wt.%	-	max. 0.20	24.00 – 26.00	1.50	19.00 – 22.00	Bal.
	at.%	-	max. 0.92	25.37 – 27.48	1.50	17.79 – 20.60	Bal.

Tab. 2 *Chemical composition of soda-lime glass*

Composition (wt.%)	SiO_2	Al_2O_3	Fe_2O_3	CaO	MgO	K_2O	Na_2O	SO_3
Soda – lime glass (transparent container glass)	74.03	1.67	0.05	10.08	0.54	0.62	12.68	0.13

2.1 Methodology

The cross section of the surface was investigated by using light optical microscopy, see Fig. 1 A. The shape of the surface - dividing line between the alloy and glass (boundary curve) was evaluated (Fig. 1 B) and described by image analysis using a software tool developed in Matlab.

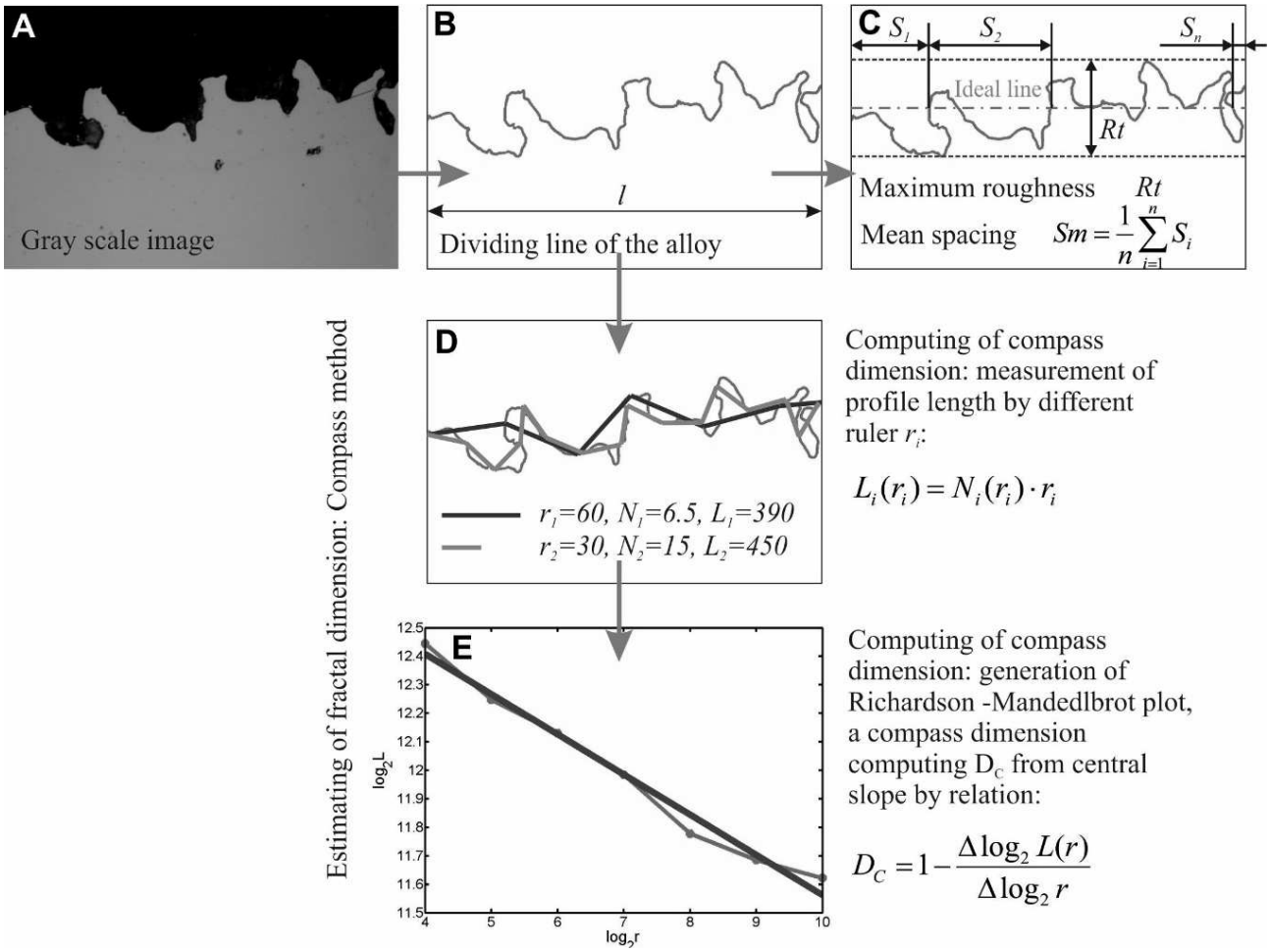

Fig. 1 *Image analysis: A - gray scale image from light optical microscopy, B - evaluated dividing line between the alloy and glass (boundary curve), C - parameter of amplitude (Rt – maximum roughness) and parameter of frequency (Sm – mean spacing), D - computing of compass dimension, E - compass dimension D_C computed from slope*

The evaluation of roughness parameters was carried out on ten places for each sample (each alloy and time interval). The corrosion attack of the tested alloy may be described also using the roughness of the surface. Many types of parameters can be used for a quantification of the metal roughness. The parameters can be divided into three groups:

- parameters of amplitude, useful for depth characterization (Std - Standard Deviation, Ra - Average Roughness, Rt - Maximum Roughness, etc.).
- parameters of frequency, used to describe surface profile spacing parameters and for corrugation frequency characterization (e.g. Sm - Mean Spacing),
- parameters of complexity and deformation, estimation of fractal dimension by Compass Dimension (Dc) [1, 2, 3], by Relative Length (LR) of the profile.

The mentioned parameters of amplitude and frequency are commonly used in industrial practice. These parameters are based on statistics. Average Roughness, Maximum Roughness, and Mean Spacing are surface profile parameters defined by standard ISO 4287-1997 [20]. The parameters of complexity and deformation were selected based on previous experiences.

Standard deviation *Std* is a commonly known statistical tool.

Average Roughness (*Ra*) is also known as the Arithmetical Mean Roughness. The Average Roughness is the area between the roughness profile and its mean line, or the integral of the absolute value of the roughness profile height over the evaluation length:

$$R_a = \frac{1}{l}\int_0^l |z(x)|dx \quad , \tag{1}$$

(where *l* is the evaluation length, *z* is the deviation from the centre line *m*). When evaluated from digital data, the

integral is normally approximated by a trapezoidal rule:

$$R_a = \frac{1}{n}\sum_{i=1}^{n}|z_i| \quad , \tag{2}$$

(where n is the number of measurements). In this field of research, a filtered profile is not being used. For this reason the Average Roughness is called *Pa*.

Maximum Roughness (*Rt*), also Maximum Height, or Total Roughness, is the vertical distance from the deepest trough to the highest peak, Fig. 1 C. For the unfiltered profile, Maximum Roughness is denoted *Pt*.

Sm is the Mean spacing between peaks, now with a peak defined relative to the mean line. A peak must cross above the mean line and then cross back below it. If the width of each peak is denoted as *Si*, then the mean spacing is the average width of a peak over the evaluation length, Fig. 1 C:

$$Sm = \frac{1}{n}\sum_{i=1}^{n} S_i \quad , \tag{3}$$

The estimated Compass Dimension expresses the degree of profile complexity by means of a single number [1]. A compass method [1, 2, 3] is based on measuring the profile (curve) using different ruler sizes (Fig. 1 D) according to the equation:

$$L_i(r_i) = N_i(r_i)\cdot r_i \quad , \tag{4}$$

Where L_i is the length in i-step of the measurement, r_i is the ruler size and N_i is the number of steps needed for the measurement. If the profile is fractal, and hence the estimated fractal dimension is larger than the topological dimension, then the length measured increases as the ruler size is reduced. The logarithmic dependence between $\log_2 N(r_i)$ and $\log_2 r_i$ is called the Richardson-Mandelbrot plot (Fig. 1 E). The Compass Dimension is then determined from the slope *s* of the regression line:

$$D_C = 1 - s = 1 - \frac{\Delta \log_2 L(r)}{\Delta \log_2 r} \quad , \tag{5}$$

For better comparison of the results, the dimension is multiplied by 1000 ($D_{C\ 1000}$). The fractal dimension can also be estimated using a different method [2, 3].

The rate of profile deformation can be evaluated from its Relative Length L_R. This fast and reliable method measures the ratio of the profile length l_{PIXEL} (red curve in Fig. 1 B) using the smallest ruler (1 pixel) r_{PIXEL} and the length of the projection l (Fig. 1 B)

$$L_R = \frac{l_{PIXEL}}{l} \quad . \tag{6}$$

3 Results and discussion

Graphs in Fig. 2 to Fig. 6 show the results of analysis for the dividing line between alloys and glass. Average values were used in order to compare results. The analysis using the developed methodology has two steps.

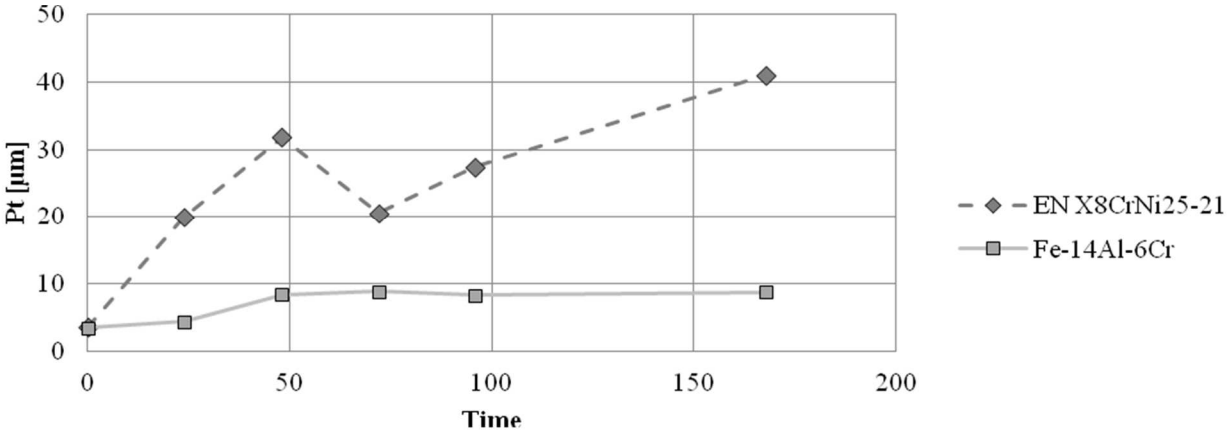

Fig. 2 *The average value of Maximum Roughness of profile, Pt as a function of time for corrosion in molten soda-lime glass*

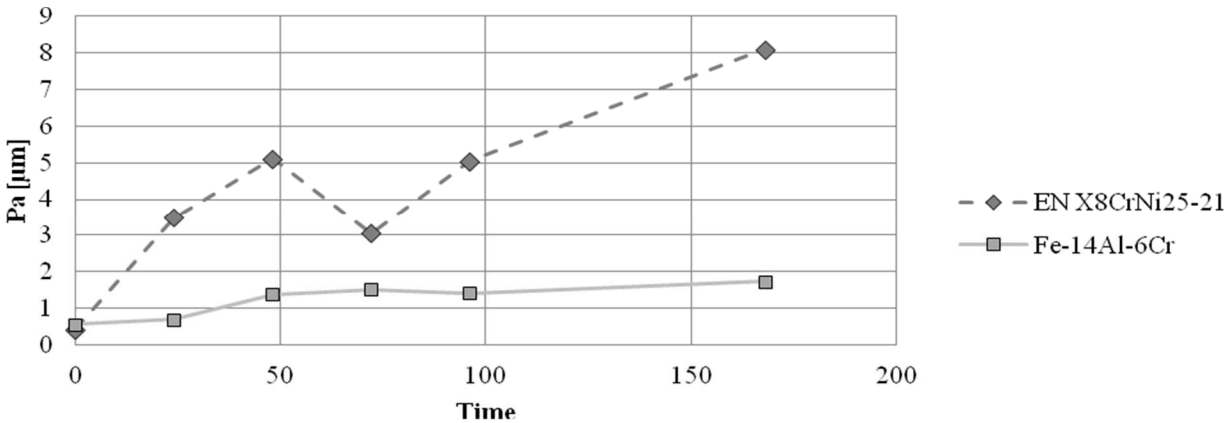

Fig. 3 *The average value of Average Roughness of profile, Pa as a function of time for corrosion in molten soda-lime glass*

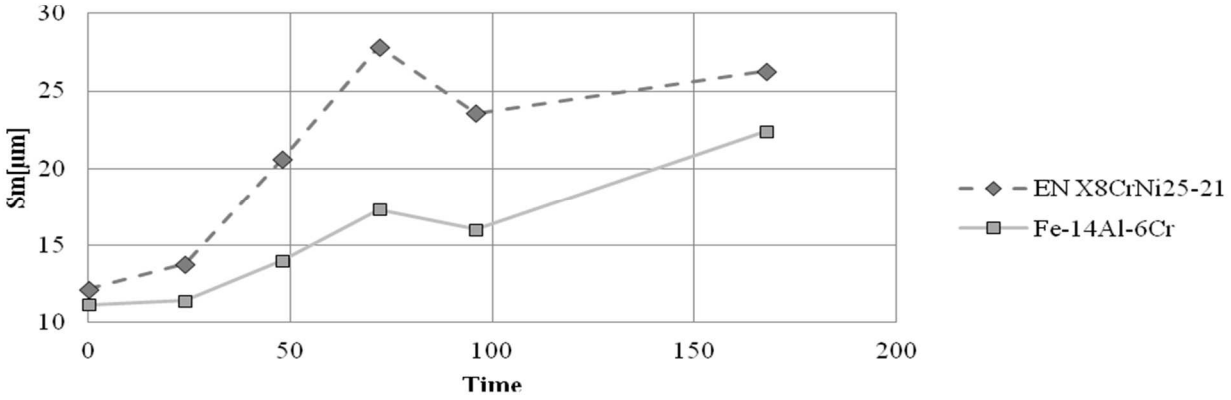

Fig. 4 *The average value of Mean Spacing of profile, Sm as a function of time for corrosion in molten soda-lime glass*

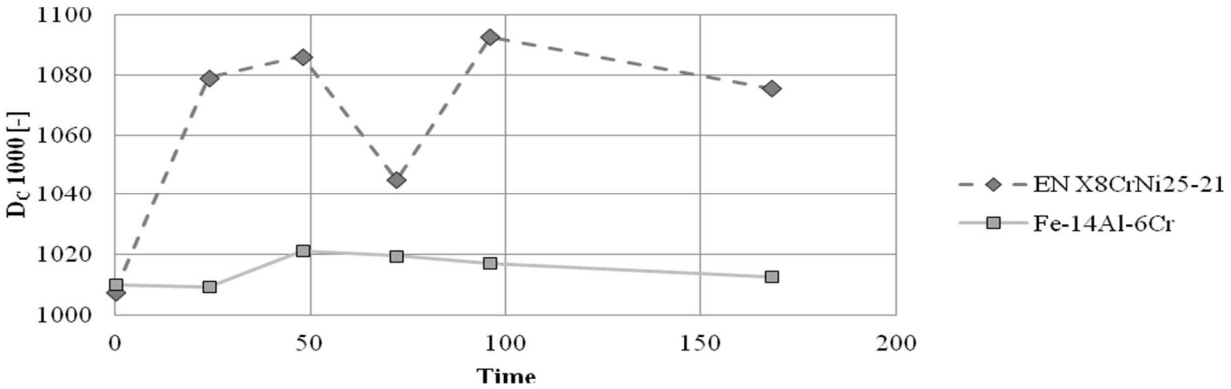

Fig. 5 *The average value of fractal dimension estimation, Compass Dimension of profile DC 1000 as a function of time for corrosion in molten soda-lime glass*

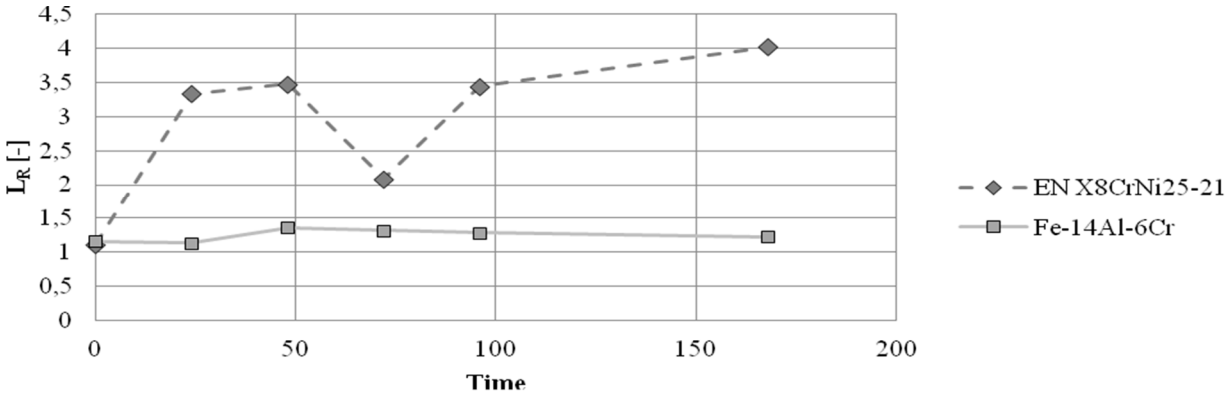

Fig. 6 *The average value of Relative Length measurement, L_R as a function of time for corrosion in molten soda-lime glass*

The first step is a specification of appropriate parameters for fast and reliable analysis for data evaluation. Mentioned methodology contains 22 parameters. However, only chosen parameters were used for a complete analysis in order to simplify the analysis and to reduce the processing time.

Some parameters linearly correlate with the others (they provide similar information about the data). To evaluate the parameters objectively, Pearson's correlation coefficients were computed, see Tab. 3. A correlation between the chosen parameters is clearly visible (*Pa* and *Pt*). The L_R parameter correlates less with the parameters *Pa* and *Pt*, but still significantly. The $D_{C\ 1000}$ parameter correlates less with the parameters *Pa* and *Pt*, but correlates with the L_R parameter. The *Sm* parameter does not correlate. If the situation is simplified and a linear correlation is assumed, we can specify suitable parameters for evaluation of these types of data as: Maximum Roughness, *Pt* (*parameter of amplitude*), Mean Spacing, *Sm* (*parameter of frequency*), Compass Dimension, $D_{C\ 1000}$ (*parameter of complexity and deformation*). These 3 parameters provide diverse information about the data.

Second, it is possible to objectively describe a character of metal structure after corrosion attack. We are able to draw the conclusions:

Parameter of amplitude, Maximum Roughness *Pt* (Fig. 2), shows deepness of corrosion attack of metal surface by glass melt. The average dividing line deepness of alloy Fe-14Al-6Cr grows slowly up to 168 hours because iron aluminide dissolved slowly and uniformly in the molten glass than EN X8CrNi25-21 [16, 17]. The average dividing line deepness of austenitic steel grows from raw state during attack to 48 hours (Fig. 7). After 48 hours, it is apparent that corrosion protrusions penetrate less

deeply into the surface of steel. It does not mean increase of corrosion resistance, but probably a progress of corrosion attack is more uniform in this time period. This should be analysed with using other methods e.g. the measurement of weight loss, chemical analyses etc. The maximal deepness of corrosion attack is after 168 hours.

Tab. 3 *Correlation coefficients of selected parameters*

	Relative Length, L_R [-]	Compass Dimension, $D_{C\,1000}$ [-]	Mean Spacing, *Sm* [µm]	Average Roughness, *Pa* [µm]	Maximum Roughness, *Pt* [µm]	Standard Deviation, *Std* [µm]
Standard Deviation, *Std* [µm]	0,9	0,83	0,5	0,99	0,98	1
Maximum Roughness, *Pt* [µm]	0,88	0,85	0,47	0,96	1	
Average Roughness, *Pa* [µm]	0,91	0,82	0,49	1		
Mean Spacing, *Sm* [µm]	0,33	0,3	1			
Compass Dimension, $D_{C\,1000}$ [-]	0,92	1				
Relative Length, L_R [-]	1					

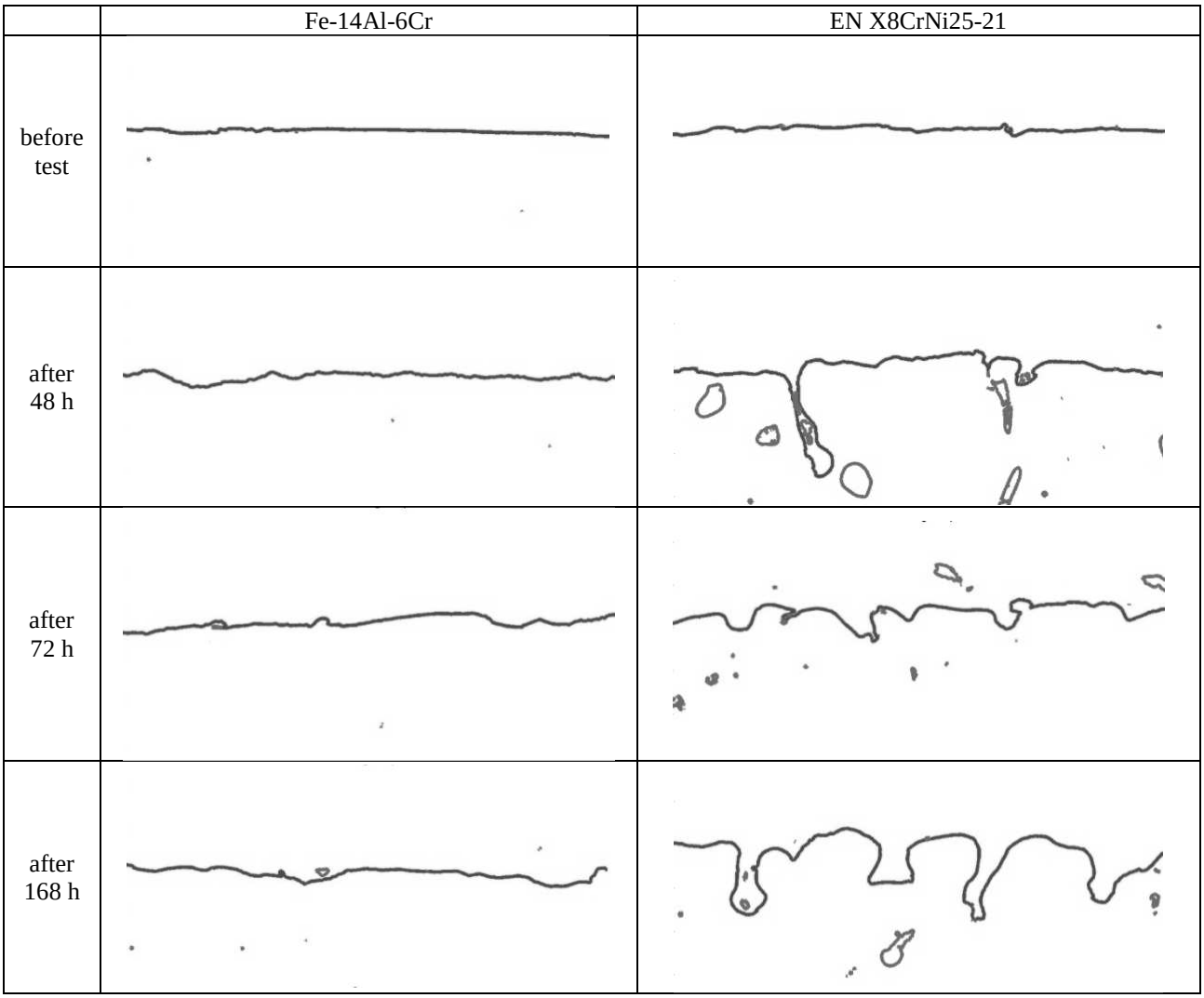

Fig. 7 *Examples of dividing lines between alloy and glass*

Parameter of frequency, Mean Spacing *Sm* (Fig. 4), shows surface profile spacing. The parameter describes corrugation frequency of the dividing line after corrosion attack, how many wavelets can be observed on the surface. For both alloys grows the parameter to 72 hours, where the maximum is. The frequency is connected to the corrosion mechanism.

Parameter of complexity and deformation, Compass Dimension $D_{C\ 1000}$ (Fig. 5), shows level of dividing line complexity. In case of alloy Fe-14Al-6Cr, the average complexity of surface expressed as Compass Dimension grows from 24 to 48 hours, and then slowly decreases. On the other hand, the average surface complexity of alloy EN X8CrNi25-21 increases significantly from raw state during attack up to 48 hours, then falls down, and grows to the maximum after 72 hours. After 96 hours, slight decrease of $D_{C\ 1000}$ was observed. The significant decrease in value of $D_{C\ 1000}$ after 48 hours is probably related to more uniform a progress of corrosion. For understanding the corrosion mechanism of steel, it is necessary to carry out further analysis.

It is obvious, that dividing lines of alloy Fe-14Al-6Cr after corrosion attack are smoother and lower complex. It seems that the corrosion resistance of Fe-14Al-6Cr is higher than steel EN X8CrNi25-21. Austenitic steel showed corrosion protrusions due to probably intergranular corrosion (preferential attack of some phases at grain boundaries). However, this statement should be supported by structural and phase analysis.

4 Conclusion

The article shows that developed methodology can be used for quantification of surface changes of alloys or metals during corrosion attack by molten glass. The suitable parameters for evaluation of these types of data were found: Maximum Roughness, *Pt* (*parameter of amplitude*), Mean Spacing, *Sm* (*parameter of frequency*), Compass Dimension, $D_{C\ 1000}$ (*parameter of complexity and deformation*). The developed methodology was applied to iron aluminide (Fe-14Al-6Cr) and austenitic steel (EN X8CrNi25-21), which were tested in molten soda-lime glass at 1200°C. The results confirmed that it is possible to compare easily corrosion resistance of materials with different chemical composition. These findings extend the possibilities (besides other methods e.g. measurement of weight loss) of quantification of corrosion resistance of metallic materials against molten glass.

Acknowledgement

This research was supported by The Czech Science Foundation GACR (P108/12/1452).

References

[1] MANDELBROT, B.B. (1982). *The fractal geometry of nature*, second ed., Freeman WH and Co., New York.

[2] PEITGEN, H. O., JUERGENS, H., SAUPE, D. (1992). *Chaos and Fractals: New Frontiers of Science*. Springer-Verlag, New York, Berlin, Heidelberg

[3] EVERTSZ, C. J. G., PEITGEN, H. O., VOSS, R. F. (1996). *Fractal Geometry and Analysis*. World Scientific Publishing Co.Pte. Ltd. Singapore

[4] *HILBORN, R. C. (2003). Chaos and Nonlinear Dynamics. New York: Oxford.*

[5] *GULICK, D. (1992). Encounters with Chaos. McGraw-Hill, Inc.*

[6] LEVY, V.J., LUTTON, E., TRICOT, C. (1997). *Fractals in Engineering.* Springer-Verlag, New York, Berlin, Heidelberg

[7] CONCI, A., PROENCA, C.B. (1998). A fractal image analysis system for fabric inspection based on a box-counting method. In: *Computer Networks and Isdn Systems*, Vol. 30, pp. 1887-1895.

[8] YU, L., QI, D.W. (2011). Applying multifractal spectrum combined with fractal discrete Brownian motion model to wood defects recognition. In: *Wood Science and Technology*, Vol. 45, pp. 511-519.

[9] MUGUTHU, J.N., GAO, D. (2013). Profile Fractal Dimension and Dimensional Accuracy Analysis in Machining Metal Matrix Composites (MMCs). In: *Materials and Manufacturing Processes*, Vol. 28, pp. 1102-1109.

[10] ZHENG, C.X., SUN, D.W., AND ZHENG, L.Y. (2006). Recent applications of image texture for evaluation of food qualities - a review. In: *Trends in Food Science & Technology*, Vol. 17, pp. 113-128.

[11] HOTAR, V. (2013). Fractal geometry for industrial data evaluation. In: *Computers & Mathematics with Applications*, Vol. 66, pp. 113-121.

[12] HOTAR, V., NOVOTNY, F., AND REINISCHOVA, H. (2011). Objective evaluation of the corrugation test for sheet glass surfaces. In: *Glass Technology-European Journal of Glass Science and Technology Part A*, Vol. 52, pp. 197-202.

[13] HOTAŘ, V., NOVOTNÝ, F. (2005). Surface Profile Evaluation by Fractal Dimension and Statistic Tools. *In proceedings: 11th International Conference on Fracture. CCI Centro Congressi Internazionale s.r.l.*, pp. 588, Turin.

[14] HOTAR, V., NOVOTNY, F. (2004). Evaluation of surface defects by fractal geometry and statistical analysis. In: *Glass Science and Technology*, Vol. 77, pp. 230-237.

[15] HOTAŘ, V., SALAČ, P. (2014) *Surface Evaluation by Estimation of Fractal Dimension and Statistical Tools.* The Scientific World Journal, vol. 2014, Article ID 435935, 10 pages.

[16] HOTAR, A., KRATOCHVIL, P., AND HOTAR, V. (2009). The corrosion resistance of Fe_3Al-based iron aluminides in molten glasses. In *Kovove Materialy-Metallic Materials*, Vol. 47, pp. 247-252.

[17] HOTAR, A., HOTAR, V., AND NOVOTNY, F. (2014). Corrosion behaviour of Fe-40Al-Zr (at.%) alloy in molten soda-lime glass. In: *Kovove Materialy-Metallic Materials*, Vol: 52, pp. 149-155.

[18] DEEVI, S.C., SIKKA, V.K. (1996). Nickel and iron aluminides: an overview on properties, processing, and applications. In *Intermetallics*, Vol: 4, pp. 357-375

[19] ŠVEC, M., VODIČKOVÁ, V. (2014). The Effect of Niobium Addition and Heat Treatment on the Phase Structure of Fe_3Al – Type Intermetallic Alloys. In *Manufacturing Technology*, Vol. 14, pp.456 – 461.

[20] ISO 4287 (1997). *Geometrical Product Specifications (GPS) - Surface texture: Profile method - Terms, definitions and surface texture parameters.* International Organization for Standardization, Geneva.

Paper number: M201592

Surface Roughness Optimization in Milling Aluminium Alloy by Using the Taguchi´s Design of Experiment

Julia Hricova[1], Natasa Naprstkova[2]
[1]Faculty of Environmental and Manufacturing Technology, Technical University in Zvolen, Studentska 26, 960 53 Zvolen, Slovak Republic, E-mail: julia.hricova@tuzvo.sk
[2]Faculty of Production Technology and Management, J. E. Purkyne University in Usti nad Labem. Pasteurova 3334/7, 400 01 Usti nad Labem. Czech Republic. E-mail: naprstkova@fvtm.ujep.cz

A unique combination of properties makes aluminium one of the most versatile engineering and construction materials. The aluminium alloys can be machined easily and economically if suitable practice and proper tools are used. A statistical design of experiments was performed to investigate the effect of selected cutting parameters and a cutting fluid on the surface roughness of AlMgSi1 aluminium alloy (EN AW 6082) machined by end milling. For the experimental procedure, three cemented carbide end milling cutters of diameter 12 mm with 3 cutting edges were used. The input parameters taken into consideration were helix angle, cutting speed, and using a cutting fluid. With application of ANOVA, the helix angle was investigated as the most significant parameter. The other ones were not statistically significant. To eliminate the negative impact of the cutting fluid on the health and environment, dry machining is recommended in this research.

Keywords: surface roughness, aluminium alloy, design of experiment, end milling

1 Introduction

Surface roughness is an important measure of product quality since it greatly influences the mechanical properties like fatigue behaviour, corrosion resistance, creep life, etc. of automobile parts as well as the production costs. The accuracy of finished parts after machining is defined as the elimination of dimensional deviations, the deviation of surface roughness, geometric shape and position [1]. Surface roughness is traditionally defined by two profile parameters – the arithmetical mean deviation of the assessed profile *Ra* and maximum height of the profile *Rz* in the engineering industry. These parameters are the most commonly used and accepted by research community and industrial engineers because of the simplicity of their geometrical meaning [2, 3].

According to [4] *Ra* is the arithmetic average value of the profile departure from the mean line within a sampling length *l*, which can be defined as in (1).

$$Ra = \frac{1}{l}\int_0^l |z(x)|dx \approx \frac{1}{n}\sum_1^n |z_i|, \qquad (1)$$

Where:

z(x) is the height profile deviation from the mean line.

As mentioned in [5] modern manufacturing encompasses an ever-increasing variety of processes and the engineer's challenge is to select the most economic combination of processes to make a high quality product at the right price. To meet this challenge the manufacturing engineer needs to have a broad knowledge of the ways in which materials can be processed, and the shapes which

Corrosion Science 133 (2018) 141–149

Contents lists available at ScienceDirect

Corrosion Science

journal homepage: www.elsevier.com/locate/corsci

Fractal dimension used for evaluation of oxidation behaviour of Fe-Al-Cr-Zr-C alloys

Vlastimil Hotař[a,*], Adam Hotař[b]

[a] Department of Glass Producing Machines and Robotics, Technical University of Liberec, Studentská 2, 461 17 Liberec, Czech Republic
[b] Department of Material Science, Technical University of Liberec, Studentská 2, 461 17 Liberec, Czech Republic

ARTICLE INFO

Keywords:
A. Intermetallics (based on Fe_3Al)
B. Fractal geometry
C. Oxidation

ABSTRACT

The article describes the possibility of using a methodology for the quantification of oxidised surfaces. The methodology is based on determining the parameters on a dividing line between alloy and air which has been generated from images of a cross-section sample. The parameters are obtained from the methodology using fractal geometry, surface roughness characterisation and statistic tools. The methodology is presented on oxidised iron aluminides (Fe-29.7Al-3.8Cr-0.3Zr-0.2C and Fe-26.4Al-2.8Cr-0.2Zr-0.6C) at high temperatures (900–1200 °C). The results show that methodology can be used for easy quantification of alloy oxidation attacks and for easy comparison of alloy oxidation resistance.

1. Introduction

Iron aluminides have been studiedas potential alloys for structural applications at high temperatures. The reason for choosing them was that binary Fe-Al alloys have very good high-temperature oxidation and corrosion resistance [1,2]. Binary Fe-Al alloys are frequently alloyed to improve mechanical properties, especially at high temperatures. However, alloying could have a detrimental effect on corrosion resistance, for example zirconium content above 0.1 at.% causes the formation of oxide protrusions due to preferential attack of Zr-rich precipitates [3–5]. In the case of alloying by tantalum, the spallation of oxide film was observed, possibly because Laves phase Fe_2Ta formed underneath the oxide scales at temperatures above 900 °C [6]. Therefore, the high-temperature oxidation and corrosion resistance of alloys should be tested and analysed. Measurements of mass changes, analysis of phases in and under the oxide layer, changes of chemical compositions depending on distance from the surface are usually applied to understand the corrosion mechanism and behaviour. Besides these "standard" methods, fractal dimension is increasingly being applied to describe the corrosion behaviour.

1.1. Fractal dimension

Fractal dimension is part of the wider theory of fractal geometry. Fractal geometry is closely connected to chaos theory. Furthermore, the obtained structures were produced by real dynamic systems, and the obtained data was influenced by these systems [7–9]. The data can also be tested for chaotic properties and also simulated. A chaotic system can be identified by standard tools like Lyapunov coefficient, Hurst coefficient and also by fractal dimension.

The fractal dimension was defined by Benoit Mandelbrot [10], though scientists found some geometric problems with specific objects (e.g. the measurement of coastlines using different lengths of rulers by Richardson). A potentially powerful property of fractal dimension is the ability to describe complexity using a single number that defines and quantifies structures [7,11]. The number is mostly a non-integer value and the fractal dimension is higher than the topological dimension. For example, the Koch curve (one of the most famous mathematical deterministic fractals) has the topological dimension $D_T = 1$, but the fractal dimension $D_F = 1.2619$. In contrast, a smooth curve, as a line, has the topological dimension $D_T = 1$ and the fractal dimension $D_F = 1$. The fractal dimension can be computed or estimated for a set of points, curves, surfaces, topological 3D objects, etc. If the fractal dimension is higher than the topological dimension, we name the objects fractals. The fractal dimension of mathematical deterministic fractals can be calculated, while the fractal dimension of natural objects, series and sets can only be estimated using an appropriate method.

Even though applications of fractal dimension in industrial practice are quite rare and experimental [12], it is possible to find a promising test and applications [13–19]. However, the fractal dimension does not substitute other tools like statistics; the dimension provides additional information about the data. Previous research [15,20–24] shows that

* Corresponding author at: Technical University of Liberec, Faculty of Engineering, Department of Glass Producing Machines and Robotics, Studentská 2, CZ 46117 Liberec, Czech Republic.
E-mail addresses: vlastimil.hotar@tul.cz (V. Hotař), adam.hotar@tul.cz (A. Hotař).

https://doi.org/10.1016/j.corsci.2018.01.017
Received 15 June 2017; Received in revised form 5 January 2018; Accepted 18 January 2018

fractal dimension in conjunction with statistics can be used as a useful and powerful tool for an explicit, objective and automatic description of production process data (laboratory, off-line and potentially on-line).

A significant field of application for fractal dimension has been describing the morphology, roughness and texture of material surfaces. Fractal dimension was often used for evaluation or quantification of metallic corrosion previously by many authors. Most of the authors used the estimated fractal dimension for analyses of whole images of a corroded surface using the box counting method [25–31]. Analysis of a dividing line (boundary curve) can also be found [32], but authors also use the box counting method. The fractal dimension of a surface can also be estimated by the triangulation method [18] or using multifractal methods [33]. However, the box counting method has several problems, especially associated with repeatable image acquisition and processing. This method works with binary (black & white) images of fractals, however images of corroded structures are mostly displayed as grey-level or even colourized images. To ensure repeatability, transformation to a binary image must be made in the same way (using the same level of grey for thresholding). The transformation also requires the same image format (the same grey-level, colour mask, compression …). These requirements can be fulfilled with strict adherence, which guarantees repeatability. Complications occur in determining the illumination and hardware conditions. The key issue is surface lighting to capture images: light position (especially angle), irradiance, wavelength of light, and the character of lighting (diffuse or directional). Furthermore, a camera has many parameters to be set, such as shutter speed (exposure time), aperture settings (f-number or f-stop), gain (ISO sensitivity) etc. Problems may occur in the comparison of surfaces with different reflection properties. All these problems make using the box counting method difficult to use for the comparison of several types of surfaces. Ensuring the same conditions independently on a device is impossible.

Pursuant to the given problems, we carry out research on the application of other methods for fractal dimension estimation. The compass method for a dividing line (boundary curve) seems to be suitable for estimating the fractal dimension [15–17,20–22]. Information on roughness or corrosion attack must be reduced to a 1D representation, into the dividing line between alloy and air, or glass and other environments. Cross-section samples must be prepared for image obtaining that make the analysis more time consuming. However, conditions for obtaining the dividing line are not as strict as for the Box-Counting method. It is important to have a sufficient visible contrast between the alloy and the surroundings, a well-focused image, and to use the same scale for comparing a given set of samples. Furthermore, cross-section sample images are used commonly while investigating alloy corrosion behaviour.

In general, cross-sections of corroded samples have different levels of surfaces, Fig. 1. The surfaces are represented by a dividing line between the alloy and oxide layer. The dividing line can be smooth, corrugated or complex on a different level and the line can be compared or described by words or using suitable photos. However, objective quantification can give additional information or can substitute some parameter of the corrosion obtained from other methods.

The selected parameters of fractal dimension and statistical tools were used in [16,17] for the quantification of corrosion resistance against molten glass. Iron aluminides with different chemical compositions and austenitic steel were tested in lead molten glass and in molten soda-lime glass. The results revealed the detrimental effect of zirconium on the corrosion resistance of iron aluminides and the comparable or better corrosion resistance of Fe-25Al-5Cr compared to austenitic steel. Nevertheless, these parameters were evaluated only for comparison between the state of samples surface before and after the corrosion test. The paper [15] described the methodology application for corrosion attack of Fe-14Al-6Cr in molten soda-lime glass depending on time. The basics of the methodology were described earlier in [20,21].

The purpose of this paper is to present a developed objective methodology for quantification of the surface roughness of oxidised alloys for easy comparison of oxidation resistance of alloys, which have different chemical compositions. The methodology, which takes advantage of fractal geometry, was developed and applied on alloys based on Fe-Al-Cr-C-Zr. The high-temperature oxidation behaviour of these alloys were investigated using “standard” methods such as light optical microscopy (LOM), X-ray diffraction (XRD), scanning electron microscopy (SEM), and energy-dispersive X-ray spectrometry (EDS) previously in [3].

2. Experiment

2.1. Samples and oxidation test

Two Fe–Al–Cr–Zr–C alloys were melted in a vacuum furnace and ingots were produced by investment casting [3]. The composition of the alloys (in at.%) is given in Table 1. The ingots with dimensions $30 \times 40 \times 350\,mm^3$ were rolled at 1200 °C to sheets with a final thickness of 13 mm. For oxidation tests rolled samples with dimensions $10 \times 10 \times 1\,mm^3$ were cut by electrical discharge machining (EDM) and then the surfaces of the samples were finely ground to 1200 grit (initial state).

The oxidation tests were carried out using a Setaram SETSYS 16/18 thermobalance with continuous recording of the mass gains and a heating rate of 9 °C/min. Samples of both alloys were oxidised in synthetic air (20.5% O_2, 79.5 N_2) at a flow rate of $1.54 \times 10–6\,m^3/s$ at temperatures ranging from 900 to 1200 °C.

2.2. Methodology

After the oxidation test, samples were carefully cut and encapsulated in the conductive resin. Then the samples were ground and polished with diamond suspensions, the last step was polishing with 0.05 μm of colloidal silica. The cross section of the surface was investigated using light optical microscopy, see Figs. 1 and 2 and Fig. 2a. The images were evaluated and described by image analysis using a software tool developed in Matlab (release R2009a and R2013b). The objective evaluation of a dividing line must solve three key steps:

- repeatable and reliable determination of the dividing line (preprocessing, Fig. 2b),
- evaluation of the dividing line by appropriate parameters (processing, Fig. 2c–f) and
- selection of useful information from the results (post-processing, Fig. 2g).

2.3. Repeatable and reliable determination of dividing line

The same conditions of image acquisition for the determination of the dividing line were provided. The images used were sharp and had a sufficient contrast between the alloy and oxides (scales) or products of corrosion. The images were in the same magnification and the same grey-level, also captured under the same light conditions, using the same exposure setting (shutter speeds, lens aperture, gain) and using the same equipment for image capturing. The borderline (dividing line) between the alloy and oxide layer must be continual from left to right in captured images, without a break, because the aim was to simplify and to objectify the image processing and also to strictly use only the surface for image analysis.

Matlab was used for determining the dividing lines low-level contour plot computation *contour* in software. A toolbox for finding and verifying dividing lines was developed. The toolbox is able to automatically determine the dividing line.

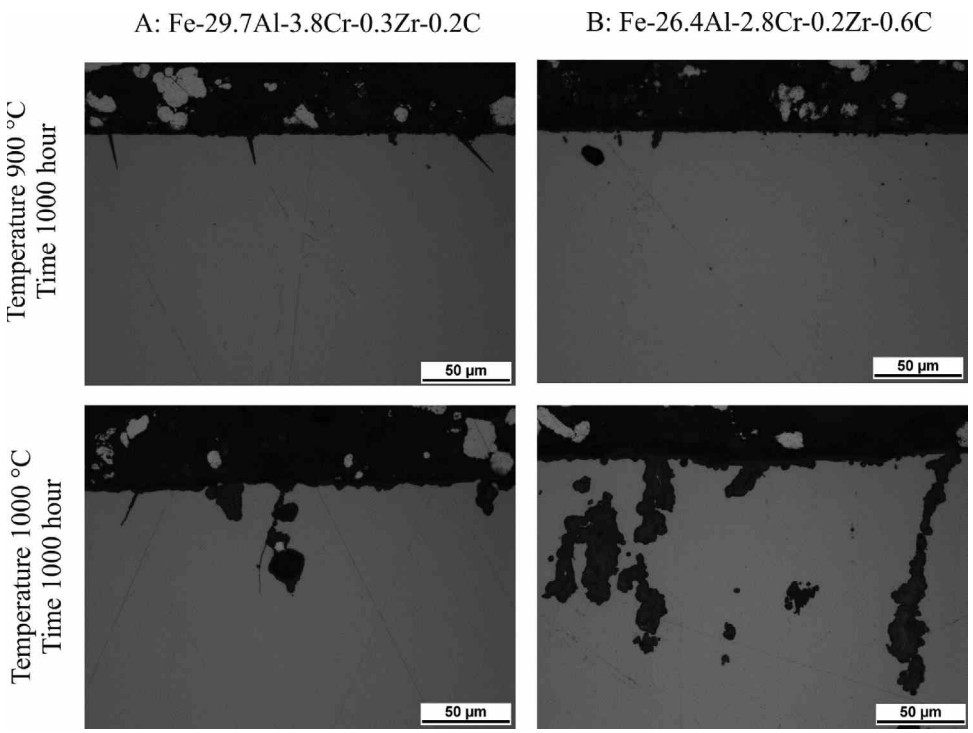

Fig. 1. Grey scale image from cross-sections of corroded samples (light optical microscopy), corrosion test on high temperature for materials: Fe-29.7Al-3.8Cr-0.3Zr-0.2C and Fe-26.4Al-2.8Cr-0.2Zr-0.6C.

Table 1
Chemical composition of alloys in at.%.

Alloy	Al	Zr	Cr	C	Fe
A	29.7	0.3	3.8	0.2	Bal.
B	26.4	0.2	2.8	0.6	Bal.

2.3.1. Evaluation of dividing line by appropriate parameters

Many types of parameters can be used for the quantification of metal roughness. The parameters can be divided into three groups:

- *parameters of amplitude,* useful for depth characterization (*Std* – Standard Deviation, *Pa* – Average Roughness, *Pt* – Maximum Roughness, etc.);
- *parameters of frequency,* used to describe surface profile spacing parameters and for corrugation frequency characterization (e.g. *Sm* – Mean Spacing);
- *parameters of complexity and deformation,* estimation of fractal dimension by Compass Dimension (*Dc*), by Relative Length (L_R) of the profile.

The mentioned parameters of amplitude and frequency are commonly used in industrial practice. These parameters are based on statistics. Typically, standard deviation *Std* is a widely used statistical tool. Average Roughness (*Pa*), Maximum Roughness (*Pt*), and Mean Spacing (*Sm)* are commonly used surface profile parameters defined by standard ISO 4287-1997 [34]. In this field of research, a filtered profile is not used. For this reason, the Average Roughness of profile is called *Pa* (commonly labelled *Ra* after filtered profile) and Maximum Roughness is denoted as *Pt* (commonly labelled *Rt* after filtered profile).

The parameters of complexity and deformation were selected based on previous experience. The estimated Compass Dimension expresses the degree of profile complexity by means of a single number. The compass method [7,10,11] is based on measuring the profile (curve) using different ruler sizes (Fig. 1d) according to the equation:

$$L_i(r_i) = N_i(r_i) \cdot r_i \tag{1}$$

Where L_i is the length in i-step of the measurement, r_i is the ruler size and N_i is the number of steps needed for the measurement. If the profile is fractal, and hence the estimated fractal dimension is larger than the topological dimension, then the length measured increases as the ruler size is reduced. The logarithmic dependence between $\log_2 N(r_i)$ and $\log_2 r_i$ is called the Richardson-Mandelbrot plot (Fig. 2e). The Compass Dimension is then determined from the slope s of the regression line:

$$D_C = 1 - s = 1 - \frac{\Delta \log_2 L(r)}{\Delta \log_2 r} \tag{2}$$

For better comparison of results, the dimension is multiplied by 1000 (D_{C1000}). The fractal dimension can also be estimated using other methods [11].

The rate of profile deformation can be evaluated from its Relative Length L_R. This fast and reliable method measures the ratio of the profile length l_{PIXEL} using the smallest ruler (1 pixel) r_{PIXEL} and the length of the projection l (Fig. 2f)

$$L_R = \frac{l_{PIXEL}}{l} \tag{3}$$

The evaluation of parameters must be carried out at multiple locations. We use 10 locations for each sample (each alloy and time interval), which is sufficient for statistical evaluation.

2.3.2. Selection of useful information from results

The developed methodology contains 22 parameters. However, for complete and reliable analysis significantly fewer parameters can be used, which simplifies analysis and reduces processing time. The reason is that some parameters linearly correlate with others (they provide similar information about the data). Using parameters with the same information should be reduced. For this reason, Pearson's correlation coefficients were computed to evaluate the parameters objectively.

If a linear correlation is assumed, we can specify suitable parameters for the evaluation. A suitable strategy is to get one parameter from each group: parameter of amplitude, parameter of frequency, and parameter of complexity and deformation. We choose the lowest correlation parameter in comparison with another group. These 3 parameters provide diverse information about the data, and thus we would be able to objectively describe the character of oxidation attack of alloys.

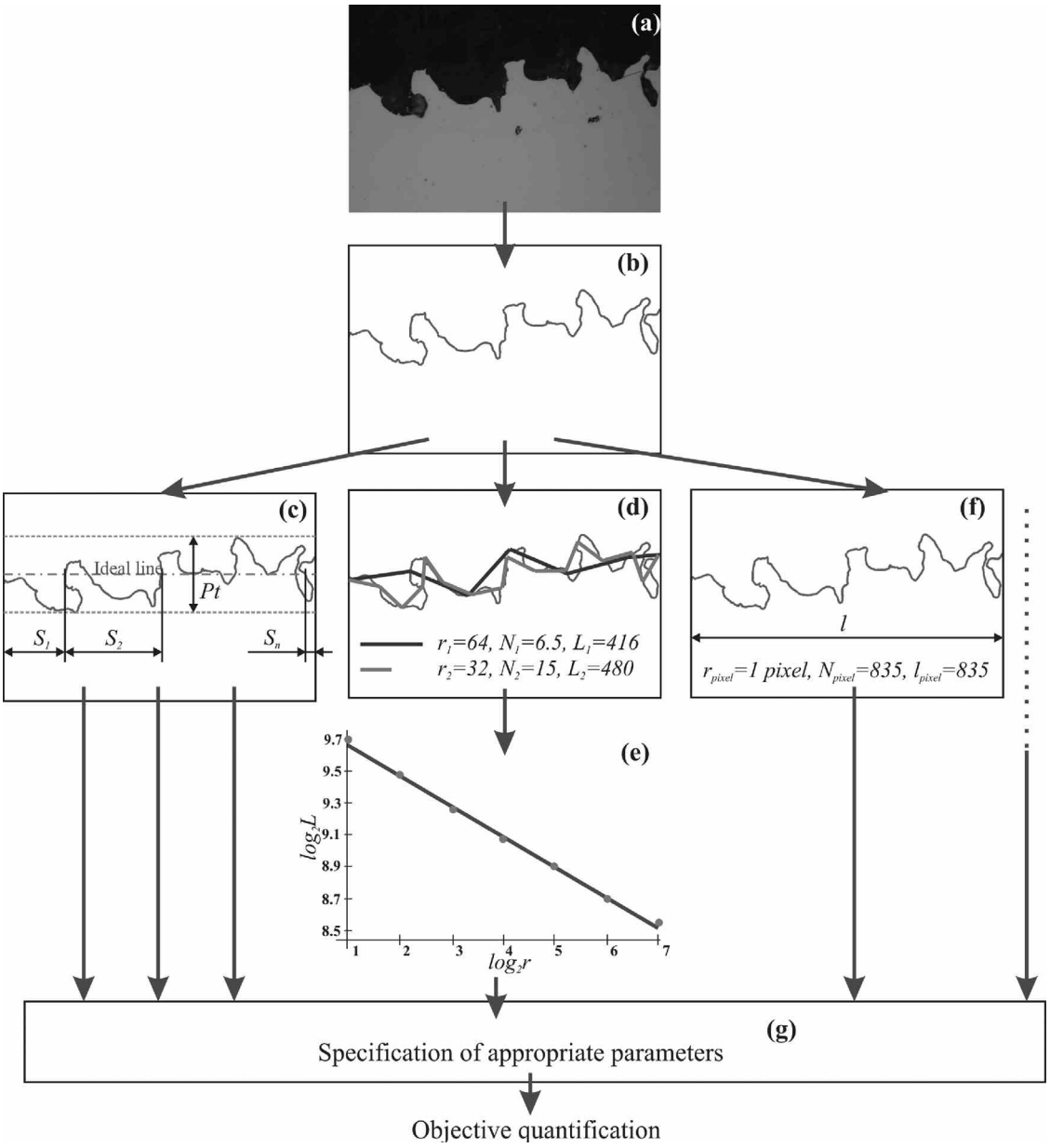

Fig. 2. Image analysis: a – grey scale image from light optical microscopy, b – determined dividing line between the alloy and surroundings – oxides (scales) or products of corrosion (boundary curve), c – parameter of amplitude (*Pt* – maximum roughness) and parameter of frequency (*Sm* – mean spacing), d – computing of compass dimension, e – compass dimension D_C computed from slope, f – computing of relative length L_R, g – specification of parameters for objective quantification.

3. Result and discussion

The structures of tested alloys were described in [35] in detail. Alloy A is characterised by an Fe_3Al matrix with elongated particles of the Laves phase $(Fe,Al)_2Zr$, which occur mostly along the grain boundaries (Fig. 3). On the other hand, alloy B contains ZrC particles instead of the Laves phase. ZrC precipitates were observed not only at the grain boundaries but also inside the grains (Fig. 3). In the case of both alloys, the grain size is about 500 μm.

Alloys A and B were oxidised for up to 1000 h in synthetic air, in a temperature range from 900 to 1200 °C. Corrosion behaviour of alloys A and B, analysis of scales and change of chemical composition near the surface were carefully investigated in [3]. The following text reveals the possibilities of fractal analysis for determination and quantification of oxidation attack of alloys A and B. First, the effect of chemical composition on oxidation resistance (the comparison of oxidation resistance of alloys A and B) was observed at 900 and 1000 °C. The next investigation shows the development of the corrosion attack of alloy B depending on temperature (from 900 to 1200 °C).

3.1. Comparison of oxidation attack of different alloys

The surface roughness parameters of previously specified alloys A and B were measured before and after exposure to air at 900 and 1000 °C. Fig. 4 shows an example of dividing lines from greyscale images in Fig. 1. The roughness of samples before the oxidation test was caused by grinding. During the oxidation of samples, the effect of grinding was suppressed and the effect of high-temperature oxidation became evident on the surface roughness especially at 1000 °C (Fig. 4).

Pearson's correlation coefficients were calculated for evaluation of the obtained parameters using the methodology described, Table 2. Some parameters linearly correlate with others and it can be assumed that they provide similar information on the data. We can specify suitable parameters for the evaluation of these types of data such as:

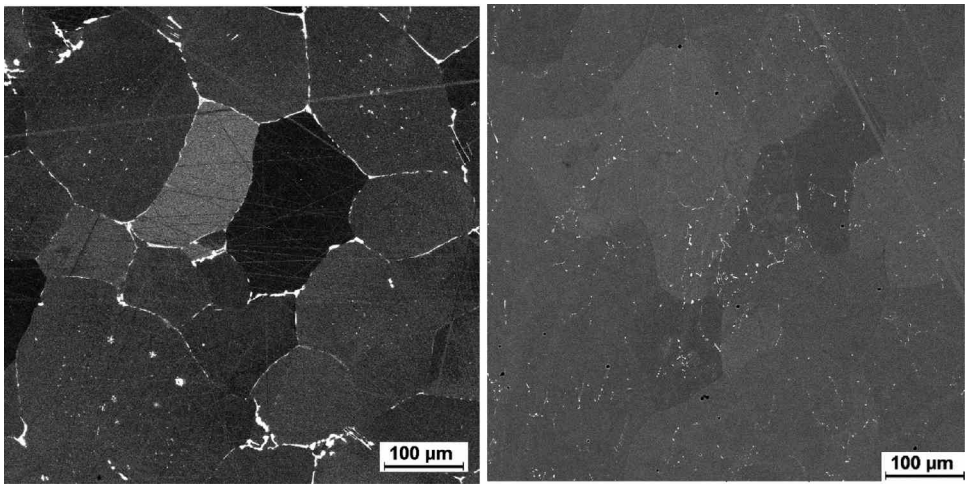

Fig. 3. Structure of alloy A (on the left) and alloy B (on the right).

Standard deviation, *Std* (parameter of amplitude), Mean Spacing, *Sm* (parameter of frequency), Compass Dimension, $D_{C\ 1000}$ (parameter of complexity and deformation). These 3 parameters provide diverse information about surface roughness.

The graphs in Fig. 5–7 show the values of the relevant parameters of alloys A and B oxidised at 900 °C and 1000 °C. Average values were calculated from 10 dividing lines for each sample and they are represented as point in the graphs. Calculated standard deviations are represented as a vertical line in the graphs.

3.1.1. Corrosion at 900 °C

The oxidation processes of both alloys at 900 °C are slightly different [3]. Thin and adherent oxide scales were observed on the surfaces of both alloys but alloy A has higher weight gain than alloy B (Fig. 8). This difference between alloys A and B revealed inspection of cross-section using roughness parameters (Figs. 4–7). In the case of alloy A, higher values of *Std* and $D_{C\ 1000}$ are mainly caused by the presence of cracks, which is observed on surface [3] and on cross-section (Fig. 4). The cracks are oxidised, therefore the formation of cracks relates to the heating of the sample. Besides the cracks, oxide protrusions were also observed. On the other hand, the distance between the cracks (*Sm*) of alloy A is longer as the cracks are deeper and fewer than the small oxide protrusions formed on alloy B. The parameters of amplitude (*Std*) and of complexity ($D_{C\ 1000}$) for alloy A are slightly higher than the parameters of alloy B and these results are well in agreement with values of mass gain, see Fig. 8.

3.1.2. Corrosion at 1000 °C

After oxidation at 1000 °C, inspection of the cross-section shows ingress of the oxidation into the samples of both alloys. Therefore, the evaluated parameters of both alloys grew significantly compared with oxidation at 900 °C (Figs. 5–7). The values of roughness parameters reveal differences of corrosion resistance between alloys A and B against the high-temperature oxidation. Alloy A has lower values of *Std* (Fig. 5) as its oxidation protrusions are smaller than the oxide protrusions into alloy B. In addition, the lower value of the parameter *Sm* shows that frequency of protrusion is lower than in the case of alloy B, see Fig. 6. The surface in initial state (0°) was ground, therefore values

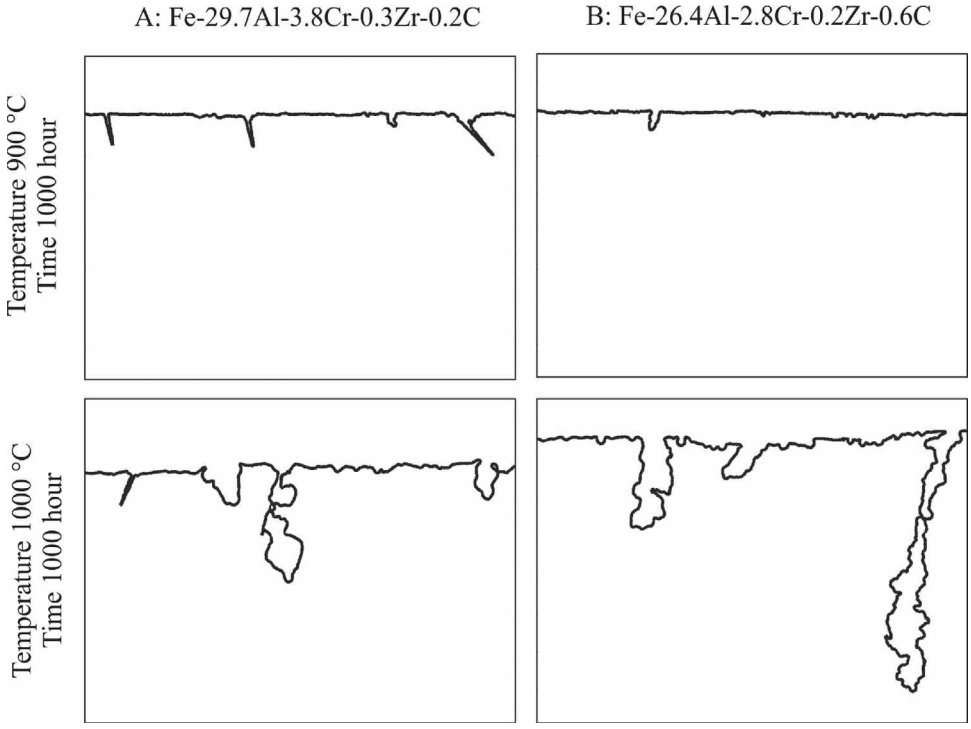

Fig. 4. Evaluated dividing lines between the alloy and oxide layer (from grey scale images in Fig. 1).

Table 2
Correlation coefficients of selected parameters, comparison of oxidation attack of different alloys.

	Relative Length, L_R [—]	Compass Dimension, D_{C1000} [—]	Mean Spacing, *Sm* [μm]	Average Roughness, *Pa* [μm]	Maximum Roughness, *Pt* [μm]	Standard Deviation, *Std* [μm]
Standard Deviation, *Std* [μm]	0.96	0.90	0.63	1.00	1.00	1.00
Maximum Roughness, *Pt* [μm]	0.96	0.91	0.65	0.99	1.00	
Average Roughness, *Pa* [μm]	0.95	0.89	0.62	1.00		
Mean Spacing, *Sm* [μm]	0.62	0.62	1.00			
Compass Dimension, D_{C1000} [—]	0.92	1.00				

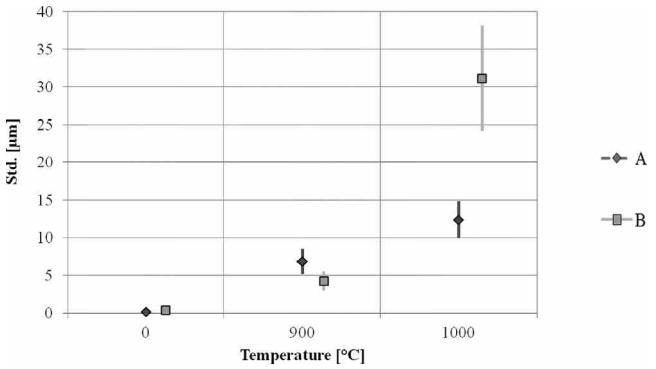

Fig. 5. Standard deviation of profile, *Std* versus temperature of oxidation in air.

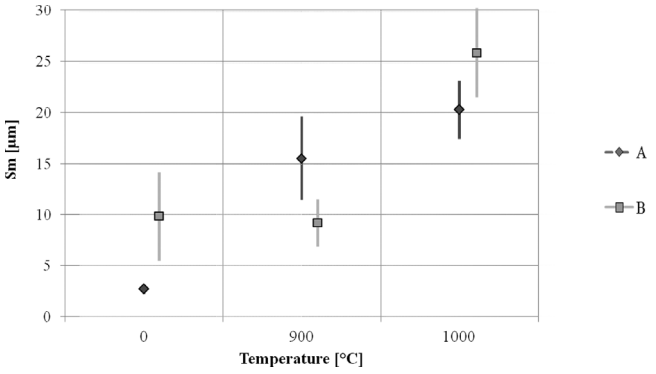

Fig. 6. Average Mean spacing,*Sm*versus temperature of oxidation in air.

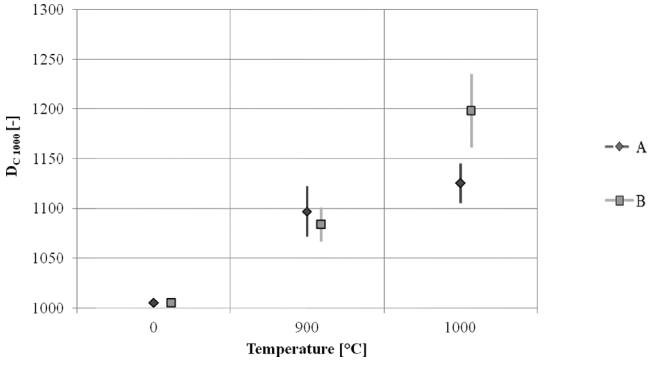

Fig. 7. Average Compass Dimension, $D_{C\ 1000}$ versus temperature of oxidation in air.

of *Sm* is not 0. D_{C1000} also confirms higher oxidation resistance of alloy A in air at high temperature. In the case of alloy B, oxides protrude more frequently and deeply from the surface into the sample (Fig. 4). Therefore, all the obtained parameters of alloy B are higher. The calculated results of the parameters are in correspondence with the

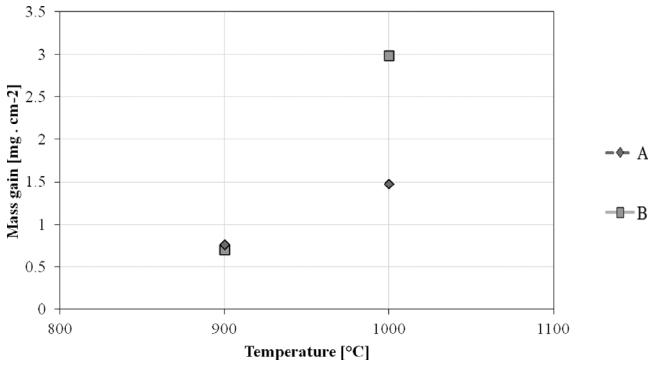

Fig. 8. Mass gain after 1000 h of oxidation versus temperature [3].

investigation in [3]. The difference of oxidation behaviour is caused by the different structure of alloys. The structure of alloy A consists of a Fe_3Al matrix with particles of the Laves phase, but alloy B is characterized by the presence of Fe_3Al matrix and ZrC precipitates instead of the Laves phase. Although both types of Zr-rich particles (Laves phase, ZrC) are preferentially oxidised, ZrC oxidised more readily than Laves phase. Moreover, for alloy B it is typical that oxidation is not limited to ZrC particles and propagates into the Fe_3Al matrix. The lower corrosion resistance of alloy B is also apparent from mass gain, see Fig. 8 (for a better view of the defects in the image, a magnification of 100 was used, for image analysis a magnification of just 500 was used). Fig. 8 reveals that the oxidation of the alloy B was significantly faster and the oxide thickness achieved double the value of that of alloy A after 1000 h.

3.2. Influence of temperature on oxidation of alloy

The influence of temperature on oxidation of alloy B was investigated. The roughness parameters of the oxidised surface were measured before and after exposure to air at different temperatures (at 900, 1000, 1100 and 1200 °C) for the same time periods (1000 h), Fig. 9. First, suitable parameters were specified using Pearson's correlation coefficients for evaluation of such types of data as: Average Roughness, *Pa* (*parameter of amplitude*), Mean Spacing, *Sm* (*parameter of frequency*), Relative Length, L_R (*parameter of complexity and deformation*). The results of Pearson's correlation are summarised in Table 3. The selected parameters provide diverse information about the data and the development of these parameters is seen in Figs. 10–12. Average values (represented as point in graphs) and standard deviations (represented as a vertical line) were calculated from 10 dividing lines, as in the previous analysis. The oxidation at 900 °C caused only a very slight increase in parameters of amplitude and parameters of complexity and deformation. On the other hand, the parameter Average Mean spacing (*Sm*) decreased because oxidation protrusions are deeper, but they are fewer than in the case of surface grinding, see Fig. 11.

Inspection of the surface roughness of oxidised alloy B showed that

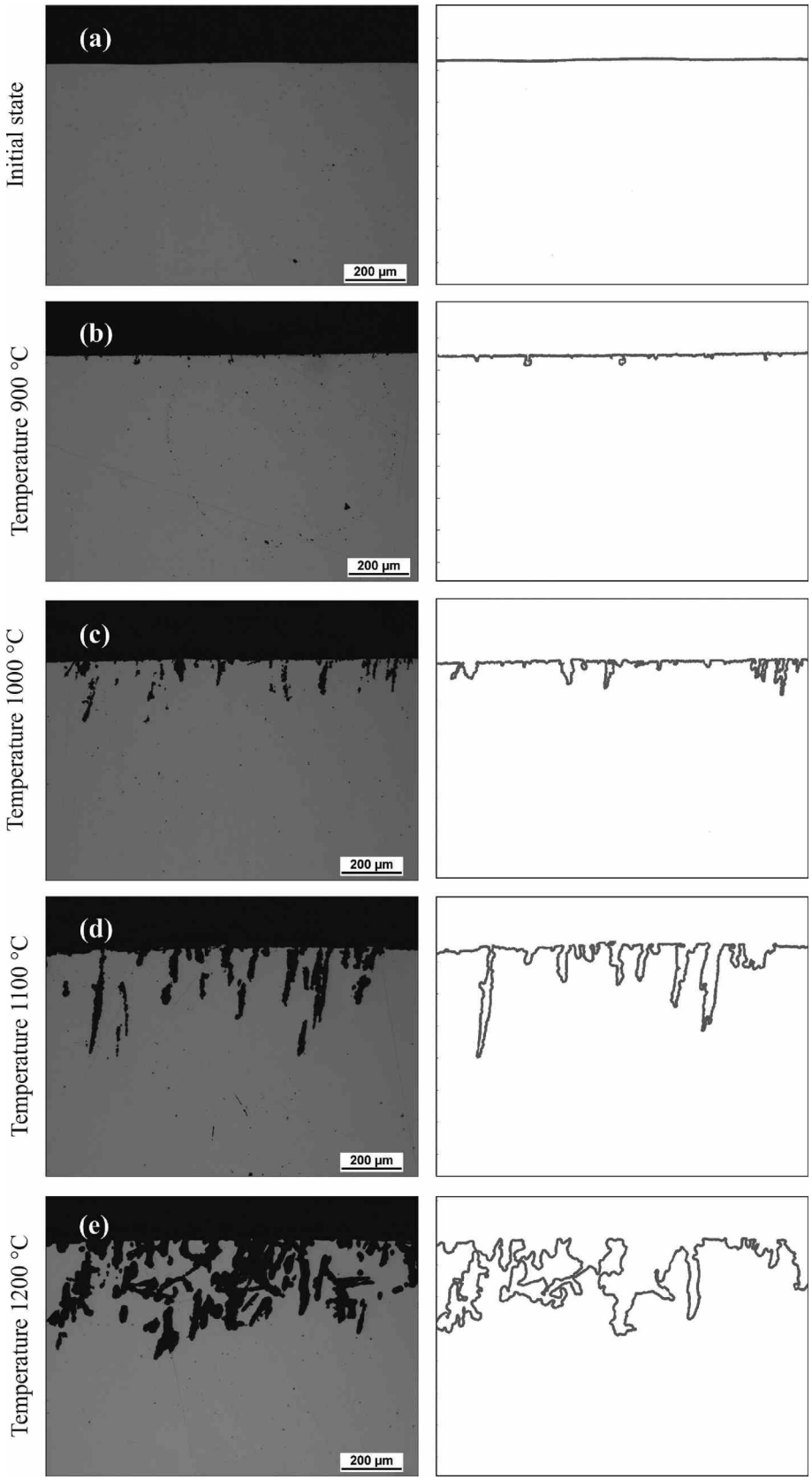

Fig. 9. Grey scale image of oxidised surface in cross-sections after different temperatures (light optical microscopy) – left column; evaluated dividing line between the alloy and oxide layer – right column.

after oxidation at 900 °C, oxides penetrated very little in places of Zr-rich precipitates (Fig. 9 – b). The cross section reveals few oxide protrusions and the protrusions are small. Therefore, parameters *Pa* and L_R increased slightly and parameter *Sm* decreased in comparison with ground surface.

The oxidation at 1000 °C is characterized by the increase of all observed parameters. From Fig. 9 – c it is clear that oxidation penetrated into the surface of alloy B more frequently and more deeply than after

Table 3
Correlation coefficients of selected parameters, influence of temperature on oxidation of alloy B.

	Relative Length, L_R [—]	Compass Dimension, D_{C1000} [—]	Mean Spacing, *Sm* [μm]	Average Roughness, *Pa* [μm]	Maximum Roughness, *Pt* [μm]	Standard Deviation, *Std* [μm]
Standard Deviation, *Std* [μm]	0.93	0.94	0.75	1.00	0.98	1.00
Maximum Roughness, *Pt* [μm]	0.92	0.92	0.74	0.97	1.00	
Average Roughness, *Pa* [μm]	0.93	0.94	0.75	1.00		
Mean Spacing, *Sm* [μm]	0.59	0.71	1.00			
Compass Dimension, D_{C1000} [—]	0.94	1.00				
Relative Length, L_R [—]	1.00					

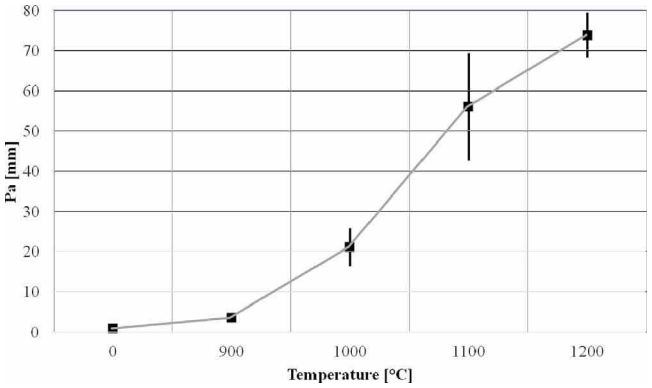

Fig. 10. Average Roughness of profile, *Pa* versus temperature of oxidation in air.

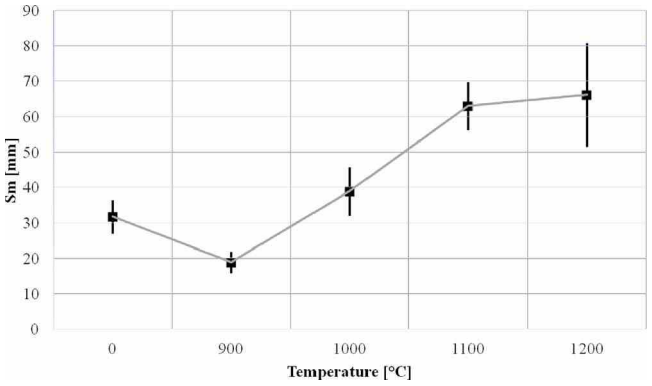

Fig. 11. Average Mean spacing, *Sm* versus temperature of oxidation in air.

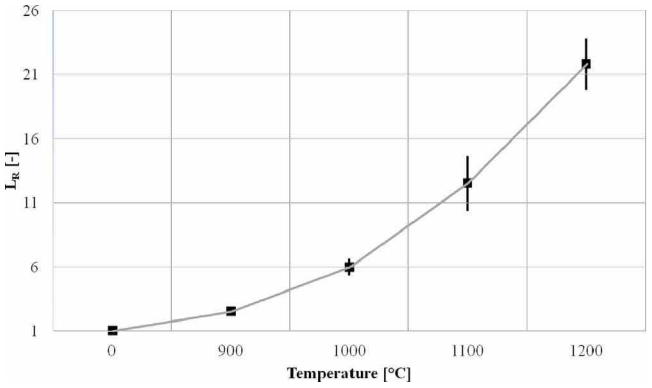

Fig. 12. Average Relative Length, L_R versus temperature of oxidation in air.

oxidation at 900 °C. The oxide protrusions are slender and deep because Zr-rich particles are preferentially oxidised. Further deepening and an increase in the number of protrusions is caused by increasing the temperature to 1100 °C. Mean spacing *Sm* clearly shows the growth in the number of protrusions and the increase of the protrusion size is clearly defined by the Roughness of profile *Pa* and Relative length L_R. The shape of the protrusion (Fig. 9 – d) and early investigation [3] reveal that ZrC precipitates are still preferentially oxidised. On the other hand, for oxidation at 1200 °C it is typical that the oxidation is not limited to the ZrC particles but extends into the Fe-Al matrix. The oxidation does not progress only perpendicularly from the surface into the core but it is branched, see Fig. 9 – e. The branching of oxidation is well reflected by Relative length L_R. The value of the Relative length again significantly increased while the growth of parameters *Pa* and *Sm* slowed down after oxidation at 1200 °C. In addition, a relationship between the lengths of the curve can be called area size, and weight gain is also apparent from Figs. 12 and 13 and .

4. Conclusion

The oxidation attack of alloys based on iron aluminide (Fe-29.7Al-3.8Cr-0.3Zr-0.2C and Fe-26.4Al-2.8Cr-0.2Zr-0.6C) by high temperatures (900–1200 °C) was quantified by methodology using fractal geometry and statistic tools. For the definition of an oxidised surface, one parameter was applied from each specific group: parameter of amplitude, parameter of frequency, and parameter of complexity and deformation.

The results can be summarized as follows:

1. The results reveal that the methodology can be used for describing and comparing oxidation of the surface attack of alloys with different chemical compositions. The methodology is useful for definition of attack degree, and then it is easy to determine the corrosion resistance of alloys. In the case of the tested alloys, the values of surface parameters show that alloys Fe-29.7Al-3.8Cr-0.3Zr-0.2C and Fe-26.4Al-2.8Cr-0.2Zr-0.6C have similar corrosion resistance at 900 °C. On the other hand, Fe-29.7Al-3.8Cr-0.3Zr-0.2C has greater corrosion resistance than Fe-26.4Al-2.8Cr-0.2Zr-0.6C after oxidation by 1000 °C.
2. The temperature also has a significant influence on corrosion resistance besides the chemical composition. The growth of oxide protrusions during temperature increase has been well recorded by all parameters. In the temperature range 900–1100 °C, the parameter of amplitude, parameter of frequency, and parameter of complexity and deformation grew rapidly. Above 1100 °C, the oxide protrusions therefore branched by a parameter of amplitude, and the parameter of complexity and deformation only grew.
3. This and also previous research shows that the fractal dimension in conjunction with statistics can be used as a useful and powerful tool for an explicit, objective and automatic description of corrosive attacks.

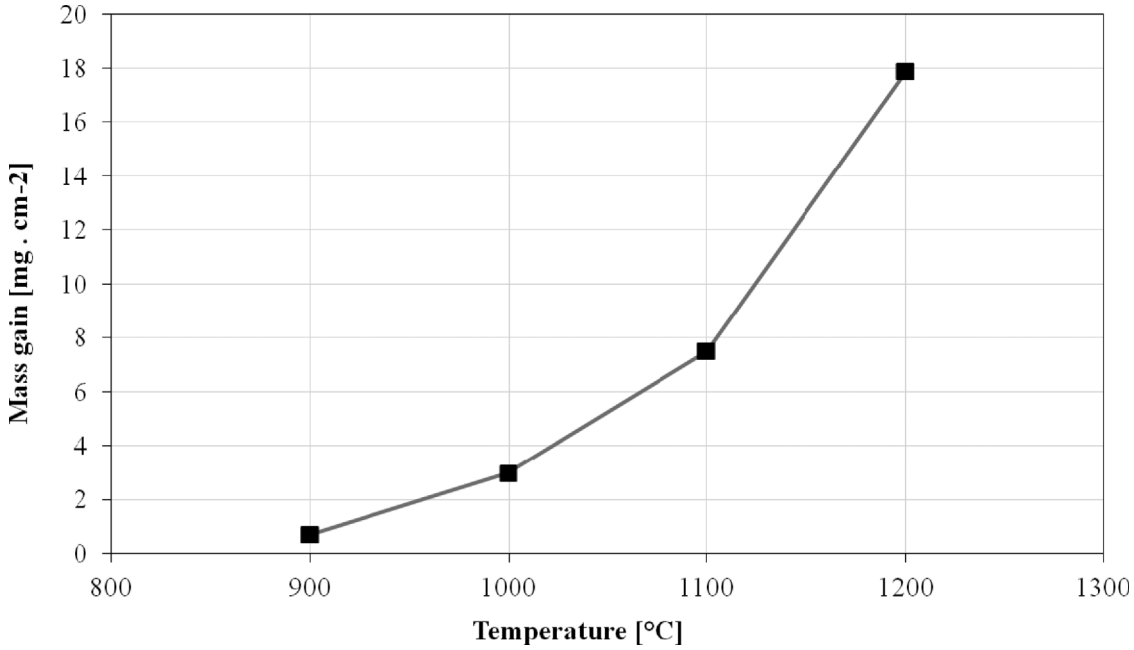

Fig. 13. Mass gain of alloy B after 1000 h of oxidation versus temperature [3].

4. The investigation in this manuscript confirms that the application of the tested methodology is not limited by the used material and environments (air, glass, etc.).

Acknowledgements

This article was written at the Technical University of Liberec as part of the project "Research and development in the field of glass-producing machines, industrial and service robotics" (SGS 21128/115) with the support of the Specific University Research Grant, as provided by the Ministry of Education, Youth and Sports of the Czech Republic in the year 2017. The authors would like to thanks Max-Planck-Institut für Eisenforschung GmbH for performing the corrosion tests.

References

[1] C.G. McKamey, J.H. DeVan, P.F. Tortorelli, V.K.J. Sikka, A review of recent developments in Fe_3Al-based alloys, J. Mater. Res. 6 (1991) 1779–1805.
[2] P.F. Tortorelli, K. Natesan, Critical factors affecting the high-temperature corrosion performance of iron aluminides, Mater. Sci. Eng. A 58 (1998) 115–125.
[3] A. Hotar, M. Palm, P. Kratochvil, V. Vodickova, S. Danis, High-temperature oxidation behaviour of Zr alloyed Fe3Al-type iron aluminide, Corros. Sci. 63 (2012) 71–81.
[4] D. Janda, et al., The effect of micro-alloying with Zr and Nb on the oxidation behavior of Fe_3Al and FeAl alloys, Intermetallics 41 (2013) 51–57.
[5] A. Hotar, P. Kejzlar, M. Palm, J. Mlnařík, The effect of Zr on high-temperature oxidation behaviour of Fe_3Al-based alloys, Corros. Sci. 100 (2015) 147–157.
[6] A. Hotar, M. Palm, Oxidation resistance of Fe-25Al-2Ta (at.%) in air, Intermetallics 18 (2010) 1390–1395.
[7] H.O. Peitgen, H. Juergens, D. Saupe, Chaos and Fractals New Frontiers of Science, Springer-Verlag, New York, Berlin Heidelberg, 1992.
[8] R.C. Hilborn, Chaos and Nonlinear Dynamics, (2003) (Oxford New York).
[9] D. Gulick, Encounters with Chaos, McGraw-Hill, Inc, New York, 1992.
[10] B.B. Mandelbrot, The Fractal Geometry of Nature, second, Freeman WH and Co., New York, 1982.
[11] C.J.G. Evertsz, H.O. Peitgen, R.F. Voss, Fractal Geometry and Analysis, World Scientific Publishing Co. Pte Ltd., Singapore, 1996.
[12] V.J. Levy, E. Lutton, C. Tricot, Fractals in Engineering, Springer-Verlag, New York, Berlin Heidelberg, 1997.
[13] A. Conci, C.B. Proenca, A fractal image analysis system for fabric inspection based on a box-counting method, Comput. Netw. ISDN 30 (1998) 1887–1895.
[14] J.N. Muguthu, D. Gao, Profile fractal dimension and dimensional accuracy analysis in machining metal matrix composites (MMCs), Mater. Manuf. Process. 28 (2013) 1102–1109.
[15] A. Hotar, V. Hotar, Fractal geometry used for evaluation of corrosion resistance of Fe-14Al-6Cr wt.% against molten glass, Manuf. Technol. 15 (2015) 534–541.
[16] A. Hotar, P. Kratochvil, V. Hotar, The corrosion resistance of Fe_3Al-based iron aluminides in molten glasses, Kovove Mater. 47 (2009) 247–252.
[17] A. Hotar, V. Hotar, F. Novotny, Corrosion behaviour of Fe-40Al-Zr (at.%) alloy in molten soda-lime glass, Kovove Mater. 52 (2014) 149–155.
[18] E.J. Kim, S.J. Park, J.H. Heo, H. Ch. Shin, Corrosion resistance of stainless steels analyzed by fractal geometry, J. Electrochem. Sci. Technol. 1 (2) (2010) 112–116 http://koreascience.or.kr/journal/view.jsp?kj=E1JTC5&py=2010&vnc=v1n2&sp=112 (Accessed 24 April 2017).
[19] F. Novotny, M. Horak, M. Stary, Abrasive cylindrical brush behaviour in surface processing, Int. J. Mach. Tool Manuf. 118–119 (2017) 61–72.
[20] V. Hotar, F. Novotny, Surface profile evaluation by fractal dimension and statistic tools, Proc. 11th International Conference on Fracture, CCI Centro Congressi Internazionale s.r.l. Turin, 2005, p. 588.
[21] V. Hotar, F. Novotny, Evaluation of surface defects by fractal geometry and statistical analysis, Glass Sci. Technol. 77 (2004) 230–237.
[22] V. Hotar, Fractal geometry for industrial data evaluation, Comput. Math. Appl. 66 (2013) 113–121.
[23] V. Hotar, F. Novotny, H. Reinischova, Objective evaluation of the corrugation test for sheet glass surfaces, Glass Technol.-Eur. J. Glass Sci. Technol. Part A 52 (2011) 197–202.
[24] V. Hotar, P. Salač, Surface evaluation by estimation of fractal dimension and statistical tools, Sci. World J. 24 (2014), http://dx.doi.org/10.1155/2014/435935 Article ID 435935, 10 pages (Accessed 24 April 2017).
[25] J.J. Park, S.I. Pyun, Pit formation and growth of alloy 600 in Cl- ion-containing thiosulphate solution at temperatures 298–573 K using fractal geometry, Corrros. Sci. 45 (2003) 995–1010.
[26] F.F. Feliciano, F.R. Leta, F.B. Mainier, Texture digital analysis for corrosion monitoring, Corrros. Sci. 93 (2015) 138–147.
[27] Ch. Liang, W. Zhang, Fractal characteristic of pits distribution on 304 stainless steel corroded surface and its application in corrosion diagnosis, J. Wuhan Univ. Technol. 22 (2007) 389–393.
[28] N. Lin, J. Guo, F. Xie, J. Zou, W. Tian, X. Yao, H. Zhang, B. Tang, Comparison of surface fractal dimensions of chromizing coating and P110 steel for corrosion resistance estimation, Appl. Surf. Sci. 311 (2014) 330–338.
[29] R.M. Pidaparti, B.S. Aghazadeh, A. Whitfield, A.S. Rao, G.P. Mercier, Classification of corrosion defects in NiAl bronze through image analysis, Corrsion. Sci. 52 (2010) 3661–3666.
[30] F. Jin, F.P. Chiang, Nondestructive evaluation of corrosion by fractal geometry, Res. Nondestruct. Eval. 7 (1996) 229–238.
[31] J.M. Costa, F. Sagués, M. Vilarrasa, Fractal patterns from corrosion petting, Corrros. Sci. 32 (1991) 665–668.
[32] D.X. Yang, Y.G. Liu, M.H. Fang, Z.H. Huang, D.Y. Ye, Study on the slag corrosion resistance of unfired Al2O3–SiC/β-Sialon/Ti(C, N)–C refractories, Ceram. Int. 40 (2014) 1593–1598.
[33] S. Xu, S. Ren, Y. Wang, Three-Dimensional surface parameters and multi-Fractal spectrum of corroded steel, PLoS One 24 (2015) Article ID e0131361, http://journals.plos.org/plosone/article?id=10.1371/journal.pone.0131361 (Accessed 24 April 2017).
[34] I.S.O. 4287, Geometrical Product Specifications (GPS) – Surface texture: Profile method – Terms, definitions and surface texture parameters, International Organization for Standardization, Geneva, 1997.
[35] P. Kratochvíl, F. Dobeš, J. Pešička, P. Málek, J. Buršík, V. odičková V, P. Hanus, Microstructure and high temperature mechanical properties of Zr-alloyed Fe3Al-type aluminides: the effect of carbon, Mater. Sci. Eng. A 48 (2012) 175–182.